UNIVERSITY OF SOUTHAMPTON

FACULTY OF ENGINEERING, SCIENCE & MATHEMATICS
School of Engineering Sciences

A phenomenological rapid sloshing model for use as an operator guidance system on Liquefied Natural Gas carriers

by

Bernhard Godderidge

Thesis for the degree of Doctor of Engineering

June 2009

UNIVERSITY OF SOUTHAMPTON

ABSTRACT

FACULTY OF ENGINEERING, SCIENCE & MATHEMATICS

SCHOOL OF ENGINEERING SCIENCES

Doctor of Engineering

A PHENOMENOLOGICAL RAPID SLOSHING MODEL FOR USE AS AN OPERATOR GUIDANCE SYSTEM ON LIQUEFIED NATURAL GAS CARRIERS

by Bernhard Godderidge

A concept for a non-intrusive sloshing guidance system based on a phenomenological Rapid Sloshing Model is proposed to reduce the operational risk of sloshing damage to LNG carriers. A numerical sloshing model is implemented in a commercial Navier-Stokes Computational Fluid Dynamics (CFD) code which uses a volume-of-fluid approach for the simulation of multi-fluid problems. The effect of spatial and temporal discretisation and turbulence is investigated using systematic variation. Dimensional analysis of the multiphase flow regime and examination of the relative velocity at the fluid interface show that an *inhomogeneous* multiphase model is appropriate for the simulation of a violent sloshing flow. This is confirmed by the good agreement with the experimental data of Hinatsu. The effect of fluid compressibility is investigated for sloshing impacts and a criterion based on wave propagation is developed to assess the importance of compressibility. When modelling sloshing with large air bubble entrainment, the choice of fluid compressibility model is shown to have a significant influence on pressure magnitude and frequency of oscillation required for structural assessment and a thermal energy model is required.

The Rapid Sloshing Model (RSM) is based on the observation that the centre of mass of a sloshing fluid tends to follow a particular trajectory. Using a phenomenological modelling approach, the forces affecting the sloshing response are approximated with mathematical functions for restoring force, damping and sloshing impacts. Calculation times for the resulting equations are typically 0.1% of real time on a desktop PC.

A case study of sloshing induced by periodic rotation and translation of two-dimensional longitudinal and transverse sections of membrane LNG tanks is carried out using RSM. RSM is set up using one CFD simulation not considered in the case study and the RSM solutions are then compared to the independent CFD solutions. The fluid momentum from RSM is usually within 5%–15% of the CFD solution for excitation at and near the first resonant period at a filling level near the critical depth. An irregular surge motion profile from an ITTC two-parameter spectrum is applied to the tank and the mean error from the RSM solution remains below 15% when using momentum and transverse force. When applied to sloshing with a 10% filling level excited by an irregular seaway a mean error of 9.6% is obtained. Compared to existing phenomenological modelling approaches the RSM methodology reduces the error by an order of magnitude in sloshing scenarios of practical interest.

A non-intrusive sloshing guidance system based on the Rapid Sloshing Model which is suitable for installation on existing and newbuild LNG carriers can be implemented by applying motion data measured onboard to the RSM to provide operator guidance on the sloshing severity in partially filled LNG tanks. The RSM is set up for a particular LNG carrier with existing sloshing data from the design and class approval stages.

Table of Contents

List of Figures

List of Tables

DECLARATION OF AUTHORSHIP

I, **Bernhard Godderidge** declare that the thesis entitled
A phenomenological rapid sloshing model for use as an operator guidance system on Liquefied Natural Gas carriers
and the work presented in the thesis are both my own, and have been generated by me as the result of my own original research. I confirm that:

- this work was done wholly or mainly while in candidature for a research degree at this University;
- where any part of this thesis has previously been submitted for a degree or any other qualification at this University or any other institution, this has been clearly stated;
- where I have consulted the published work of others, this is always clearly attributed;
- where I have quoted from the work of others, the source is always given. With the exception of such quotations, this thesis is entirely my own work;
- I have acknowledged all main sources of help;
- where the thesis is based on work done by myself jointly with others, I have made clear exactly what was done by others and what I have contributed myself;
- parts of this work have been published as listed in Appendix A.

Signed: ....

Date: ....

Acknowledgements

It is a pleasure to acknowledge the help, support and interest of the people who went along on this rather interesting journey. First of all I wish to thank my supervisors Mingyi Tan and Steve Turnock in Ship Science and Chris Earl (who has since gone on to build yachts for Billionaires) and Nick Cowlan at BMT SeaTech - it certainly was an exciting four years! A big thank you to Ajit Shenoi who got me interested in LNG carriers (seven, or is it eight years ago now?) and helped set up this Engineering Doctorate (EngD).

The industrial partner BMT SeaTech originally suggested that the development of a sloshing guidance system would make an interesting EngD project (it certainly did) and provided invaluable industrial expertise and guidance throughout the project. I was based at the SeaTech office for the last two years of my EngD continuing my work on the sloshing guidance system as well as supporting a number of quite interesting commercial projects.

I also want to thank Sebastian at Rostock University and Y-B for working together and our many interesting discussion on the intricacies of sloshing. A special thank you to Bill Wayne and Teo Popa at SIGTTO who put my work in perspective.

Also, a word of appreciation to the guys at CFX and also to RINA and the IMarEST for their support. Of course, thanks to Richard and Duncan, who shared our office, for our highly entertaining but distinctly non-academic discussions...

And for their support and encouragement my deepest gratitude to my parents, my brother - and Butschi!

Thank you all very much, Bernhard.

Nomenclature

Symbols are defined at the point of first use in the text and the most widely used are listed here. Some characters such as a are used differently in separate chapters.

Latin symbols

g	gravity
h	filling level (height)
L	tank length
m	mass
p	pressure
P	fluid momentum
r	volume fraction of a fluid
t	time
T	excitation period
T_1	first resonant sloshing period
u_i	Cartesian velocity tensor
U	velocity
$\mathbf{v}$	velocity vector
x	spatial location
x_0	translatory motion amplitude

Greek symbols

χ	angular motion amplitude
μ	dynamic viscosity
ν	kinematic viscosity
ϕ	any fluid-specific quantity
ρ	density
ψ	non-dimensional impact parameter defined in Equation (3.21)
Ψ	non-dimensionalised fluid momentum defined in Equation (5.4)
θ	angular location
θ_0	impact angle
ω	excitation frequency
ω_n	n$^{\text{th}}$ resonant sloshing frequency

Glossary of terms

ABS	American Bureau of Shipping
BV	Bureau Veritas
CFD	Computationl Fluid Dynamics
DNV	Det Norske Veritas
DOF	Degree(s) of Freedom
fast time	faster than real time
filling ratio	the ratio between filling height and tank length (h/L)
FLNG	Floating LNG
FPSO	Floating Production, Storage and Offloading unit
FSRU	Floating Storage and Regasification Unit
GTT	Gaz Transport and Technigaz
IAPWS	International Association for the Properties of Water and Steam
IMO	International Maritime Organization
ITTC	International Towing Tank Conference
LNG	Liquefied Natural Gas
LR	Lloyd's Register
MAC	Marker and Cell
mass fraction	the ratio between the total fluid mass in a tank and the effective mass associated with a particular sloshing mode
metocean	meteorological and oceanographic
(U)RANS	(Unsteady) Reynolds-Averaged Navier-Stokes equations
RAO	Response Amplitude Operator
RSM	Rapid Sloshing Model
SIGTTO	Society of International Gas Tanker and Terminal Operators
UKCS	United Kingdom Continental Shelf
VLCC	Very Large Crude Carrier
VOF	Volume of Fluid

Chapter 1

Introduction

1.1 Aims and objectives

Liquefied Natural Gas (LNG) carriers are susceptible to sloshing damage (Abramson *et al.*, 1974) and there have been recent sloshing incidents which rendered the vessels inoperable (Hine, 2008). The changes in operational profiles of LNG carriers, outlined in Section 1.2, as well as the introduction of offshore LNG liquefaction and regasification vessels make the permanent restriction of permissible filling levels for the avoidance of dangerous sloshing impractical. Fitting further structural reinforcements to the cargo tanks is an expensive option and the restriction of operational areas to suitably calm waters would negate most advantages of offshore LNG operation.

The aim of this work is to propose a concept for a non-intrusive sloshing guidance system suitable for installation on existing and newbuild LNG carriers using detailed numerical modelling and the development of a simplified mathematical sloshing model. There are two main objectives and the first is the development of a CFD model which is capable of simulating violent sloshing using an implementation of the Navier-Stokes equations in a commercial CFD code. It is validated using the sloshing experiments by Hinatsu (2001) which have been used in previous CFD validation studies. The second objective is the development and validation of a fast-time phenomenological sloshing model based on a pendulum equation using the CFD model. The output phenomenological sloshing model forms the basis of the concept for a sloshing guidance system which uses motion data measured onboard an LNG carrier to assess the sloshing response in real time and warn the master of dangerous sloshing conditions. The effect of the sloshing LNG and resulting impacts on the structural integrity of containment system and the structural response are the principal consideration during LNG carrier design but the present work is limited to LNG carrier operation and does not take the structural response into account.

1.2 Liquefied Natural Gas

By 2025, the global market for natural gas is expected to grow to the same size as the petroleum market (Economist, 2004) as power generation, industry and households increase their reliance on natural gas. Figure 1.1(a) shows a projection of the primary energy mix in the UK in 2020. Renewable energy sources such as wind, wave and tidal energy will play an increasingly important role and there may be significant investment in additional nuclear energy capacity. But in the scenario considered in the Energy White Paper 2007 (Department of Trade and Industry, 2007), the bulk of all energy will be provided by fossil fuels and in 2020, the single largest source of energy will be natural gas. The changes in the origins of the natural gas consumed in the UK are illustrated in Figure 1.1(b). In 2005, approximately 80% of the total demand was met using gas produced from the UK continental shelf (UKCS) and the rest was made up with imports from mainly Norway and other European nations.

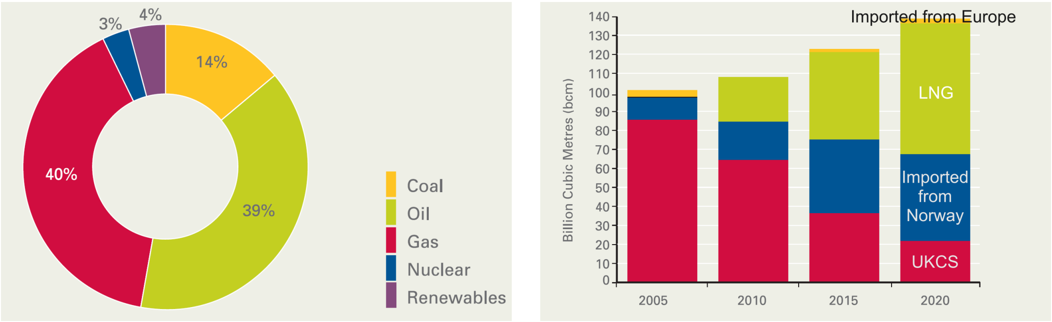

(a) Primary energy sources projected for 2020 (b) Current and projected sources of natural gas

Figure 1.1: Energy consumption in the UK: current and projected sources of energy and the future importance of LNG (from Department of Trade and Industry, 2007)

As North Sea gas production declines, Liquefied Natural Gas and imports from Norway will be needed to satisfy the growing demand for natural gas in the UK while maintaining security of supply (Department of Trade and Industry, 2007). Recently commenced gas projects in Qatar and Sakhalin require a considerable increase in LNG carrier availability and size. In 2005 and more recently in the Winter of 2008-2009, Gazprom and the Russian government gave a stark illustration of the weaknesses of pipelines when disagreements with the Ukraine over piping fees escalated. Russia suspended the gas supply and consequently several Western European nations which normally obtain a large proportion of their gas supply from Russia were forced to compensate a near 30% supply shortfall (Economist, 2006). Others, such as Spain, who rely on LNG imports were able to deal with the supply impasse with less difficulty. Consequently, European energy policy has been adjusted to diversify gas supplies and increase the use of LNG shipping (Directorate-General for Energy and Transport, 2008). Although LNG only accounted for 5% of the total gas consumption in the UK in 2007-2008, this is expected to rise to 35% in the next ten years (Select Committee on Business and Enterprise, 2008).

The transport of natural gas in liquefied form by ship over transoceanic distances (more than 1,600 nautical miles) is more cost effective than the construction and operation of pipelines (Jensen, 2002). In addition, LNG shipping is not at the mercy of pipeline host nations. The transportation of LNG by ship has its origins in the 1950s and the world's first LNG carrier was the *Methane Pioneer* (Ffooks, 1993), making her maiden voyage from Lake Charles in the US to Canvey Island in 1959.

The size of LNG carriers has progressed significantly from the 5,000 m^3 capacity of the *Methane Pioneer* to today's LNG carriers with capacities in excess of 160,000 m^3. The *qmax*-class LNG carrier, built for the Qatar III LNG project, has a capacity of 266,000 m^3 (Oil Online, 2006) and the *Mozah*, the first *qmax* LNG carrier, commenced service at the end of 2008. A total of 14 *qmax* ships is expected to be built and the 70 Billion cubic meters of LNG imports to the UK projected in 2020 would require 439 *qmax* cargoes to be delivered each year. Further increases in LNG carrier size are unlikely in the short term as there are no export or import terminals with sufficient storage capacity.

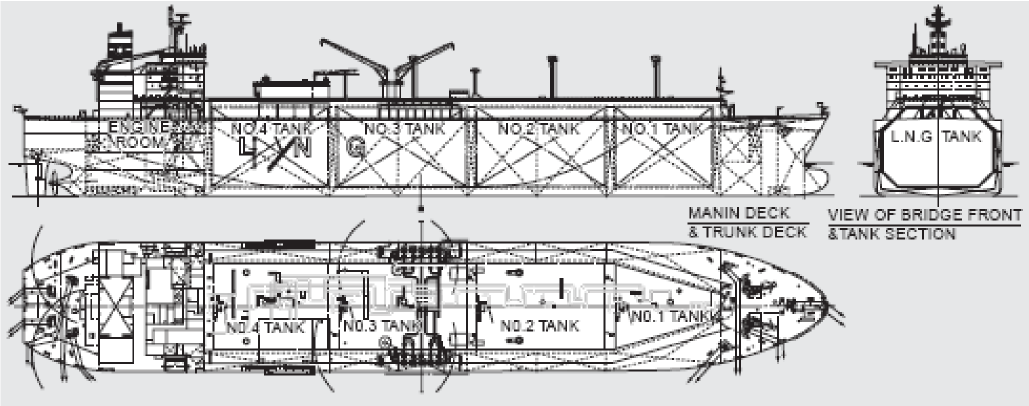

Figure 1.2: Arrangement of a membrane-type 137,000 m^3 Liquefied Natural Gas carrier (from Ishimaru *et al.*, 2004). Length is 276 m, beam 44 m, draught 12 m and deadweight 76,110 t. Typical speeds for LNG carriers are 20 kts

The cargo tanks of LNG carriers are never completely filled. This is due to cargo boil-off of approximately 0.1% to 0.2% per day on laden journeys (Cuneo *et al.*, 1981) and partial filling levels encountered during loading/unloading. A small amount (usually 3% to 7% of the total tank capacity) of LNG is carried on return journeys to maintain the tank temperature (Lloyd's Register Denmark, 2007) and for the supply of LNG boil-off to dual-fuel engines. By removing the boil off gas, the tank pressure is maintained at a constant level and excess thermal energy is removed from the cargo. However, when a tank is only partially filled with liquid and excited by an external force, the fluid can experience sloshing which is the dynamic displacement of the free surface (Olsen, 1976b). Sloshing is a danger to the safety of LNG carriers and it is usually avoided by the judicious selection of tank size and filling level restrictions appropriate for the expected meterological and oceanographic (metocean) conditions. The current economic climate in the global gas market has precipitated three principal developments challenging the status quo in the design and operation of LNG carriers:

1. Increased Ship Size. The global increase in demand for LNG has resulted in larger-scale LNG production facilities. As a result the capacities of newbuild LNG carriers are nearly doubling to 266,000 m^3 (Ginsburg and Bläske, 2007).
2. Flexible Filling Levels. This requirement is caused by a shift in the pattern of LNG trade. Whereas in the past LNG carriers were built for a certain LNG project with a fixed route, today's gas market is becoming more flexible and spot trading is starting to emerge as an alternative to the traditional trading arrangements (Crooks, 2007).
3. Offshore Liquefaction and Gasification. Political, operational and financial considerations have led to the development of Floating LNG (FLNG) technologies. This includes locating the liquefaction or regasification facilities on FPSOs (Floating Production, Storage and Offloading units - usually converted crude carriers) and transferring LNG offshore.

Consequently, a greater range of tank filling levels is encountered, there is less certainty of the sloshing loads experienced by LNG carriers and floating LNG and sloshing has become a key concern in the design and operation of FLNG facilities (Mokhatab and Wood, 2007; Nakamura and Manabe, 2007).

1.3 Background

1.3.1 LNG containment systems

The main attraction of the transport of natural gas in liquefied form by ship is that the specific volume of natural gas decreases by a factor of 600 (Mann, 1977) when it is cooled below its liquefaction temperature of approximately $-163°$ C[1]. The LNG cannot be stored in normal cargo tanks because carbon steel used in shipbuilding is brittle at the low temperatures required for LNG transportation and thus unsuitable for an LNG tank (Mann, 1977). Therefore the LNG is carried in special containment systems which protect the structure of the ship from the low temperatures of the LNG. The two main groups of containment systems in use today are membrane, shown in Figure 1.3 and spherical designs, shown later in Figure 1.7.

---

[1] the precise value depends on the composition of the LNG (Mann, 1977)

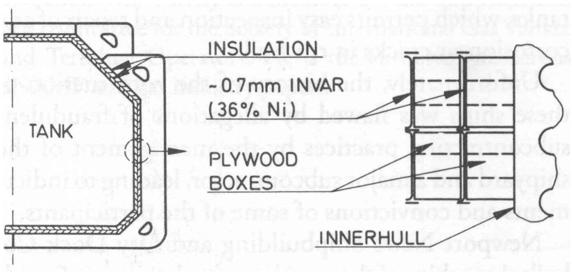

Figure 1.3: Membrane LNG tank schematic drawing (from Benford and Fox, 1993)

The most popular membrane containment systems are the Technigaz Mk III and the Gaz Transport GT No 96 designs and they are marketed by Gas Transport - Technigaz (GTT). The Mk III system uses a primary barrier made of corrugated stainless steel, shown in Figure 1.4(a), with a thickness of 1.2 mm and a secondary barrier made of triplex, which is aluminium foil sandwiched between glass clothes (Chauvin, 1996). The primary and secondary barriers are separated by a primary insulation layer made of polyurethane foam contained in plywood boxes. The thickness of the primary insulation is approximately 100 mm. The secondary insulation, separating the triplex barrier from the ship's structure is also polyurethane foam and its thickness is approximately 200 mm. The barriers and insulation are joined with glue and the secondary insulation is fixed to the hull using a load-bearing mastic (Chauvin, 1996).

The GT No 96 system, shown in Figure 1.5, also has a primary and secondary barrier made of 0.7 mm thick Invar[2] and two layers of insulation. The insulation is made of plywood boxes filled with pearlite and the thickness of the primary and secondary layers is 230 mm and 300 mm respectively. The barriers and insulation are held together using longitudinal Invar tounges sliding into the plywood boxes. The thickness of the insulation layers is driven by the desired boil-off rates and a thinner insulation layer results in greater cargo carrying capacity and hence increased revenue. Recently GTT have introduced the new CS-1 containment system, shown in Figure 1.6, which combines the simpler Invar membrane of the GT No 96 system with the thinner insulation of the Mk III system. The secondary barrier is made of Triplex and the individual components are joined using glue.

Spherical containment systems, also known as Moss-Rosenberg tanks, are marketed by Kvaerner-Moss. They are classified as self-supporting tanks and as such do not require the same level of redundancy as membrane containment systems. The Moss-Rosenberg system consists of insulated aluminium spheres which are joined to the ship via an equatorial ring which also acts as a thermal brake. The diameter of a spherical tank contracts by about 200 mm when it is cooled to transport LNG (Liddle, 2009). Figure 1.7 shows the arrangement of a Moss-Rosenberg containment system.

---

[2] Invar is a steel with a 36 % Nickel content, giving it superior low-temperature characteristics compared to most other structural materials.

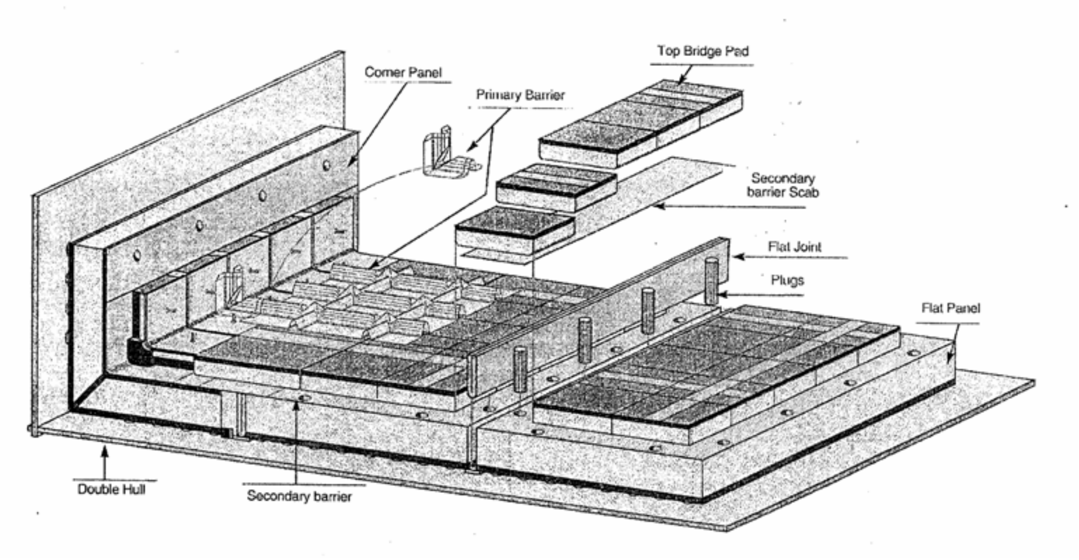

(a) Schematic drawing

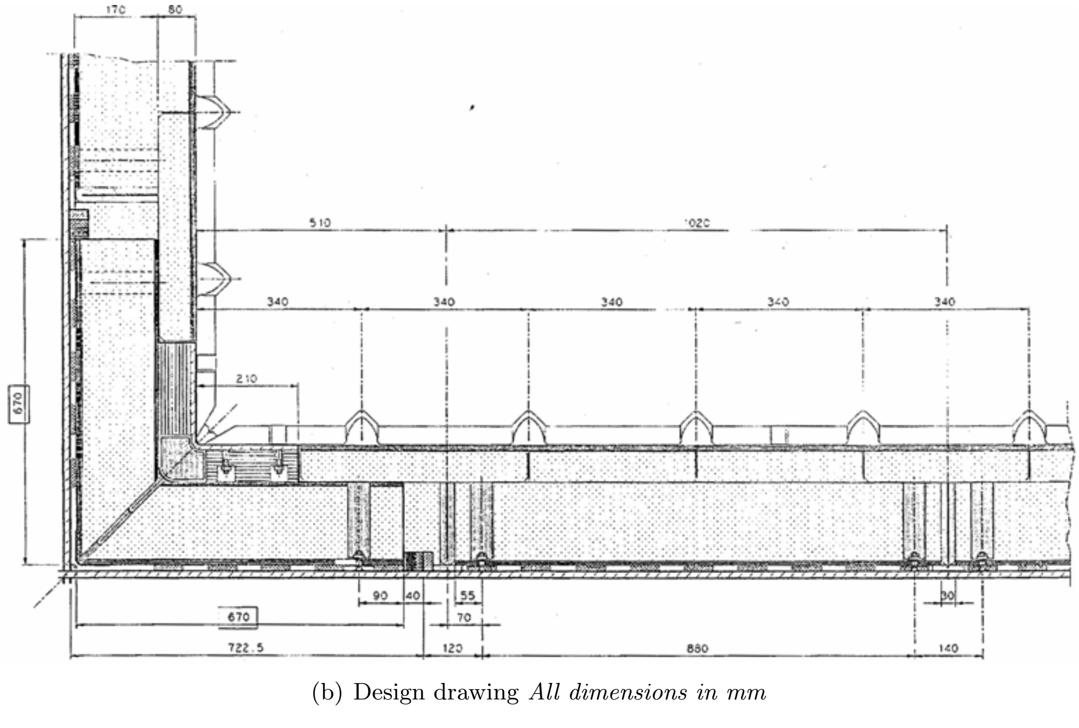

(b) Design drawing *All dimensions in mm*

Figure 1.4: Technigaz Mk III LNG containment system (from Chauvin, 1996)

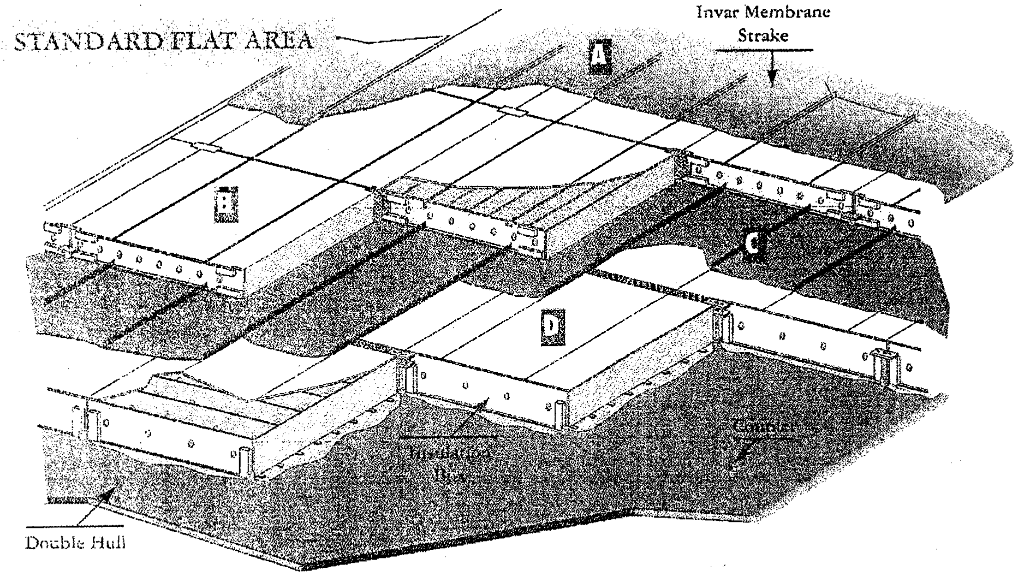

(a) Schematic drawing

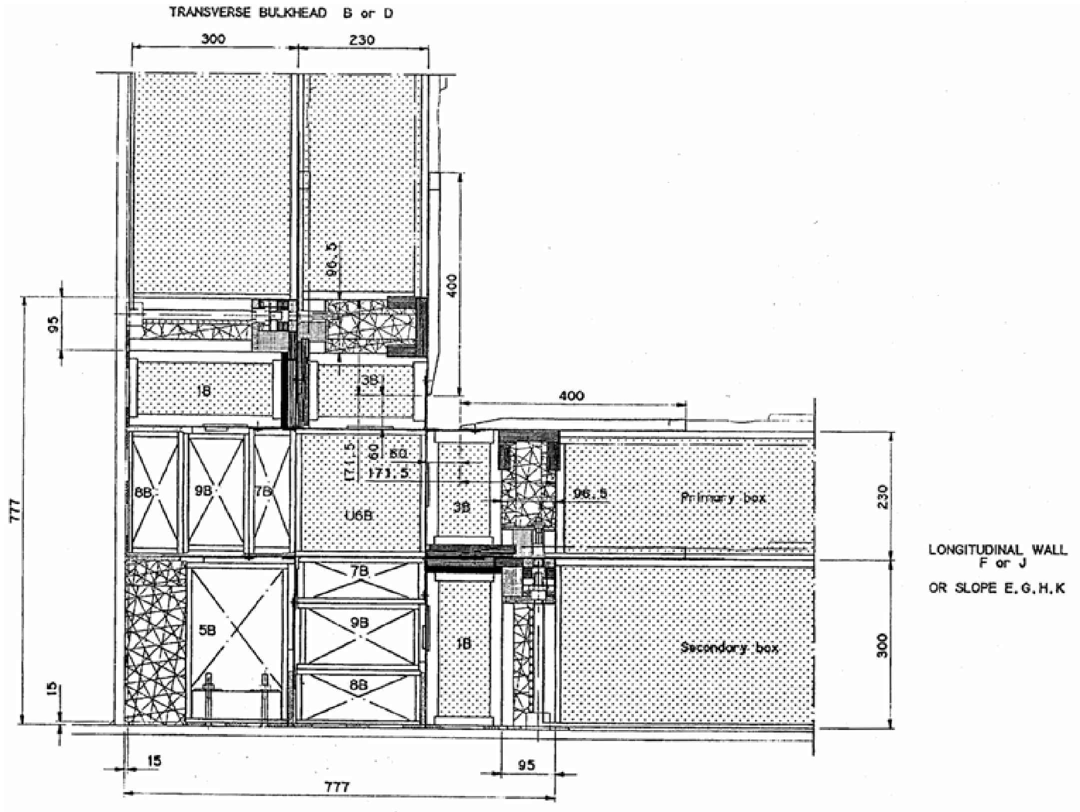

(b) Design drawing *All dimensions in mm*

Figure 1.5: Gaz Transport GT No 96 LNG containment system (from Chauvin, 1996)

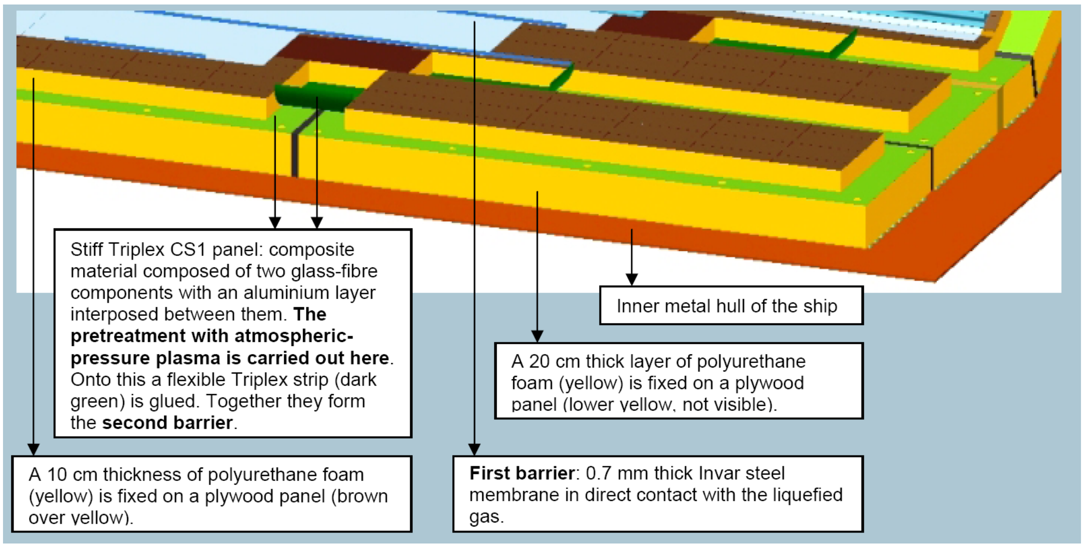

Figure 1.6: CS-1 Containment system: the follow on from GT No 96 and Mk III (from Melamies, 2007)

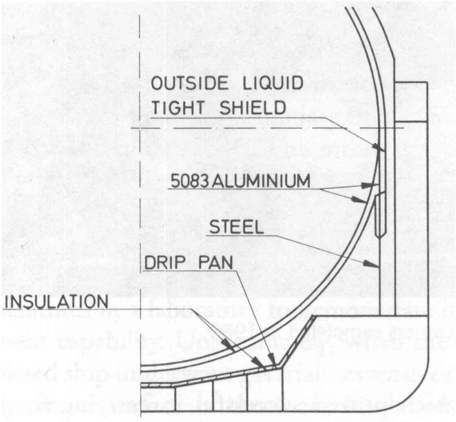

Figure 1.7: Moss Rosenberg LNG tank schematic drawing (from Benford and Fox, 1993)

There is greater confidence in the calculated sloshing loads acting on the Moss-Rosenberg design and there have been no sloshing incidents affecting LNG carriers using the Moss-Rosenberg containment system (Liddle, 2009). However, the relatively large weight (600-800 tonnes per tank), less efficient use of space within the ship and the higher fees required for Suez canal transit have resulted in less frequent use of this system. Despite the susceptibility of membrane containment systems to sloshing and recent sloshing incidents involving GTT designs (Hine, 2008), they account for approximately 60% of the LNG carriers currently in service and 80% of all newbuilds, including the *qmax* LNG carriers. However, the glue used with the CS-1 system has been problematic and delayed the launch of the first LNG carrier using CS-1 (Liddle, 2009). The operation of floating LNG requires more resistance to sloshing loads and greater fatigue life than normally needed for LNG carriers. This has increased the attractiveness of the Moss-Rosenberg design and led to a novel proposal for an LNG containment system by Aker yards which is designed for slosh suppression (vom Baur, 2009).

1.3.2 LNG carrier motions

When designing LNG carriers the expected range of motions is a prerequisite to determine the expected sloshing loads, required fatigue life and the strength of the selected containment system. The correct simulation of this problem requires the coupling of vessel seakeeping with a sloshing model (Gaillarde *et al.*, 2004). The absence of sloshing effects in seakeeping analysis has been addressed only recently with a number of studies of the interaction between sloshing and the seakeeping properties of a vessel. Kim *et al.* (2005) developed a two way coupled seakeeping-sloshing model, where the sloshing force is determined using an external model and then added to the seakeeping equation. Rognebakke and Faltinsen (2003) used a multimodal system for the sloshing and coupled the resulting solution with a seakeeping equation which is then analysed in the frequency domain. Mikelis *et al.* (1984) and Mikelis and Journee (1984) coupled a numerical viscous sloshing model with a seakeeping model by using the sloshing load as an input to a seakeeping equation at each time step of the numerical solution of the sloshing model. The resulting tank motion was then used as the updated input motion in the sloshing model.

A simpler approach is the approximation of the liquid cargo as solid mass and ignoring the liquid motions but this can lead to incorrect predictions of the response amplitude operators (RAOs) (Huang *et al.*, 2007; Lee *et al.*, 2009). This approach is adopted in LNG carrier design due to the difficulty in the accurate prediction of the coupled sloshing-seakeeping response (Lloyd's Register, 2009) and despite its shortcomings, this approach is usually taken at the preliminary design stage (level two) sloshing assessment (Lloyd's Register, 2005). For this study a seakeeping analysis is carried out using the strip-theory code *Ship Motions* (Wolfson Unit for Marine Technology and Industrial Aerodynamics, 2000) for a typical membrane tank LNG carrier based on the general arrangement in Figure 1.2. The main particulars are given in Table 1.1 and a body plan is shown in Figure 1.8.

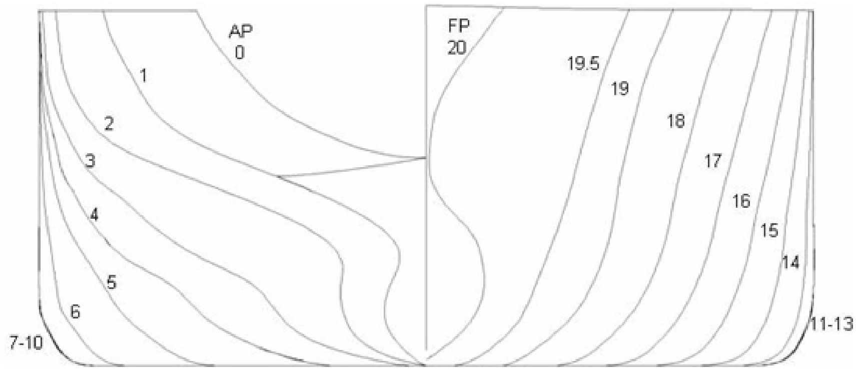

Figure 1.8: LNG carrier body plan used for seakeeping analysis - the general arrangement is shown in Figure 1.2

Table 1.1: Particulars of LNG carrier used for seakeeping analysis

Length between perpendiculars	277 m
Beam	42.4 m
Draught	11.0 m
Displacement	103,000 t
Service speed	20 kts
Vertical centre of gravity	16.5 m from keel
Longitudinal centre of gravity	4.5 m fwd from amidships
Radius of gyration k_{xx} (roll)	12.6 m
k_{yy} (pitch)	66.0 m
k_{zz} (yaw)	66.0 m
LNG tanks	5 (tank 1 forward and tank 5 aft)
Tank length	40.0 m
Tank width	40.0 m
Tank height	25.0 m

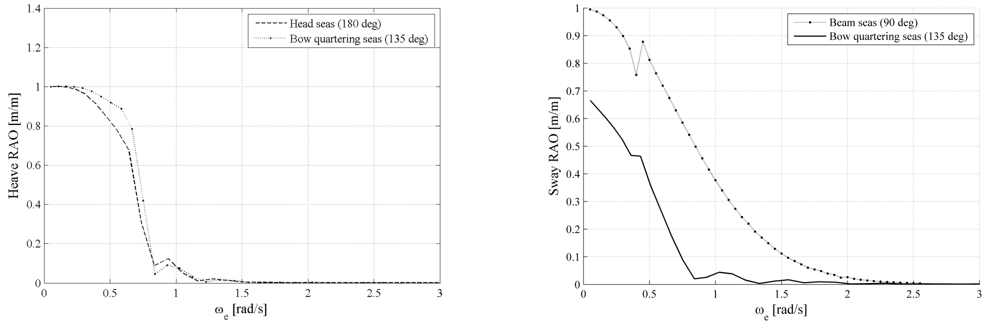

(a) Heave RAO

(b) Sway RAO

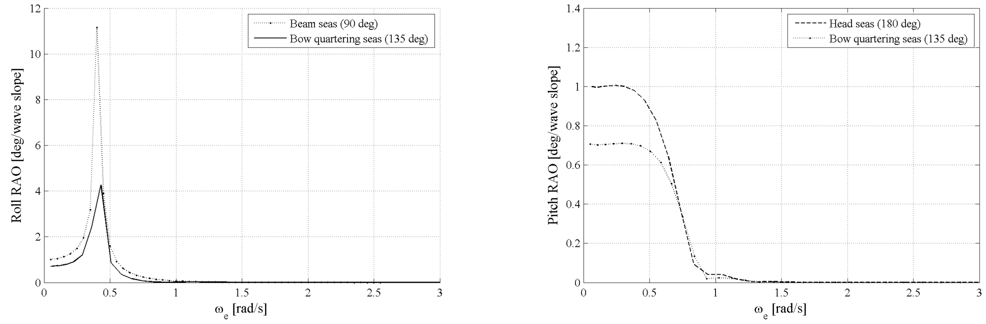

(c) Roll RAO

(d) Pitch RAO

Figure 1.9: Motion response amplitude operators for the LNG carrier in Figure 1.8 obtained with a strip theory seakeeping code where liquid motions are ignored

The motions were computed for a Pierson-Moskowitz wave spectrum (Lloyd, 1989) with a significant wave height of 7.5 m. The resulting RAOs are given in Figure 1.9, where the RAOs are comparable to those expected from a similarly sized vessel such as a large bulk carrier. Although the LNG carrier used in the analysis has bilge keels, no viscous roll damping was introduced because of limitations in the seakeeping code and the roll RAO in Figure 1.9(c) is excessively large when encountering beam seas.

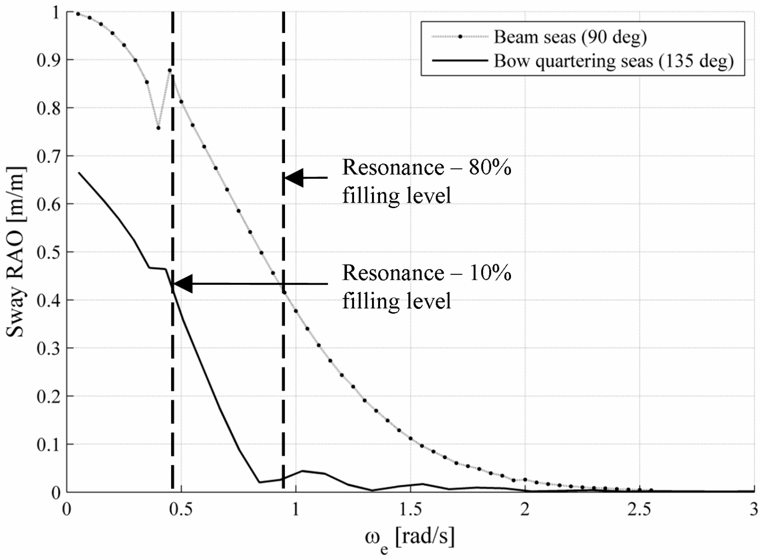

Figure 1.10: Combining the sway RAO and LNG tank resonance characteristics is the first pass to identify possible sloshing problems

Once the vessel motion RAOs are obtained, level two sloshing analysis compares the RAOs with the sloshing resonant frequencies (Lloyd's Register, 2005). This is carried out for sway in Figure 1.10 and a substantial liquid motion response is expected near the sloshing resonance frequency. The proximity of motion peaks and sloshing resonance entails a detailed (level three) analysis using the standard methodologies for the simulation of sloshing. The procedure used by Lloyd's Register uses irregular motions determined by the sea state and the effect of wave height is assessed in the initial screening phase by varying the wave height in a two meter interval (Lloyd's Register, 2009). Other procedures such as ABS also use amplitude variations but a regular motion is applied.

This approach risks neglecting transient effects and consequent impact pressures observed in the experimental investigation by Schreier *et al.* (2009). The principal weakness of this approach is that influence of the liquid motions on the overall vessel response is not considered. This is of particular concern when the avoidance of the motion peaks found leads into regions of large motions which would be observed with coupled analysis (Molin *et al.*, 2002) and recent interest in the interaction of sloshing and mooring systems have renewed interest in the coupled analysis of sloshing and seakeeping (Gaillarde *et al.*, 2004).

1.3.3 Sloshing analysis for design

Experimentation is used by classification societies (e.g. American Bureau of Shipping (2004), Bureau Veritas, Det Norske Veritas and Lloyd's Register) for the assessment of sloshing loads. The model size varies between $1/70^{\text{th}}$ to $1/25^{\text{th}}$ of full scale (Jeon *et al.*, 2008), but the correct scaling of the sloshing physics and measured loads is often difficult (Abramson *et al.*, 1974). Typical sloshing analyses follow a comparative approach, where the measured sloshing pressures for a new tank design are compared to an existing design with similar size. This helps overcome some of the uncertainties encountered when scaling sloshing pressure loads. Another modelling technique is the numerical solution of the Navier-Stokes equations using Computational Fluid Dynamics (CFD). CFD is established as a suitable methodology for the study of sloshing flows (Lloyd's Register, 2005). CFD based simulations are carried out at full scale and LNG is approximated as an incompressible liquid of appropriate density. The excitation motion should be in all available degrees of freedom and results are taken from the steady state response (American Bureau of Shipping, 2006).

Sloshing severity can be described by computing the mean of the 10% highest pressures measured during a sufficiently long simulation time (Graczyk *et al.*, 2006) or by fitting a Weibull distribution to the recorded pressures and computing a design pressure with low probability of exceedance (American Bureau of Shipping, 2004, 2006). The comparative approach is suitable when the tank sizes are similar, however, when there is a significant change in LNG tank size or shape, the sloshing loads have to be computed directly. The last significant change in LNG carrier capacity was in the 1970s and sloshing incidents experienced by the larger vessels have led to the introduction of filling level restrictions (Abramson *et al.*, 1974).

Another option for the avoidance of dangerous conditions during vessel operation is the use of operator guidance and condition monitoring systems. Following several losses of bulk carriers due to structural failure during the 1980s and early 1990s the International Maritime Organization (IMO) adopted resolution A.713(17) in 1991, which recommended the installation of hull stress monitoring systems onboard bulk carriers (Forestier and Austin, 2009). The real-time monitoring of hull stress gives the master an indication of the loads experienced by the vessel and it is then possible to adjust heading and speed to reduce the structural loads. After the introduction of hull stress monitoring the number of bulk carrier casualties decreased and the use of hull stress monitoring systems has since spread to other vessels such as crude carriers and also LNG carriers. A similar approach is currently proposed for sloshing to avoid the risk of damage to the containment system and a non-intrusive concept sloshing guidance system is proposed in this thesis.

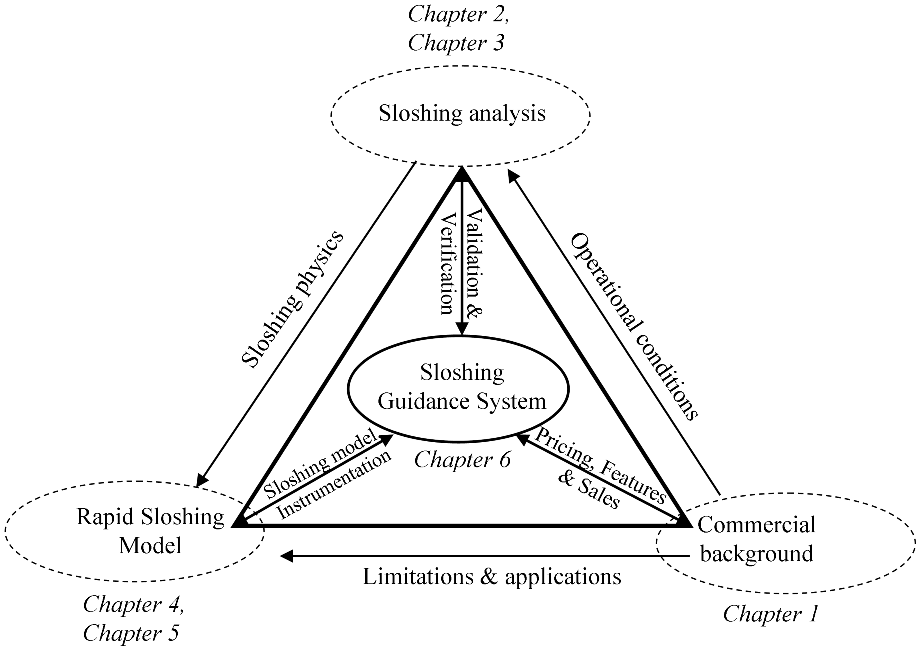

Figure 1.11: Organisation of the project and the interdependence of the commercial and technical constraints

1.4 Layout of the thesis and novel contributions

The importance of LNG to a future world economy and the resulting motivation for the development of a sloshing guidance system have been outlined in the Introduction and the impact of sloshing on the design and operation of LNG carriers has been detailed in Section 1.3. As indicated in Figure 1.11, commercial considerations restrict the available resources and limit the range of operation of the sloshing guidance system.

An analysis of sloshing is carried out in two stages. Chapter 2 gives a discussion of the physics affecting sloshing behaviour and compares and contrasts different solution methods used for the assessment of sloshing flows. The importance of the physics influencing sloshing is investigated with the development and validation of a numerical sloshing model implemented in a commercial CFD code in Chapter 3.

The sloshing physics identified in the Chapter 2 are approximated with specific computational models. The computational models and sloshing impacts, which are a critical hazard to the containment system of an LNG carrier, are studied in Chapter 3. Novel contributions made in the course of this work include an investigation of the significance of the phase interaction model (Godderidge *et al.*, 2009) which is given in Section 3.2 and a study of the effect of the fluid compressibility model on the impact pressure magnitude and frequency of oscillation (Godderidge *et al.*, 2009) which is outlined in Section 3.3.

The principal novel contribution of this thesis is the the Rapid Sloshing Model (Godderidge *et al.*, 2008, 2009a,b) intended for use with the concept sloshing guidance system. The theoretical foundation of the Rapid Sloshing Model is introduced in Chapter 4. The restoring force due to the displacement of the sloshing fluid from its quiescent location is approximated from numerical simulation and the coefficients correspond with the well-known detuning characteristics of sloshing. Damping is included with a linear and third-order damping model and the damping coefficients are obtained using published results and measurement of the logarithmic decrement. The impact dynamics are approximated using an existing impact potential modelling approach which is enhanced for low filling level sloshing impact dynamics.

The comparison of the Rapid Sloshing Model for medium filling level ($h/L = 0.3$ to 0.4) near the critical depth is given in Chapter 5. Both longitudinal and transverse membrane tank cross sections are used with translatory and rotational excitation motions. An irregular motion profile is then applied to the the longitudinal tank section and the Rapid Sloshing Model methodology reduces the mean error by an order of magnitude when compared to conventional modelling techniques. The modelling approach and the impact model are extended for sloshing with low filling ratios ($h/L = 0.1$) and preliminary results are shown in Section 6.3, where the Rapid Sloshing Model predicts the sloshing response to an irregular excitation with a mean error similar to the previous cases.

The integration of the Rapid Sloshing Model in a non-intrusive sloshing guidance system is considered further in Chapter 6. Other possible application of the Rapid Sloshing Model include sloshing-seakeeping interaction (Lee *et al.*, 2009) and FLNG design and operation (Godderidge *et al.*, 2009) and these are also considered in Chapter 6. Chapter 7 concludes the thesis, emphasises the most significant novel contributions and outlines possible directions of further work.

Chapter 2

Sloshing

2.1 Introduction

2.1.1 Review of sloshing

Sloshing, the dynamic behaviour of liquids with a free surface in moving containers, is a fascinating subject that has attracted the attention of scientists, engineers and mathematicians for many years (Abramson, 1966). Lamb (1879) gives a theoretical treatment of sloshing when considering tidal waves in 1879 and Fox and Kuttler (1983) report that the sloshing problem was studied by Euler as early as 1761. Sloshing research received a substantial boost with the use of liquid fuels in spacecraft after World War II. The NASA report SP-106, published by Southwest Research Institute in 1966, summarises the sloshing research carried out in support of the US space programme (Abramson, 1966). Its contents remain relevant to this day and it is one of the most frequently cited publications in sloshing. Dodge (2000) has published an updated version and Ibrahim (2005) surveys modern theoretical and numerical approaches for the simulation of sloshing.

Sloshing is encountered in a wide range of engineering applications. In the design of high-performance automobiles, the reduction of noise due to fuel sloshing is becoming an increasingly important consideration (aus der Wiesche, 2006). A more pressing concern is the effect of fuel slosh on the stability of road vehicles during acceleration (aus der Wiesche, 2003). Tanker lorries are particularly susceptible to loss of control due to sloshing (Rumold, 2001; Dai *et al.*, 2004) and Gertsch *et al.* (2004) have proposed an operator guidance system for lorry drivers to avoid dangerous sloshing conditions.

In large buildings, fluid sloshing in tuned liquid dampers counteracts earthquake or wind-induced motions and vibration. Water tower, reservoir and dam design also includes sloshing considerations. Aeroplanes are susceptible to sloshing due to gradual fuel burn and linear potential flow analysis for the assessment of the influence of sloshing on vehicle dynamics was carried out in the aerospace field in the 1950s (Graham and Rodriguez, 1952). The use of liquid fuels in spacecraft propulsion has generated further interest in sloshing and sloshing remains a concern in the design of spacecraft (Dodge, 2000).

The use of anti-roll tanks in ships is a case of desired sloshing motion (Lloyd, 1989), but the liquid motion in slack cargo or ballast tanks can compromise the stability and structural strength of ships. During the first LNG boom in the 1970s the airplane manufacturer McDonnell Douglas (now a part of Boeing) proposed an LNG containment system (Ffooks, 1993). McDonnell Douglas later collaborated with Gaz Transport (now part of GTT) and the design and choice of materials are similar to the present GT No 96 containment system (Ffooks, 1993).

2.1.2 Sloshing damage on LNG carriers

Olsen (1976b) observed that an open, liquid-filled container needs only be exposed to a small movement or impulse before the free liquid is set into movements with surprising large amplitudes. Because of the large size of the tanks on LNG carriers, sloshing can affect both the stability and the structural integrity and the catastrophic damage caused to an LNG containment system by sloshing impacts is shown in Figure 2.1.

Figure 2.1: Severe damage to a membrane LNG containment system due to sloshing at a low filling level (from vom Baur, 2009). The primary barrier is detached and the primary insulation is visible. In some locations primary insulation boxes are missing and the secondary barrier can be observed

Peregrine (2003) carried out experimental investigations of water wave impacts on walls and observed fluid accelerations in excess of three orders of magnitude of gravity and impact pressures up to two orders of magnitude greater than the static pressure.

Sloshing has become an issue frequently encountered in naval architecture (Kaminski *et al.*, 2006). Hansen (1976) reported on the locations of sloshing damage on bulk carriers and tankers. Most sloshing damage incidents on crude oil and bulk carriers involved seawater, usually in ballast tanks, rather than the more viscous crude oil. Abramson *et al.* (1974)

reported incidents of substantial damage to LNG containment systems at a 15% - 30% filling level which extended in some instances to a full breach of the membrane and electrical damage. The surveys of sloshing damage in crude oil and bulk carriers by Hamlin *et al.* (1986); Hamlin (1990) and more recently Rizzuto and Tedeschi (1997) report that sloshing damage is not usually confined to a particular area. However, impact loads are most frequent at the lower end of the hopper and joining structure as shown in Figure 2.2 (Hamlin *et al.*, 1986; Hamlin, 1990; Rizzuto and Tedeschi, 1997). The variation in filling level further complicates the identification of tank regions at risk to sloshing impacts.

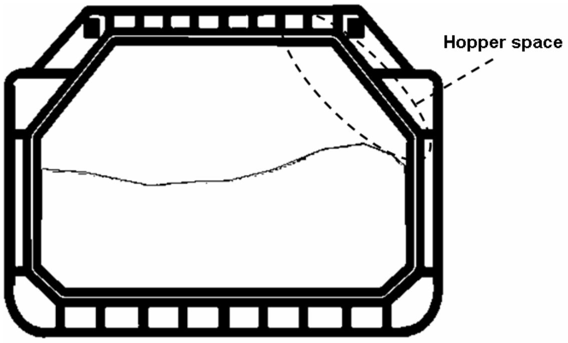

Figure 2.2: Membrane LNG tank schematic with hopper space (from MacDonald, 2005). The lower edge of the hopper space is particularly susceptible to damage due to sloshing.

The LNG carrier *Catalunya Spirit* suffered sloshing damage in 2006 which was only discovered during scheduled dry dock inspection. The repairs cost $4.1 million and the operators incurred an additional loss of $2.4 million, as the *Catalunya Spirit* remained in dry dock for repairs for 47 days (Teekay LNG Partners, LP, 2006). Three further incidents of sloshing damage on LNG carriers with the Mk III containment system were reported in 2008 (Hine, 2008).

2.1.3 Sloshing guidance systems

The use of onboard sloshing guidance systems can help identify and avoid the occurrence of dangerous sloshing incidents. A sloshing guidance system needs to quantify the severity of a sloshing flow and a viable solution will meet the following requirements

1. Estimation of sloshing loads in real and fast time. This gives the master up-to-date information of the sloshing loads being exerted on the tank structure and warns of impending dangers due to sloshing, allowing the initiation of evasive action.

2. Cost-efficient installation and maintenance. The dry docking required for the installation of instrumentation in the tank containment system entails financial and organisational cost. A cost-effective system would minimise access to the containment system and maximise the use of already installed on-board instrumentation.

3. Shipboard operation. While a complicated system may predict sloshing pressures with greater accuracy, the required computational resources would make its use impractical. A balance between model sophistication and complexity, realism and operability has to be achieved.

4. Flexibility to provide additional accuracy for critical operating conditions. Operators may be willing to pay for greater accuracy in certain operational conditions or sea states. A sloshing guidance system should be flexible enough to incorporate such improvements.

Currently there are three proposals for sloshing guidance systems. The *HULLMOS* system, which is intended specifically for LNG carriers, is developed by Rouvari Oy (2005). Kim *et al.* (2006) found that an arrangement of strain gauges in the containment system may constitute a useful warning system for sloshing damage and this approach is also adopted by *HULLMOS*. Strain gauges record the loads experienced by the containment system and microphones are used to listen for the sound of sloshing impacts. The effectiveness of this approach is limited by the number of sensors installed in a tank and retrofitting existing LNG carriers is expensive due to extended dry-docking periods. The installation of penetrating sensors voids the warranty of a GTT membrane containment system[1] which may deter ship operators from installing a sloshing guidance system based on tank measurements.

Gertsch *et al.* (2004) also developed a sloshing warning system for drivers of tanker lorries based on the measurement of tank accelerations. Dangerous accelerations are identified using prior analysis of sloshing loads and the stability of a particular tanker trailer design. Future vehicle accelerations are then predicted by vehicle position and intended movement which are calculated using digitised road maps and Global Positioning System data. The system can give advance warning to the driver of a tanker lorry of an impending dangerous situation and recommend a change of vehicle speed.

This system is unsuitable for direct application to the marine environment because the future motions of an LNG carrier cannot be predicted in the same manner as those of a tanker lorry. While tanker lorry operation is concerned with the overturning moment due to sloshing, LNG carriers are susceptible to local damage to the containment system caused by sloshing.

Lloyd's Register have recently issued operator guidance for the avoidance of sloshing loads (Lloyds Register, 2008; MacDonald and Maguire, 2008). For a particular filling level and sea state, the risk of sloshing is indicated with a traffic light system on polar plots, shown in Figure 2.3. The sloshing risk calculations are carried out using the design procedure

---

[1] Nigel White, (Head of Research, Lloyds Register), private communication

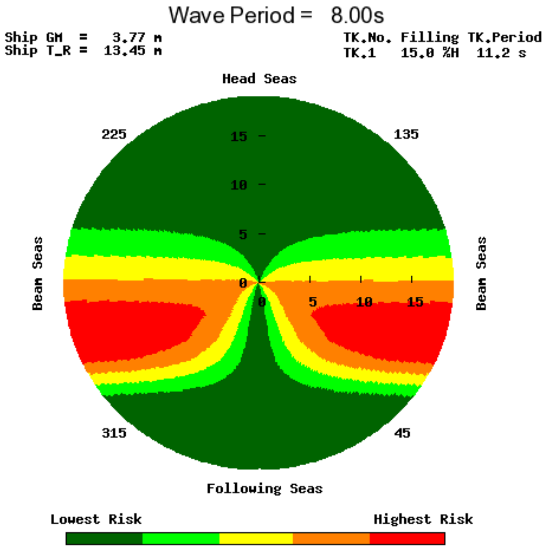

Figure 2.3: Polar plot of sloshing risk for operator guidance for 8 s wave period and low filling level (from Lloyds Register, 2008). Red regions indicate the highest risk of sloshing, while green indicates safe areas.

in Section 1.3.3 and nonlinearities such as detuning and the coupled LNG carrier-sloshing response are not considered (Lloyds Register, 2008).

2.2 Sloshing physics

2.2.1 Classification of sloshing

Sloshing behaviour can be classified using the filling height, type of impact or the bulk fluid behaviour. Abramson *et al.* (1974) differentiate between shallow $h/L \leq 0.2$ and non-shallow $h/L > 0.2$ filling ratios. Depending on the proximity of the tank motion to resonance, travelling waves (see Figure 2.4(a)) or hydraulic jumps are formed at shallow filling ratios (Lloyd's Register, 2005). In the non-shallow case, a large standing wave response is observed in the resonance frequency range (Abramson *et al.*, 1974). Olsen (1976b) identifies three separate types of sloshing behaviour using the direction of the excitation motion

1. Lateral sloshing, the most important kind of sloshing. It is generated by both translatory and angular tank movements.
2. Swirling, or rotational sloshing is a fully three dimensional phenomenon. Its occurrence depends on the tank shape as well as the motion amplitude and frequency. Simultaneous excitations of the fluid in orthogonal planes, such as surge and sway, can result in swirling.

3. Vertical sloshing can result in standing waves, but this is unlikely to occur in ship tanks (Olsen, 1976b). Rather, vertical sloshing tends to increase lateral sloshing loads.

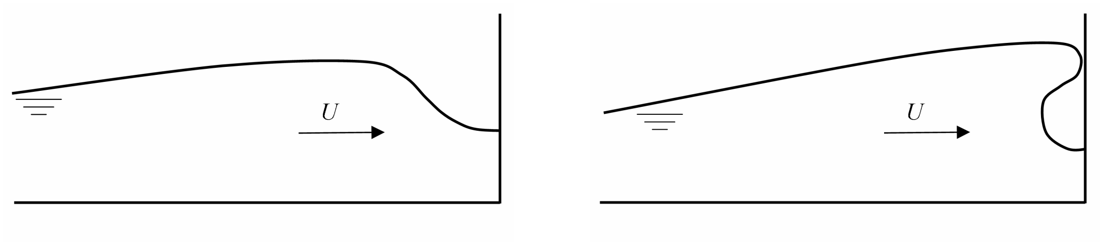

(a) Steep wave, increased steepness can approach a hydraulic jump with a sharp wave front. The resulting impact is usually hydrodynamic and no gas entrainment takes place.

(b) Breaking wave, where the interaction between liquid and gas phase is significant. The resulting oscillating pressure in the gas bubble can cause dynamic amplification of stresses with fluid-structure interaction.

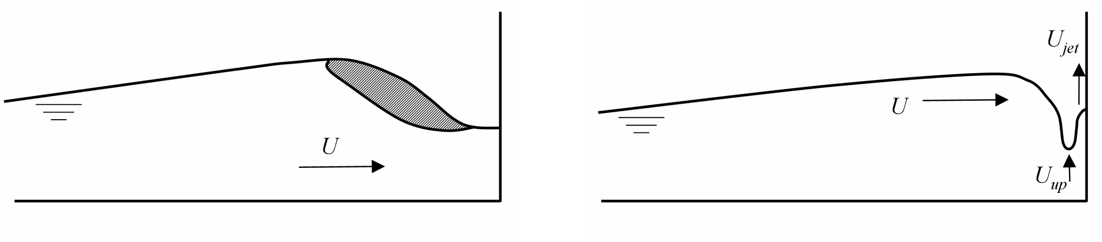

(c) Aerated wave impact (aerated region shown in the shaded region), with a mixed liquid/gas region at the wave front. Large impact pressures can result in cavitation-induced erosion in the impact region.

(d) Flip-through, considered to be the most severe type of impact. The wave breaks before reaching the tank wall and the rapidly rising water forms a jet, with accelerations of up to 1,500 g reported in experiments by Lugni *et al.* (2006).

Figure 2.4: Classification of sloshing according to four different types of impact scenario, with implications to the structural response

The fluid impact resulting from the liquid motion offers a second scheme for the classification of sloshing. The steep wave impact scenario in Figure 2.4(a) has a well-defined wave front and results in an impact without inclusion of the gas phase[2]. Depending on the angle between the wave front and tank wall, it can be likened to a Wagner-type hydrodynamic impact (Malenica *et al.*, 2009) with one pressure spike. This type of impact can occur at shallow and non-shallow filling levels (see e.g. Schreier and Paschen, 2008) The breaking wave-type impact shown in Figure 2.4(b) results in a trapped gas pocket which can give rise to a decaying oscillating pressure within the gas pocket. Depending on the oscillation frequency and natural modes of the structure, dynamic amplification of the structural loading can occur (Rognebakke and Faltinsen, 2005; Lloyd's Register, 2009). When considering a liquid-vapour system rather than water and air vapour-liquid phase transition can be possible, but this has not been investigated. An aerated impact illustrated in Figure 2.4(c) has a mixture of liquid and gas phase at the wave front. During

---

[2] The term *gas* can refer to either air or LNG vapour

impact the gas phase results in an increase in the compressibility of the gas-liquid mixture but when a liquid-vapour system is considered cavitation may be an issue (Abramson *et al.*, 1974). The flip-through in Figure 2.4(d) is caused by wave breaking without gas entrapment and the uprising water forms a jet (Hull and Muller, 2002; Lugni *et al.*, 2005).

Lugni *et al.* (2006) observed large pressures and fluid accelerations in excess of 1,500g in experimental investigation of flip-through during sloshing impacts. Malenica *et al.* (2009) considers the flip-through type impact to produce the highest local pressures but Schreier *et al.* (2009) observed pressures during hydrodynamic impact nearly three times greater than those in the study by Lugni *et al.* (2006). When the impact pressure is near the critical pressure of the entrained vapour the resulting phase change during breaking wave impact may result in even greater pressures than those expected from flip-throughs.

The bulk fluid motion, which may be approximated with a spring-mass or pendulum system, offers another methodology for the classification of sloshing in three separate categories (Pilipchuk and Ibrahim, 1997). When the free surface remains planar, the sloshing can be described by a linearised equation of the first asymmetric sloshing mode, given by e.g. Abramson (1966). This type of sloshing is illustrated in Figure 2.5(a) and a corresponding pendulum model (or Rapid Sloshing Model introduced in Chapter 4) would use the assumption $\sin(\theta) \approx \theta$. When the motion amplitude is increased or the excitation frequency nears resonance, the sloshing response is classified as weakly nonlinear. It is illustrated in Figure 2.5(b), where the fluid experiences non-planar motions as well as rotation. The assumption of linearity is no longer valid and higher order mathematical models are required (Faltinsen, 1974; Ibrahim, 2005). A pendulum model for this sloshing regime would employ the approximation

$$\sin(\theta) \approx \theta - \frac{\theta^3}{3!}, \tag{2.1}$$

which corresponds to a Duffing-type oscillator. Strongly nonlinear sloshing occurs when the severity of the sloshing response is increased even further (Pilipchuk and Ibrahim, 1997). In this regime, illustrated in Figure 2.5(c), near-instantaneous changes in the fluid velocity and travelling waves occur. Other flow features such as wave overturning and air entrapment complicate its description with a closed-form mathematical model and this sloshing regime is usually simulated using model testing or numerical approaches.

The classification of sloshing depending on the nature of the resulting impact and the effect of the sloshing impact pressure on the containment system is most relevant for design. Membrane containment systems consist of several layers of different materials, described in Section 1.3.1, which results in a non-homogeneous composite structure. The response of the the Technigaz Mk III containment system to impact loads was considered

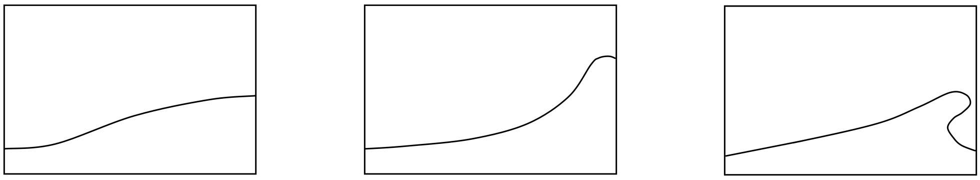

(a) Linear sloshing, which can be modelled using linear potential flow analysis

(b) Weakly nonlinear sloshing, which requires higher-order analytical methods such as multimodal analysis

(c) Strongly nonlinear sloshing with impacts and near-instantaneous changes of flow velocity

Figure 2.5: Classification of sloshing according to the bulk fluid motion

by Arswendy and Moan (2006); Paik (2006) and it was found that the membrane tank containment system is a structure that does not lend itself to straightforward analysis. An experimental investigation of structural loading experienced by a membrane insulation system when subjected to static and dynamic pressure loads was carried out by Kim *et al.* (2006). The filling level-dependent classification provides insight in the dominant physics and can identify likely impact scenarios. The classification used by Pilipchuk and Ibrahim (1997) is useful for the development of phenomenological models but it lacks applicability for the assessment of the effect of sloshing on the containment system.

2.2.2 What determines the sloshing response?

A linear potential flow model can be used to identify the factors influencing the sloshing response. It can be shown that the dynamic transverse force due to liquid sloshing induced by translatory motion of a rectangular tank is (Abramson, 1966)

$$\frac{F}{\rho g h L b} = \overbrace{\ddot{x}\left(t\right)}^{\text{acceleration}} \frac{1}{g} \left[1 + \sum_{n=0}^{\infty} \overbrace{\frac{8 \tanh\left\{\left(2n+1\right)\pi \frac{h}{L}\right\}}{\pi^3 \left(2n+1\right)^3 \frac{h}{L}}}^{\text{tank geometry \& filling level}} \overbrace{\frac{1}{\left(\frac{\omega_n}{\omega}\right)^2 - 1}}^{\text{excitation frequency}} \right], \tag{2.2}$$

where b is tank width, g gravity, h filling level, L tank length, ρ density, ω excitation frequency, ω_n the natural sloshing frequency defined in Equation (2.3) and $\ddot{x}\left(t\right)$ the acceleration applied to the tank.

Equation (2.2) shows that the proximity of the excitation frequency to the resonance frequencies has a significant influence on the sloshing response. The natural sloshing frequencies ω_n are given as

$$\omega_n^2 = gk \tanh\left(kh\right), \tag{2.3}$$

where

$$k^2 = \pi^2 \frac{n^2}{L^2}, \tag{2.4}$$

and g is gravity, h filling level, L tank length in the sloshing direction and $n = 1, 2, 3\ldots$. Olsen (1976a) considers the first (lowest) natural frequency to be the most important for modelling but modal analysis indicates that higher modes can influence the sloshing response (Faltinsen *et al.*, 2005). The sloshing response is also directly proportional to the tank acceleration.

Flow history effects can also influence the sloshing response. Lepelletier and Raichlen (1988) studied the time-dependent behaviour of sloshing excited by periodic tank motion and observed that the peak sloshing response is usually in the first transient phase. The tank is subjected to periodic motion for two oscillations and then stopped with the peak sloshing response observed two periods after the tank motion was stopped (Lepelletier and Raichlen, 1988). Schreier *et al.* (2009) carried out further investigations of transient sloshing behaviour and found that particular combinations of tank motion profiles can elicit a sloshing response which is considerably more severe with sloshing pressures up to five times greater than the design pressure. The severity is explained by the absence of entrained air bubbles prior to impact and the second mode response one half period before impact.

The nature of the fluid also determines its sloshing response. LNG is not a pure substance and the precise composition depends on the origin of the gas. Mann (1977) gives a representative breakdown using Algerian Arzew LNG as 87-90% methane, 8-9% ethane and 0.5 to 1% nitrogen. Other component gases include propane, butane and isobutane, which account for less than 0.5% of the total. When approximating the properties of LNG with those of pure methane, any results need to be treated with caution as inaccuracies of up to 20 % have been reported (Mann, 1977). Mann (1977) recommends the use of a rule of mixture model to determine the LNG properties.

Fluid compressibility has been found to be more significant in the ullage gas than for the denser liquid phase. The speed of sound for liquid methane, approximately 1,320 m s^{-1}, is similar to 1,500 m s^{-1} measured in water. Once the methane is in its gaseous state the speed of sound is about 300 m s^{-1}, which is about 10% less than the speed of sound of air. This can give rise to two phenomena not expected when approximating the gas as an incompressible fluid.

- The gas delays the impact pressure peak if located between the tank wall and sloshing liquid. This spreads the impact over a longer timescale, causing prolonged oscillating loading to the containing structure.
- As the sloshing becomes increasingly violent, the gaseous phase will become partially absorbed in the liquid phase. Provided the impact pressures are high enough, this will result in cavitation (Abramson *et al.*, 1974). The subsequent collapse of

cavitation, especially over longer durations, can cause severe erosion damage to the containment structure.

Abramson *et al.* (1974); Corrignan (1994); Olsen (1976a) and Valsgard and Tveitnes (2003) find that the ullage pressure has a significant influence on sloshing pressure and consequent force. Experiments cited by Bass *et al.* (1980) confirm that a lower ullage pressure will result in a higher impact pressure.

2.2.3 Dimensional analysis

The parameters listed in Table 2.1 characterise sloshing and its effect on the tank structure and are considered of importance in the modelling of liquid motions in a typical LNG tank (Abramson *et al.*, 1974). The importance of these parameters is compared using dimensional analysis. Abramson *et al.* (1974) has carried out a dimensional analysis for sloshing in a typical membrane LNG tank and a corresponding 1/30th scale experiment and Ibrahim (2005) gives a survey of dimensionless numbers commonly used to describe sloshing. Data are given for a typical LNG carrier described in Chapter 1 and model testing using data from Abramson *et al.* (1974). The experiment uses water and air at room temperature and the calculations for full scale use LNG consisting of 90% methane and 10% ethane. Numerical values for relevant parameters are given in Table 2.2.

Table 2.1: Parameters affecting sloshing in slack LNG carrier cargo tanks

P	pressure on tank
g	gravity
L	tank length (or diameter for spherical tank)
h	filling height
L_i	other relevant tank dimension
x_0	excitation amplitude
T	excitation period
μ	viscosity
ρ	density
σ	surface tension
c	speed of sound in medium
E	elastic modulus of tank
ΔP	difference between pressure at free surface and vapour pressure

The following non-dimensional groups are obtained by applying the Buckingham π theorem to the parameters in Table 2.1 and selecting the pressure P on the tank due to sloshing as the dependent variable:

$$\overbrace{\frac{P}{\rho\left(L/T\right)^2}}^{\pi_1} = F\left[\overbrace{\frac{g}{L/T^2}}^{\pi_2}, \overbrace{\frac{\rho L\left(L/T\right)}{\mu}}^{\pi_3}, \overbrace{\frac{\rho g L^2}{\sigma}}^{\pi_4}, \overbrace{\frac{L/T}{c}}^{\pi_5}, \right. \\ \left. \overbrace{\frac{\Delta P}{\rho\left(L/T\right)^2}}^{\pi_6}, \overbrace{\frac{E}{\rho\left(L/T\right)^2}}^{\pi_7}, \overbrace{\frac{x_0}{L}}^{\pi_8}, \overbrace{\frac{h}{L}}^{\pi_9}, \overbrace{\frac{L_i}{L}}^{\pi_{10}}\right]. \tag{2.5}$$

The first π term is a pressure coefficient, representing the Euler number[3] and is a function of the remaining π terms. Term π_2 is the Froude number and the terms π_3 to π_6 are the Reynolds, Bond, Mach and cavitation numbers respectively. Wall elasticity is accounted for with term π_7 and the remaining π terms account for geometric similitude.

Free surface shape In physical modelling of sloshing only the free surface shape and geometric similitude are considered (Abramson *et al.*, 1974 and Lloyd's Register, 2009). The Froude number,

$$Fn = \frac{U}{\sqrt{gL}}, \tag{2.6}$$

where g is gravity, L a length scale and U a characteristic velocity, is well known in naval architecture and is imperative for free surface scaling. With Froude scaling, the shape of the liquid will be geometrically similar if the gravity and inertia forces are dominant (Bass *et al.*, 1980).

Viscosity The Reynolds number is a key dimensionless parameter in fluid dynamics which compares inertia and viscous forces. It is given as

$$Re = \frac{LU}{\nu}, \tag{2.7}$$

where L is a length scale, ν kinematic viscosity and U a characteristic velocity. Bass *et al.* (1985) introduce a Froude-modified Reynolds number given as $Re_{Froude} = g^{1/2}L^{3/2}\nu^{-1}$. For a typical LNG tank size with length of about 40 m and LNG viscosity, Abramson *et al.* (1974) and Bass *et al.* (1985) obtain a Reynolds number as 10^9, compared to an experimental value of 10^6. The dynamic viscosity and density change rapidly near the boiling temperature of 112 K, but once the methane has turned liquid, the slopes of viscosity and density are similar, indicating that the kinematic viscosity does not vary

---

[3] The use of the term *Euler number* is somewhat ambiguous as e.g. Abramson *et al.* (1974) and Finnemore and Franzini (2002) use it in reference to the term π_1. Some authors (e.g. Lloyd's Register, 2009) refer to *Euler scaling* when addressing scaling of impacts with compressible fluids. In this study the terminology used by Abramson *et al.* (1974) is adopted where *Euler number* refers to the term π_1 and compressible impacts are referred to using the Cauchy number

significantly in the temperature region of interest of below 110 K.

The importance of viscosity cannot be determined with the Reynolds number alone and Abramson *et al.* (1974) carried out an experimental campaign varying the viscosity of the sloshing liquid to assess the importance of viscosity on the resulting impact pressures. It was found that for small ($x_0/L = 0.01$) excitation amplitudes viscosity influences the impact pressure due to sloshing at shallow ($h/L = 0.12$) and non-shallow ($h/L = 0.5$) filling levels. In the experiments no attempt was made to replicate the increased surface roughness due to the corrugation of the Mark III system described in Section 1.3.1 which adds to the viscous damping at the boundary layer. The Reynolds number is also used to classify a flow as laminar or turbulent and, depending on surface roughness, for external flows a Reynolds number of 10^5 to 10^6 is indicative of turbulence which implies the necessity of including turbulence and consequently viscosity at the full scale.

When the excitation amplitude is increased to $x_0/L = 0.1$, which corresponds to expected extreme motions of an LNG carrier, the effect of viscosity on the impact pressure is found to be negligible (Olsen, 1976a; Bass *et al.*, 1985). Since large liquid motions and the resulting large impact pressures are of interest in the design process, viscous scaling is considered to be of secondary importance. However, if viscosity were to be important, as may be the case in the Aker tank design (vom Baur, 2009) due to the internal tank structure, then model testing is nonconservative as the viscosity of water is too large and the liquid motions are overdamped (Abramson *et al.*, 1974).

Compressibility The Cauchy number,

$$Ca = \frac{\rho U^2}{E}, \tag{2.8}$$

where ρ is density, U velocity and E the bulk modulus, given as

$$E = \rho c^2, \tag{2.9}$$

where c is the speed of sound, relates the inertial and compressibility forces of a liquid and combining Equations (2.8) and (2.9) gives the Mach number. The low magnitude $O\left(10^{-7}\right)$ of the Cauchy number indicates that the effect of compressibility is not significant but this assumption is discussed in more detail for liquid-gas mixtures in the next section. The Cauchy number can be used as the basis for scaling, which is considered in greater detail in Section 2.3.1.

Surface tension The Bond number Bo compares gravitational and surface tension forces and if greater than unity, surface tension can be neglected when modelling a free surface (Abramson *et al.*, 1974). It is defined as

$$Bo = \frac{\rho g L^2}{\sigma}, \tag{2.10}$$

where ρ is density, g gravity, L characteristic length and σ surface tension, which was obtained for LNG using data from Escobedo and Mansoori (1996). The magnitude of the Bond number of $O\left(10^5\right)$ and $O\left(10^8\right)$ for experiment and full scale shows that the effect of surface tension on the sloshing pressure is small and can therefore be neglected.

Fluid-structure interaction The elasticity of the tank walls also affects the sloshing response and since the structural integrity of the containment system is the primary concern during design the interaction between the fluid and structure is of importance. The interaction between the tank structure and the impacting fluid is currently neglected in sloshing analyses or split from the procedure determining the sloshing impact pressure (American Bureau of Shipping, 2004). Abramson *et al.* (1974) compare the natural frequency of the plywood boxes of 250 Hz with the 0.1 to 1.0 Hz for sloshing but admit the possibility of dynamic amplification of stresses due to impact pressures. The effects of fluid-structure interaction[4] have been investigated in the EUROSLOSH research programme (Dogliani, 1994) and Bunnik and Huijsmans (2007) found that elastic walls can result in 10% lower pressures than a rigid wall.

The main concern for the assessment of sloshing is the structural response to a sloshing pressure and the dynamic amplification of the sloshing-induced pressure due to fluid-structure interaction can exacerbate the stress on the containment system. Malenica *et al.* (2009) studied fluid-structure interaction effects for a symmetrical triangular impulsive pressure loading and found a peak amplification factor in excess of 1.5 which is comparable to the design guidelines given by Lloyd's Register (2009). When considering the breaking wave impact in Figure 2.4(b), the impact pressure history is oscillatory (e.g Godderidge *et al.*, 2009) and if the oscillation frequency coincides with a structural mode of vibration further amplification of the stress due to the pressure loading can be expected.

2.2.4 Multiphase flow analysis

The dimensional analysis has assumed single phase fluid properties, but LNG is transported close to its boiling temperature and the fluid sloshing can cause mixing between the liquid and vapour phases. Although the main location of LNG boil-off is at the free surface[5], the bubble formation due to heating through the containment system can be

---

[4] Hydroelasticity is concerned with the motion of deformable bodies through liquids (Bishop and Price, 1979)

[5] Teo Popa (Techical Advisor, SIGTTO), private communication

Table 2.2: Comparison for model and full scale sloshing tank. Data for experiment are taken from Abramson *et al.* (1974) and full scale date for the LNG carrier in Section 1.2.

	Experiment - model scale	LNG tank - full scale
Geometric scale	$1/40^{\mathrm{th}}$	–
Length L [m]	1.0	40.0
Fluid	Water	LNG
Density ρ [kg m^{-3}]	1,000	470
Kinematic viscosity ν [m^2 s^{-1}]	$1.01 \cdot 10^{-6}$	$1.60 \cdot 10^{-6}$
Surface tension σ [N m^{-1}]	0.0728	0.0165
Speed of sound c [m s^{-1}]	1,500	1,320
Wave speed U [m s^{-1}]	1.0	8.0
Reynolds number	$1 \cdot 10^{6}$	$2 \cdot 10^{8}$
Cauchy number	$4 \cdot 10^{-7}$	$7 \cdot 10^{-8}$
Bond number	$1 \cdot 10^{5}$	$5 \cdot 10^{8}$

analysed using the approach by Fay (2007).

Provided that buoyancy and fluid dynamic drag are the only forces acting on a bubble, for equilibrium

$$\rho_b U_b^2 d^2 \sim \rho_l g d^3, \tag{2.11}$$

where d is bubble diameter, g gravity, ρ_b pool density which is related to the LNG density ρ_l using the bubble volume fraction η as $\rho_b = (1-\eta)\,\rho_l$ and U_b bubble velocity. For low bubble volume fractions $\rho_p \approx \rho_l$ and Equation (2.11) can be simplified to

$$U_b \sim \sqrt{gd}. \tag{2.12}$$

The bubble diameter is determined by the balance between the buoyant and surface tension forces acting on the bubble (Fay, 2007), so that the bubble diameter is given by

$$d \sim \sqrt{\frac{\sigma}{\rho_b g}} \tag{2.13}$$

where σ is the surface tension the bubble velocity is

$$U_b \sim \left(\frac{\sigma g}{\rho_b}\right)^{1/4}. \tag{2.14}$$

Thus, an approximate bubble size of $d \sim 2 \cdot 10^{-3}$ m and velocity $U_b \sim 0.15$ m s^{-1} is obtained for LNG with Equations (2.13) and (2.14).

Sloshing impacts can also result in mixing between the liquid and gas phases (Bunnik and Huijsmans, 2007) which is shown in Figure 2.6. There is no simple model analogous to

Equations (2.13) and (2.14) to quantify the bubble dynamics and experimental measurement of gas bubble behaviour is not straightforward (Colicchio, 2004). Gas entrainment results in an increase in bulk fluid compressibility and a speed of sound up to three orders of magnitude lower than in a pure liquid (Kieffer, 1977; Sherstyuk, 2000). This increases the Cauchy number in Equation (2.8) to approximately 0.5 which implies that the fluid-gas mixture must be treated as compressible.

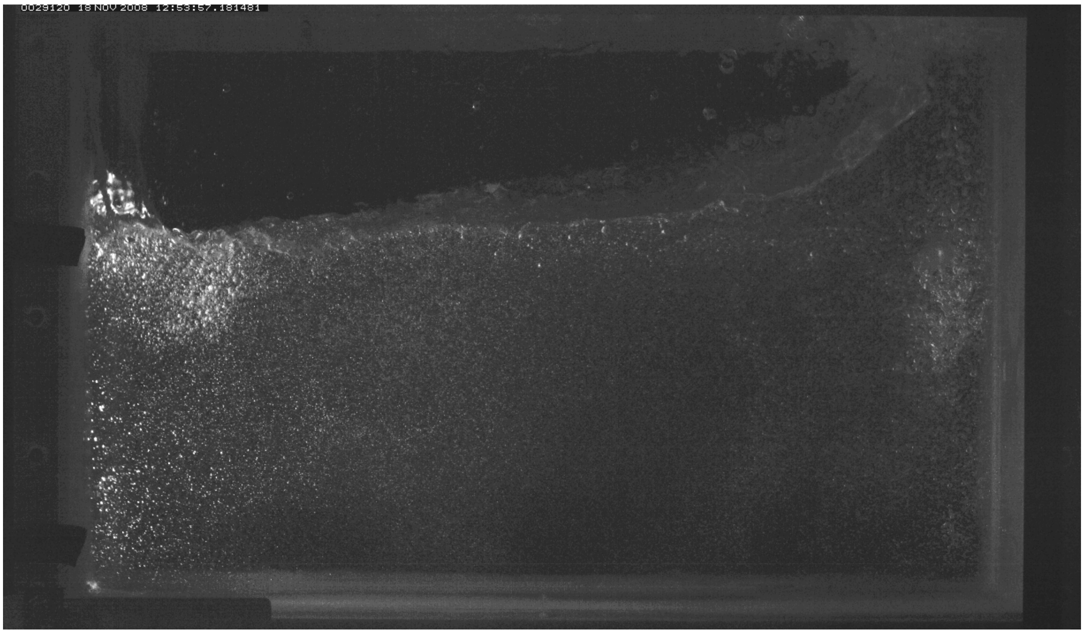

Figure 2.6: Air entrainment due to sloshing impacts and fluid overturning (Schreier *et al.*, 2009). The presence of the gas in the fluid increases the compressibility of the mixture and results in lower impact pressures.

The influence of gas bubbles on the flow can be quantified using the approach by Brennen (2005). A size parameter X and a mass parameter Y are used in conjunction with a particle Reynolds number. They are defined as

$$X = \frac{R}{l}\left|1 - \frac{m_p}{\rho_c v}\right|, \tag{2.15}$$

$$Y = \left|1 - \frac{m_p}{\rho_c v}\right| / \left(1 + \frac{2m_p}{\rho_c v}\right) \tag{2.16}$$

and the particle Reynolds number

$$R_{N,\alpha} = \frac{\left|U_\beta - U_\alpha\right| R}{\nu_\alpha}, \tag{2.17}$$

where l is a length scale, m_p particle mass, ν_c kinematic viscosity, ρ_c liquid density, R bubble radius, U characteristic velocity and v particle volume. With the above results, $X = 2.492 \cdot 10^{-5}$, $Y = 0.99$ and $R_{N,\alpha} = 3.33 \cdot 10^4$.

Figure 2.7 illustrates the regions of homogeneous and inhomogeneous multiphase flow. The flow in the upper right quadrant is inhomogeneous (transient) and it is characterised by large velocity W_m/U between the phases. In the transient region the interaction between the liquid and gas phases must be modelled explicitly. As the relative velocity decreases the flow regime proceeds in the quasi-static (homogeneous) fields in the lower left and right quadrants. Flows in the quasi-static fields are considered homogeneous and the phases share a single velocity field.

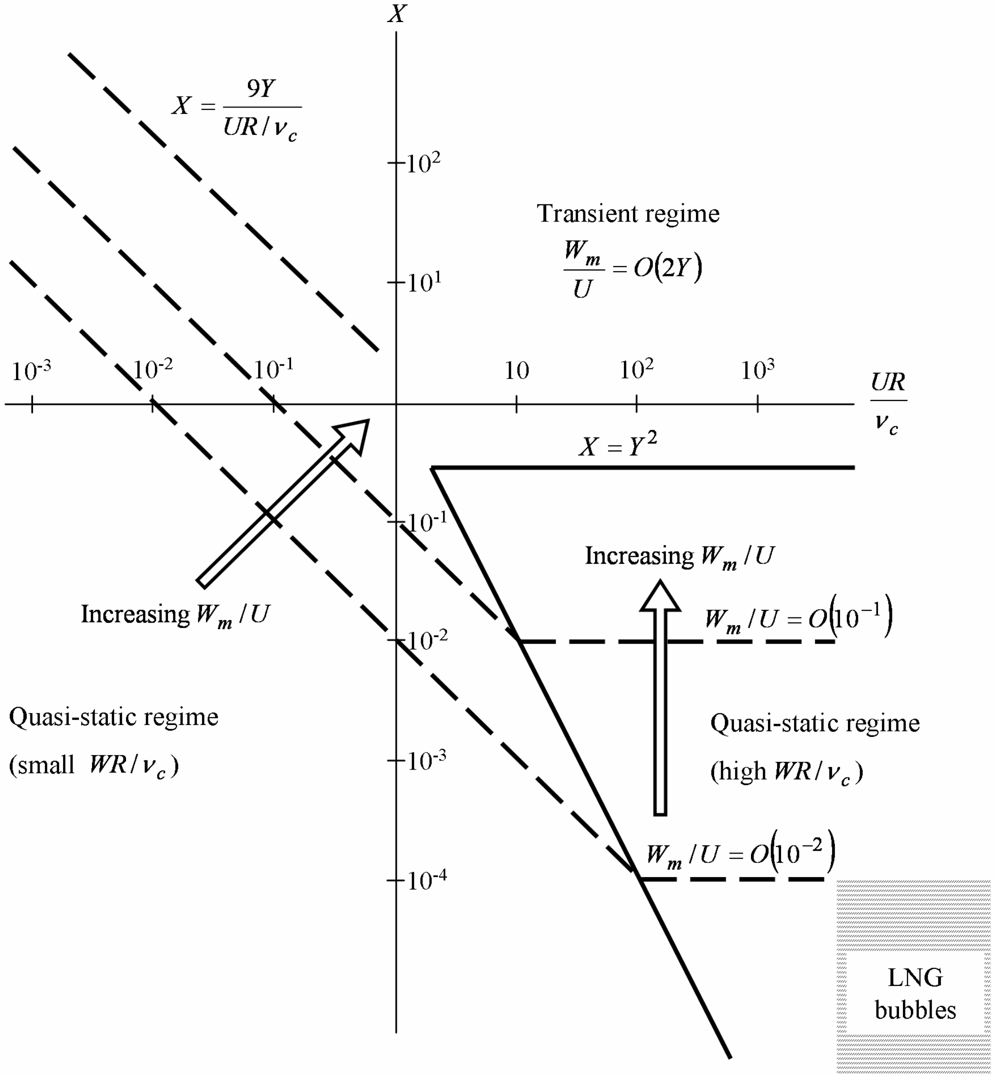

Figure 2.7: Relative motion regimes for a multiphase flow (Brennen, 2005). The bubbles due to LNG boil-off are in the quasi-static regime and do not affect the bulk fluid motion

The relative velocity between the liquid and the gas bubbles is approximately 0.02 and the multiphase flow regime due to boil-off can be considered quasi-static, which is indicated in Figure 2.7. As long as the bubble size and velocities are similar to those expected from boil-off, an analogous argument can be made for gas bubbles entrained after impact, but the effect of relative velocity on bubbles formed during air entrainment are discussed separately in Chapter 3.

LNG is transported as a boiling liquid and both liquid and gas (vapour) phases present in an LNG tank are from the same material. The possible effect of vapour bubbles on sloshing impacts has been identified by Abramson *et al.* (1974) and later by Bass *et al.* (1985). Abramson *et al.* (1974) quote previous studies by DNV where little difference was observed between boiling and non-boiling water, but pumping procedures suggests that vapour-liquid phase transition can be expected to occur[6] at pressures which may be experienced in LNG tanks during sloshing.

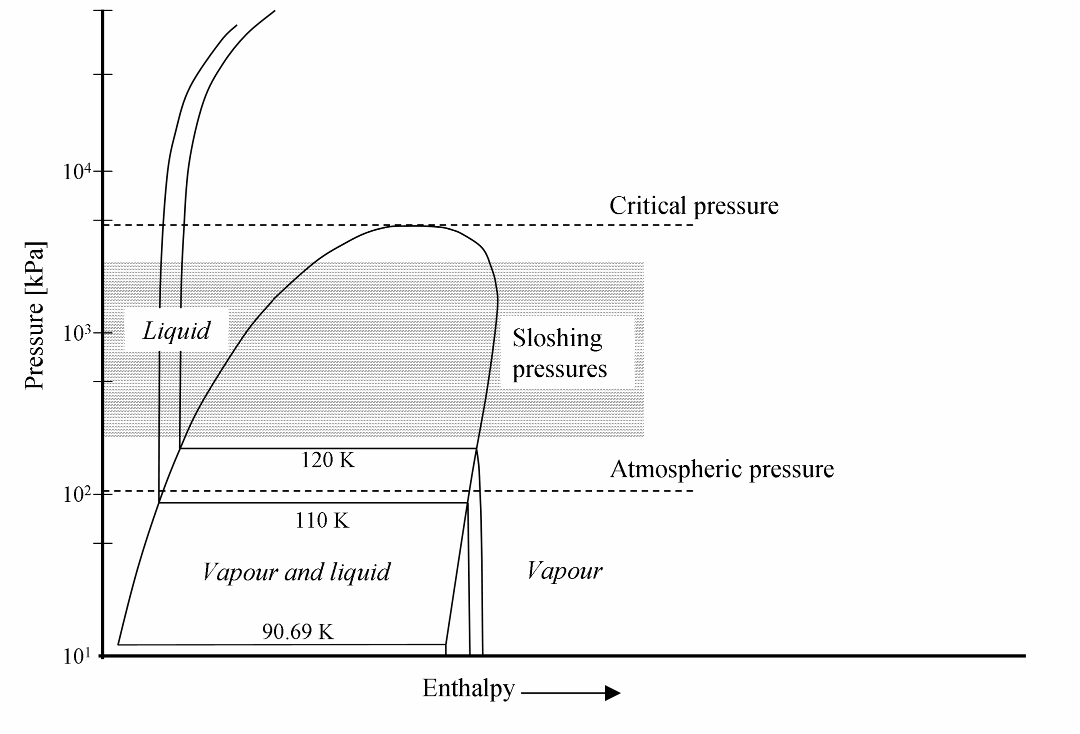

Figure 2.8: Methane phase diagram (Setzmann and Wagner, 1991). Impact pressures due to sloshing can reach the critcal pressure for LNG which results in change from vapour to liquid phase.

Figure 2.8 shows a pressure-enthalpy diagram of LNG with isothermal lines for 110 K and 120 K. The LNG is normally transported at atmospheric pressure. When a vapour bubble is subjected to a sufficient increase in pressure, the vapour undergoes a rapid phase change to liquid which is analogous to cavitation (Abramson *et al.*, 1974) but current design guidelines do not take phase change into account.

2.3 Methodologies for sloshing analysis

Sloshing can be analysed using experimental, theoretical and numerical techniques. Each of these approaches relies on the correct representation of sloshing physics and has certain advantages and drawbacks.

---

[6] Alan Campion (lecturer at Warsash Maritime Academy) private communication

2.3.1 Experimental model scale testing

Model testing continues to be a popular and cost-effective method for the assessment of sloshing loads and classification societies use model tests to determine the sloshing pressures for a particular tank design. The tests scale are usually between 1/70th and 1/25th scale and Jeon *et al.* (2008) found in a series of systematic tests that the results from 1/25th and 1/50th scale are suitable for scaling but a 1/100th scale is too small. The experimental study by Hinatsu (2001) is used in numerous studies for the validation of sloshing simulations and it is described in greater detail in Chapter 3.

The principal difficulty in sloshing model testing is scaling of the sloshing pressures which is caused by a large number of sometimes conflicting scaling laws (Abramson, 1966; Bass *et al.*, 1985). The pressures and motions for LNG sloshing model tests are scaled using the Froude number (Bass *et al.*, 1980, 1985) so that the recorded pressure is related to the full-scale tank as

$$p \sim l_f U^2. \tag{2.18}$$

The application of this scaling law to impact pressures can result in excessively large values at full scale and an alternative compressible formulation based on the Cauchy number (by e.g. Lloyd's Register (2009) also referred to as Euler scaling) is

$$p \sim l_f c U, \tag{2.19}$$

where c is speed of sound, l_f scale factor and U velocity. Abramson *et al.* (1974) use values for l_f considerably less than 1 (as low as 0.05) by comparing recorded impact pressures and containment system strength but the conservativeness in Froude scaling justifies its preference in design over the compressible formulation (Lloyd's Register, 2009).

Jeon *et al.* (2008) conclude that the choice of scaling law depends on the sloshing response and the sloshing pressures resulting from hydrodynamic impacts are best scaled using Froude scaling in Equation (2.18). Other impact pressures where phase mixing is an important feature are more suited for scaling using the compressible formulation in Equation (2.19). This may be explained by the influence of the gas phase in the liquid during sloshing (see Figure 2.6). This possibility was dismissed by Jeon *et al.* (2008), but only a small amount of gas entrained in the liquid is sufficient to change the compressibility of the fluid-gas mixture. Air cushioning during impact of a flat plate at an angle of incidence was investigated by Shin *et al.* (2003).

A further step in the reduction of model-scale uncertainty is the measurement of sloshing loads at full scale. The classification societies DNV, Lloyds Register as well as the ship

Figure 2.9: 6 DOF sloshing rig used for LNG carrier design with hydraulic actuators (from Jeon *et al.*, 2008). Costs including instrumentation can approach £250,000.

operator Teekay and shipbuilder Daewoo carried out full-scale measurements of sloshing loads on LNG carriers in 2008 (Tinsley, 2007). Another consortium including BV, Shell and MARIN participated in the SLOSHEL project which measured sloshing loads on an LNG carrier and results are to be presented at Gastech and ISOPE 2009.

2.3.2 Theoretical models

While experimental methods are suited for the detailed study of pressure fields caused by the sloshing fluid, theoretical fluid dynamics using inviscid incompressible irrotational (potential) flow has also been used in the study of sloshing (Abramson, 1966; Fox and Kuttler, 1983). A key advantage of linear potential flow is that a solution can be found quickly. Closed-form solutions are normally available only for simple shapes such as rectangles and vertical circular cylinders and solutions for more complex tank shapes can be obtained using a boundary element method (Abramson, 1966).

The sloshing response most suitable for a linear potential flow model is small amplitude linear sloshing. Graham and Rodriguez (1952) developed a linear potential flow solution by dividing the sloshing problem into two-dimensional components, with separate solutions for longitudinal and transverse tank motions and a separate 3D solution for yaw motions. Nonlinear sloshing cannot be described adequately with linear methods (Faltinsen, 1974; Ibrahim, 2005) and Abramson *et al.* (1966) observed fair comparison between experimental data and a nonlinear model developed by Hutton in 1963. Faltinsen (1974) obtained a third-order closed form solution, which resembles the solution of Duffing's equation, for rectangular tanks based on potential flow and Faltinsen (1978) develops a boundary element discretisation to compute sloshing in more complicated tank shapes. Chester (1968) studied the behaviour of liquid motions at low filling ratios near the resonant frequency with a shallow water wave theory including dissipation and dispersion and Chester and Bones (1968) report good agreement between theory and experimental measurements. However, the motion amplitudes of the tank $x_0/L < 0.005$ are too low to be representative of the motions of an LNG carrier.

Faltinsen *et al.* (2000) applied multimodal analysis to the sloshing problem in a 2D rectangular tank, where the velocity potential and free surface shape are expanded in generalised Fourier series by a set of natural modes. This leads to a set of nonlinear ordinary differential equations, which can be solved rapidly for long simulation times. The solution takes approximately 1% of real time (Faltinsen *et al.*, 2000), which is a vast improvement over conventional full-field solution methods such as CFD. However, the theory is restricted to non-overturning waves and intermediate water depths. Faltinsen and Timokha (2001) extended the multimodal system to lower filling levels and successfully simulated a sloshing flow induced by translatory tank motion at a filling ratio $h/L = 0.173$.

Shallow water sloshing is addressed further by Faltinsen and Timokha (2002). A damping model is introduced for the inclusion of dissipation at the boundary layer and internal dissipation in the liquid. The inclusion of higher modes was necessary to simulate sloshing at $h/L \leq 0.10$ but the multimodal system experiences convergence problems at $h/L \leq 0.05$ and its performance depends on the correct estimation of a damping coefficient (Faltinsen and Timokha, 2002). The multimodal theory has been extended by Faltinsen *et al.* (2003, 2005, 2006) to simulate three dimensional sloshing in a square and nearly-square basin.

An alternative phenomenological description of sloshing is the use of pendulum models which assume that the fluid can be separated into a moving and stationary component and the sloshing fluid in the tank behaves as a uniform mass. The utility of pendulum models was illustrated by Aliabadi *et al.* (2003) where the sloshing force computed using a CFD solution on finite elements was compared to the force obtained from the pendulum. At low filling levels, the results match well, but as the filling level is increased the pendulum overpredicts the sloshing load.

However, Aliabadi *et al.* (2003) used a linear two-dimensional pendulum model and more complex models have been derived as well. Pilipchuk and Ibrahim (1997) developed a pendulum model to study sloshing in a moving container. El-Sayad *et al.* (1999) developed a similar combined pendulum system to model the sloshing motion in a water tower where the pendulum is used for the fluid motion and a spring-mass model for the tower reaction. The behaviour of this system was studied in greater detail by Ibrahim and El-Sayad (1999) and the model was enhanced by Pilipchuk and Ibrahim (2000).

2.3.3 Computational Fluid Dynamics

Computational Fluid Dynamics (CFD) is primarily associated with, but not limited to, the numerical solution of viscous flows which are described by the Navier-Stokes Equation. CFD has turned into a practical design tool with the advent of powerful computers. CFD is often considered the sledgehammer approach to solving fluid dynamics problems and results can sometimes be deceptive. Transient three-dimensional CFD simulations require large computational resources and are not viable for a large number of simulations.

As increased reliance is placed on CFD results, it is vital to ensure the results are appropriate for the problem being addressed. The correct choice of mathematical model for the problem is an obvious prerequisite. The UK Health and Safety executive (Lea, 2003) as well as the EU-wide MARNET (WS Atkins Consultants, 2003) have developed guidelines to aid in this process. Especially when solving numerous variations of one specific problem, identifying the best trade-off between modelling complexity and computational speed is of considerable economic importance.

There are three main methods within CFD, each solving a fluid model of increasing complexity:

1. Panel methods. These are the natural progression from closed-form solutions in the previous Section 2.3.2 obtained from potential flow. Surfaces with complex shapes are represented using discrete panels which are usually quadrilaterals. Although Hirsch (1988) recommends that this approach is replaced by more sophisticated methods, panel methods continue to be used, both on their own and in combination with other methods. This may be explained by the fact that panel methods need only to discretise the boundaries of the fluid domain, a reduction in computational cost of several orders of magnitude compared to the methods below.
2. Euler equations. The Euler model still assumes inviscid flow but the conditions requiring irrotationality and incompressibility are lifted, permitting more realistic representation of fluid behaviour. However, the full fluid domain, as opposed to only the boundaries, has to be discretised.
3. Navier-Stokes equations. A Navier-Stokes model includes viscosity and provides the most faithful representation of true fluid behaviour. This is offset by increased computational requirements due to the discretisation of viscous terms as well as the need to discretise the full fluid domain.

Sometimes, two models are combined in one problem to reduce computational cost, for example when using Euler equations or potential flow in the far-field region when solving the flow over a wing. However, this requires some prior knowledge of the problem and introduces an additional unknown into the solution.

The Navier-Stokes equations describe the behaviour of a viscous (usually Newtonian) fluid. This considerably more general model introduces nonlinearities rendering a closed-form solution for all but the simplest cases impossible. The term ‘Navier-Stokes equations’ refers to the conservation of momentum equations, which when coupled with a continuity and other applicable equations and the appropriate boundary conditions for time and space yield a solvable system. However, in the field of CFD ‘Navier-Stokes equations’ is often used to refer to the full set of equations used and this terminology will be adopted here as well. Two main variations of the Navier-Stokes equations are used for flow modelling.

The assumption of incompressible flow (i.e. $\rho = \text{const}$) is a satisfactory simplification for most marine applications. The incompressible Navier-Stokes equations can be written in Cartesian tensor notation as

$$\frac{\partial u_i}{\partial x_i} = 0, \tag{2.20a}$$

$$\frac{\partial u_i}{\partial t} + u_j \frac{\partial u_i}{\partial x_j} = -\frac{1}{\rho}\frac{\partial p}{\partial x_i} + \frac{\partial \left(\tau_{ij}\right)}{\partial x_j} + b_i, \tag{2.20b}$$

$$\tau_{ij} = \nu \left(\frac{\partial u_i}{\partial x_j} + \frac{\partial u_j}{\partial x_i}\right) \tag{2.20c}$$

where b_i is the body force, ν kinematic viscosity, ρ fluid density, p pressure, t time and u_i the Cartesian velocity vector components.

Compressible flow allows density variations in time and space, but the introduction of density as an additional variable requires a further equation to complete the system - usually an ideal gas equation of state (2.21e) or more sophisticated equations of state:

$$\frac{\partial \rho}{\partial t} + \frac{\partial}{\partial x_i}\left(\rho u_i\right) = 0, \tag{2.21a}$$

$$\frac{\partial}{\partial t}\left(\rho u_i\right) + \frac{\partial}{\partial x_j}\left(\rho\ u_j\ u_i\right) = -\frac{\partial p}{\partial x_i} + \frac{\partial \left(\tau_{ij}\right)}{\partial x_j} + b_i \tag{2.21b}$$

$$\tau_{ij} = \mu \left(\frac{\partial u_i}{\partial x_j} + \frac{\partial u_j}{\partial x_i}\right) - \delta_{ij}\frac{2\mu}{3}\nabla \cdot \mathbf{v} \tag{2.21c}$$

$$\frac{\partial}{\partial t}\left(\rho I\right) + \frac{\partial}{\partial x_i}\left(\rho\ I\ u_i\right) = -p\frac{\partial u_i}{\partial x_i} + k\frac{\partial^2 T}{\partial x_i \partial x_i} + \Phi + T_{ext} \tag{2.21d}$$

with

$$p = \rho R T \tag{2.21e}$$

and

$$I = C_v T, \tag{2.21f}$$

where C_v is the specific heat at constant volume, I internal energy, k thermal conductivity, μ dynamic viscosity, Φ viscous dissipation (heat generated by fluid viscosity), R the Boltzmann constant, T absolute temperature, T_{ext} external heat sources and $\mathbf{v}$ velocity vector. Compressibility reduces the 'stiffness' of the numerical system and often improves the speed of convergence for iterative solution techniques.

The Navier Stokes Equations can be discretised using an Eulerian or Lagrangian approach. In the Eulerian approach the discretisation scheme is fixed to the computational domain. The two main groups of Eulerian discretisation schemes are finite difference and finite volume methods (Ferziger and Peric, 2002). A finite difference approach uses the conservation equations (2.20) or (2.21) in differential form and the partial differentials are approximated with Taylor series or polynomial fitting using the surrounding nodes (Ferziger and Peric, 2002). Finite difference methods can be applied to regular grids and it is easy to obtain higher-order schemes for such grids but the finite difference method is difficult to apply to complex geometries and conservation is not enforced unless special care is taken (Ferziger and Peric, 2002).

The finite volume method uses an integral form of the conservation equations and the computational domain is divided into a finite number of control volumes (Ferziger and Peric, 2002). The principal advantages of the finite volume method are its suitability for complex geometries and the conservation of relevant properties for each control volume (Versteeg and Malalasekera, 1995). Most commercial CFD codes[7] use a finite volume discretisation scheme. One of the drawbacks of the finite volume method is that higher-than second order schemes are difficult to develop for 3D (Ferziger and Peric, 2002) because the finite volume approach requires an interpolation, differentiation and integration step.

In the Lagrangian approach the discretisation is fixed to the material and moves with the material (Liu and Liu, 2003). The finite element approach uses a continuous grid which moves with the fluid (Liu and Liu, 2003) and the equations are multiplied by weight functions prior to integration (Ferziger and Peric, 2002). Finite element methods are capable of dealing with arbitrary geometries which is an important advantage for CFD applications, but the resulting matrices are not as well structured as those from regular finite difference or finite volume based discretisations which makes it more difficult to solve the resulting system (Ferziger and Peric, 2002).

Smoothed Particle Hydrodynamics (SPH) (Lucy, 1977; Gingold and Monaghan, 1977) and the Moving Particle Semi-implicit Method (MPS) (Koshizuka *et al.*, 1995) are particle methods, where the fluid is resolved into a finite number of particles and the particles are moved according to the flow field. The particles interaction is modelled with a weight or kernel function. SPH was originally developed for the study of astrophysical problems

---

[7] CFX, Flow-3D, Fluent, Phoenix and Star-CD as well as the open-source code OpenFOAM

(Liu and Liu, 2003), but it has since been applied to hydrodynamics problems with large boundary deformations such as explosions and sloshing (Colagrossi and Landrini, 2003; Liu and Liu, 2003). MPS gives a strictly conservative discretisation of the governing equations (Koshizuka *et al.*, 1995; Koshizuka and Oka, 1996) and it has also been applied to sloshing (Godderidge, 2004) and wave breaking problems (Koshizuka *et al.*, 1998).

The governing Equations (2.20) and (2.21) are valid for all flow regimes satisfying the restrictions imposed by the assumptions made. The successful numerical solution depends on sufficient grid resolution and time step size to capture the relevant flow features. Turbulence takes place at often very small spatial and time scales and in order to capture the effects of turbulence using the governing equations in their present form grids with extremely high resolution and very small time steps would be required. As turbulence is a three-dimensional time-dependent phenomenon (Pope, 2000), no two-dimensional simulation is permissible. Direct Numerical Solution (DNS) attempts to model turbulent flows using sufficiently fine resolution of space and time (Anderson, Jr, 1995) but DNS is currently confined to problems of mainly academic interest, as no computers powerful enough exist to make it a practical reality.

By using a time-averaging approach the random component of a turbulent signal (e.g. pressure or velocity) when averaged over time would equal zero. Defining the mean of a time dependent fluid property $\phi(t)$ over the averaged time T as

$$\overline{\phi} = \frac{1}{T}\int_0^T \phi(t)\ dt, \tag{2.22}$$

so that

$$\phi(t) = \overline{\phi} + \phi'(t), \tag{2.23}$$

with the rapidly varying component ϕ'

$$\overline{\phi'(t)} = 0. \tag{2.24}$$

The application of this procedure to the governing Navier-Stokes Equations (2.20) results in the unsteady Reynolds-Averaged Navier-Stokes Equation (RANS) for incompressible flows

$$\frac{\partial\left(\overline{U}_i\right)}{\partial x_i} = 0, \tag{2.25a}$$

$$\frac{\partial\left(\overline{U}_i\right)}{\partial t} + \frac{\partial}{\partial x_j}\left(\overline{u}_i\overline{u}_j + \overline{u_i'u_j'}\right) = -\frac{1}{\rho}\frac{\partial\overline{P}}{\partial x_i} + \nu\frac{\partial}{\partial x_j}\left(\frac{\partial\overline{U}_i}{\partial x_j} + \frac{\partial\overline{U}_j}{\partial x_i}\right). \tag{2.25b}$$

This procedure introduces, for a three dimensional problem, six additional unknowns to the momentum Equation (2.25b). There is no readily available exact formulation to close the system by expressing the Reynolds (or Turbulence) stress $\rho\overline{u_i'u_j'}$ in terms of quantities known from the flow field and the closure of the turbulence problem generated by Reynolds averaging is the starting point for turbulence modelling.

The boundary conditions required for the sloshing problem are solid walls at the tank boundary and a free surface. The sloshing takes place in an enclosed container and the fluid velocity and, if applicable, temperature can be specified explicitly on the tank walls. However, an absolute reference pressure value needs to be specified at some location within the fluid domain. The temporal boundary, or initial condition, was implemented by specifying zero fluid motion at $t = 0$ and applying the sloshing motion to the container.

In the sloshing problem more than one fluid is present and the dynamic location of the free surface - the boundary between the fluids - cannot be specified *a priori* and must be obtained as part of the solution. Since the free surface represents a jump in the density and viscosity fields, it is challenging to capture and maintain the sharpness a free surface with computational fluid dynamics.

Interface tracking methods treat the free surface as a sharp boundary whose location is followed during the simulation by adjusting the grid location or tracking the fluid (Ferziger and Peric, 2002). Consequently a sharp free surface is maintained and there is no numerical smearing between the phases but problems associated with mesh motion and deformation arise. This limits wave steepness and the simulation of overturning waves and fluid fragmentation is not possible with grid-based interface tracking methods.

Particle methods such as Smoothed Particle Hydrodynamics and Moving Particle Semi-Implicit methods do not use a computational grid and they are well suited for the simulation of violent free surface flow problems because the discretised fluid particles are moved according to the flow field. This advantage is offset by a large computational penalty incurred by updating lists of neighboring particles. Pressure data obtained from particle methods usually has a high-frequency noise component due to the particle interaction model (e.g. Molteni and Colagrossi, 2008; Koshizuka *et al.*, 1998). Particle methods also suffer from a difficulty in applying numerical analysis, most of which was originally developed for Eulerian approaches, to establish stability, accuracy and convergence properties (Liu and Liu, 2003). Lagrangian finite element approaches do not suffer from these drawbacks, but the re-meshing due to the displacement of the free surface consumes computational resources and introduces errors due to interpolation.

Interface capturing methods use an Eulerian approach and do not define the interface as a sharp boundary (Ferziger and Peric, 2002). The Marker and Cell (MAC) approach (Harlow and Welch, 1965) uses massless particles to track the location of the free surface. Only the liquid phase needs to be discretised which makes it computationally efficient (Reddy and Radosavljevic, 2006). Flow phenomena such as fluid fragmentation and air entrapment cannot be simulated with MAC.

The Level Set method (Sussman *et al.*, 1994) uses a colour function to capture the location of the fluid interface. The colour function is 0 at the free surface and it is allowed to move with the solution of a transport equation. When the colour function becomes too complicated due to the deformation of the free surface it needs to be re-initialised (Sussman *et al.*, 1994). The re-initialisation of the colour function needs to ensure the conservation of mass but this results in increased computational cost. Level-set methods have been applied to the solution to sloshing flows by e.g. Chen *et al.* (2009) but there was poor agreement between experiment and computational result when fluid impacts occurred. After about 20 oscillations, 3% to 6% of the fluid mass was lost, affecting the resonance characteristics of the sloshing flow and consequently the computational result.

The volume-of-fluid (VOF) approach was introduced by Hirt and Nichols (1981) to model flows with a free surface using a finite volume discretisation by solving a transport equation for the liquid in each cell. It is possible to simulate fluid fragmentation with this approach but there is no interaction between the liquid and the surrounding (or entrapped) gas. This drawback is overcome by the use of a suitable multiphase approach which is discussed in the next section.

The main disadvantage of the VOF approach is that the thickness of the free surface is limited by the control volume size and some smearing of the fluid interface occurs. This is overcome by local mesh refinement in cells with partial filling. Conservation of mass is also a problem with VOF-based methods (Faltinsen and Rognebakke, 2000) due to the iterative solution of the conservation equations. The advantage of VOF is that it is possible to simulate an arbitrary number of fluids as well as addressing the interaction between the phases.

The VOF approach has been used for CFD sloshing simulation by Hadzic *et al.* (2002) and Aliabadi *et al.* (2003) and Godderidge *et al.* (2009) compared two multiphase models for VOF simulation of sloshing. VOF can deal with violent sloshing beyond the limitations of theoretical models, but its application is restricted by considerable computational costs. Dias *et al.* (2009) have recently developed a numerical model which treats the discontinuities in the free surface and the mixing of gas and fluid using averaged quantities.

2.3.4 Assessment

The solution methods identified in this section are now compared and assessed for their suitability in a sloshing guidance system. The different approaches to solving the sloshing problem have different restrictions and assumptions and the selection of the most appropriate approach is dependent on the sloshing response. A well-founded solution to a fluid dynamics problem will usually resort to more than one of the approaches shown in Figure 2.10 and a synthesis of CFD, experimental methods and theoretical analysis will give the best overall result (Anderson, Jr, 1995).

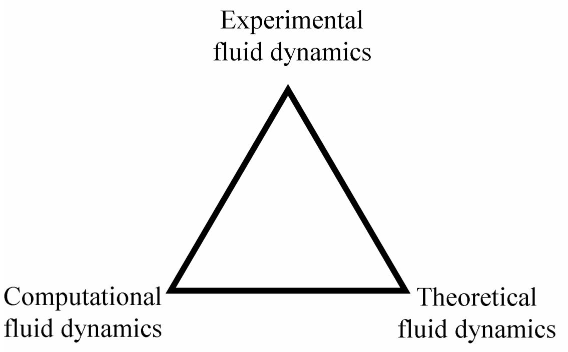

Figure 2.10: Solution approaches for problems in fluid dynamics

Table 2.3: Assessment of sloshing guidance system requirements included in sloshing models

	Experimental methods	Theoretical methods	CFD
Generality of a solution	motion-specific	shape-dependent	motion-specific
Sloshing regime	no restrictions	weakly nonlinear	strongly nonlinear
Free surface	no restrictions	wave steepness depends on theory	VOF: no restrictions, MAC: no breaking, SPH: no restrictions
Solution errors	difference between applied and measured tank motion	numerical integration in time (if required)	numerical solution for time and space
Speed of solution	real time	faster than real time	slower than real time
Tank motion	displacement	displacement or acceleration	displacement or acceleration
Cost of infrastructure (£)	10K to 250K	small	5K to 50K

Table 2.3 summarises the comparison of experimental, theoretical and CFD approaches when they are applied to the sloshing problem. Experimental methods include the relevant sloshing physics and there are no restrictions to the sloshing regime and free surface shape but scale effects such as ullage pressure may be lacking. The two main assumptions are scaling and the simplification of a liquid-vapour system with two separate fluids, usually water and air. Model tests are specific to a particular tank shape and separate tests are required for different tank shapes. The costs of experimental facilities can vary significantly, with a 6 DOF sloshing rig illustrated in Figure 2.9 costing up to £250,000[8] and, unlike for e.g. wind tunnels or towing tanks, there is no alternative use for sloshing test rigs.

---

[8] Y-B. Lee, private communication

The solution of a theoretical sloshing model can be expressed in terms of the tank shape (e.g. Equation 2.2) so that one theoretical solution is applicable over a wide range of excitation motions. Although such closed-form solutions are usually only available for simple shapes, potential flow solutions can be found rapidly using boundary element methods. The main drawback of theoretical models based on potential flow is that their applicability is restricted to particular sloshing regimes. Linear potential flow solutions are valid for linear sloshing and higher-order methods such as the third order method by Faltinsen (1974) or the multimodal approach by Faltinsen *et al.* (2000) are valid for weakly nonlinear sloshing. The sloshing regimes of greatest interest normally include sloshing impacts and are difficult to model with potential flow approaches. There is very little additional infrastructure required for the development and operation of theoretical sloshing models.

CFD is applicable to a wider range of sloshing regimes and modern VOF-based CFD codes can simulate nonlinear sloshing including sloshing impacts (Faltinsen and Rognebakke, 2000). As in the experiment the solution is only applicable to a particular sloshing motion. The conservation of mass is a concern for the validity of a CFD solution (Faltinsen and Rognebakke, 2000; Godderidge *et al.*, 2009) and long simulation times require tight convergence of the numerical solution to prevent a build-up of a cumulative error in the solution. CFD solutions cannot be obtained in either real or fast time despite parallelisation of the calculations. While the costs of CFD simulation are substantial, a general-purpose CFD code can be used for other applications and capital is not tied up exclusively for sloshing analysis.

An experimental approach for sloshing guidance has been carried out in the HULLMOS system (Rouvari Oy, 2005) but the high costs associated with installation and maintenance of sensors make this approach impractical. The on-board installation of a model-scale tank (analogous to an experimental tank) is also costly. The recorded accelerations need to be scaled to correspond to the model tank and the tank motions need to be corrected for vessel motions which makes the real-time operation impossible. Although the recorded vessel motions can be used as inputs the speed of economically feasible CFD solutions is too slow. Theoretical models can be solved in fast time, but the restrictions associated with potential flow do not permit the simulation of strongly nonlinear sloshing.

Thus, the most suitable approach for a sloshing guidance system is a simplified mathematical model which can include information from the results obtained with detailed numerical or experimental modelling. In this study, a numerical model based on the unsteady Reynolds-Averaged Navier-Stokes (URANS) Equations (2.20a) - (2.20b) is used to provide detailed results for validation and customisation of the mathematical sloshing model.

2.4 URANS CFD approach

The unsteady Reynolds-Averaged Navier-Stokes (URANS) Equations (2.20a) - (2.20b) are solved in this study using the commercial CFD code ANSYS CFX[9]. CFX provides models for compressible and incompressible flow problems with an arbitrary number of fluids and approximately 20 different turbulence models with a wide range of complexity. Fluid-structure interaction is made relatively easy by coupling the CFX solution process with the finite element code ANSYS. CFX is split into a graphical preprocessor, where the problem is defined, a solver and a postprocessor, which outputs the solver results in a useful format.

CFX, as most other commercial CFD codes, uses a finite volume method for the discretisation of the governing equations. The finite volume method, which is described in greater detail by Ferziger and Peric (2002), attributes its popularity to the ease of discretising complicated geometries and the inherent conservation of physical quantities such as mass and momentum by virtue of Gauss' divergence theorem

$$\int\limits_{CV} (\nabla \cdot F) \; dV = \int\limits_{A} F \cdot n \; dA, \tag{2.26}$$

where A is the border enclosing a control volume CV, F a vector field and n a unit vector normal to A . Gauss' theorem is used to replace the divergence operator ∇ in the Navier-Stokes equations when discretising the governing equations on the mesh. This discretisation scheme ensures that the exact same physical quantity leaving one control volume enters the adjacent control volume.

2.4.1 Governing equations

The volume-of-fluid methodology captures the fluid interface by the advection of the amount of each fluid in a control volume according to the velocity field. Figure 2.11 shows a two phase flow consisting of water and air with a dislocated free surface and the water volume fraction in each control volume.

The interaction between the phases can be modelled using a *homogeneous* or *inhomogeneous* multiphase model. The homogeneous or average property approach is commonly used for VOF-based simulation of free surface flow problems because the increased computational effort is restricted to the solution of the additional transport equations for the fluid volume fraction. The fluid properties in each control volume are averaged according to the volume fractions r of the water and gas phases so that the average density ρ in each control volume is given as

---

[9] currently version 11 SP1

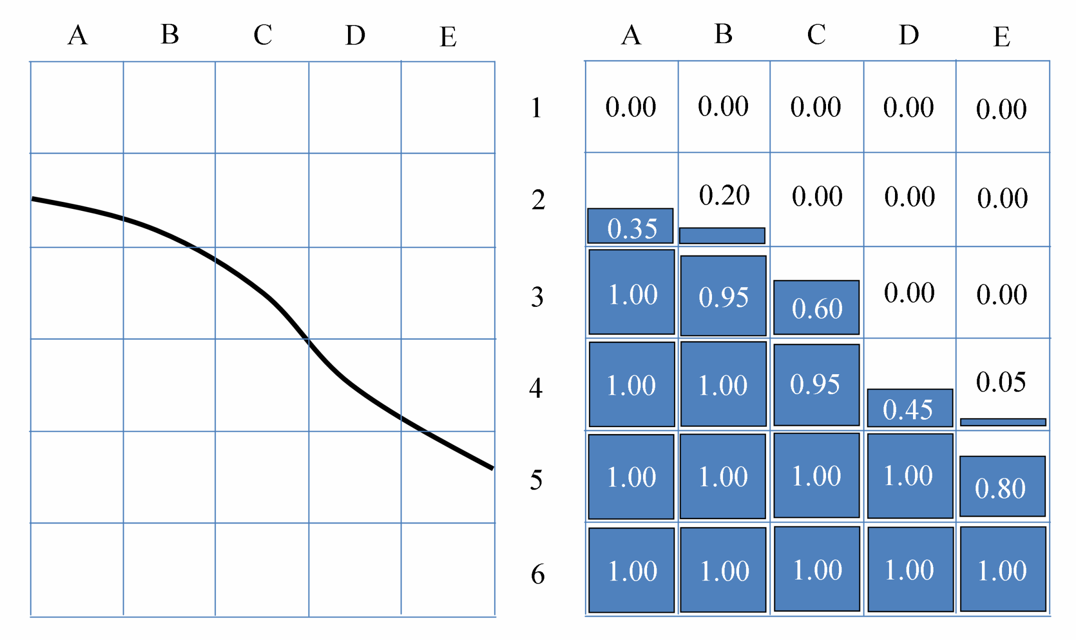

	A	B	C	D	E
1	0.00	0.00	0.00	0.00	0.00
2	0.35	0.20	0.00	0.00	0.00
3	1.00	0.95	0.60	0.00	0.00
4	1.00	1.00	0.95	0.45	0.05
5	1.00	1.00	1.00	1.00	0.80
6	1.00	1.00	1.00	1.00	1.00

Figure 2.11: Application of the VOF methodology to the simulation of free surface flow problems. A dislocated free surface is shown with superimposed control volumes (left) and the water volume fraction in each volume using a VOF model (right)

$$\rho = \sum_{l=1}^{2} r_l \rho_l \tag{2.27}$$

and the dynamic viscosity μ is

$$\mu = \sum_{l=1}^{2} r_l \mu_l. \tag{2.28}$$

The components of the average property fluids are moving at the same velocity in each control volume. For example, in the control volumes in column B in Figure 2.11 the average property fluid goes from pure air in control volume B1 to 20% water and 80% air in B2, 95% water and 5% air in B3 and pure water in B4 and B5. This average property fluid is computed for the entire domain and applied to the Navier Stokes Equations so that the conservation of mass is given as

$$\frac{\partial \left(r\rho \right)}{\partial t} + \frac{\partial}{\partial x_i} \left(r\rho u_i \right) = 0, \tag{2.29}$$

and the conservation of momentum is defined as

$$\frac{\partial}{\partial t} \left(\rho u_i \right) + \frac{\partial}{\partial x_j} \left(\rho u_i u_j \right) = -\frac{\partial p}{\partial x_i} + \frac{\partial \tau_{ij}}{\partial x_j} + b_i \tag{2.30}$$

where b_i are body forces and the stress tensor τ_{ij} is expressed as

$$\tau_{ij} = \mu \left(\frac{\partial u_i}{\partial x_j} + \frac{\partial u_j}{\partial x_i} \right) \tag{2.31}$$

When two incompressible fluids are used the spatial and temporal variations of density and viscosity require their inclusion in the difference terms, unlike in the Navier Stokes Equation (2.20b). The homogeneous multiphase approach is suitable when the phases share a single velocity field, but when motion between the phases is significant an inhomogeneous multiphase model should be used (Brennen, 2005).

The inhomogeneous multiphase approach permits motion between each fluid within a control volume by solving a separate momentum equation for each phase rather than one momentum equation for an averaged fluid. The governing equations for an inhomogeneous viscous incompressible multiphase flow with phases α and β consist of the conservation of mass for the phase α (Ishii and Hibiki, 2006)

$$\frac{\partial}{\partial t}(r\rho) + \frac{\partial}{\partial x_i}(r\rho u_i) = m + \Gamma^{\alpha\beta}, \tag{2.32}$$

where $\Gamma^{\alpha\beta}$ is mass transfer between the phases and m mass sources, ρ density, r volume fraction and u_i velocity of phase α. The corresponding equation for conservation of momentum for phase α is given as

$$\frac{\partial}{\partial t}(r\rho u_i) + \frac{\partial}{\partial x_j}(r\rho u_i u_j) = -r\frac{\partial p}{\partial x_i} + \frac{\partial (r\tau_{ij})}{\partial x_j} + M^{\Gamma} + M^{\alpha} + b_i, \tag{2.33}$$

Since the momentum fields for each phase expressed in Equation (2.33) are not independent of each other, there are additional momentum transfer terms in Equation (2.33) (Ishii and Hibiki, 2006). The term $M^{\Gamma}\left(= \Gamma^{\alpha\beta}u_i^{\beta} - \Gamma^{\beta\alpha}u_i\right)$ is interphase momentum transfer caused by mass transfer. In a problem with two distinct materials such as water and air this term is neglected. The momentum transfer to phase α due to forces acting on the interface caused by the presence of phase β is included with M^{α}

This term may be modelled by a linear combination of the momentum transfer caused by known forces acting across the fluid interface, such that

$$M^{\alpha} = M^D + M^V + M^B + M^L + M^W, \tag{2.34}$$

where M^D is the momentum transfer due to interface drag force, M^V momentum transfer due to virtual mass force, M^B momentum transfer due to Basset force, M^L momentum transfer due to lift force due to fluid rotation and M^W momentum transfer due to wall lubrication force (Ishii and Hibiki, 2006; ANSYS Inc, 2005). The Basset force accounts for unsteady effects due to particle motion in the fluid and because of its complicated nature it is generally ignored in practical multiphase analysis (Ishii and Hibiki, 2006). The virtual mass force is used to model the interaction of small, subgrid-scale particles with the surrounding fluid. This is ignored in the present analysis. The lift force is generated by fluid rotation around particles. The correct modelling of wall lubrication force requires a particularly fine grid (ANSYS Inc, 2005), making its inclusion in transient simulations impractical. The interphase drag force is expressed using the drag coefficient

$$C_D = \frac{D}{1/2\rho \left| U_\alpha - U_\beta \right|^2 A}, \tag{2.35}$$

where A is interfacial area, D drag, ρ density and $|U_\alpha - U_\beta|$ velocity between the phases α and β. For the current Newtonian flow regime, a drag coefficient of 0.45 is used (Ishii and Hibiki, 2006).

Figure 2.12 compares the homogeneous (in Figure 2.12(a)) and inhomogeneous (in Figures 2.12(b) and 2.12(c)) multiphase models for a sloshing case studied by Godderidge *et al.* (2009c). The solution obtained with the homogeneous multiphase solution results in a continuous velocity field because only one momentum equation is solved for an average-property fluid. There is a vortex just above the breaking wave and some water remains at the left tank wall from the previous impact.

The inhomogeneous multiphase approach is computationally twice as intensive (Godderidge *et al.*, 2009) because a separate velocity field is solved for each fluid in the simulation and the solution is constructed by combining the separate solutions in Figures 2.12(b) and 2.12(c) using the momentum transfer terms in Equation (2.34). There are several differences in the solution from the inhomogeneous multiphase model compared to the homogeneous multiphase model:

- there are several individual vortices located in the velocity field for the gas phase,
- the top left hopper space does not have any remaining water attached to the wall (which can be a source of numerical instability in the homogeneous model)and
- there is a difference in the velocity of the breaking wave which is influenced in Figure 2.12(a) by the assumption of a continuous velocity field. This is the most significant difference when simulating sloshing impacts as the direction of the wave front influences the impact pressure.

2.4.2 Discretisation

The governing Equations (2.32)-(2.33) for the inhomogeneous or Equations (2.29)-(2.30) for the homogeneous multiphase model are discretised using a finite volume method

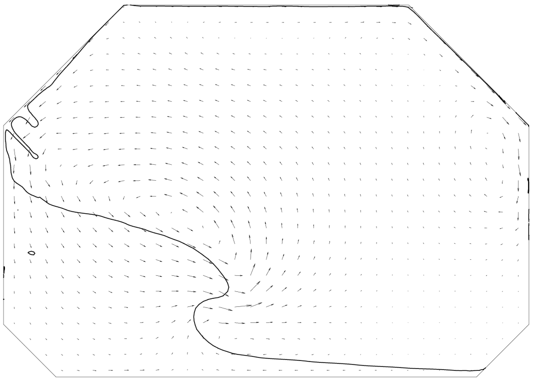

(a) Flow field obtained using the homogeneous (average property) VOF approach

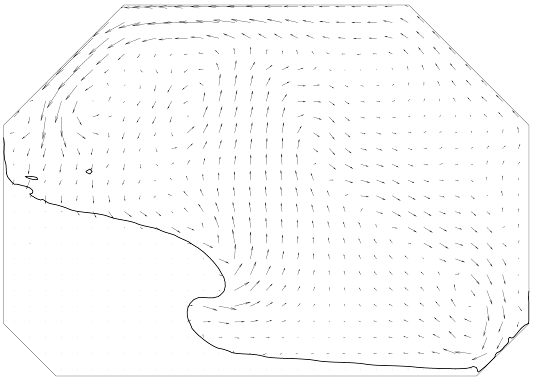

(b) Flow field for air obtained using the inhomogeneous VOF approach. Note the near-zero speed in the region occupied only by water.

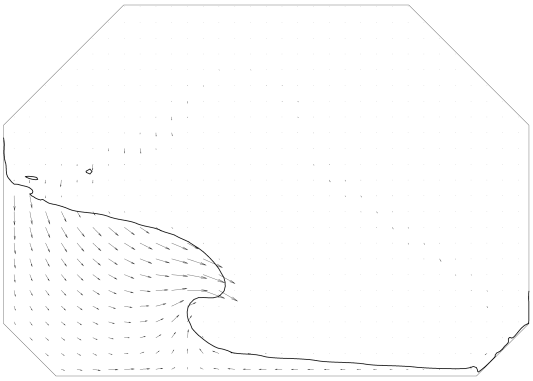

(c) Flow field for water obtained using the inhomogeneous VOF approach. Note the near-zero speed in the region occupied by air.

Figure 2.12: Flow fields computed for low filling level sloshing at resonance $x_0/L = 0.2$ with homogeneous and inhomogeneous multiphase models. The fluid interface is shown with a black line. Note that in there is a small, $O(10^{-10})$ amount of phase mixing in regions of 'pure' air and water in the inhomogeneous model in Figures (b) and (c)

(Zwart, 2004). Figure 2.13 shows the control volume A-B-C-D-E-F-G-H with unit depth obtained from hexahedral element discretisation. The locations marked by crosses are the centres of the faces of the control volume. Conservation of mass for phase α (Equation 2.29) with no mass sources is discretised using Gauss's divergence theorem and an implicit second-order backward Euler scheme (Zwart, 2004) as

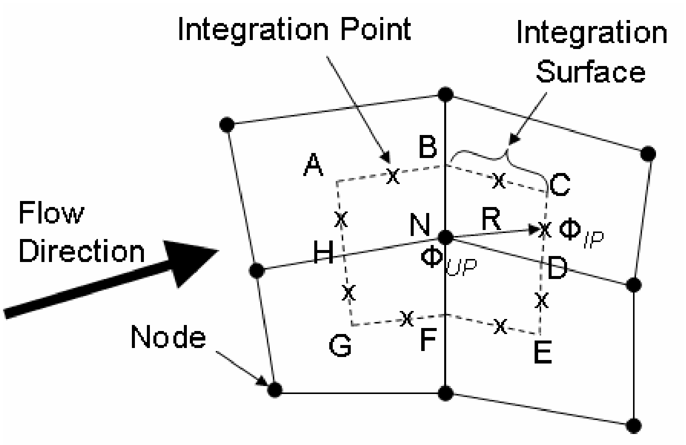

Figure 2.13: Location of the integration points and nodes

$$\frac{V}{\delta t}\left[\frac{3}{2}\left(\rho_\alpha r\right)^{n} - 2\left(\rho_\alpha r\right)^{n-1} + \frac{1}{2}\left(\rho_\alpha r\right)^{n-2}\right] + \sum_k \left(r\rho_\alpha u_i \underline{n}_i\right)_k^n S_k = 0, \tag{2.36}$$

where δt is time step, superscript n the time step currently computed, $n - n_p$ the n_p^{th} time step before n, $\underline{n}_i$ the unit vector orthogonal to the k^{th} area of a control volume S_k and V is the volume of a control volume. The phases α and β must fill the available volume so that

$$r_\alpha + r_\beta = 1. \tag{2.37}$$

Equation (2.37) can be combined with Equation (2.29) to give a volume continuity equation instead of writing an additional mass conservation equation for phase β (Zwart, 2004)

$$\sum_{l=1}^{2} \frac{1}{\rho_l}\left[\frac{V}{\delta t}\left(\frac{3}{2}\rho_l^{n} - 2\rho_l^{n-1} + \frac{1}{2}\rho_l^{n-2}\right) + \sum_k \left(r_l\rho_l u_i \underline{n}_i\right)_k^n S_k\right] = 0. \tag{2.38}$$

The equations of momentum conservation, Equations (2.33) for inhomogeneous and Equations (2.30) for homogeneous multiphase flows, are discretised in a similar manner. For simplicity, only the discretisation of Equation (2.30) is shown, but an analogous result can be written for Equation (2.33). As in the equations discretised previously, an implicit second order backward Euler scheme is used for the time derivative. The discretised momentum equation for phase α is written as

$$\frac{\partial\left(\rho u_i\right)}{\partial t} + \sum_k \left(\rho u_i u_j \underline{n}_j\right)_k^n S_k = -\sum_k p_k^n I_{ij}\underline{n}_j S_k + \rho^n g_i V + \sum_k \left(\tau_{ij}^n I_{jl}\underline{n}_l\right) S_k, \tag{2.39}$$

where

$$\frac{\partial(\rho u_i)}{\partial t} = \frac{V}{\delta t}\left[\frac{3}{2}(\rho u_i)^n - 2(\rho u_i)^{n-1} + \frac{1}{2}(\rho u_i)^{n-2}\right], \tag{2.40}$$

I_{ij} is the unit vector in the x_i direction (and j is a dummy subscript) and p pressure. Density ρ, viscosity μ and the stress tensor τ_{ij} are defined by Equations (2.27), (2.28) and (2.31) respectively. The equations governing the $k-\epsilon$ turbulence model can be found in (Ferziger and Peric, 2002). The flow quantities are computed at the node points, but the discretisation of the governing equations requires the quantities at the integration points of the control volume associated with each node, as shown in Figure 2.13. The present model uses a 'high-resolution' advection scheme which varies between first and second order depending on the spatial gradient. For a scalar quantity ϕ the advection scheme is written in the form

$$\phi_{IP} = \phi_{UP} + b\nabla\phi \cdot R, \tag{2.41}$$

where ϕ_{IP} is the value at the centre of an integration surface, ϕ_{UP} the value at the upwind vertex and R the vector from the upwind vertex to the integration point (see Figure 2.13). The model is a second order, upwind-biased scheme for $b = 1$, but reverts to first order when $b = 0$ (Zwart, 2004). The computation of b follows an approach similar to that given by Barth and Jesperson (1989), which aims to maintain b as close to unity as possible while ensuring that the computed ϕ at the integration points are bounded (Zwart, 2004). Since the present model uses a colocated grid for pressure and velocity, an interpolation scheme based on that proposed by Rhie and Chow (1982) is used (Zwart, 2004). Gradients are computed at integration points using tri-linear shape functions (ANSYS Inc, 2005).

The advection scheme can be modified to improve the resolution of a free surface. By allowing $b > 1$, while enforcing the boundedness of quantities at the integration points, the advection scheme compresses the 'thickness' of the free surface (Zwart, 2004). The compressiveness of the advection scheme arises from the fact that it is anti-diffusive when b exceeds unity (Zwart, 2004). The compressiveness of the advection scheme is not dependent on the reduction of the time step size which is an important consideration for transient simulations with long durations. The ability of this scheme to maintain the shape of a free surface without smearing over extended time scales has been shown by Zwart (2004).

The discretised equations yield a 6×6 coupled system at each node for a two phase system. The resulting system is solved with a coupled solver (Zwart, 2004). The solution for the two-phase system is obtained by

1. solving the equations for volume continuity (2.38) and conservation of momentum (2.39),
2. solving the mass conservation equation (2.29) for water,

3. solving Equation (2.37) for air and
4. solving the turbulence kinetic energy and dissipation equations (Zwart, 2004)

using an algebraic multigrid approach.

In CFX-11 steps 1-3 can be coupled which improves the mass conservation in the solution compared to the segregated solution. The segregated solution reduces the required memory overhead but introduces the need for additional iterations to obtain a solution (ANSYS Inc, 2005). For every time step in the transient simulation, the iterative solution of each sub-system in this list is obtained using the Incomplete Lower-Upper (ILU) factorisation technique (ANSYS Inc, 2005). Depending on the flow field and time step size, between five to ten iterations are required for a converged solution.

2.4.3 Turbulence modelling

There is no consensus apparent whether and when sloshing flow should be modelled as turbulent or laminar. Previous studies by El Moctar (2006), Hadzic *et al.* (2002), Rhee (2005) and Standing *et al.* (2003) assume the flow to be turbulent, while e.g. Price and Chen (2006) use a laminar flow model. Lee *et al.* (2007) reported that the effects of turbulence are negligible for a sloshing flow in a 1.0 m x 0.6 m tank, where the period of excitation is 85% of the first resonant period. Rhee (2005) observed significant variations between laminar and turbulent flow models in the test cases used in the next chapter and concluded that turbulence effects should be taken into account in a CFD model for this particular case. Similar effects have been observed in the sensitivity study by Godderidge *et al.* (2006).

The $k - \epsilon$ model has been used for a considerable time in industry with a broad range of applications. Its popularity is attributed to the comparative simplicity for a complete turbulence model (Pope, 2000) and robustness. It is based on the Boussinesq assumption which relates the turbulence stress to mean flow properties through turbulent viscosity. However, there are several weaknesses of the $k - \epsilon$ model:

1. Inaccuracies in strong or adverse pressure gradients (Pope, 2000),
2. inability to model the law of the wall without viscous correction (Wilcox, 1998),
3. difficulties modelling problems more complex than simple shear (Pope, 2000) and
4. the specification of initial values throughout the domain.

Wilcox (1998) does not consider the popularity of the $k - \epsilon$ model to be supported by its performance characteristics and more sophisticated turbulence models based on the

Boussinesq assumption such as the $k-\omega$ and the Shear Stress Transport (SST) models have been developed. These turbulence models overcome some of the limitations of the $k-\epsilon$ model (QNET CFD, 2002). The SST model was found to be more sensitive to the changing y^+, which is the non-dimensional distance from the wall defined as

$$y^+ = \frac{\sqrt{\tau_w/\rho} \cdot n}{\nu} \tag{2.42}$$

where ν is viscosity, n grid spacing perpendicular to the wall, ρ density and τ_w shear stress. Most simulations attempted with the SST model diverged before completion but El Moctar (2006) reports the successful use of the SST model in a sloshing flow.

Reynolds stress models do not rely on the Boussinesq assumption because the turbulence stresses are modelled directly. The advantage of this approach is a far greater level of generality and many of the drawbacks associated with $k-\epsilon$ models do not apply (ANSYS Inc, 2005). The Reynolds stress model used in this study was introduced by Speziale, Sarkar, and Gatsi (1991). The strengths of this particular model are:

1. better performance in complex flow regimes, especially in strongly curved streams (ANSYS Inc, 2005) and
2. improved stability as the asymptotic solution attracts all initial conditions (Speziale *et al.*, 1991).

The main drawback of a Reynolds stress model is the introduction of five additional transport equations (in a 2D problem) for the turbulence stress terms. In addition, convergence problems are identified (ANSYS Inc, 2005) when using the Reynolds Stress Model by Speziale *et al.* (1991).

2.4.4 Verification

CFD is an approximation of an actual problem and the global conservation of solution quantities such as mass and momentum is required (WS Atkins Consultants, 2003). The introduction of inaccuracies and errors into a numerical model which is solved with an iterative procedure can be attributed to three distinct sources (Ferziger and Peric, 2002).

1. Modelling errors. The selection of the correct computational model to represent a physical process is vital. The UK Health and Safety executive (Lea, 2003; Ivings *et al.*, 2004; Saunders, 2003) as well as the MARNET best practice guidelines for maritime CFD (WS Atkins Consultants, 2003) recommend systematic variations if there is no clearly identifiable choice of computational model.

2. Discretisation errors. A physical problem can be represented in the computational space for CFD analysis using a grid which is often referred to as mesh and the two terms are used interchangibly. Alternatively, gridless methods such as particle methods discretise the fluid directly. The relationship between the quality of the representation of a problem and the obtained result is self-evident. Thompson *et al.* (1999) provided guidelines for generating grids for a wide range of applications. A sound CFD analysis uses a series of refined grids to establish the independence, or decreasing dependence, of a computational result from the grid used. Roache (1997) provided a powerful method for determining the grid independence error estimation and uncertainty assessment for CFD solutions. Stern *et al.* (2001) developed a technique for uncertainty assessment of CFD results and apply it to the flow field of a ship computed using a RANS code (Wilson *et al.*, 2001). Simonsen and Stern (2003) described and applied a verification procedure for the flow field around a container ship with Froude number 0.316. In this case, the uncertainty analysis is not limited to grid independence of the results.

3. Numerical errors are due to the finite numerical precision used by a digital computer. Thus a small error may grow if a large number of iterations is required, or a result may not converge at all due to numerical noise. Most literature (e.g. WS Atkins Consultants, 2003; Hirsch, 1988; Anderson, Jr, 1995) recommends the use of double precision (64 bits) for CFD.

Chapter 3

CFD Analysis

The Navier-Stokes CFD model described in Section 2.4 is now applied to the simulation of sloshing. As shown in Figure 3.1, the CFD model is used to aid the development and validation of the Rapid Sloshing Model for the sloshing guidance system. The selective inclusion and exclusion of particular physics is used in the assessment of their effects on the sloshing response and development of a suitable description in the Rapid Sloshing Model.

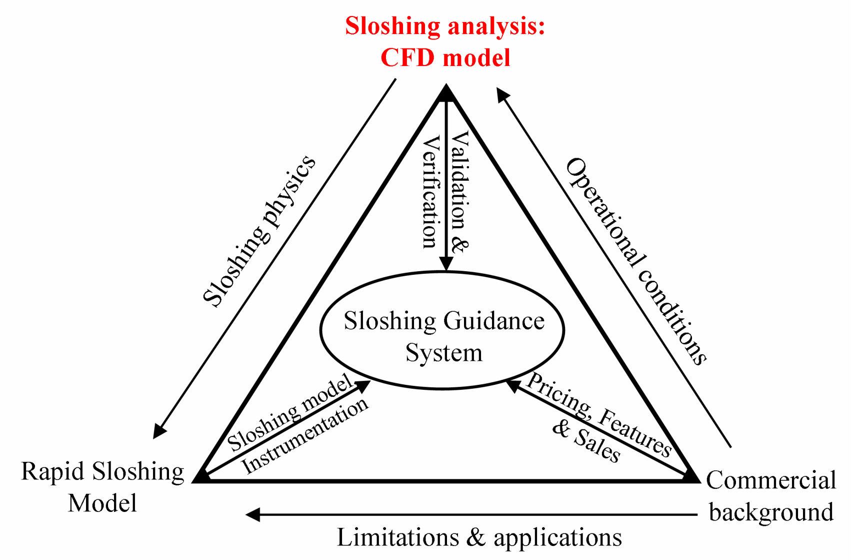

Figure 3.1: The role of the CFD model in the project

This chapter summarises the validation of the CFD model. Validation is ‘the process of determining to which degree a model is an accurate representation of the real world from the perspective of the intended users of the model’ (American Institute of Aeronautics and Astronautics, 1998). This includes confirmation of the consistency and convergence of a CFD solution, a space and time discretisation independence study, examination of the effect of the turbulence, multiphase and compressibility models and a comparison with experimental data.

3.1 Sloshing test problems

3.1.1 Experimental validation data

The CFD sloshing model is validated with sloshing experiments carried out by Hinatsu (2001) at the National Maritime Research Institute of Japan. These experiments involve translatory and angular motion only and there are no results for combined motions. Olsen (1976b) observed that the predominant and most important kind of sloshing is the lateral sloshing, generated primarily by translatory and angular tank movements and therefore the validation study is restricted to these sloshing problems. Experiments were carried out with an excitation period near and at $T_1 = 1.474$ s, which is the first natural sloshing period.

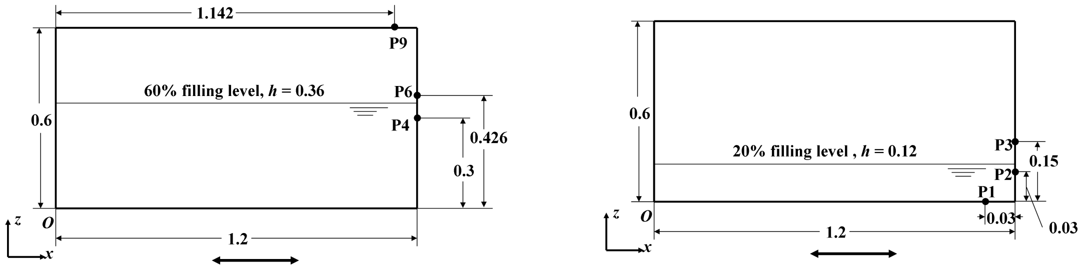

(a) 60% filling level

(b) 20% fillinglevel

Figure 3.2: Experimental arrangement and location of pressure sensors. All dimensions in m, tank width is 0.2 m

The tank is subjected to periodic motion with the displacement defined as

$$x = A \sin(\omega t), \tag{3.1}$$

where A is the displacement amplitude, ω the excitation frequency which is related to the excitation period by $\omega = 2\pi/T$ and t the elapsed time. The pressure data is recorded at the monitor points indicated in Figure 3.2. Translatory motions are along the x-axis and the centre of rotation is at the geometric centre of the tank. Table 3.1 summarises the particulars of the validation cases. Because of the three dimensional nature of fluid impacts and the consequent difficulty of their simulation with a two-dimensional CFD model, the validation study uses a near-resonant sloshing flow (case A) with nonlinear sloshing. Sloshing impacts are then studied in greater detail with case B. Finally, the suitability of the computational model for the simulation of sloshing induced by rotational tank motions is confirmed using case C.

Table 3.1: Details of the experimental validation cases

Case	Filling level	Motion		
		Type	A	T
A	60%	translation	0.015 m	1.404 s
B	20%	translation	0.060 m	1.74 s
C	20%	rotation	10 deg	2.25 s

The sampling rate in the experiment is 10 kHz, which is lower than in similar studies by e.g. Rognebakke and Faltinsen (2005), who used a sampling rate of 19.2 kHz. The raw experimental data for case A had to be corrected for drift, which was carried out using the procedure outlined by Godderidge *et al.* (2006).

3.1.2 Tank motion

The acceleration experienced by the tank due to application of the displacement in Equation (3.1) can be written using its second derivative

$$\ddot{x} = -A\omega^2 \sin\left(\omega\ t\right). \tag{3.2}$$

The actual tank acceleration recorded during the experiment for case A is shown in Figure 3.3(a) which bears little resemblance to the acceleration specified by Equation (3.2). Using a Fourier series decomposition it is possible to isolate the most significant components. Figure 3.3(b) shows the reconstructed tank acceleration obtained with the first five terms of the computed Fourier decomposition. Equation (3.1) represents the low frequency properties of the actual tank acceleration with reasonable accuracy but a small offset is observed. However, as higher frequency terms are introduced shown in Figure 3.3(c) the Fourier transform plot resembles the measured acceleration.

While the specification of the tank motion using Equations (3.1) or (3.2) for the tank displacement or acceleration does not strictly represent the motion profile of the tank, it is at this stage deemed suitable for the validation of the CFD results. Further confidence is given by the fact that they have been used in by Hadzic *et al.* (2002); El Moctar (2006); Rhee (2005) for validation of CFD models. However, when considering unstable sloshing motion profiles, the validity of this assumption must be reassessed.

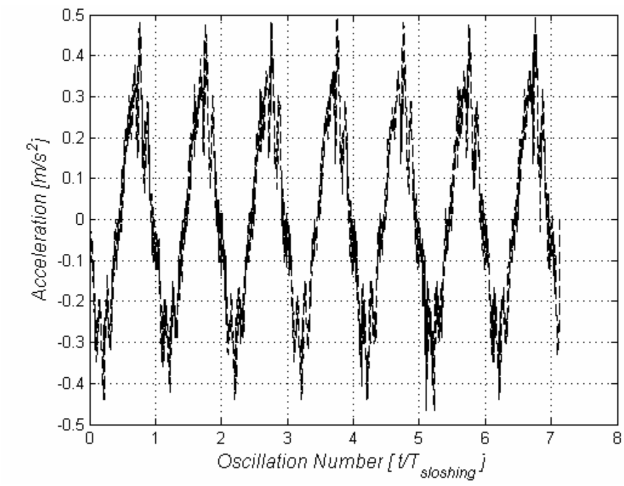

(a) Recorded acceleration from experiment (Hinatsu, 2001)

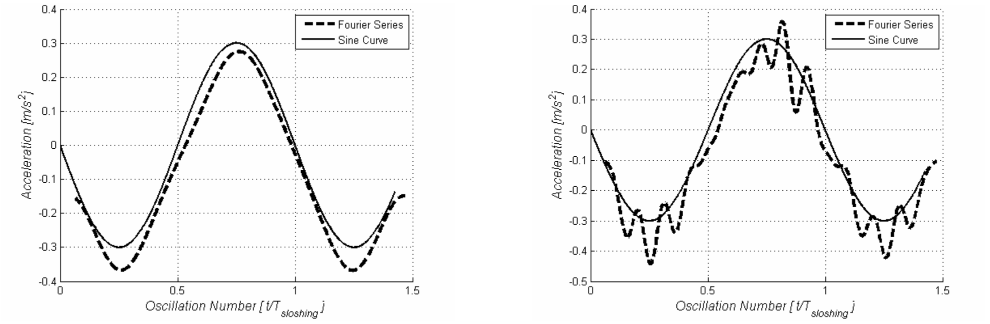

(b) Reconstructed acceleration using 5 Fourier series components

(c) Reconstructed acceleration using 20 Fourier series components

Figure 3.3: Application of Fourier series filtering to compare measured and specified tank motion

3.2 Computational models

3.2.1 Sloshing motion

The body force approach is a popular method of applying the tank motion to the sloshing fluid through the gravity vector in the governing equations. The tank displacement described in an inertial (X, Z) coordinate system with origin O is given by Equation (3.3) as

$$x_{X,Z} = \sin(\omega t), \tag{3.3}$$

assuming the displacement of the tank is sinusoidal with origin o and axis system (x, z). Therefore the acceleration of the tank at o relative to (X, Z) is given by

$$\ddot{x}_{X,Z} = -\omega^2 \sin(\omega t). \tag{3.4}$$

Keeping the same notation, the displacement of the tank observed at O relative to o is

$$X_{x,z} = -\sin(\omega t)\,. \tag{3.5}$$

Similarly, the acceleration is given as

$$\ddot{X}_{x,z} = \omega^2 \sin(\omega t)\,. \tag{3.6}$$

Therefore, a periodically oscillating tank, can be described both within the problem, as shown in Equation (3.5) or using an external reference system. This is the essence of the body force approach. By applying an additional acceleration to the domain it is possible to simulate the sloshing motion without having to move the grid relative to an inertial reference system. Equation (3.6) uses a sinusoidal motion, but any arbitrary translatory motion can be simulated by splitting the accelerations into their Cartesian components. Since the mesh displacement is not calculated during the simulation, the required computational effort is less than in an equivalent simulation which moves the mesh according to the tank displacement. A further benefit of the body force approach is that accelerations, more readily measurable on a moving body such as an LNG carrier than velocities or displacements, are required as inputs.

The effect of initialisation was also examined by Faltinsen *et al.* (2000) for sloshing with a particular flow history and it was found that the start-up can have a significant effect on the flow evolution. Hadzic *et al.* (2002) examined the difference between specified mesh motion and the body force approach for the problems also used in this investigation and found that after a brief transient period of disagreement both approaches give the same pressure result.

The simplicity and lower computational cost of the body force approach suggests the use of an analogous model for rotational motions. The velocity in a reference frame rotating about the origin can be related to an inertial frame with a coincident origin by

$$\langle \dot{x} \rangle_I = \langle \dot{x} \rangle_r + \Omega \times x \tag{3.7}$$

where $\langle \dot{x} \rangle_I$is the velocity in the inertial frame, $\langle \dot{x} \rangle_r$the velocity in the rotating frame, x the position vector and $\Omega(t)$ the rotational speed. The resulting acceleration is given as

$$\langle \ddot{x} \rangle_R = \langle \ddot{x} \rangle_I - 2\Omega \times \langle \dot{x} \rangle_R - \Omega \times (\Omega \times x) - \dot{\Omega} \times x. \tag{3.8}$$

There are three additional terms and these correspond to the Coriolis, Centripetal and Euler forces, given in Equations (3.9a)-(3.9c).

$$F_{CO} = -2m\Omega \times \langle \dot{x} \rangle_r \tag{3.9a}$$

$$F_{CE} = -m\Omega \times (\Omega \times r) \tag{3.9b}$$

$$F_E = -m\dot{\Omega} \times x \tag{3.9c}$$

While the inclusion of the Coriolis and Centripetal forces is confirmed in the CFX-11 users guide (ANSYS Inc, 2007), the inclusion of the Euler force was verified by the simulation of a test problem. A fluid mass was subjected to a periodic rotational motion and it was found that the force predicted by CFX coincided with the calculated Euler force using Equation (3.9c) (Godderidge, 2008b). Thus, all rotational forces required for the use of a rotating frame of reference are included in CFX-11 and a rotating body force approach is feasible.

3.2.2 Space discretisation

The grid represents the problem in computational space and establishing the grid independence of a CFD result is an important part of a rigorous CFD analysis (WS Atkins Consultants, 2003; Roache, 1997) The UK Health and Safety Executive requires grid independence of critical CFD analyses (Lea, 2003). Therefore any result of practical interest should conform to this requirement. This section summarises the grid independence study carried out by Godderidge *et al.* (2006)

A structured hexahedral grid shown in Figure 3.4(a) was used in the grid independence study. Figure 3.4(a) shows the baseline grid which was then subjected to three levels of systematic refinement detailed in Table 3.2. Case A, with $T = 1.404$ s and a 60% fillling level as specified in Table 3.1 is used as the test problem.

The advection scheme used for spatial discretisation, which is given in Equation (2.41), is specified as a pure second order scheme by setting the coefficient $b = 1$ (ANSYS Inc, 2007). This scheme does not introduce uncertainties about the order of accuracy as is the case with the high resolution scheme while the conservation properties are better than the first order scheme. A second order time marching scheme, given in Equation (2.36) was used and the effect of time step and time marching scheme is considered in Section 3.2.3.

The results obtained with grids 1-3 are compared to the result obtained with the most refined grid 4 as shown in Table 3.3. A trend toward convergence of the solution can be observed from the results obtained with grid 2 when using the wall force as a basis for comparison but the pressure data at the monitor point P6 does not follow this trend. This is attributable to the dependence of the solution on time discretisation as well as grid size. Grid 3 shows a smaller difference relative to grid 4 but the computational cost

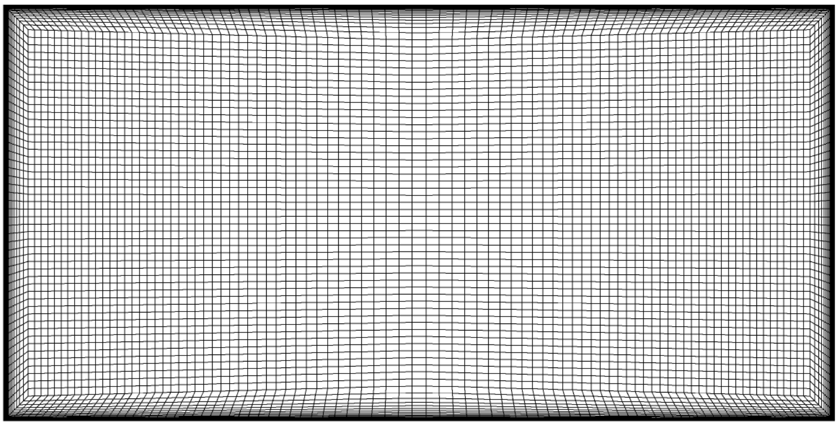

(a) Structured hexahedral element mesh

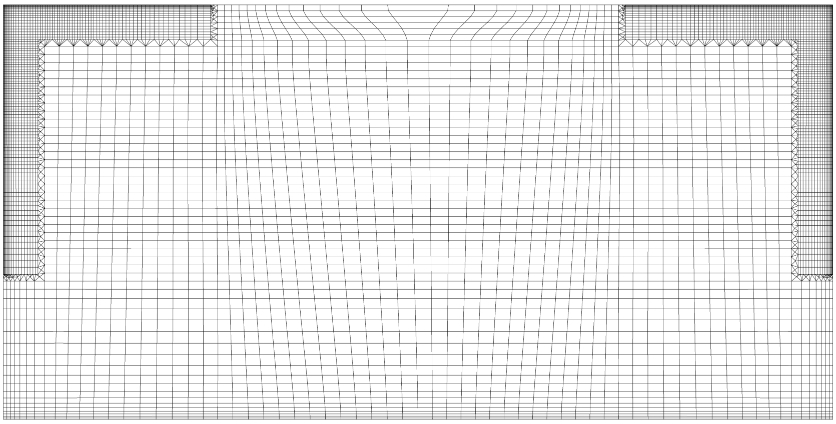

(b) Hybrid hexahedral and wedge element mesh

Figure 3.4: Computational meshes used for test problem A

Table 3.2: Grid statistics for the grid independence study

Grid	Nodes			Elements		
	Total Nodes	x-dir	z-dir	Total Elements	x-dir	z-dir
1	5600	140	80	2691	69	39
2	12000	200	120	5841	99	59
3	28000	280	200	13761	139	99
4	56000	400	280	27661	199	139

is prohibitive as the same simulation would take more than ten times as long on grid 4 and take up correspondingly more storage space. It should be emphasised that a more severe sloshing flow, a significant change in geometry, or different flow physics such as wave breaking during sloshing would require another grid independence study but the results from this study can be used for an initial estimate of the required grid resolution (Godderidge *et al.*, 2007). The best compromise between computational cost and grid independence of the result appears to be grid 2 and for a problem of this size a grid of about 6000 elements with an initial wall spacing of 1 mm, compared to the depth of penetration of the viscous wave of 4.2 mm (Godderidge *et al.*, 2007), is sufficient. The

Table 3.3: Summary of results analysis for grid independence. Differences are relative to the finest grid 4.

Model	Reference	Pressure			Wall force			
		P4 [%]	P6 [%]	P9 [%]	North [%]	East [%]	South [%]	West [%]
Grid 1	Grid 4	5.23	5.05	2.39	0.0023	0.0059	0.0091	0.0052
	(RMS)	8.51	11.1	7.67	0.0057	0.0093	0.0138	0.0073
Grid 2	Grid 4	3.44	4.98	1.75	0.0020	0.0032	0.0052	0.0027
	(RMS)	6.98	12.7	6.38	0.0051	0.0076	0.0118	0.0051
Grid 3	Grid 4	3.88	6.14	1.81	0.0019	0.0023	0.0034	0.0020
	(RMS)	8.13	15.9	9.00	0.0066	0.0072	0.0119	0.0059

limiting factors for near-wall grid spacing are machine accuracy and the aspect ratio of the near-wall cells.

The order of convergence of an algorithm using three grids with two grid refinement ratios r_1 and r_2 can be written as (Roache, 1997):

$$\frac{\epsilon_{1,2}}{r_1^k - 1} = r_2^k \left[\frac{\epsilon_{2,3}}{r_2^k - 1} \right], \tag{3.10}$$

where refinement ratio $r_1 = \frac{n_2}{n_1}$, $r_2 = \frac{n_3}{n_2}$ with $r_1 \neq r_2$ and k is the algorithmic rate of convergence. In this notation grid 1 is the coarsest and grid 3 the finest. Equation (3.11) defines ϵ

$$\epsilon_{i,i+1} = \phi_{i+1} - \phi_i, \tag{3.11}$$

where $i = 1, 2$ for the global or local flow property ϕ. Equation (3.10) does not lend itself to a direct solution, so the following iterative procedure proposed by Roache (1997) is used:

$$k = \omega\rho + (1-\omega)\frac{\ln\beta}{\ln r_2} \tag{3.12a}$$

$$\beta = \frac{r_2^\rho - 1}{r_1^\rho - 1}\left(\frac{\epsilon_{1,2}}{\epsilon_{2,3}}\right) \tag{3.12b}$$

where $\rho = k_{previous}$ and $\omega = 0.5$ is a relaxation parameter.

The order of grid convergence of the present algorithm was established with the force results for grids 1-4 using Equation (3.12) as $k = 1.87$, which is 6.5% less than a value of 2.0 expected from second order discretisation. When solving an unsteady problem small changes in the solution can be amplified over time (Strogatz, 1994) and this may account for the difference in the order of grid convergence.

A hybrid grid which combines structured hexahedral and unstructured wedge or tetrahedral elements has the advantages of both structured and unstructured meshes. Figure 3.4(b) shows a hybrid mesh containing 9,605 hexahedral elements, with the first node offset 0.3 mm from the wall with a mesh 20 nodes thick in the adjacent 35 mm from the tank wall. The element diagonal varies between 10 mm near the wall and 25 mm at the tank centre. This grid was used in most simulations and the pressure data obtained with this grid were in good agreement with converged results identified in this section.

3.2.3 Time discretisation

The transient nature of the sloshing flow requires the discretization of the problem in time as well as space. The inclusion of time as an additional dimension to the problem increases the computational cost accordingly and adds a requirement to capture the essential physics in time as well as a potential source of numerical error. The time marching is implemented in CFX with first and second order implicit Euler schemes (ANSYS Inc, 2007). The first order scheme is more stable, but the second order has better conservation properties and its use is recommended for transient simulation (WS Atkins Consultants, 2003).

As the flow velocity varies throughout the simulation, the variation of the time step for the duration of the simulation depending on the flow field is more efficient than the specification of a fixed time step. The second order scheme needs data from the two previous time steps but its implementation assumes that the time step size is constant in both cases. This approximation has been found to work satisfactorily for small local changes in time step size (Godderidge, 2008a). However, when the time step size increases by 5-10% or more, the consequent computational instabilities generally result in the termination of a simulation (Godderidge, 2008a). This behaviour was frequently encountered during fluid impact simulations and has also been reported in explosion modelling[1]. The maximum increase in the time step size can be limited to avoid these computational instabilities.

An adaptive time step can be specified so that the Courant number at node i

$$C_n = u_i \frac{\Delta t}{\Delta x_i}, \tag{3.13}$$

is no greater than a particular specified value. An alternative approach is the computation of the root-mean-square of the Courant number for the entire flow field at each time step and specification of limiting value. This approach normally gives a better reflection of the bulk flow behaviour and it was selected for this part of the study. The specification of a maximum local Courant number is more suitable for detailed CFD studies of fluid impacts.

The difference between the first and second order time marching scheme is shown in Table 3.4. There are some differences but these are comparable to the differences observed in the grid independence study. The most significant difference between the schemes is in the

---

[1] Ian Jones (Technical Director, ANSYS UK), private communication

conservation of mass and momentum, where the first order scheme results in numerical diffusion of momentum up to an order of magnitude greater and diffusion of mass three times greater than in the second order scheme (Godderidge *et al.*, 2006). Therefore the second order scheme is used for all sloshing simulations carried out in support of the work in this thesis.

Table 3.4: Differences between first and second order time discretisation (Godderidge *et al.*, 2007)

	Mean (% of peak)	RMS (% of peak)
P4	3.36	5.37
P6	2.77	5.37
P9	0.80	4.10
West wall	2.16	3.05
South wall	0.68	1.00
East wall	2.24	3.25

While the choice of an appropriate time marching scheme is important, the time step size influences the accuracy, stability and computational cost of a transient CFD simulation. The timescales of fluid impacts are several orders of magnitude smaller compared to the period of a sloshing oscillation, but computational efficiency usually improves with increased time step size. Case A is simulated with a second-order time marching scheme and the Courant number limit is varied.

The results of the time independence study (Godderidge *et al.*, 2007) are summarised in Table 3.5 where the differences are relative to the smallest time step obtained with $C_{N,RMS} \leq 0.05$. The most significant differences are observed when using the largest time step, but there is negligible difference between $C_{N,RMS} \leq 0.10$ and $C_{N,RMS} \leq 0.05$. For sloshing simulations in excess of 20-30 oscillations, a Courant number control of $C_{N,RMS} \leq 0.15$ may be suitable, especially as the smaller number of total time steps required reduces total imbalances of mass and momentum.

Table 3.5: Results of the time step size independence study (Godderidge *et al.*, 2007)

Limit $C_{N,RMS}$	CPU time hrs	Time steps	$C_{N,MAX}$	Difference P4 (%)	P6 (%)	P9 (%)
$\leq 0.50^a$	21.0	3,117	4.5	3.19	3.14	6.60
$\leq 0.30^b$	24.1	3,975	2.3	2.01	1.90	6.04
$\leq 0.10^a$	30.9	9,928	0.6	0.68	0.88	1.31
$\leq 0.05^b$	41.5	19,231	0.3	-	-	-

---

[a] 3.4 GHz, 32-bit processor

[b] 2.2 GHz, 64-bit processor

3.2.4 Turbulence models

Rhee (2005) observed significant variations between laminar and turbulent flow models in a systematic study of the experiments by Hinatsu (2001) and concluded that turbulence effects should be taken into account in a CFD model. Given the wide range of available turbulence models, lack of consensus on a turbulence model suitable for sloshing simulations and the additional computational costs associated with the simulation of turbulence the influence of a turbulence model on the CFD solution is established in this section. A laminar flow, a $k-\epsilon$ model with scalable wall function and the Speziale, Sarkar and Gatsi (SSG) Reynolds Stress Model (Speziale *et al.*, 1991) are compared in the simulation of case A on Grid 2 with an adaptive time step controlled with the Courant number criterion $C_{N,RMS} \leq 0.15$.

The Reynolds stress model required a computational time of 107.7 hrs for 6.9 s of sloshing compared to 15.8 hrs for the same time duration with the $k-\epsilon$ model. The Reynolds stress model was sensitive to the grid and time step choice and coefficient loop convergence was difficult to achieve throughout the simulation. Thus a better quality grid compared to the $k-\epsilon$ turbulence model is required. The ideal time step control was identified using a trial and error approach as $C_{N,RMS} \leq 0.2$ which is somewhat higher than the time step control established in Section 3.2.3. Even small deviations from these control parameters resulted in the termination of the simulation.

The first 10 sloshing oscillations with sloshing impacts are used for the comparison of the turbulence models. The effect of the turbulence models on the computational results is summarised in Table 3.6, where the differences are relative to the solution obtained with a $k-\epsilon$ model . The differences between the laminar flow assumption and the $k-\epsilon$ model exceed those expected from the grid independence study. When using a homogeneous multiphase model which is given in Section 2.4.1, the differences are similar to those obtained in the grid independence study. Using an inhomogeneous multiphase model results in further reduction of the calculated difference and the pressure histories obtained with the SSG and $k-\epsilon$ model are in good agreement (Godderidge *et al.*, 2006).

Table 3.6: Summary of results analysis for turbulence model variations (Godderidge *et al.*, 2006)

Model	Multiphase model	Difference	Pressure		
			P4 [%]	P6 [%]	P9 [%]
Laminar	homogeneous	mean	12.2	9.41	3.66
		RMS	19.7	22.4	12.1
SSG	homogeneous	mean	5.98	5.27	2.92
		RMS	10.9	9.81	10.3
SSG	inhomogeneous	mean	1.83	1.58	3.63
		RMS	4.17	4.35	15.8

Considering the two turbulence models, the SSG model is not practical for further use due to the large computational requirements (nearly six times more than with $k - \epsilon$) as well as the sensitivity of this model to the grid and time step. The $k - \epsilon$ model offers the best trade-off between accuracy of result, representation of the flow physics and computational time.

3.2.5 Multiphase models

In considering computational efficiency alone, the homogeneous multiphase model, which is used in sloshing investigations by Aliabadi *et al.* (2003); Hadzic *et al.* (2002); Rhee (2005); Standing *et al.* (2003), will be the most effective but the interaction between the phases is ignored. When the water impacts a tank wall, a small air pocket usually remains. This behaviour is observed in experimental studies of sloshing by Lugni *et al.* (2006) as well as the present simulations. The properties of this bubble and surrounding fluid can be used in the multiphase analysis by Brennen (2005) in Section 2.2.4 to determine the flow regime and thus a suitable multiphase model (Godderidge *et al.*, 2009). The terms and numerical data for a typical air bubble in water observed during sloshing impact are given in Table 3.7.

Table 3.7: Quantities used in Equations (2.15) and (2.16) for multiphase analysis

	Quantity	CFD data	Lugni *et al.* (2006)
l	length scale [m]	1.2	1.0
m_p	particle mass [kg]	$1.23 \cdot 10^{-6}$	$2.66 \cdot 10^{-7}$
ν_c	kinematic viscosity [$\mathrm{m}^2\ \mathrm{s}^{-1}$]	$1.00 \cdot 10^{-6}$	$1.00 \cdot 10^{-6}$
ρ_c	density[a] [$\mathrm{kg\ m}^{-3}$]	1000	1000
R	particle radius[b] [m]	≈ 0.01	0.006
U	characteristic velocity [$\mathrm{m\ s}^{-1}$]	≈ 4	≈ 5
v	particle volume [m^3]	$4.19 \cdot 10^{-6}$	$9.05 \cdot 10^{-7}$
	X	$1.66 \cdot 10^{-2}$	$5.99 \cdot 10^{-3}$
	Y^2	$9.93 \cdot 10^{-1}$	$9.93 \cdot 10^{-1}$
	$Y/(UR/\nu_c)$	$1.25 \cdot 10^{-5}$	$3.32 \cdot 10^{-5}$

---

[a] This applies to water, the suspending fluid.

[b] A *particle* is defined as a finite piece of the dispersed phase, e.g. an air bubble in water

Using data both from the CFD results described within and experimental findings by Lugni *et al.* (2006) given in Table 3.7 it is found that $X << Y^2$. However, the second condition $X << Y/(UR/\nu_c)$ is not satisfied and the large velocity between the phases W_m/U corresponds to the transient flow regime in the upper-right quadrant of Figure 2.7. This suggests that the use of an inhomogeneous multiphase model is required for the analysis of this violent sloshing problem and the effect of the multiphase model is examined in this section.

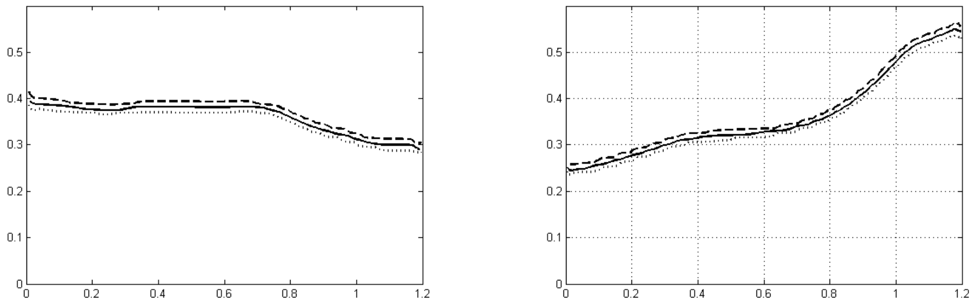

(a) $t = 5.85T$: Free surface 0.3 s before impact. A standing wave consistent with a non-shallow sloshing response is observed.

(b) $t = 5.99T$: Free surface immediately before impact

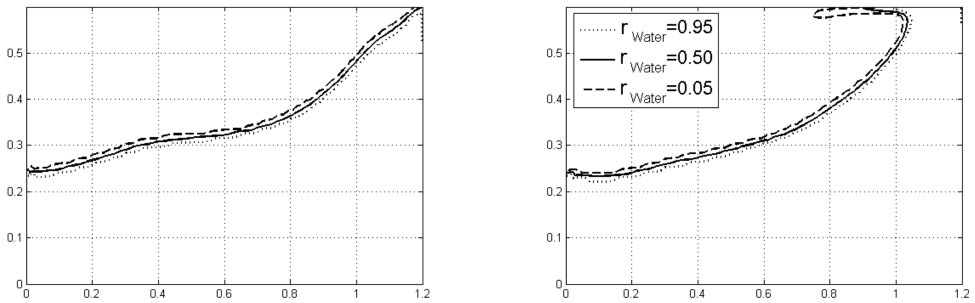

(c) $t = 6.01T$: Wagner-type impact at the right tank top corner

(d) $t = 6.08T$: Post impact jet is visible at the top right corner

Figure 3.5: Free surface location during impact at the tank roof. The free surface is usually contained within 1.5 control volumes as expected from a VOF discretisation scheme

Figure 3.5 shows the water motion during a sloshing impact. Immediately before impact a jet of fluid forms just below the top wall in the right corner of Figure 3.5(b). As the water impacts the top wall, a large local pressure peak is observed at the top right corner of the tank in Figure 3.5(c). After impact the resulting water column breaks as indicated in Figure 3.5(d). For resonant sloshing a more violent flow field is expected.

A free surface smearing index is proposed to assess the extent of interface smearing during the simulation. The minimum distance of contour c_2 (corresponding to $r_{water} = 0.50$) to contours c_1 ($r_{water} = 0.05$) and c_3 ($r_{water} = 0.95$) is calculated along contour c_2 and compared to the mesh element diagonal d_{mesh} at the corresponding locations on contour 2. An ideal value of this index is unity, as it indicates that the free surface is captured within one element. The free surface smearing index at element i is given as

$$\Delta FS^i = \frac{\overline{c_1^i c_2^i} + \overline{c_2^i c_3^i}}{d^i_{mesh}}. \tag{3.14}$$

The mesh diagonal has been chosen as length scale since two different computational models are compared on the same grid. Other applications, such as grid independence studies, would employ a different length scale such as the reference grid element diagonals or tank height.

An average value of ΔFS is computed at each time interval of 0.01 s (not each time step) and subsequently over the duration of the simulation. A straight line $(ax + b)$ fit to the obtained ΔFS gave $b = 1.57$ for the inhomogeneous and $b = 2.27$ for the homogeneous multiphase model. For both models, $a = O(10^{-3})$, indicating that the free surface sharpness does not increase during the simulation. A value of 2.14 was obtained for b for the reference grid in the grid independence study. While the inhomogeneous multiphase model resolves the free surface more sharply than the homogeneous multiphase model the mean difference between the models is $0.7d_{mesh}$. This corresponds to a static pressure of approximately 50 Pa.

The homogeneous multiphase flow model conserved the fluid mass for the duration of the simulation, with the water mass fraction $\frac{m(t)}{m_0}$ remaining constant at unity. Godderidge *et al.* (2009) reported significant mass loss with the inhomogeneous multiphase model when using the segregated solution strategy in CFX-10, but this is not observed with the fully coupled solution strategy in CFX-11 (Godderidge *et al.*, 2009a) described in Section 2.4.2.

Figure 3.6 compares the power spectra of the experimental and computational homogeneous and inhomogeneous steady-state pressures. At P4, shown in Figure 3.6(a), good agreement between the inhomogeneous CFD results and the experimental data is observed near the excitation period. The peak value is well predicted, but experimental and computational high-frequency noise is observed as well. However, the homogeneous model underpredicts the peak by approximately 50%.

Figure 3.6(b) shows the power spectrum for P6 where the experimental peaks are at the excitation period T and at approximately $0.5T$. Again the inhomogeneous mass-corrected model predicts both peaks, but the trough between the peaks is not matched. The homogeneous model underestimates the experimental power spectrum by one order of magnitude.

Figure 3.7 shows the pressure history for the CFD solution between oscillations 20 and 30, where it has reached a steady state and compares them to the steady-state experimental data. The pressure data obtained with the homogeneous multiphase model underpredicts the experimental pressure in excess of 50%. The inhomogeneous model produces a much better match with the peak pressure observed in the simulation within 10 to 15%, but the double-peak shape of the experimental data is not replicated.

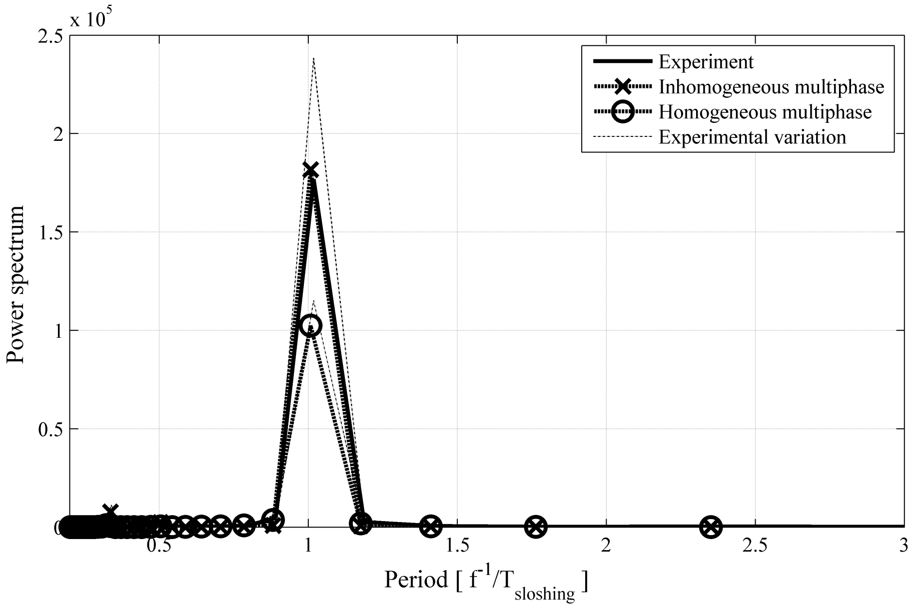

(a) Spectrum for P4: A single peak at the excitation frequency is visible. The result from the inhomogeneous multiphase model is within the experimental data but the homogeneous result does not agree with experimental data.

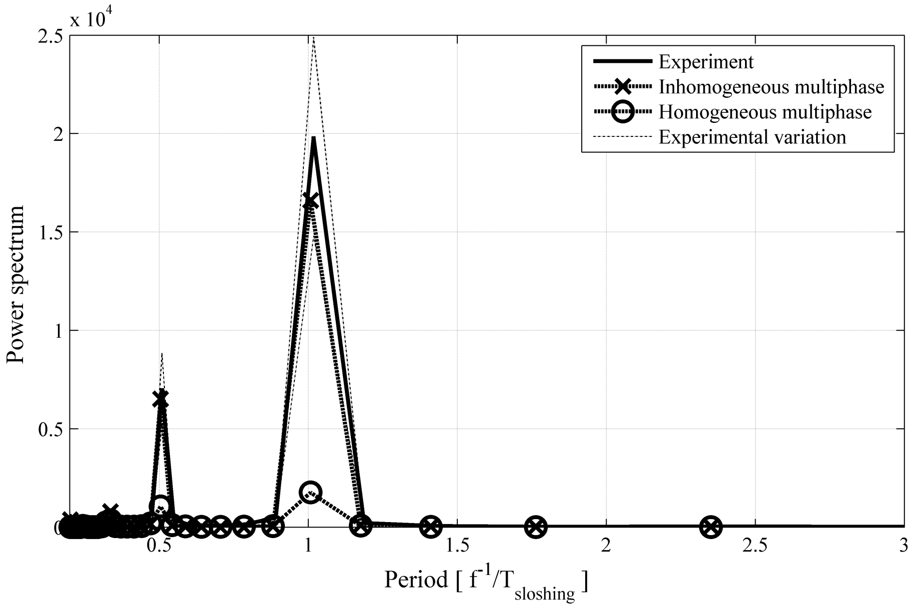

(b) Spectrum for P4: There are separate peaks at the excitation frequency and at $0.5T_1$. The inhomogeneous multiphase model agrees with the experimental data but the homogeneous model fails to predict either peak.

Figure 3.6: Frequency domain analysis of the pressure history obtained with CFD and corresponding experiment for test case A

The static pressure component is more significant at P4 than at P6, where the predictions of the homogeneous model are poor. This indicates that the dynamic properties of the sloshing flow are not simulated correctly by the homogeneous multiphase model. The difference in air and water velocity fields at the fluid interface, given as $r_{air} = 0.5 = r_{water}$, is examined in greater detail. The free surface position near the impact is shown in greater

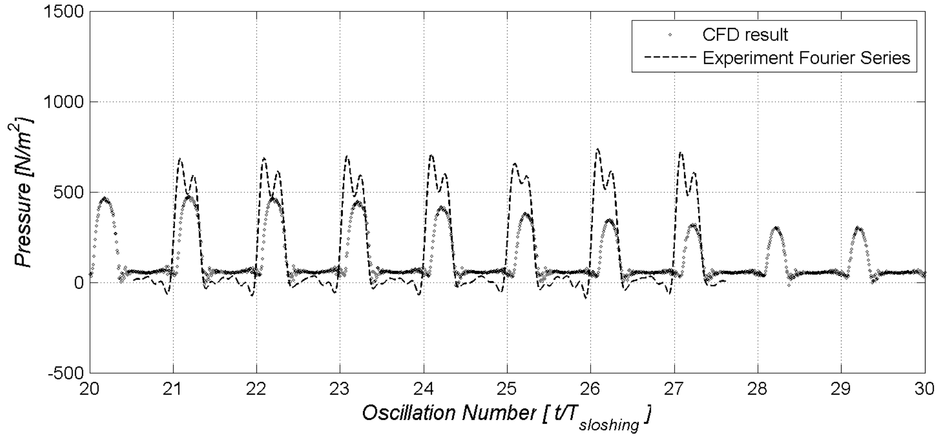

(a) Homogeneous multiphase model: poor agreement with the experiment and the peaks are underpredicted by about 50%

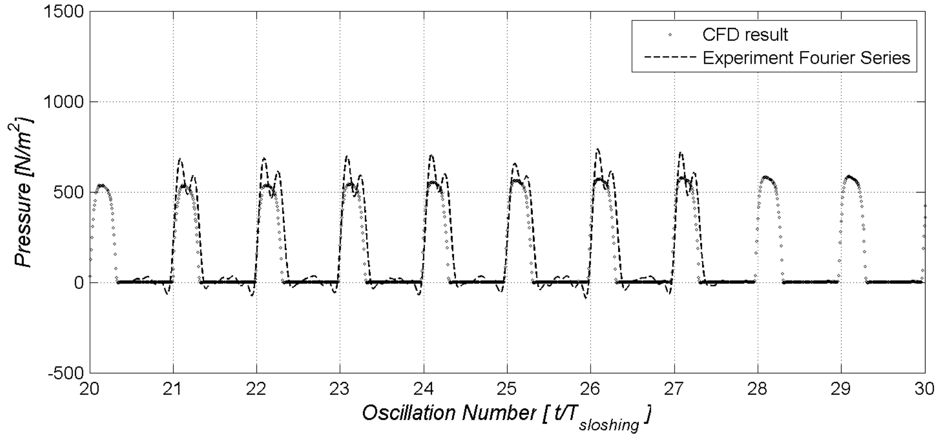

(b) Inhomogeneous multiphase model: good agreement with the experimental data, but the double-peak in the experimental data is not replicated in the CFD solution

Figure 3.7: Comparison of the pressure history at P6 between oscillation 20 and 30 obtained with CFD and experiment for test case A

detail in Figure 3.8(b) and the free surface displacement in the entire tank is given in Figure 3.8(a). The difference in velocity vector direction, shown in Figure 3.8(c), is defined as

$$\Delta\theta = \cos^{-1}\left(\frac{\mathbf{v}_{air}\cdot\mathbf{v}_{water}}{|\mathbf{v}_{air}|\,|\mathbf{v}_{water}|}\right). \tag{3.15}$$

The directional difference is greatest immediately prior to the water impacting the top wall. Once the post-impact jet is formed, the velocity vectors are well aligned near the front of the jet, but differ by up to 30° near the base of the jet. Figure 3.8(d) shows the difference in the magnitude of the air and water velocity

$$\Delta U = \frac{|\mathbf{v}_{air}| - |\mathbf{v}_{water}|}{0.5\,(|\mathbf{v}_{air}| + |\mathbf{v}_{water}|)} \tag{3.16}$$

where the velocity vector $\mathbf{v} = (u, v)$.

Before fluid impact the relative velocity is greatest near the left wall and ΔU is small. During impact the peak relative velocity has increased to equal the mean flow velocity. Near the wall, ΔU reaches a peak value of 0.8. Once the deflected jet has formed, the relative velocity is greater than the mean flow velocity, and 10% of the jet velocity. The difference in velocity magnitude is greatest at the front of the post-impact jet. As is the case with the directional difference, a large ΔU is observed at the base of the post-impact jet.

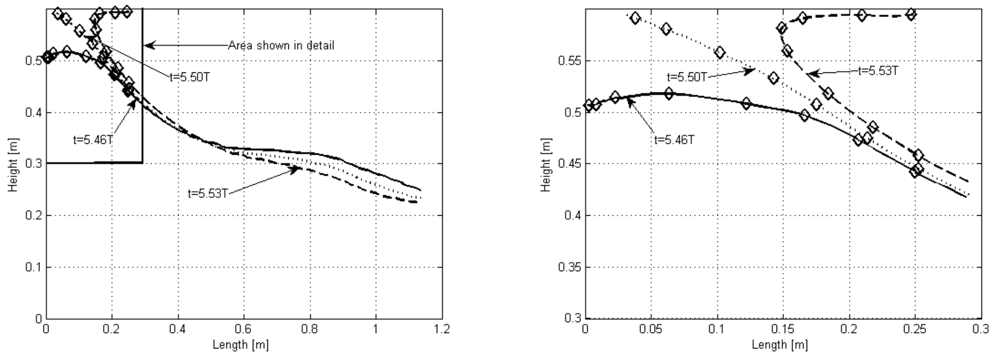

(a) Tank free surface location before, at and after impact

(b) Zoom on the boxed region at the upper-left corner in Figure 3.8(a) showing the three free surface locations considered

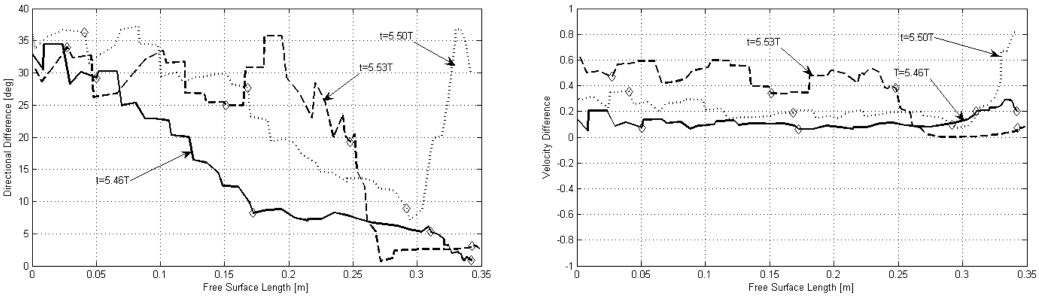

(c) Difference in velocity vector direction at the free surface

(d) Difference in velocity vector magnitude at the free surface

Figure 3.8: The effect of relative velocity during impact

3.3 Fluid impact simulation

This section compares the influence of fluid compressibility models on pressure modelled in resonant and near-resonant sloshing flows using the present CFD model. Case A is simulated with various compressibility models for water and air and the computational results are validated with experimental pressure data from Hinatsu (2001). Subsequently case B with a 10% filling ratio is excited with $T = 0.77T_1$ and the pressure histories, impulse magnitudes and durations obtained with each compressibility model are compared. The results are then used to select the most suitable combination of fluid models for the simulation of strongly nonlinear sloshing flows.

3.3.1 Fluid impact

The effect of fluid compressibility on sloshing was examined with dimensional analysis in Section 2.2.3 and it was found that for a pure liquid with no air entrapment the liquid can be treated as incompressible. Typically, when the flow velocity is much less than the fluid speed of sound,

$$\frac{u}{c} \ll 1, \tag{3.17}$$

where c is the speed of sound and u fluid velocity, a flow can be treated as incompressible. In this case fluid density is constant and the governing equations in Section 2.4.1 can be simplified further. If the Mach number limit (Equation 3.17) is exceeded, a compressible flow model should be used. The system of equations created by this model can be closed by using an equation of state if the compressible fluid behaves as an ideal gas. An isothermal compressibility model assumes that the fluid temperature remains constant and it relates density directly to pressure. No additional transport equations are introduced.

When temperature effects are significant, an ideal gas model can again be used and an additional transport equation for thermal energy must be solved (WS Atkins Consultants, 2003). Godderidge *et al.* (2006) observed a 20% increase in the required computational effort. Other fluids do not lend themselves to an ideal gas model. In this case, bespoke fluid models or property tables are used. The associated increase in computational cost depends on the type of model and differences in fluid response.

While Equation (3.17) aids in the selection of a suitable compressibility model, it is not suitable for certain unsteady flows and a different criterion is needed. A pressure disturbance (wave) travels with the speed of sound in the medium, which can be related to density as

$$\frac{\partial p}{\partial \rho} = c^2, \tag{3.18}$$

where p is pressure and ρ density. In an incompressible medium the speed of sound c tends to infinity.

The wave equation in one dimension

$$\frac{\partial^2 p}{\partial t^2} = c^2 \frac{\partial^2 p}{\partial x^2}, \tag{3.19}$$

can be used to model the propagation of a pressure disturbance. When Equation (3.19) includes only one spatial dimension, it can represent a travelling wave. The application of velocity a to one boundary of the system described by Equation (3.19) may be considered analogous to the evolution of a pressure disturbance in a fluid. Its propagation can be written using d'Alembert's solution as

$$p = \int_{x-ct}^{x+ct} \frac{a}{c} dx. \tag{3.20}$$

The term $\frac{a}{c}$ can be non-dimensionalised as ψ using a characteristic length of propagation L' (container length for sloshing) and pressure p' (reference pressure, usually atmospheric) so that the pressure impact parameter is

$$\psi = \frac{(p_{\max} - p)}{p'} \cdot \frac{L'}{c\tau}, \tag{3.21}$$

where τ is a characteristic timescale from p to $p_{\max}$. A flow with a gradually applied pressure disturbance (e.g. the slow entry of a solid body into a fluid) such that $\psi \ll 1$, is usually represented with an incompressible fluid model. Since the difference between the behaviour of this flow and its incompressible representation, where the entire disturbance propagates instantly, is small, the incompressibility assumption is valid. The condition $\psi \ll 1$ is violated by reducing the duration of the pressure disturbance or increasing the value of $p_{\max} - p$.

3.3.2 Compressibility

A systematic variation of available compressibility models is now applied to the simulation of case A using the hybrid grid shown in Figure 3.4(b). Table 3.8 identifies each combination of the compressibility models used and compares the computational costs. The most expensive was case 4, and a 10% saving can be realised by treating the water as an incompressible liquid.

Table 3.8: Computational cost

Compressibility Model	Case	CPU Time per oscillation
Water compressible, air compressible	case 1	8.44 hrs
Water incompressible, air compressible	case 2	7.80 hrs
Water incompressible, air incompressible	case 3	7.60 hrs
Water compressible, air incompressible	case 4	9.11 hrs

Figure 3.9 shows the pressure history at monitor points P4 in Figure 3.9(a) and P6 in Figure 3.9(b) for all permutations of compressible and incompressible fluids for air and water and compares them to experimental data from Hinatsu (2001). There are no discernible

differences between the compressibility model combinations studied, and they compare well to the experimental data.

The pressure evolution during the seventh oscillation is shown in greater detail in Figure 3.10. At P4 and P6, the results are similar for the combinations of compressibility models. This is confirmed by the corresponding pressure impulses, shown in Table 3.9 where the impact pressure profile is converted to an equivalent rectangular pressure impulse with the observed peak pressure P_{max} and time duration τ. Both magnitude and duration are similar for all combinations of compressibility models. There are some differences at P9, where the choice of incompressible water and compressible air results in the shortest impulse with the highest magnitude. The fully incompressible case gives the lowest pressure, while the inclusion of a compressible fluid model for water and incompressible model for air gives the longest impulse. The difference between selecting a compressible model for both fluids and air only is less than 3% of the pressure magnitude. A slightly longer lasting impulse is observed when only air is treated as compressible.

Table 3.9: Pressure impulse caused by fluid motion

Case	P4		P6		P9	
	P_{max} [Pa]	τ [ms]	P_{max} [Pa]	τ [ms]	P_{max} [Pa]	τ [ms]
Case 1	1,705	605	855	390	675	50.6
Case 2	1,695	602	885	368	695	54.0
Case 3	1,685	607	825	398	605	57.3
Case 4	1,705	603	835	397	645	62.9

3.3.3 Trapped air bubble

Case B, where the filling level is reduced to 20% of the tank height and a filling ratio $h/L = 0.1$, is now simulated. A travelling wave is formed during sloshing and a large air pocket is observed when the wave breaks into a tank side wall which gives rise to an oscillating impact pressure. The computational model used for the detailed study of the fluid impact is the same as in the previous simulations for case A. The convergence criterion is lowered to $2 \cdot 10^{-6}$, because the present flow is more sensitive to numerically induced disturbances. A locally refined grid, shown in Figure 3.11, is used. The refined region contains 4602 hexahedral elements, with horizontal and vertical cell spacing at impact of 0.05 mm and 2 mm respectively. There are approximately 1300 nodes within the air bubble at impact. A further grid independence study for this problem was carried out by Godderidge *et al.* (2007). The time step is controlled dynamically so that the local Courant number remains below unity for all control volumes. The isothermal ideal gas and thermal energy compressibility models are compared for air and water is treated as an incompressible liquid and the IAPWS 1997 industrial formulation (Wagner *et al.*, 2000).

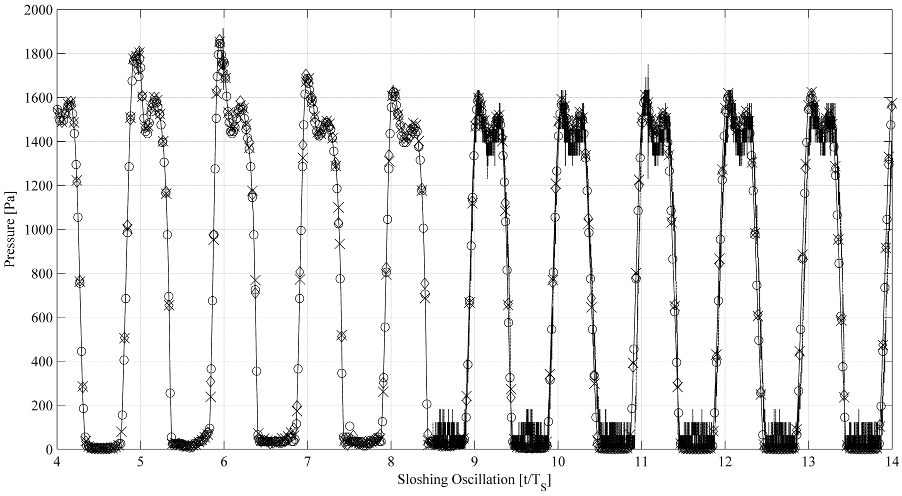

(a) Pressure history at P4

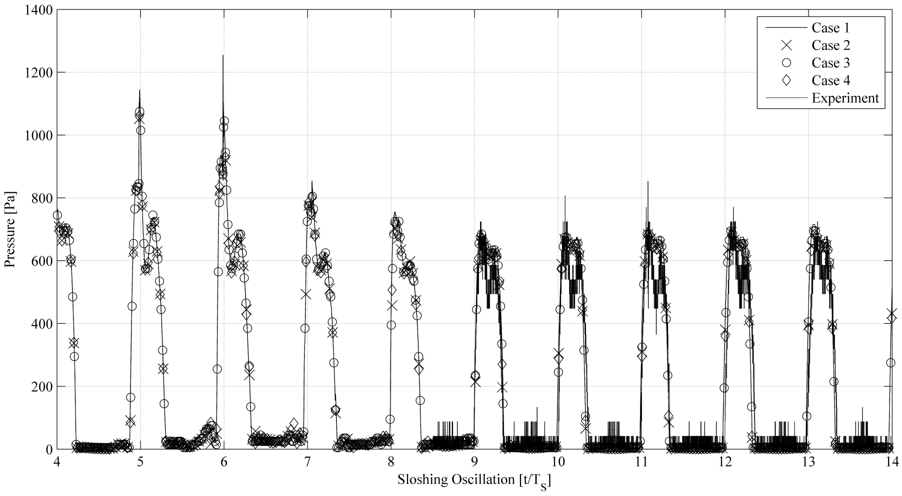

(b) Pressure history at P6

Figure 3.9: Comparison of the different fluid compressibility models in Table 3.8 for case A

The four combinations of fluid compressibility models in Figure 3.12 illustrate the dependence of the pressure history on the inclusion of the thermal model. The pressure history at P2, located near the bottom of the tank, is shown in Figure 3.12(a) and the pressure history at P3, situated at the centre of the air bubble is given in Figure 3.12(b). At both P2 and P3, the pressure histories of the simulations using an ideal gas have a lower frequency and decay slower, while those using a thermal energy model have a considerably higher frequency.

During and immediately after impact, air and water are mixing with a wide range of air bubbles entrained in the water. Depending on grid resolution, large air bubbles can be captured explicitly with the current multiphase model, but small scale air bubbles

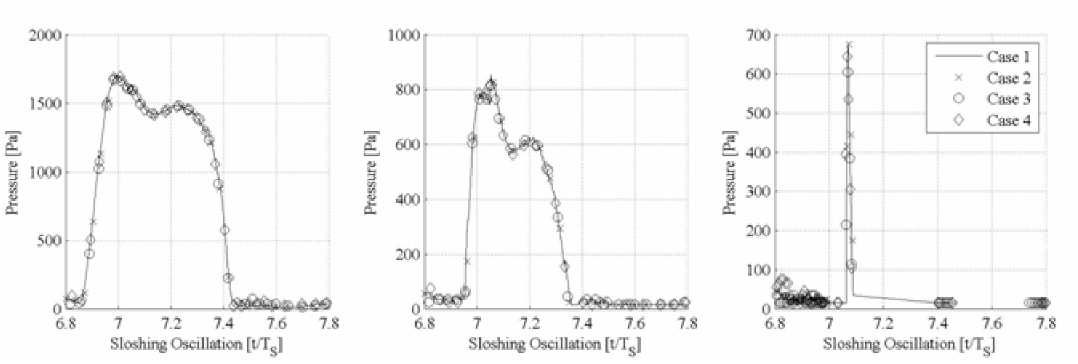

Figure 3.10: Zoom on oscillation 7 for the case considered in Figure 3.9. The result for P4 (left) and P6 (centre) shows that the effect of the compressibility model is small. When considering fluid impact at P9 (right) the influence of compressibility on pressure magnitude and duration becomes apparent.

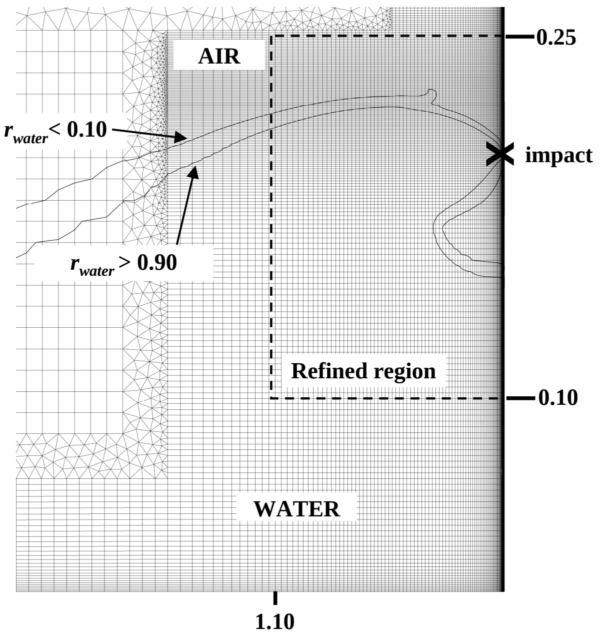

Figure 3.11: Computational grid used for the detailed study of sloshing impacts. The refined region contains 4,602 hexahedral elements and there are approximately 130 elements in the trapped air bubble during impact.

reported in the sloshing impacts studied by e.g. Schreier *et al.* (2009) are not captured. The air bubbles increase the compressibility of the impacting fluid mixture (Dias *et al.*, 2009) and consequently a lower pressure is observed. Therefore, the pressure magnitudes and oscillation frequencies are investigated in the air bubble rather than the initial point of impact.

The fluid impact on the tank wall results in the formation of an air bubble shown in Figure 3.13. The size of the air bubble is determined using the water volume fraction r_{water}. The

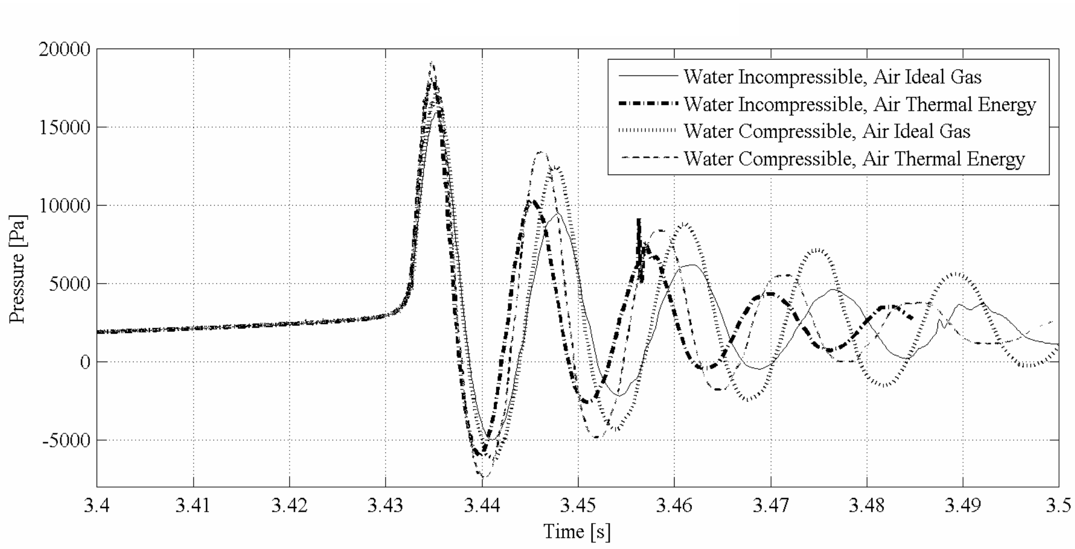

(a) Pressure history at P2

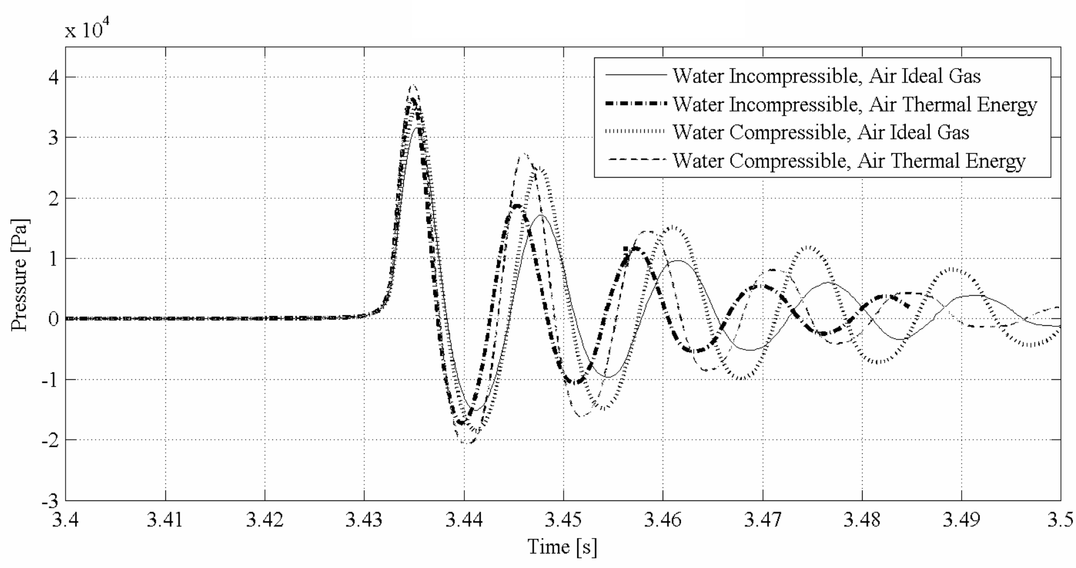

(b) Pressure history at P3

Figure 3.12: Pressure history for resonant sloshing flow with different fluid compressibility models. The effect of the compressibility model on the oscillation frequency and rate of decay of the pressure can be observed. A thermal energy compressibility model results in a higher oscillation frequency and faster rate of decay. The use of a compressible model for water reinforces this trend.

contours for $r_{water} = 0.10$ and 0.90 show that the air-water interface in the bubble is not smeared or subject to numerical diffusion. The flow evolution produces an oscillating pressure history in the bubble region. CFD can be used to visualise the flow development. Figure 3.14 shows the evolution of the fluid impact. As the top water jet in Figure 3.14(a) impacts the side wall, the air bubble is enclosed and compressed by the bulk fluid motion. This results in the air pressure exceeding the surrounding water pressure, shown in Figure 3.14(b). This pressure gradient redirects the water flow away from the air bubble, giving a lower pressure in the air than in the surrounding fluid. The resulting pressure gradient

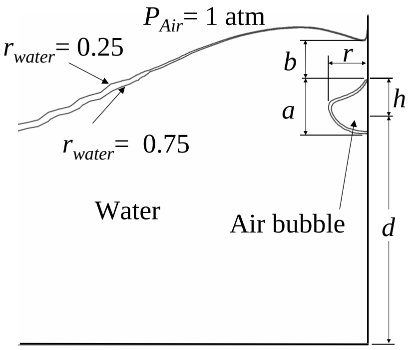

Figure 3.13: Impact bubble geometry and dimensions

causes the water velocity to change toward the bubble, as shown in Figure 3.14(d). This process is repeated until the air bubble is dissipated or moves to the free surface.

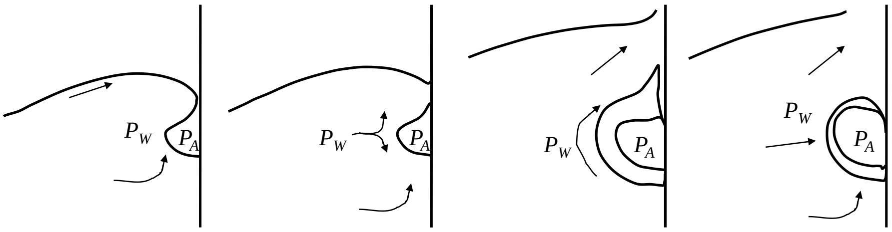

T=3.432 s
$P_W = P_A$
(a)

T=3.434 s
$P_W < P_A$
(b)

T=3.440 s
$P_W > P_A$
(c)

T=3.445 s
$P_W < P_A$
(d)

Figure 3.14: Impact bubble and pressure evolution. Figure 3.14(a) shows the wave breaking into the vertical wall just before impact. Impact has occurred in Figure 3.14(b) and a vertical jet forms. Figure 3.14(c) illustrates the start of the second pressure oscillation with a smeared fluid interface in the trapped air bubble. The trapped air bubble is subjected to buoyant forces and starts to move toward the free surface in Figure 3.14(d).

The bubble size along the tank wall at the initial pressure peak, 0.002 sec after the initial jet impact illustrated in Figure 3.13, is $a = 0.032$ m and the adjacent water thickness b extends 0.030 m beyond the bubble. At impact, the bubble centre is 0.173 m from the tank bottom d, 0.036 m from the free surface h and extends 0.031 m into the fluid, as shown in Figure 3.13. The variation in the pressure oscillation frequency observed in Figure 3.12(a) and 3.12(b) is computed using spectral analysis. Figure 3.15 shows that the calculated pressure oscillation frequency depends primarily on the compressibility model selected for air.

The choice of compressibility model for either air or water did not influence the pressures observed in sloshing flows with a low level of fluid impact. Computed pressure impulses

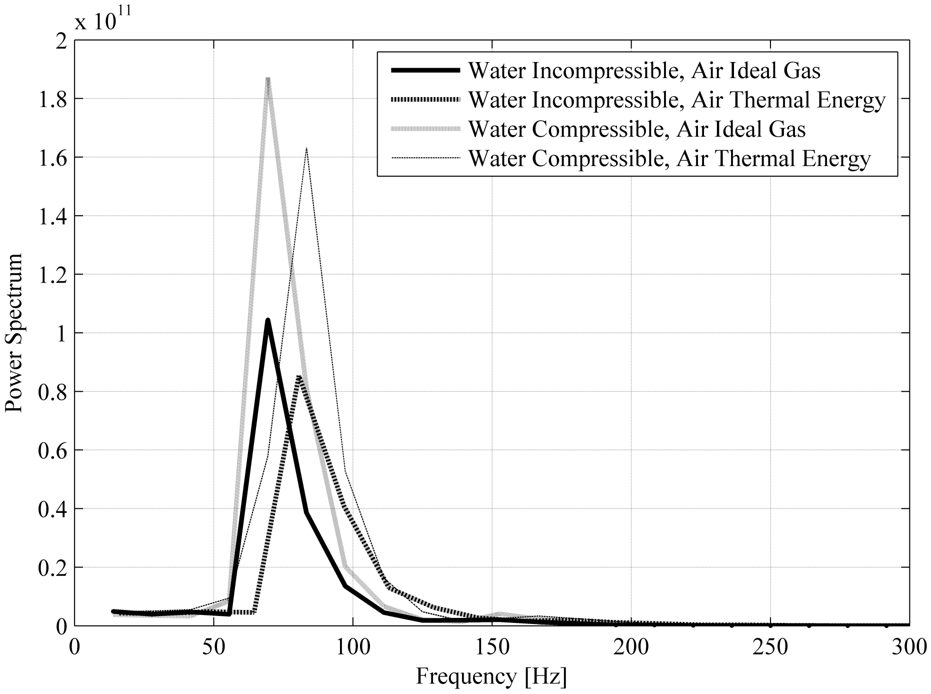

Figure 3.15: Power spectrum of air bubble pressure history at P3. The effect of the compresibility model on pressure magnitude and frequency is illustrated - compare to Figure 3.12

Table 3.10: Pressure impulse caused by fluid impact. P_{max} in [Pa] and τ in [ms]

Compressibility Model		P2		P3		$\mathrm{P_{Imp}}$	
Water	Air	P_{max}	τ	P_{max}	τ	P_{max}	τ
Incompressible	Ideal Gas	16,400	3.87	31,600	3.31	86,500	0.543
Incompressible	Thermal Energy	18,700	3.55	36,300	3.03	81,400	0.620
IAPWS-IF97	Ideal Gas	17,700	3.76	35,100	3.03	72,200	0.637
IAPWS-IF97	Thermal Energy	20,000	3.53	38,800	3.14	71,000	0.720

in Table 3.8 are within 5% of the mean and the computational times are similar. The parameter ψ, determined using the magnitude and duration of the pressure impulse, shows that the criterion $\psi = O\left(10^{-5}\right) \ll 1$ for incompressible flow is satisfied. However, the fluid impact observed in the simulation of case B does not meet this criterion as $\psi = O\left(1\right)$. Table 3.10 shows the equivalent rectangular pressure impulse magnitude P_{max} and duration τ computed for the fluid impact with air bubble entrainment. Both duration and magnitude vary with the selected compressibility model. The influence of the compressibility model can be studied further by considering the oscillation frequency of the pressure history in the air bubble.

Rognebakke and Faltinsen (2005) developed a theoretical model for sloshing impacts with air bubble formation. In experiment, an air bubble was observed with the bubble diameter/depth ratio $a/b = 1$ (see Figure 3.13). The pressure observed in the air bubble oscillated with a frequency of 90 Hz. The boundary-element based mathematical model developed by Rognebakke and Faltinsen (2005) predicted an oscillation frequency of approximately 75 Hz.

Topliss *et al.* (1992) developed a potential flow solution for the pressure in an air bubble during water impact and deduce the frequency of the pressure oscillation as

$$\omega^2 = \frac{2\gamma p \left(1 + 0.5\lambda^2 r^2\right)}{\rho r^2 \left(\log\left(0.5\lambda r \tan\lambda d\right) + 0.25\lambda^2 r^2\right)} \tag{3.22}$$

where d is the distance from the bubble centre to the bottom, γ the ratio of specific heats, p atmospheric pressure, ρ density, and r bubble radius. The bubble size parameter λ is defined as

$$\lambda = \frac{\pi}{2\left(d + h\right)}, \tag{3.23}$$

where h is the distance the centre of the bubble is below the free surface. The dependence of the pressure oscillation frequency on the bubble size underlines the importance of capturing the shape of the impact bubble with a high level of accuracy.

The bubble size ratio a/b is near unity in the present problem and the pressure oscillation frequency obtained from Equation (3.22) is 94 Hz. Using the inhomogeneous multiphase CFD model with a thermal energy model for air given in Equation (2.21d), the pressure oscillation frequency is approximately 84 Hz with compressible water and 81 Hz with incompressible water, with an error band of about ±7%, calculated using Equation (3.22). This compares well with the value reported by Rognebakke and Faltinsen (2005). Equation (3.22) was found to overestimate the frequency when compared with the corresponding experimental data by approximately 10% (Topliss *et al.*, 1992). The difference between the observed CFD result and the corresponding calculation using the model by Topliss *et al.* (1992) is 10.6%. The frequency obtained with the ideal gas model and either compressible or incompressible water is approximately 69 Hz, which corresponds to the theoretical result given by Rognebakke and Faltinsen (2005). It is 20% lower than the value obtained with the thermal energy compressibility model.

3.4 Closure

This chapter summarised the validation of an unsteady RANS CFD sloshing model which is implemented in the commercial CFD code CFX-11. Figure 3.16(a) shows the good agreement between the experimental result and CFD model for translatory sloshing in case A. An analogous result is obtained for rotational tank motions for case C and the results are compared in Figure 3.16(b).

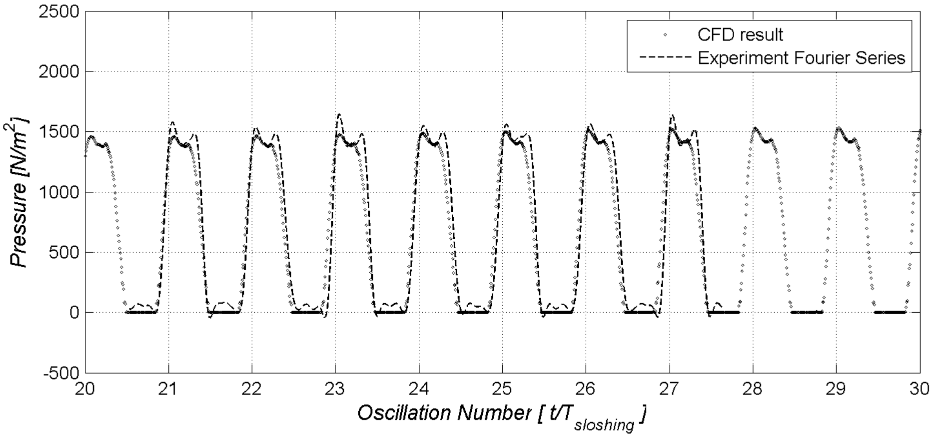

(a) Sloshing induced by tank translation

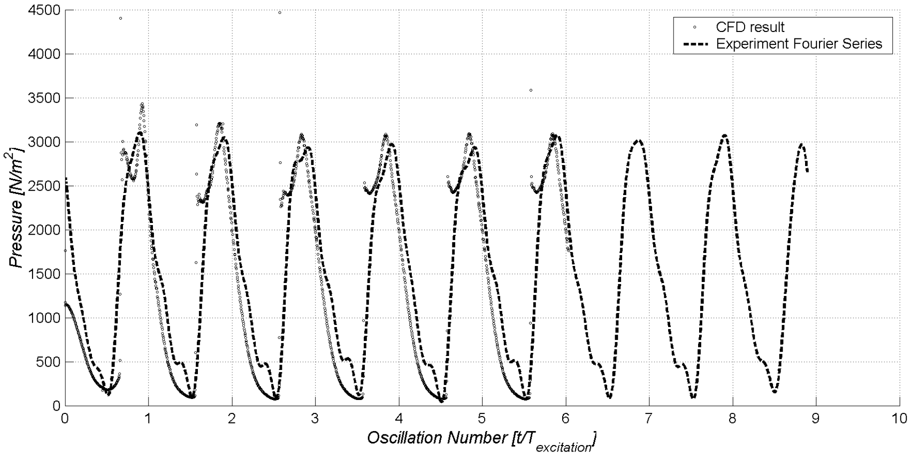

(b) Sloshing induced by tank rotation

Figure 3.16: Experimental validation of the CFD sloshing model: summary and proof of capability for the CFD model.

Novel contributions during this work include the multiphase analysis in Section 3.2.5, which has been published in Godderidge *et al.* (2009) and applied to other free surface flow problems with fluid-gas dynamics (Lewis *et al.*, 2008). The analysis of the compressibility models is published in Godderidge *et al.* (2009) and the findings from the validation study are used in a contribution to the ISOPE 2009 sloshing comparative study (Godderidge *et al.*, 2009c).

Upon the successful validation of the CFD-based sloshing model with experimental data the CFD model can be applied for the assessment of sloshing (American Bureau of Shipping, 2006). Although the limitations of CFD prevent its use in a sloshing guidance system, the current validated CFD model is applied as a testing and validation tool for the Rapid Sloshing Model methodology.

Chapter 4

Rapid Sloshing Model

Full-field numerical techniques such as Navier-Stokes CFD can capture strongly nonlinear sloshing but large computational requirements restrict their range of application. Analytical approaches can be computed in faster than real time but they are limited to linear and some cases of weakly nonlinear sloshing (Ibrahim, 2005). The sloshing guidance system approach (in Figure 4.1) requires a sloshing model which can be applied to nonlinear sloshing including sloshing impacts and is solved at the same speed as analytical models.

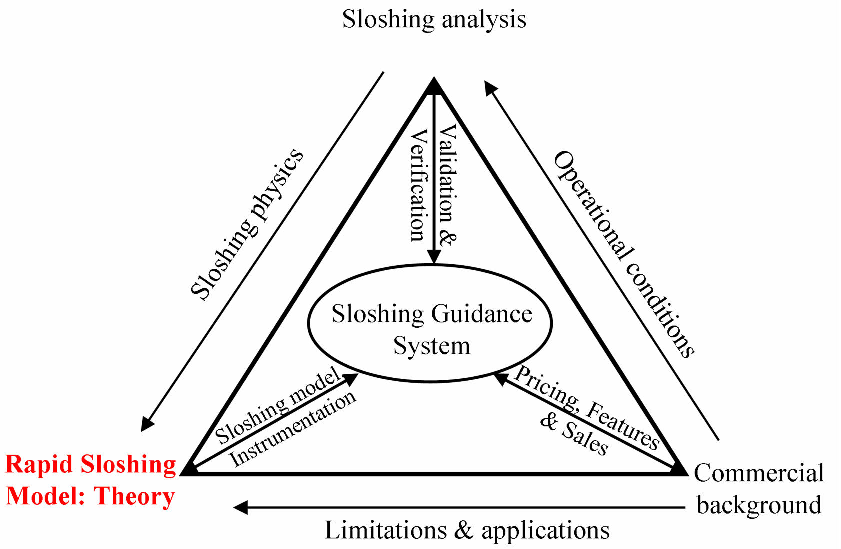

Figure 4.1: The Rapid Sloshing Model - the centrepiece of the sloshing guidance system

This is achieved by using a phenomenological modelling approach where by virtue of modelling the sloshing fluid as a lump mass and ignoring the free surface there are no restrictions on its steepness, fragmentation and coalescence. The fast time solution on a normal desktop PC is made possible by solving what is essentially a pendulum equation. The sloshing model is applied to a particular tank using coefficients developed from a limited set of CFD calculations and theoretical results through the approach introduced in this Chapter.

The basis for studying sloshing using an equivalent mechanical system is the observation of Faltinsen *et al.* (2000) that the fluid centre of mass followed a particular path during long time series with a non-periodic weakly nonlinear sloshing response. This is also observed in Figure 4.2, which depicts the location of the fluid centre of mass during linear sloshing which is induced by tank motions at 1.25 times the first resonant period. Due to the presence of disturbances at the free surface in the developed sloshing flow, the vertical centre of mass does not return to its initial location. Although there is scatter, the centre of mass displacement is along path prescribed by a circular arc which is indicated by a solid black line in Figure 4.2.

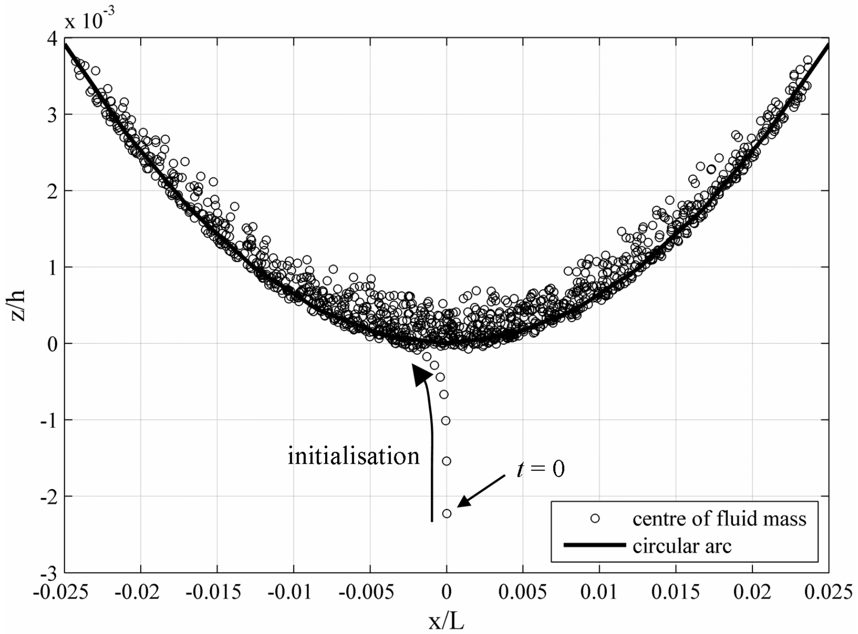

Figure 4.2: Location of the fluid centre of mass during sloshing motion with regular excitation period $T = 1.25T_1$ and filling ratio of 0.3

In this work it is proposed that as an alternative to conventional methods the understanding developed from CFD can be used to develop a pendulum-based approach for the construction of an equivalent model for the first sloshing mode. The circular path of a point mass is described by a pendulum and a mathematical description of the unforced damped pendulum is given in Equation (4.1)

$$\ddot{\theta} = -\delta\dot{\theta} - \frac{g}{l}\sin(\theta), \tag{4.1}$$

where δ is a damping coefficient, g gravity, l pendulum length and θ angular displacement. Time derivatives are indicated by superscript dots.

4.1 Forces in a sloshing flow

Figure 4.3 illustrates the forces acting on an arbitrary nonlinear sloshing flow at a low filling ratio where the sloshing fluid behaves as a standing wave. The dislocation of the fluid from its quiescent position and the influence of gravity give rise to a pressure gradient and a consequent restoring force. The wall shear force and vortices retard the fluid motion and are therefore associated with the damping force. As the fluid nears the tank ceiling, the displacement of air and the resulting boundary layers and vortices introduce additional damping. There are other forces such as surface tension acting on the sloshing flow, but their effect depends on surface contamination and fluid properties and they are ignored in most practical sloshing studies.

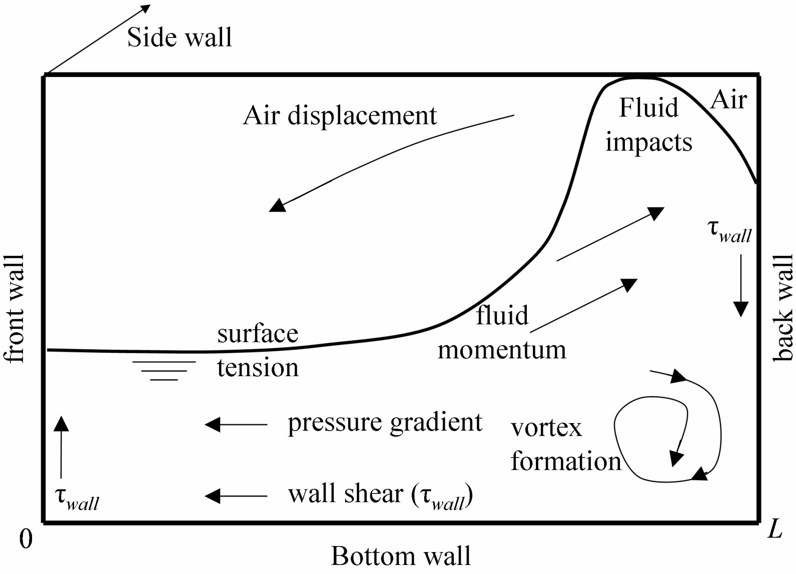

Figure 4.3: Illustration of forces acting on a sloshing flow

Phenomenological modelling replaces conceptually the sloshing fluid with an equivalent mathematical or mechanical system. Okhotsimskii (1960) showed that sloshing dynamics can be represented by a mechanical model such as a spring-mass system or pendulum with masses that are free to oscillate. When a linearised pendulum equation is employed, the parameters can be determined using either potential flow results or experimental measurements (Dodge, 2000).

The resonance characteristics of a sloshing flow are replicated in a pendulum model by adjusting its length so that the resonant frequency of the pendulum model matches that of the sloshing liquid. The resonant frequency ω_n of the pendulum can be obtained by linearising Equation (4.1) and it is given as

$$\omega_n = \sqrt{\frac{g}{l}}. \tag{4.2}$$

By approximating $\frac{g}{l}\sin(\theta)$ as $\omega_n^2\theta + \beta\theta^3$and introducing a periodic forcing term $A(t)\cos(\omega t)$ with amplitude A and frequency ω a forced Duffing Equation (4.3), given as

$$\ddot{\theta} + \delta\dot{\theta} + \omega_n^2\theta + \beta\theta^3 = x_0\cos(\omega t)\,, \tag{4.3}$$

is obtained. It is then possible to replicate the detuning characteristics of sloshing (Faltinsen *et al.*, 2000; Waterhouse, 1994) within an equivalent mechanical model. When $\beta > 0$, the response is, using Duffing equation terminology, characterized as hard spring and this behaviour corresponds to sloshing with filling ratios below the critical depth of $h/L = 0.3368$. Soft spring behaviour is expected for filling levels above the critical depth, where $\beta < 0$. However, this only applies to the small amplitude domain (Waterhouse, 1994). By letting $\beta = 0$, the linearised pendulum equation is recovered.

4.1.1 Restoring force

The restoring force due to the sloshing-induced displacement of the fluid can be likened to the $\frac{g}{l}\sin(\theta)$ term in the pendulum Equation (4.1). The restoring force coefficient is normally obtained using a potential flow solution (Dai *et al.*, 2004) or pendulum physics (Dodge, 2000). The restoring force of a pendulum is given as

$$F = m_1 g \sin(\alpha\theta) \tag{4.4}$$

where m_1 is the pendulum mass and α is a non-dimensional coefficient which is unity for a normal pendulum.

Figure 4.4 compares the non-dimensional restoring force measured for the sloshing flow in Figure 4.2 to the angle of displacement of the centre of mass, which is found using the circular path followed by the sloshing fluid centre of mass. A linear fit to this plot is used to determine the gradient at $\theta = 0$ and thereby α. The present model retains $\sin(\alpha\theta)$ rather than replacing it with the simplification $x - x^3$. This is due to the sinusoidal term being bounded between -1 and 1 for all θ of practical significance, but this is not true for the term $x - x^3$. Nonetheless, alternative polynomial formulation or the use of the Taylor expansion for the $\sin(\theta)$ term can be applied.

Figure 4.5 compares the effect of adjusting the restoring force coefficient using this procedure with a conventional pendulum model (e.g. Dodge, 2000) with and without damping. During the first three oscillations there is little difference between the various pendulum models and the corresponding CFD solution. After about ten oscillations, both the damped and undamped linear pendulum models show significant differences compared to the corresponding CFD solution. When the restoring force term in the pendulum equation

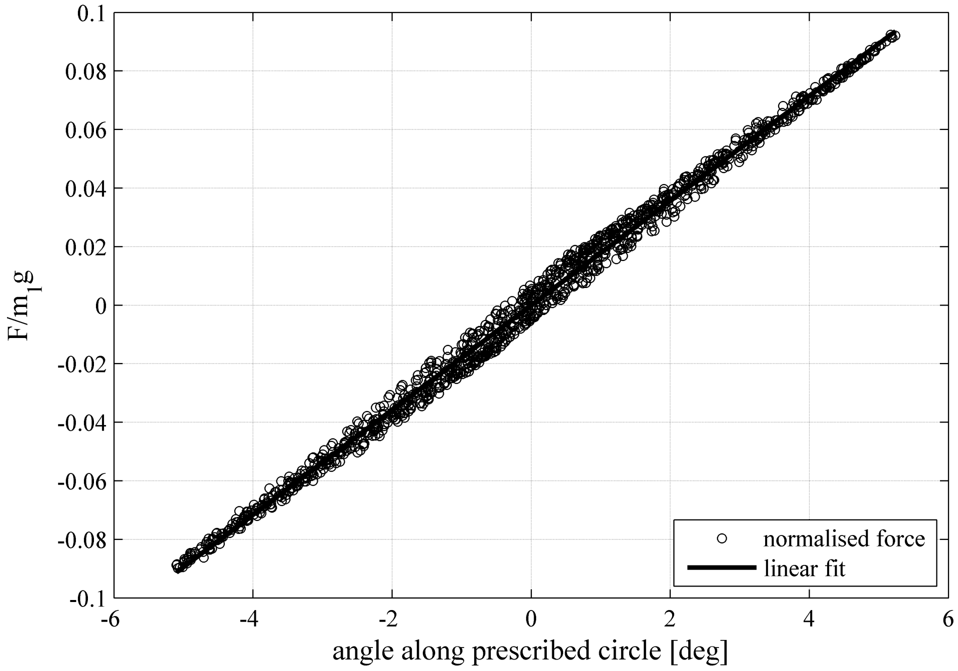

Figure 4.4: Sloshing force compared to the centre of gravity position for sloshing motion with regular excitation period $T = 1.25T_1$ and filling ratio of 0.3

is adjusted to replicate the restoring force recorded in the CFD simulation using the slope measured in Figure 4.4 and setting $\alpha = 1.025$ the results show a good match.

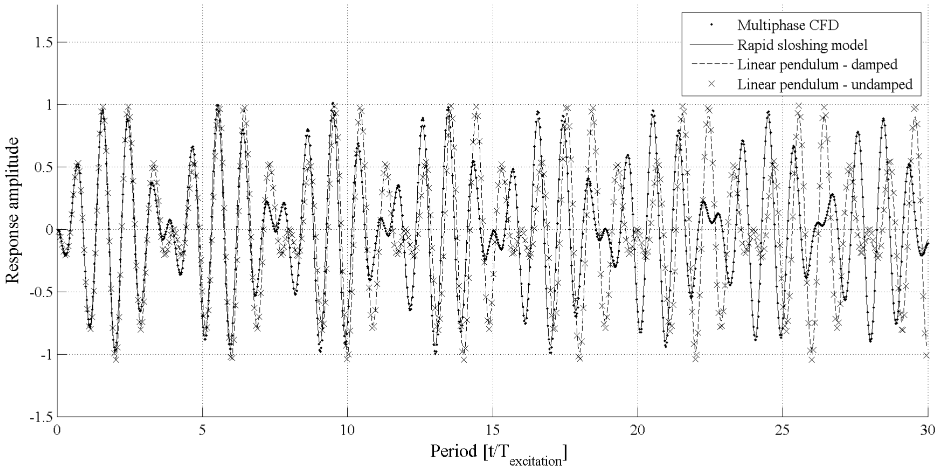

Figure 4.5: Comparison of sloshing response obtained with CFD, Rapid Sloshing Model and conventional pendulums with and without damping. The sloshing response is normalised with the peak value observed in the CFD simulation.

4.1.2 Dissipation

The significance of damping effects in the simulation of sloshing remains contentious. Sloshing studies by Faltinsen *et al.* (2000) and Frandsen (2004) do not include dissipation effects. Faltinsen and Timokha (2002) found that at low filling levels viscous damping effects need to be included and Molin *et al.* (2002) found that damping due to viscous dissipation has a considerable influence on the sloshing response in a rectangular tank. Additional damping is caused by wave breaking during sloshing.

In Figure 4.3 dissipation occurs at the tank wall boundary layer as well as within the fluid. Keulegan (1959), Miles (1967) and Decent (1997) carried out extensive investigations into the damping characteristics of surface waves which can be used to determine a suitable representation of dissipation for the present sloshing model. Miles (1967) finds that the rate of viscous dissipation in the fluid (interior damping) is proportional to the dynamic viscosity μ and Keulegan (1959) and Miles (1967) show that the rate of dissipation at the boundary layer is proportional to $\sqrt{\mu}$. In water $\mu = O\left(10^{-3}\right)$ and for LNG, $\mu = O\left(10^{-3}\right)$ to $\mu = O\left(10^{-4}\right)$ (Abramson *et al.*, 1974; Mann, 1977). Henderson and Miles (1994) observed discrepancies of up to 20% to 30% between experimental and theoretical predictions of damping using only boundary layer dissipation and Martel *et al.* (1998) find that interior damping can be comparable to the boundary layer damping. Thus Faltinsen and Timokha (2002) used both boundary layer and interior damping in the calculation of a linear damping coefficient. However, in the calculations by Henderson and Miles (1994) and Martel *et al.* (1998) the density and viscosity for water are taken at 20° C and the effect of temperature on viscosity in the experiment is not considered[1]. Therefore the development of the damping model in this study uses the approach by Keulegan (1959), where the viscosity of the fluid used was measured and there was good agreement between theoretical prediction and experimental measurements. Nonetheless, interior damping and other sources of damping such as liquid-vapour mixing can be included in the calculation of a damping coefficient if required.

Keulegan (1959) gives the total energy of a standing wave in a rectangular basin during one complete cycle as

$$E = \frac{\pi}{4}\rho g B \frac{a^2}{k} \tag{4.5}$$

where a is the wave amplitude, B tank width, $k = \pi/L$ wave number and ρ density. The dissipation at the boundary layer at a tank side wall located at $y = 0$ and $y = B$ is

$$\Delta E_1 = \frac{g^2 a^2}{\omega^2}\frac{\pi^2}{4}\sqrt{\frac{\mu\rho}{2\omega}}\frac{\sinh\left(2kh\right)}{\cosh^2\left(kh\right)} \tag{4.6}$$

where ω is the wave frequency and h is the mean free surface height (tank filling level). The dissipation at the front wall, located at $x = 0$ and $x = L$ is given by Keulegan (1959)

---

[1] Diane Henderson, private communication

as

$$\Delta E_2 = \frac{g^2 a^2}{\omega^2} \frac{\pi}{2} \sqrt{\frac{\mu\rho}{2\omega}} \frac{Bk}{\cosh^2(kh)} \left(\frac{\sinh(2kh)}{2} - kh \right). \tag{4.7}$$

Finally, the dissipation at the bottom wall, located at $z = -h$ is given as

$$\Delta E_3 = \frac{g^2 a^2}{\omega^2} \frac{\pi^2}{2} \sqrt{\frac{\mu\rho}{2\omega}} \frac{Bk}{\cosh^2(kh)} \tag{4.8}$$

The resulting damping coefficient can be written as

$$\delta = \frac{\Delta E_1 + \Delta E_2 + \Delta E_3}{2 \cdot E} \tag{4.9}$$

Figure 4.6 shows the kinetic energy observed from a CFD simulation of sloshing where the tank is excited at the resonant period and after 30.5 oscillations the tank motion is stopped. The additional damping due to impacts is illustrated by the greater damping rate observed between oscillations 30.5 and 31.5, where impacts at the tank ceiling occur. The observed total loss of kinetic energy of about 35% for one cycle with two impacts is in agreement with the calculations by Faltinsen and Timokha (2002). Once there are no further impacts, it is possible to construct a logarithmic decrement and it is found that for the present case the logarithmic decrement $\zeta = 0.00273$. This corresponds to a damping coefficient of 0.023, which is comparable to the theoretical result obtained using Equation (4.9). The agreement is somewhat surprising as the CFD simulation is 2D and does not include the effect of the tank side wall. A smaller damping rate would be expected when neglecting the effect of the side wall in Equation (4.9) and the additional damping in the CFD simulation is explained by the inclusion of turbulence.

Peters (2003) illustrated the importance of the nonlinear damping terms in the linearised pendulum equation. Computational results in Godderidge *et al.* (2008) established that a linear damping model is insufficient. Therefore a third-order damping coefficient is introduced using the approach from Decent (1997).

The importance of nonlinear damping is illustrated by the variation of the damping model. The results are shown in Figure 4.7, where the nonlinear damping model produces a good match with the corresponding CFD solution. When dropping the nonlinear damping component, there are discernible differences after the second beating phase. Using only 10% of the linear damping coefficient calculated with the results from Keulegan (1959) gives a similar result but the complete absence of damping produces a different momentum evolution. Considering the sensitivity of damping to fluid temperature or fluid/gas mixing, the dependence of sloshing on viscous damping may be greater than dimensional analysis

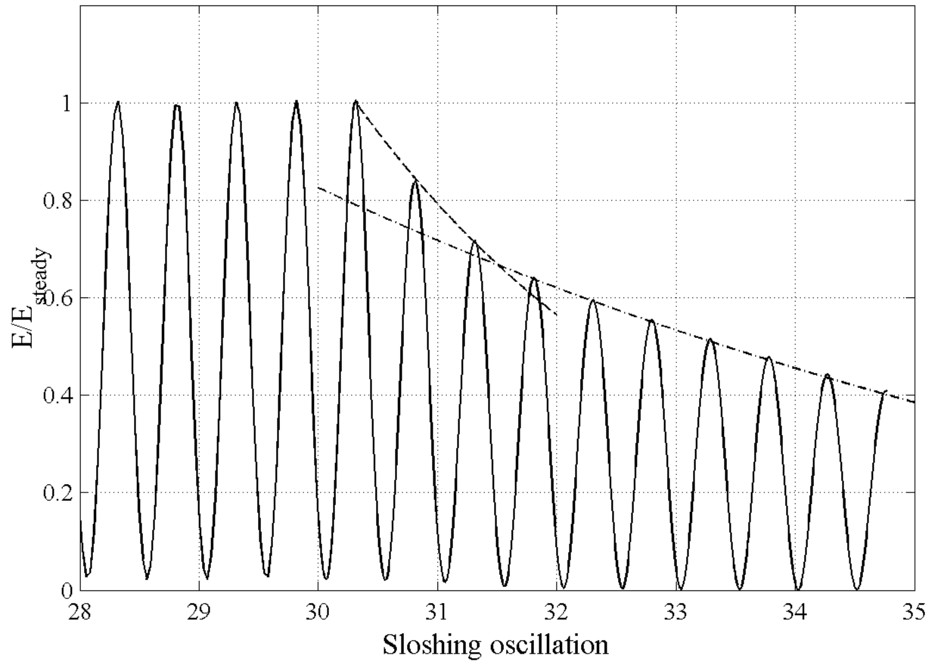

Figure 4.6: Decrease in kinetic energy of the sloshing fluid: the tank motion is suspended after 30.5 oscillations and the additional damping due to fluid impacts can be observed between oscillations 30.5 and 31.5.

would suggest.

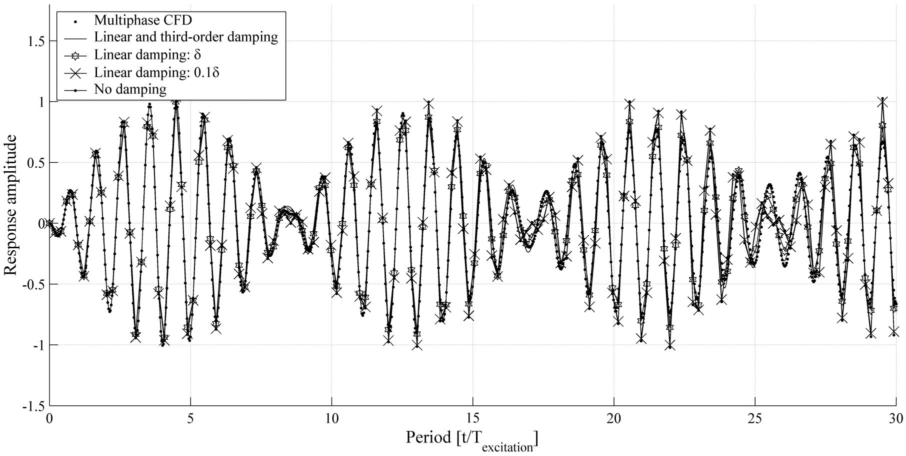

Figure 4.7: Comparison of sloshing response obtained with CFD, Rapid Sloshing Model and conventional pendulums with and without damping for $T = 1.25T_1$. The sloshing response is normalised with the peak value observed in the CFD simulation

4.1.3 Fluid impacts

When the tank excitation results in a sufficiently violent sloshing response, the fluid will impact against the tank walls which results in local pressure peaks. The impact physics can be complicated, especially when mixing between the liquid and gas phases takes place. Peregrine (2003) gives a comprehensive review of theoretical and physical modelling of fluid impacts and Pilipchuk and Ibrahim (1997) proposed a phenomenological description of sloshing impacts using a pendulum interacting with a wall.

This approach is well suited for inclusion in the pendulum-based sloshing model in this study and it was also used by Dai *et al.* (2004). The fluid impact is represented by a potential field which is weak in the region $|\theta| < \theta_0$, where θ_0 is a critical angle at which impact takes place, but grows rapidly in the region $|\theta| \rightarrow \theta_0$. This potential energy of impact can be described by

$$P_{impact} = \frac{a}{2n}\left(\frac{\theta}{\theta_0}\right)^{2n} \tag{4.10}$$

where a is a constant coefficient and the integer $n \gg 1$ (Pilipchuk and Ibrahim, 1997). The impact potential can be related to the impact force by

$$F_{impact} = \frac{\partial}{\partial\theta}\left(P_{impact}\right) \tag{4.11}$$

so that the impact force is given by

$$F_{impact} = a\left(\frac{\theta}{\theta_0}\right)^{2n-1} \tag{4.12}$$

The impact force properties, such as rise time and magnitude are determined by the coefficients in Equation (4.12). A progressively larger n corresponds to a decrease in compressibility, with a rigid body impact represented by $n \rightarrow \infty$. While water is generally considered an incompressible fluid, it is important to note that the impact model in Equation (4.12) approximates the dynamics of the fluid-gas system illustrated in Figure 4.3.

Figure 4.8 compares sloshing impact forces at the top tank wall with the fluid centre of mass location for a sloshing flow and different values for n in the impact model in Equation (4.12). It is evident that the trajectory of the fluid centre of mass along a circular arc shown in Figure 4.2 is not observed at fluid impact. The impact occurs at a fluid centre of mass displacement angle between 15 to 17 degrees. After impact, the fluid centre of mass displacement angle increases further and the force on the top wall deceases and then turns negative. The displacement angle then starts to decrease again and once the fluid is clear of the top wall, the measured force is zero. This is indicative of wave overturning and caused by the fluid behaving as a continuum rather than a point mass approximation and the coefficients for Equation (4.12) must be selected to reflect this post-impact behaviour.

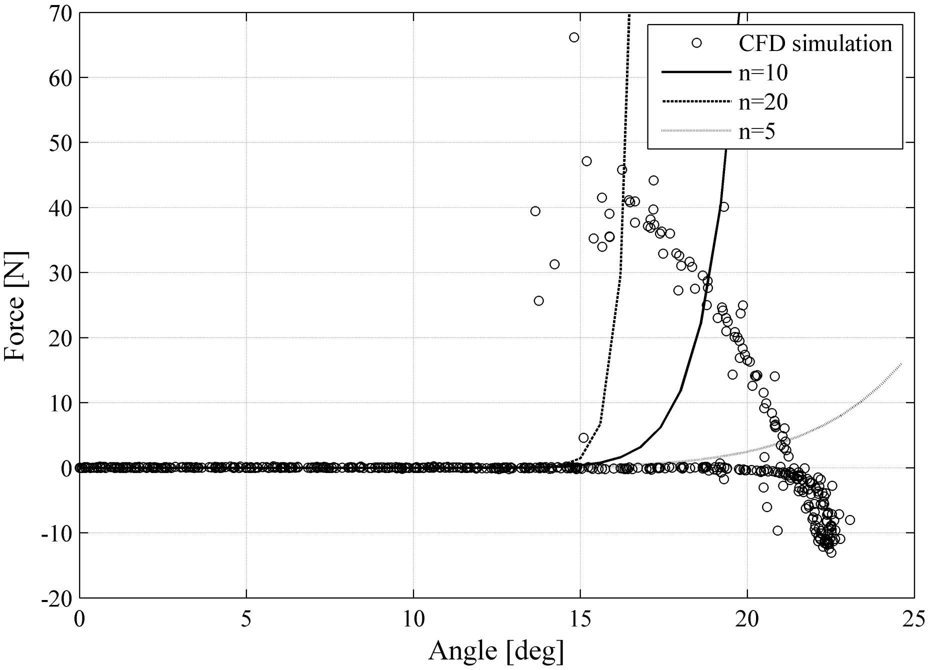

Figure 4.8: Force measured at the tank top wall compared to centre of fluid mass displacement angle. Impact occurs at a fluid centre of mass displacement angle between 15-17 deg.

As shown in the sketch in Figure 4.8 and assumed by Faltinsen and Rognebakke (1999), damping occurs during water impacts and the additional energy dissipation due to damping is illustrated Figure 4.6. As the duration of the impact is not known *a priori* Faltinsen and Rognebakke (1999) used an iterative approach to determine the loss of energy due to impact. An alternative approach is the impact potential potential used by Pilipchuk and Ibrahim (1997). The additional dissipation due to impact can be approximated with

$$B_{impact} = c \left(\frac{\theta}{\theta_0} \right)^d \dot{\theta}^m \tag{4.13}$$

where the coefficient $n \neq d$ (Ibrahim, 2005) and the coefficients c and d are obtained by experimentation or numerical simulation (Pilipchuk and Ibrahim, 1997) and m is unity. In the present study, the coefficients for the impact damping model are obtained using the measured decrease in kinetic energy due to fluid impacts shown in Figure 4.6 and replicating the impact-induced damping.

The choice of impact damping coefficients is considered in Figure 4.9, where the peaks of each oscillation are shown. The effect of changing the value of c, illustrated in Figure 4.9(a), is not significant on the decrease in fluid momentum. The rate of decrease in fluid momentum after impacts cease which occurs after oscillation 31.5 corresponds to the measured value. This confirms the choice of linear and third order damping for inclusion in the damping model. The change of the power of the damping model d is more significant and the effect of doubling and halving d from the baseline value of 24 is shown in Figure 4.9(b).

Although $d = 12$ gives the best agreement with the corresponding CFD result, consideration of the phase difference between the solution leads to a choice of $d = 24$ for the damping model. In Figure 4.9(c) the value of n is decreased from unity (Pilipchuk and Ibrahim, 1997) and it is found that a decrease in the value of n results in a similar rate of decrease due to the impact damping.

Figure 4.10 shows the fluid momentum P for a sloshing flow with impacts at the tank top. The momentum history obtained with a conventional pendulum model is in phase with the CFD solution but the peak values are overestimated by nearly 40%. Introducing the impact model proposed by Pilipchuk and Ibrahim (1997) results in the expected decrase in the fluid momentum peaks but the pendulum model solution is now out of phase with the CFD solution.

The phase difference is due to the impact model providing a rigid boundary. This is not consistent with the sloshing impact physics observed in Figure 4.8, where the centre of gravity displacement is not stopped at the critical angle and the impact force decreases after impact at the critical angle. This behaviour can be replicated by modifying the impact force model in Equation (4.12) and introducing a second critical angle θ_1 which if exceeded the impact force is zero.

An implementation is shown in Equation (4.14)

$$F_{impact} = a\left(\frac{\theta}{\theta_0}\right)^b H\left(\theta_1 - \theta\right) \tag{4.14}$$

where $b = 2n - 1$ and $H\left(\theta_1 - \theta\right)$ is a Heaviside function such that if $\theta_1 - \theta < 0$, $H = 0$.

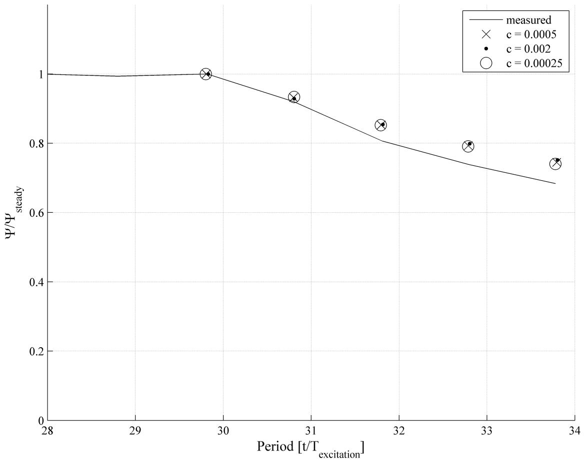

(a) Variations of c

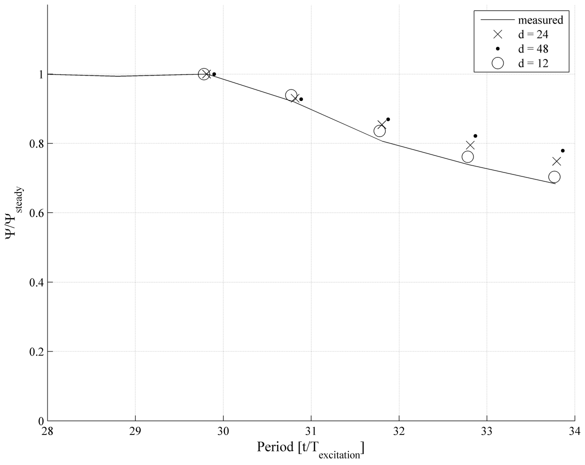

(b) Variations of d

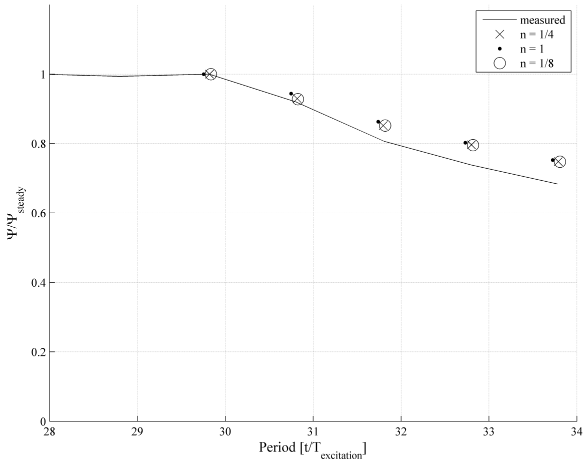

(c) Variations of n

Figure 4.9: Comparison of coefficients for the impact damping model. Ψ is non-dimensionalised fluid momentum defined in Equation (5.4)

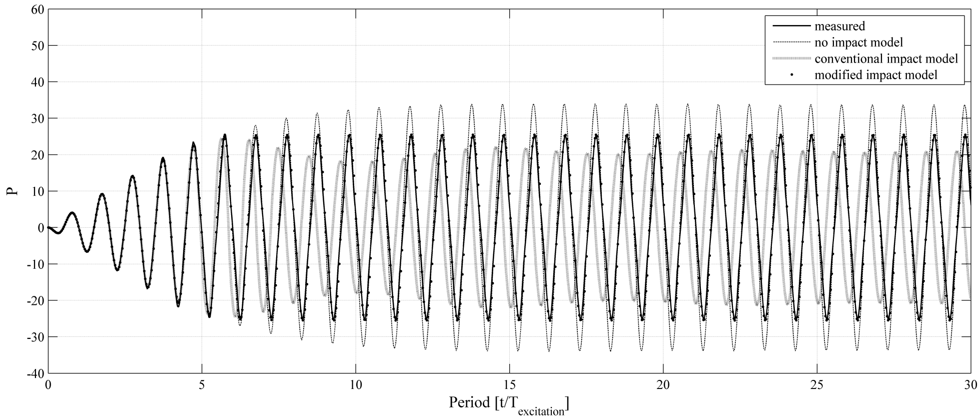

Figure 4.10: Comparison of impact models where P is fluid momentum. The pendulum model overestimates the CFD solution by about 40% but the solutions are in phase when neglecting the impact model The use of the impact model approach by Pilipchuk and Ibrahim (1997) results in a phase lag but the use of the modification to the impact model in Equation (4.14) gives good agreement with the CFD solution.

4.2 Mathematical modelling

4.2.1 Effective mass

In order to replicate the dynamic properties of the sloshing fluid, the mass included in a pendulum model is less than the total fluid mass (Dodge, 2000). For a rectangular tank this effective mass can be obtained by equating the force exerted by a pendulum and the potential flow solution, so that the effective mass for the n^{th} mode is given as

$$m_n = m\frac{8L\tanh\left((2n-1)\frac{\pi h}{L}\right)}{\pi^3(2n-1)^3 h} \tag{4.15}$$

Equation (4.15), which is based on liner potential flow, shows that for other than shallow filling levels, the mass associated with the first mode is dominant. When more complicated tank shapes are modelled and an analytical solution is not available, the effective sloshing mass can also be determined experimentally or with numerical simulation. This is carried out by exciting the sloshing tank with simple harmonic motion at a frequency substantially lower than the first resonant frequency and then stopping the sloshing tank (Sumner *et al.*, 1964; Dodge, 2000). The effective mass of the first resonant mode m_1 is then given as

$$m_1 = \frac{F_{\max}}{x_0}\left(\frac{1}{\omega^2} - \frac{1}{\omega_1^2}\right) \tag{4.16}$$

where $F_{\max}$ is the maximum force measured immediately after stopping the tank, ω the excitation frequency, ω_1 the first resonant frequency and x_0 the tank displacement amplitude. This procedure can be carried out using model tests or numerical simulation but it was found that this procedure is susceptible to numerical error.

4.2.2 External forces

The effect of gravity is included in the restoring force which is described in Section 4.1.1. Using an analogous approach, the pendulum can be subjected to forced motions by applying a translatory acceleration, which results in the forcing term

$$F_{ext} = mA(t)\cos(\theta) \tag{4.17}$$

where the periodic forcing $A(t)$ is given as

$$A(t) = -x_0\omega^2\sin(\omega t). \tag{4.18}$$

For existence of a solution $A(t)$ has to be continuous and bounded (Monteiro Marques, 1994) but there are no restrictions for non-periodic motion profiles.

Rotational motions complicate the modelling approach. Todd and Vohra (1998) investigated the response of a pendulum excited by rotational motions by moving the pendulum hinge according to the specified angular displacement. An alternative approach is the application of rotational excitations by moving the gravity vector using a moving frame of reference where the centre of rotation is taken at the fluid centre of mass in the quiescent condition. The velocity in a reference frame rotating about its origin can be related to an inertial frame with a coincident origin by

$$\langle \dot{x} \rangle_I = \langle \dot{x} \rangle_r + \Omega \times x \tag{4.19}$$

where $\langle \dot{x} \rangle_I$ is the velocity in the inertial frame, $\langle \dot{x} \rangle_r$ the velocity in the rotating frame, x the position vector and $\Omega(t)$ the rotational speed. The resulting acceleration is given as

$$\langle \ddot{x} \rangle_R = \langle \ddot{x} \rangle_I - 2\Omega \times \langle \dot{x} \rangle_R - \Omega \times (\Omega \times x) - \dot{\Omega} \times x. \tag{4.20}$$

There are three additional terms and these correspond to the Coriolis, Centripetal and Euler forces (Lanczos, 1986), given in Equation (4.21a)-(4.21c)

$$F_{CO} = -2m\Omega \times \langle \dot{x} \rangle_r \tag{4.21a}$$

$$F_{CE} = -m\Omega \times (\Omega \times r) \tag{4.21b}$$

$$F_E = -m\dot{\Omega} \times x \tag{4.21c}$$

4.2.3 Governing equations

The models in the preceding section are combined to give a governing equation for sloshing induced by translatory motions:

$$\dot{\theta}_1 = \theta_2 \tag{4.22a}$$

$$\dot{\theta}_2 = -\delta_3 \dot{\theta}_1^3 - \delta \dot{\theta}_1 + \frac{1}{l}\left[-gR(\theta_1) + A(t)\right] - F_{imp}, \tag{4.22b}$$

where $A(t)$ is the translatory acceleration applied to the tank, $R(\theta_1)$ restoring force and the impact model F_{imp} is given as

$$F_{imp} = a\left(\frac{\theta}{\theta_0}\right)^b + c\left(\frac{\theta}{\theta_0}\right)^{2d} \dot{\theta}_1^m \tag{4.23}$$

An analogous result can be obtained for rotational motions

$$\dot{\theta}_1 = \theta_2 \tag{4.24a}$$

$$\dot{\theta}_2 = -\delta_3 \dot{\theta}_1^3 - \delta \dot{\theta}_1 + \frac{1}{l}\left[-g\cos\left(\chi\left(t\right)\right)R\left(\theta_1\right) + g\sin\left(\chi\left(t\right)\right)\right] - F_{imp} + F_{Rot} \tag{4.24b}$$

where $\chi\left(t\right)$ is the angular displacement and F_{Rot} rotational forces given in Equation (4.21). A result for combined translatory and rotational excitations can be obtained using the Lagrangian and it is written as

$$\dot{\theta}_1 = \theta_2 \tag{4.25a}$$

$$\dot{\theta}_2 = -\delta_3 \dot{\theta}_1^3 - \delta \dot{\theta}_1 + \frac{1}{l}\left[g_y \sin\left(\theta_1\right) + g_x \cos\left(\theta_1\right)\right] - F_{imp} + F_{Rot} \tag{4.25b}$$

with

$$g_x = g\sin\left(\chi\left(t\right)\right) + A\left(t\right)\cos\left(\chi\left(t\right)\right) \tag{4.26}$$

and

$$g_y = -g\cos\left(\chi\left(t\right)\right)R\left(\theta_1\right) + A\left(t\right)\sin\left(\chi\left(t\right)\right) \tag{4.27}$$

Heave motions can be included with the introduction of a time-varying component in g.

4.2.4 Numerical solution of equations

The governing Equations (4.22), (4.24) and (4.25) are solved numerically using the ODE113 solution algorithm implemented in the software package MATLAB. ODE113 is a predictor-corrector Adams-Bashforth-Moulton method with adaptive time stepping (Mathworks, Inc, 2007) which was found to be the most suitable solution method. The Adams-Bashforth formula for the integration of ordinary differential equations of the form $\frac{dy}{dx} = f\left(x\right)$ is normally written as

$$y_{n+1} = y_n + h_{n+1} \sum_{i=1}^{k} \alpha_{k,i} f_{n+1-i} \tag{4.28}$$

where $h_{n+1}$is the spacing between the values y at points x_{n+1} and x_n and f_{n+1-i} is the evaluation of the function at point x_{n+1-i}. Introducing the variable $s = (t - x_n)/h$,

$$\alpha_{k,j} = \int_0^1 I_i\left(x_n + s h_{n+1}\right) ds \tag{4.29}$$

and the interpolation polynomial $I_i(x)$ is given as

$$I_i(x) = \prod_{\substack{j=1 \\ j \neq i}}^{k} \frac{x - x_{n+1-j}}{x_{n+1-i} - x_{n+1-j}} \tag{4.30}$$

The Adams-Bashforth method can be combined with the Adams-Moulton integration scheme (Shampine and Gordon, 1975) to give a predictor-corrector scheme. The predictor step p_{n+1} is the Adams-Bashforth method of order k as in Equation (4.28)

$$p_{n+1} = y_n + h \sum_{j=1}^{k} \alpha_{k,j} f\left(x_{n+1-j}, y_{n+1-j}\right) \tag{4.31}$$

and is then integrated in an Adams-Moulton expression of order $k+1$, which can be written as

$$y_{n+1} = y_n + h \sum_{j=1}^{k} \alpha^*_{k+1,j} f\left(x_{n+1-j}, y_{n+1-j}\right) + h\alpha^*_{k+1,0} f\left(x_{n+1}, p_{n+1}\right) \tag{4.32}$$

where

$$\alpha^*_{k,j} = \int_0^1 I^*_i\left(x_n + s h_{n+1}\right) ds \tag{4.33}$$

and the interpolation polynomial $I^*_i(x)$ is given as

$$I^*_i(x) = \prod_{\substack{j=1 \\ j \neq i}}^{k-1} \frac{x - x_{n+1-j}}{x_{n+1-i} - x_{n+1-j}} \tag{4.34}$$

The numerical implementation of this scheme is described by Shampine and Gordon (1975). The order of the method, which can be up to 13, and the integration step size are adapted to conform to user-specified error tolerances (Shampine and Gordon, 1975). In the present study, the error tolerances (Mathworks, Inc, 2007) are specified as $3 \cdot 10^{-6}$ for relative error and 10^{-8} for the absolute error compared to the machine accuracy of $2.2204 \cdot 10^{-16}$. During the tests it was found that there is no discernible difference between results obtained with the above error specification and a tighter error tolerance.

The suitability of the accuracy of the algorithm and error tolerance threshold are ascertained by subjecting two randomly selected cases to translatory excitation from the quiescent initial condition for 60 excitation periods (normal direction). The direction of time marching is then reversed and the result from the simulation in the normal direction is used as the initial condition (reversal). The first test with the numerical solution of Equation (4.22) is shown in Figure 4.11. Figure 4.11(a) shows the behaviour of the solution with an inadequate error tolerance of 10^{-3}, where due to numerical error the solution does not return to its initial condition upon reversal. When the error threshold is tightened to 10^{-8} the solution returns to its initial condition as depicted in Figure 4.11(b). The simulation in the normal direction and subsequent reversal are in good agreement despite a complicated response caused by choice of the excitation period.

In the second test shown in Figure 4.12, the excitation period is changed so that a higher amplitude response is caused and the fluid impact term in Equation (4.22) affects the solution. Satisfactory agreement is found between the solutions in the normal direction and the reversal throughout the solution time considered. However, there are some differences once the solution returns to its initial condition at $t = 0$, which were not observed in the previous test in Figure 4.11. These are attributed to the nonlinear terms in Equation (4.22) which are used to compute impacts.

The use of what is essentially a pendulum equation results in a mathematical sloshing model with good stability characteristics and a bounded solution. This equation is solved numerically using an Adams-Bashforth-Moulton scheme and it is shown that this scheme is sufficiently accurate. Simulation times are approximately 0.1% of real time on a desktop PC. Since the pendulum equation does not include mass or pendulum length in the numerical solution, the resonance characteristics are not affected by the numerical solution, making this approach suitable for long simulation times. The next chapter applies the Rapid Sloshing Model to a validation study with two different tank shapes with a filling ratio near the critical depth.

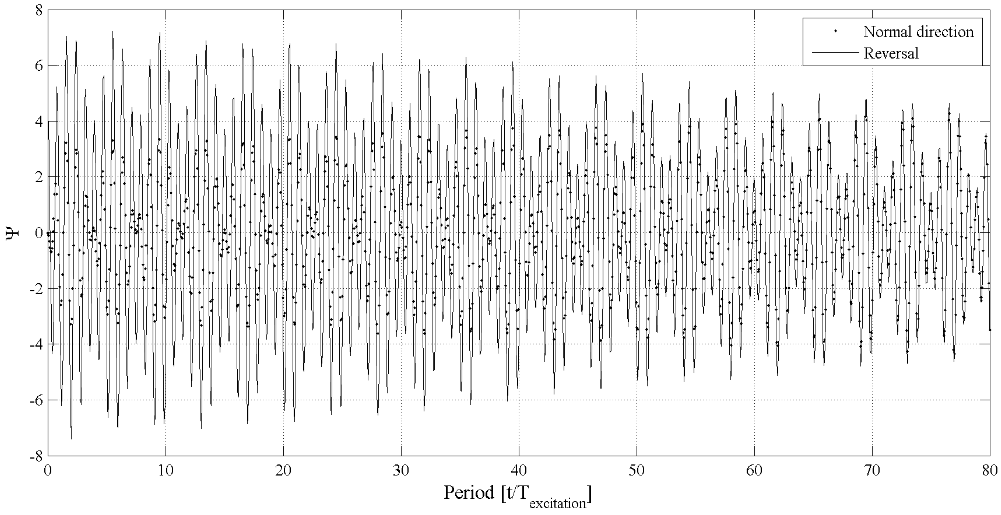

(a) Error tolerances are specified as $3 \cdot 10^{-3}$ for relative error and 10^{-3} for the absolute error. Reversing the solution in time results in unstable behaviour and the solution diverges.

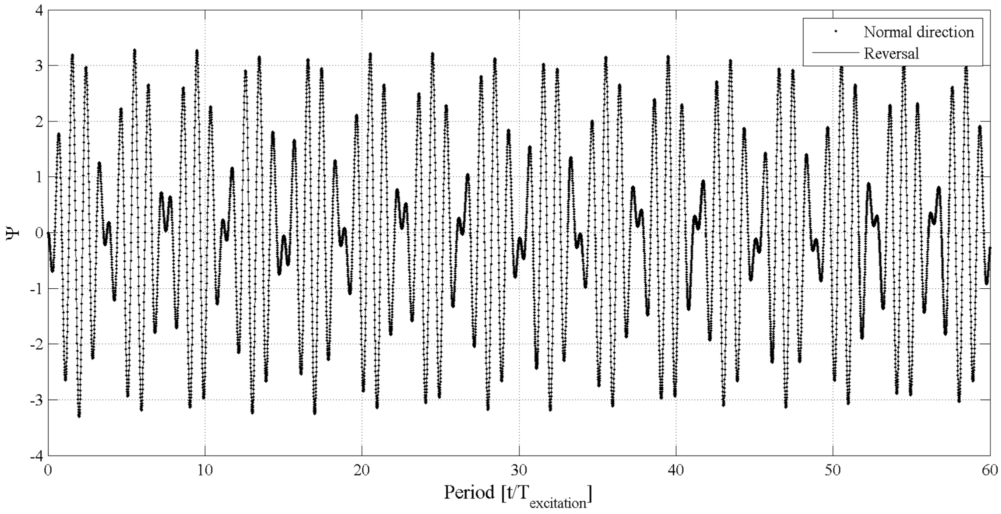

(b) Error tolerances are specified as $3 \cdot 10^{-6}$ for relative error and 10^{-8} for the absolute error. Reversing the solution in time leads back to the initial condition.

Figure 4.11: Test of the numerical solution algorithm by reversing the direction of solution. Excitation period $T = 1.25T_1$ and Ψ non-dimensionalised fluid momentum defined in Equation (5.4)

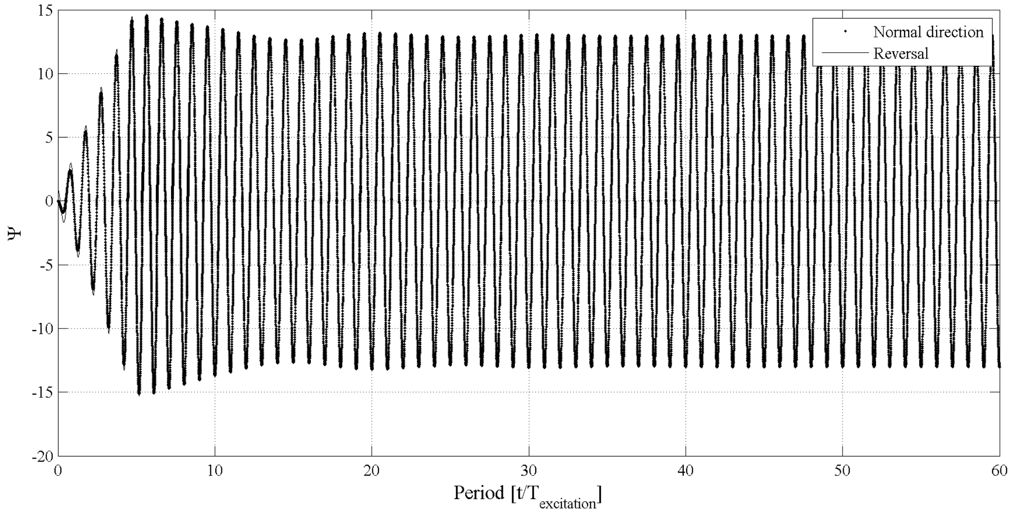

Figure 4.12: Test of the numerical solution algorithm by reversing the direction of solution. Excitation period $T = 1.00T_1$ and Ψ non-dimensionalised fluid momentum defined in Equation (5.4)

Chapter 5

Validation for sloshing near the critical depth

Although a tank will experience motions in all six degrees of freedom, the most critical motions for sloshing are roll, pitch, sway and surge (Lloyd's Register, 2005) and the largest sloshing loads tend to occur at filling level - tank length ratios (filling ratios) of $0.1 \leq h/L \leq 0.5$. (MacDonald and Maguire, 2008). The initial CFD analysis is normally undertaken by considering two dimensional sloshing motions of the longitudinal and transverse cross sections of the tank (Lloyd's Register, 2005).

This approach is adopted for the current sloshing investigation, where the sloshing characteristics of the longitudinal and transverse cross sections with a filling ratio of 0.3 and 0.4 respectively are investigated using the Rapid Sloshing Model. One CFD simulation of translatory sloshing is carried for a longitudinal and transverse membrane tank cross section using CFD with an excitation period, which was chosen for ease of simulation at 1.25 times the first resonant period to determine the imbalance force characteristics. The remaining coefficients are obtained from theoretical results and the impact model is set up using the data given in Chapter 4.

A systematic study of sloshing with increasingly realistic motion profiles is carried out in this chapter. The first stage uses periodic excitations for translatory motions in cross sections representing longitudinal and transverse LNG membrane containment systems. The excitation periods vary from $0.8T_1$ to $1.1T_1$ for the longitudinal case and the larges response is observed at resonance. The range of excitation periods for the transverse cross section is reduced to the range between $0.95T_1$ and $1.05T_1$ where the most significant sloshing response is expected. The transverse cross section is then subjected to rotational motions with a range of excitation periods between $0.95T_1$ and $1.25T_1$. The third stage considers an irregular motion profile which is obtained with an ITTC wave spectrum and

LNG carrier RAOs and variations in the motion amplitude and tank height are considered. The final stage of the systematic study uses simultaneous translatory and rotational motions where the translatory and rotational periods are not necessarily coincident.

5.1 Introduction

The longitudinal cross section for surge and pitch motions, shown in Figure 5.1, is sized to coincide with the experiments carried out by Hinatsu (2001). Figure 5.2 shows the transverse cross section of a typical membrane LNG tank with a scale factor of approximately $1/20^{\text{th}}$ and it is used for the simulation of sway and roll motions. In the first two stages of the sloshing case study, the excitation motions are periodic with the tank displacement x given as

$$x = x_0 \sin(\omega t), \tag{5.1}$$

where x_0 is the motion amplitude, $\omega = \frac{2\pi}{T}$ excitation frequency and t time. The filling levels are 60% of tank height in the longitudinal cross section and 57% of the tank height for the transverse cross section. This corresponds to a filling ratio h/L of 0.3 for the longitudinal cross section compared to the critical filling ratio of 0.3368.

The resonant sloshing periods of a rectangular tank can be calculated using Equation (2.3). For more complicated tank shapes such as the transverse cross section, the boundary element-based potential flow code FSIAP (Xing, 1992) is used to determine the resonant period. Table 5.1 summarises the key properties of the two sections.

Table 5.1: Properties of the longitudinal and transverse sections

	Longitudinal	Transverse
Filling ratio h/L	0.3	0.4
First resonant period T_1	1.474 s	1.736 s
Effective sloshing mass fraction m_1/m_{tot}	0.63	0.59

5.2 Longitudinal cross section

The sloshing model given by Equation (4.25) is validated by comparing its results for the sloshing flows identified in Section 3 with CFD results. These are independent of the corresponding solutions from the Rapid Sloshing Model . The comparisons between the sloshing model and CFD are quantified using the horizontal fluid momentum, given as

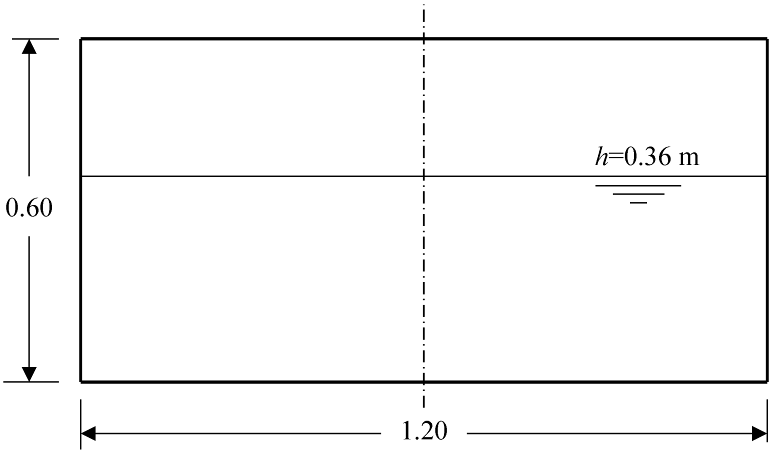

Figure 5.1: Longitudinal membrane tank cross-section (All dimensions in m)

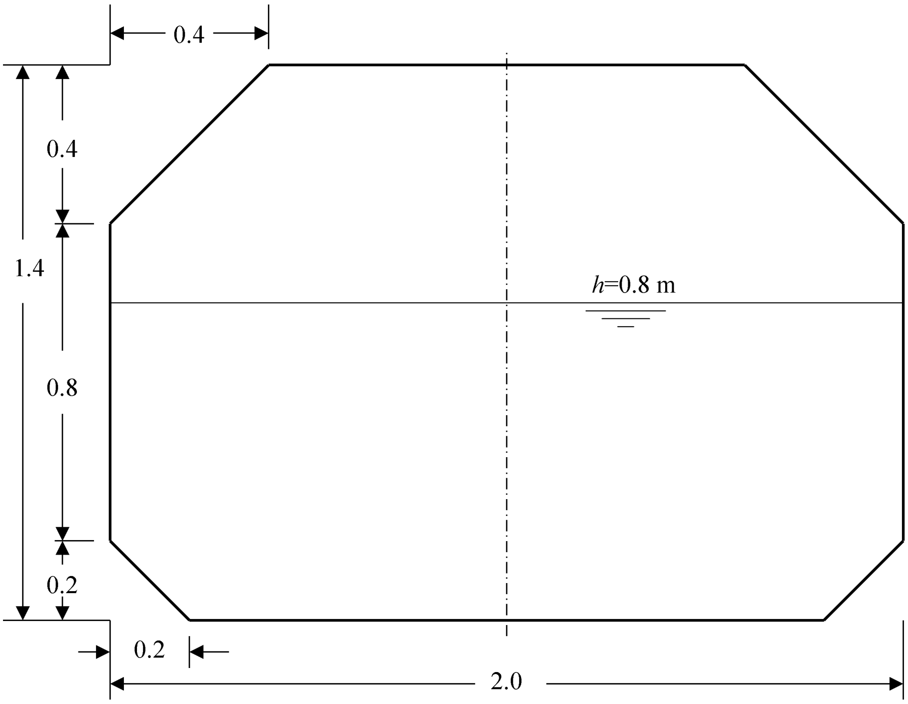

Figure 5.2: Transverse membrane tank cross-section (All dimensions in m)

$$P_{CFD} = \sum_i m_i u_i \tag{5.2}$$

for the CFD result, where m_i is the fluid mass and u_i fluid velocity in the i^{th} control volume. Horizontal fluid momentum is computed for the pendulum-based model as

$$P = l m_1 \dot{\theta} \cos(\theta) \tag{5.3}$$

where l is the pendulum length which is obtained using Equation (2.3), m_1 the effective sloshing mass defined in Section 5.1 and θ the displacement angle. The calculated fluid momentum data are normalized as follows

$$\Psi = \frac{P}{P_{rigid}}. \tag{5.4}$$

P_{rigid} is the momentum of the equivalent rigid body, given as

$$P_{rigid} = m_1 \dot{x} \tag{5.5}$$

where $\dot{x}$ is the velocity imposed on the tank by Equation (5.1). The difference between the two results is computed as

$$\Delta\Psi = \frac{P_{CFD} - P}{\max\left(P_{CFD}\right)} \tag{5.6}$$

and the mean difference for n time steps is defined as

$$\Delta\Psi_{mean} = \frac{1}{n}\sum_{i=1}^{n} \frac{\left|P_{CFD} - P\right|_i}{\max\left(P_{CFD}\right)}. \tag{5.7}$$

5.2.1 Surge

Table 5.2 summarises the settings for the Rapid Sloshing Model for the longitudinal cross section. The restoring force uses a third-order polynomial which was obtained by curve fit and this was carried out to confirm the applicability of the method to a restoring force which may not be adequately described with a periodic function such as $\sin\left(\theta\right)$.

Table 5.2: Rapid Sloshing Model settings for longitudinal cross section

Length	0.5397
Effective mass fraction	0.63
Linear damping coefficient	0.024
Third-order damping coefficient	0.044
Restoring force: function	$\alpha_1\theta + \alpha_2\theta\left|\theta\right| + \alpha_3\theta^3$
Restoring force: coefficients	$\alpha_1 = 1.0428$
	$\alpha_2 = -0.0583$
	$\alpha_3 = -0.1272$
Impact model: θ_0	16 deg
Impact model: force coefficients	$a = 0.025$
	$b = 15$
Impact model: damping coefficients	$c = 0.0005$
	$d = 24$

The longitudinal cross section is subjected to translatory motions in the first part of the sloshing case study. The excitation amplitude is 0.015 m for all surge cases and the excitation periods are $T = [0.80, 0.95, 1.00, 1.05, 1.10]\,T_1$. The result for the highest excitation frequency case with an excitation period $T = 0.80T_1$ is shown in Figure 5.3. A linear sloshing response is observed and there are no impacts at the tank top. There is a good match between the CFD result and the pendulum sloshing model, but there are some small differences during the troughs of the periodic beating. The mean error is 2.6% and the error peaks are between the beating phases.

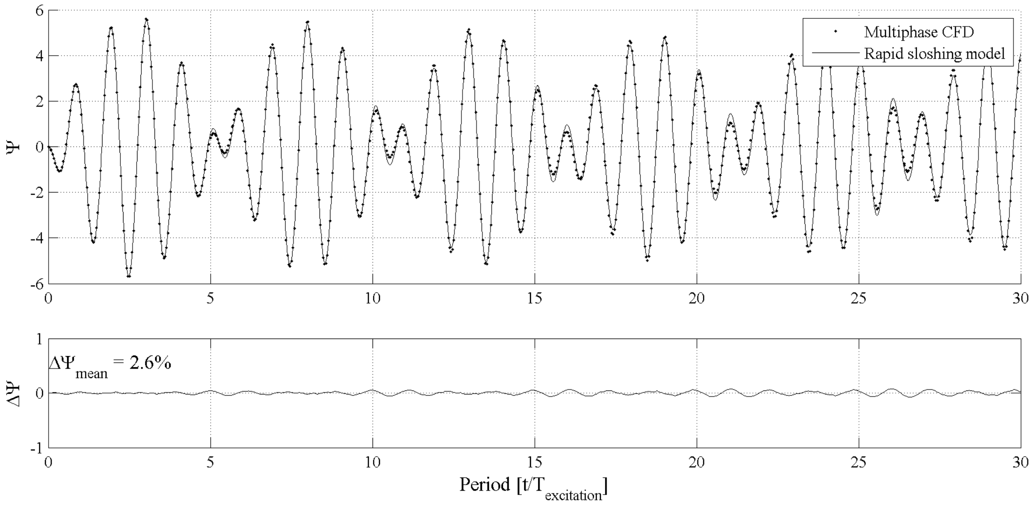

Figure 5.3: Comparison of Rapid Sloshing Model with CFD using normalised fluid momentum Ψ for regular surge with excitation period $T = 0.80T_1$

The second surge validation case, shown in Figure 5.4 uses an excitation period $T = 0.95T_1$. The sloshing response is weakly non-linear and there are impacts occurring between oscillations four and eight. The predictions match the CFD results with reasonable accuracy, but the mean error is 11%. The attenuation in the CFD result is caused by the fluid near the tank top wall interacting with the air and this is not included in the sloshing model. The mean error value is somewhat pessimistic as the Rapid Sloshing Model solution is slightly out of phase with the CFD solution.

The excitation period and sloshing resonance are coincident in the next validation case. The momentum histories are compared in Figure 5.5 and there is again good agreement between both results. The impacts against the tank ceiling continue throughout the duration of the simulation and the flow physics observed in the sloshing flow are captured by the impact model. The error stabilizes after about seven oscillations and the error envelope remains constant for the remainder of the simulation. The mean error of 5.8% is mostly due to the small phase difference between the two solutions.

The tank surge period is now increased to $T = 1.05T_1$ and the sloshing response is weakly nonlinear. There are no impacts at the tank ceiling but the CFD solution indicates that the interaction between the sloshing fluid and air near the tank ceiling affects the sloshing

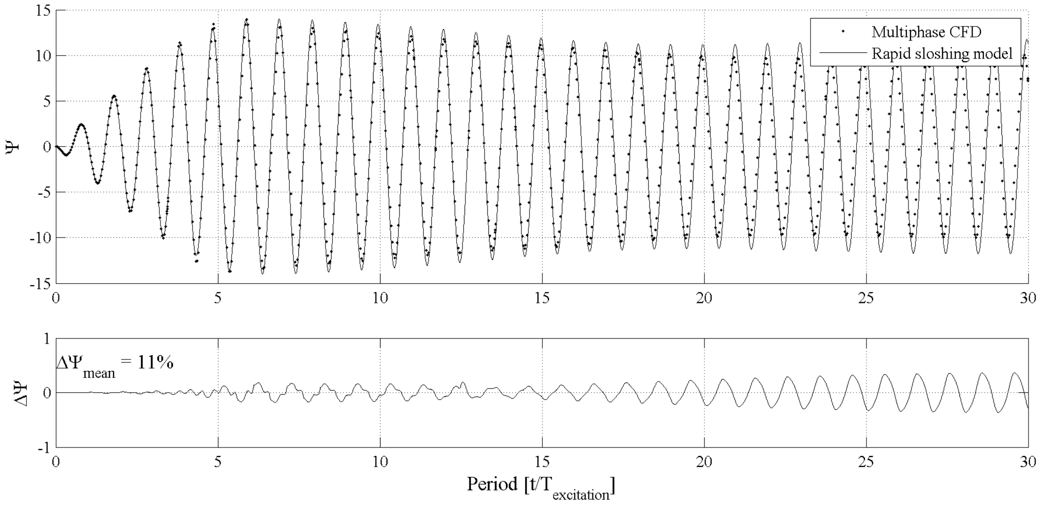

Figure 5.4: Comparison of Rapid Sloshing Model with CFD using normalised fluid momentum Ψ for regular surge with excitation period $T = 0.95T_1$

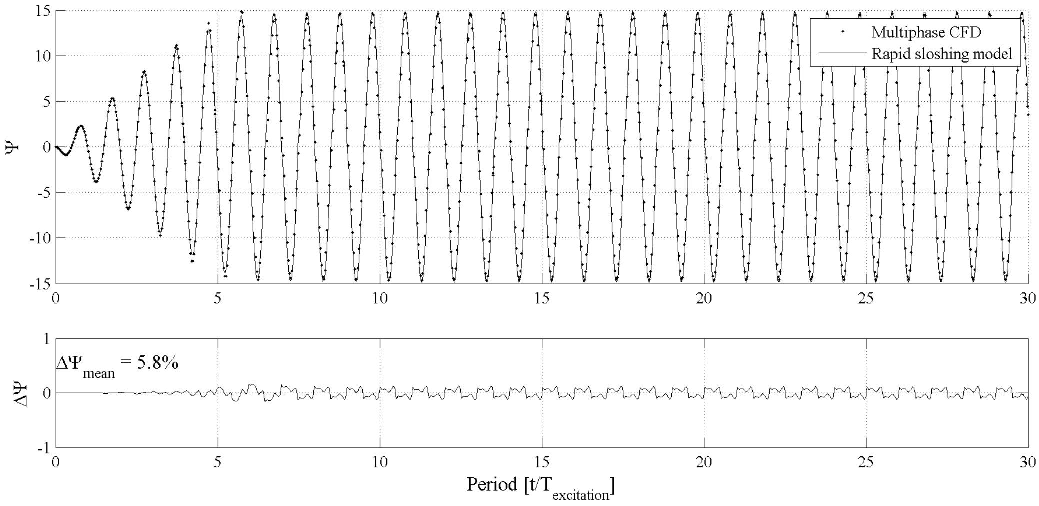

Figure 5.5: Comparison of Rapid Sloshing Model with CFD using normalised fluid momentum Ψ for regular surge with excitation period $T = 1.00T_1$

behaviour as in the case with $T = 0.95T_1$. Figure 5.6 compares Ψ obtained from the CFD simulation with the pendulum results. The peaks in the second beating phase predicted by the sloshing model are about 15% greater than those obtained using CFD and the overall mean error is 13%.

The final validation case for surge increases the excitation period to $T = 1.10T_1$. The CFD and sloshing model momentum histories are compared in Figure 5.7. The beating behaviour is well developed and is attenuated gradually. In this case, the CFD and sloshing model solutions show excellent agreement throughout the time frame considered and the mean difference of 2.4% is similar to that observed in Figure 5.3.

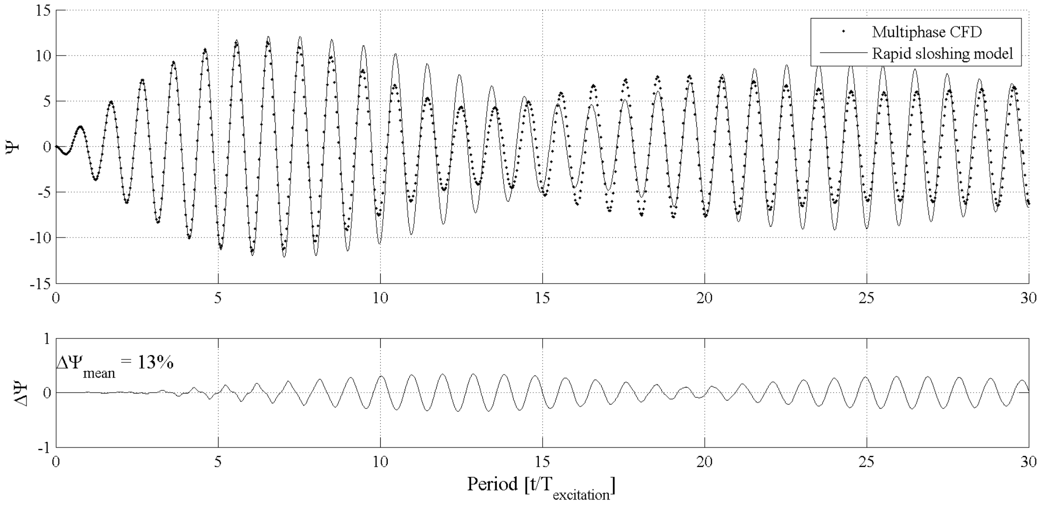

Figure 5.6: Comparison of Rapid Sloshing Model with CFD using normalised fluid momentum Ψ for regular surge with excitation period $T = 1.05T_1$

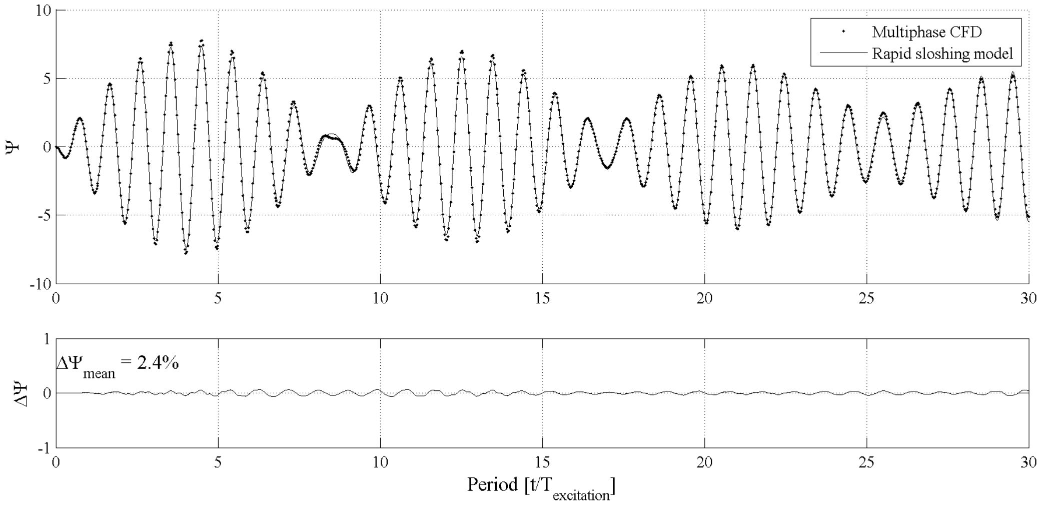

Figure 5.7: Comparison of Rapid Sloshing Model with CFD using normalised fluid momentum Ψ for regular surge with excitation period $T = 1.10T_1$

5.2.2 Analysis

A frequency domain analysis is carried out for the sloshing flows modelled in Figures 5.3 – 5.7 and the results are given in Figure 5.8. When the excitation period is located sufficiently far from resonance as is the case in Figures 5.8(a), 5.8(e) and also 5.8(f), two distinct peaks at the first resonance period and excitation period can be observed. In the surge simulation with $T = 0.95T_1$, shown in Figure 5.8(b), there is no separate peak at the excitation frequency and the spectrum is similar to that for the resonance case where the response peak coincident with the excitation period. In both cases, there is a distinct trough at the high-frequency side of the response peak and the low frequency side decreases gradually. For the sloshing flows with an excitation period of $T = 1.05T_1$ and $T = 1.10T_1$, shown in Figures 5.8(d) and 5.8(e) respectively, there is a double peak at the resonance period and excitation period. For the excitation period $T = 1.05T_1$ the trough between the two excitation peaks obtained with the Rapid Sloshing Model is not as deep as in the CFD solution and subsequent numerical experimentation has revealed that a mean error less than 5% can be obtained with slight modification to the restoring force function. The restoring force model was not optimised using multiple simulations because one of the objectives of the present investigation is the assesment of the Rapid Sloshing Model methodology with the least possible amount of prerequisite CFD data .

In all cases, there is good agreement in the low frequency range, which indicates the correct choice of damping coefficient and the high frequency behaviour up to approximately $0.5T_1$ is also well represented by the sloshing model. There are some differences in the case $T = 1.25T_1$, which was used to set up the model, shown in Figure 5.8(f). The magnitude of the response is several orders of magnitude less than in the other cases and errors are amplified in the frequency domain analysis. The time history, shown in Figure 4.5, shows excellent agreement with the CFD solution.

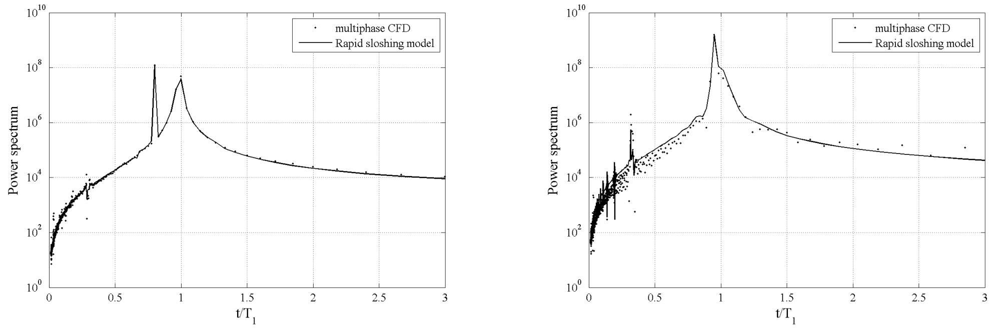

(a) $T = 0.80T_1$ (b) $T = 0.95T_1$

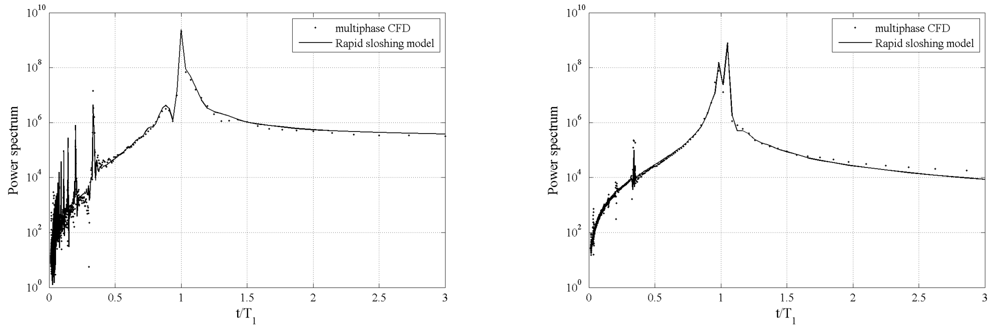

(c) $T = 1.00T_1$ (d) $T = 1.05T_1$

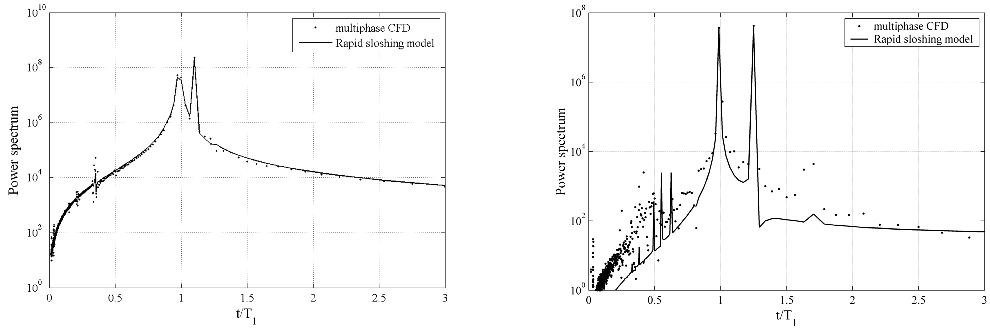

(e) $T = 1.10T_1$ (f) $T = 1.25T_1$

Figure 5.8: Comparison of power spectra for sloshing induced by regular surge

5.3 Transverse cross section

The second stage of the sloshing case study uses the transverse tank cross section in Figure 5.2. The excitation periods $T = [0.95, 1.00, 1.05, 1.25]\,T$ are located near the first resonant period to capture the most significant sloshing responses. The sloshing model is adapted to this tank geometry by applying the procedure in Chapter 4 to a CFD result obtained for sway with an excitation period $T = 1.25T_1$. Both sway and roll motions are used and the tank displacement amplitudes are 0.025 m and 2 deg, respectively. Table 5.3 summarises the settings for the Rapid Sloshing Model for the transverse cross section. The same impact model coefficients as in the previous sections are used but the imapct physics are expected differ between a rectangular and octagonal section.

Table 5.3: Rapid Sloshing Model settings for transverse cross section

Length	0.7487 m
Effective mass fraction	0.59
Linear damping coefficient	0.23
Third-order damping coefficient	0.79
Restoring force: function	$\sin \alpha\theta$
Restoring force: coefficients	$\alpha = 0.99$
Impact model: θ_0	16 deg
Impact model: force coefficients	$a = 0.025$
	$b = 15$
Impact model: damping coefficients	$c = 0.00025$
	$d = 24$

5.3.1 Sway

The results for sway are considered first and the result for $T = 0.95T_1$ is shown in Figure 5.9. It is interesting to note that the magnitude of Ψ is similar to that in the corresponding Figure 5.4 for surge. During the initial transient there are impacts at the upper hopper and, to a lesser extent, the top wall, but these cease after about 15 oscillations. The sloshing model overestimates the steady-state CFD result for Ψ, but the transient behaviour is well predicted and the mean error of 11% is comparable to the corresponding case for surge. The error envelope remains constant after the initial transient phase and the difference in the results obtained can be attributed to the impact model.

The tank is excited at resonance in the second sway validation case, which is shown in Figure 5.10. Impacts occur throughout this simulation and the sloshing model replicates this behaviour with good accuracy. The difference between the two results is constant after about 10 oscillations and the mean error is 6.3%.

The final sway test case is with an excitation period $T = 1.05T_1$ and the resulting fluid momentum plot is shown in Figure 5.11. The initial transient region is well captured

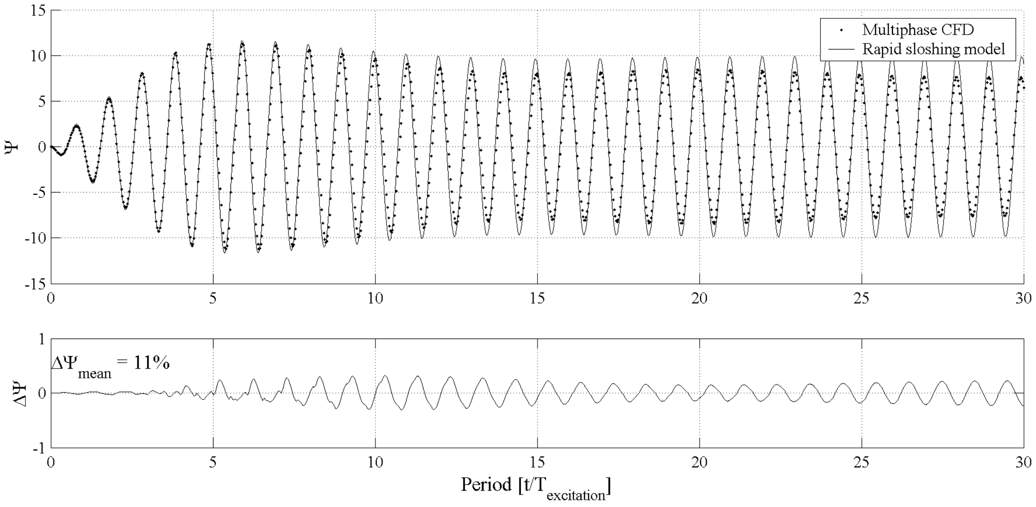

Figure 5.9: Comparison of Rapid Sloshing Model with CFD using normalised fluid momentum Ψ for regular sway with excitation period $T = 0.95T_1$

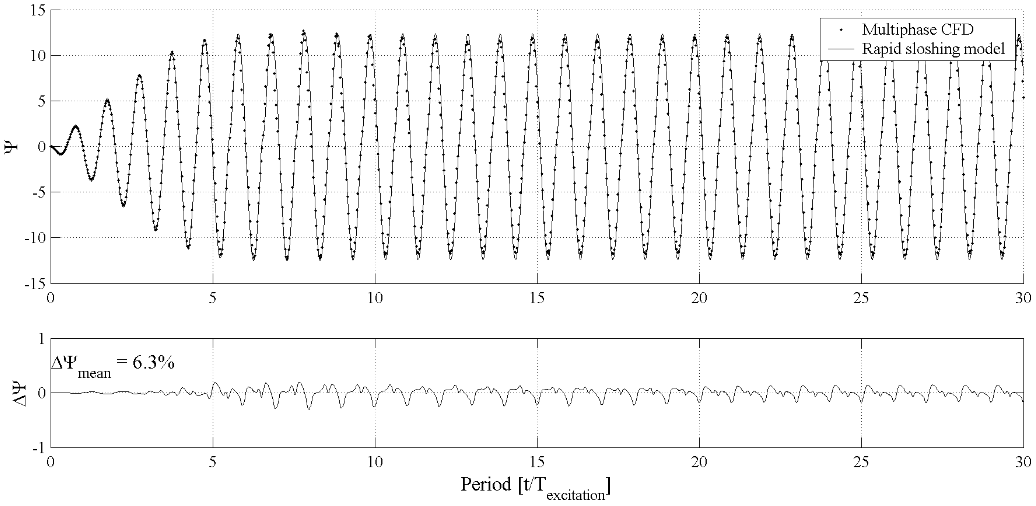

Figure 5.10: Comparison of Rapid Sloshing Model with CFD using normalised fluid momentum Ψ for regular sway with excitation period $T = 1.00T_1$

with the rapid sloshing model and although there are discernable differences as the flow approaches a steady state, the mean error for the time frame investigated is 5.4%.

5.3.2 Roll

The next set of validation cases is roll-induced sloshing. The roll centre of motion is defined at the centre of area of the cross section which requires the use of the two-degree of freedom motion model in Equation (4.25) to move the roll centre to the initial fluid centre of mass. The contribution of the sway component caused by shifting the centre of rotation to the quiescent fluid centre of mass is not found to be particularly significant but

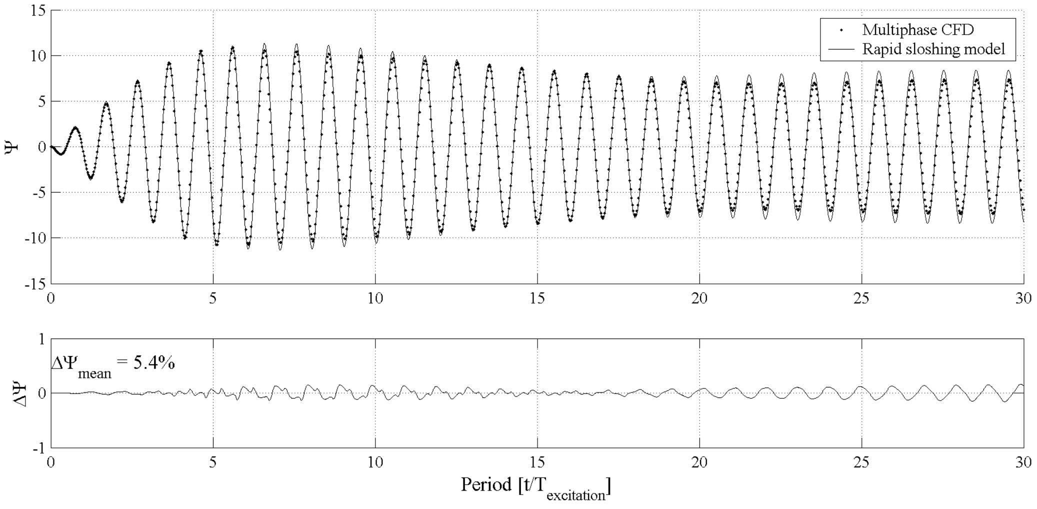

Figure 5.11: Comparison of Rapid Sloshing Model with CFD using normalised fluid momentum Ψ for regular sway with excitation period $T = 1.05T_1$

when it is neglected a different motion history is obtained for low frequency excitations. All model parameters are kept the same as in the sway induced sloshing simulations in the previous section.

The first test uses an excitation period $T = 0.95T_1$ and the fluid momentum is shown in Figure 5.12. There are some discernible differences between the CFD solution and sloshing model in the initial transient region where the CFD solution is leading the sloshing model. This does not continue into the steady state region and the mean error of 12% is comparable to values observed with sway induced sloshing simulations discussed previously.

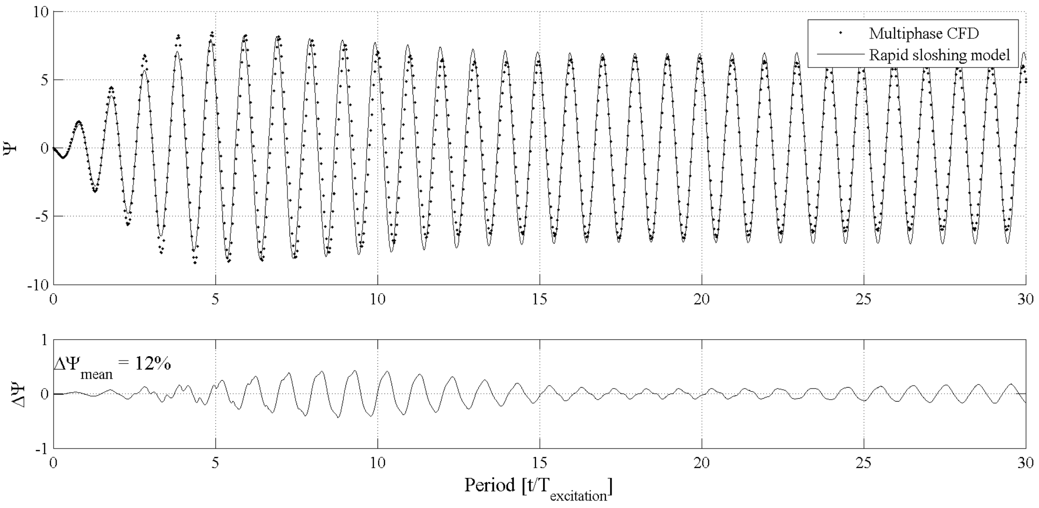

Figure 5.12: Comparison of Rapid Sloshing Model with CFD using normalised fluid momentum Ψ for regular roll with excitation period $T = 0.95T_1$

The second test, shown in Figure 5.13, excites the sloshing tank at resonance and fluid impacts occur throughout the simulation. Figure 5.14 shows three snapshots of the CFD solution, where Figure 5.14(a) depicts the first impact against the vertical side wall. There are still small quantities of fluid from the previous impact coalescing with the main bulk of fluid. In Figure 5.14(b) the flow has progressed past the second impact at the upper hopper and is moving towards the third impact at the corner between the upper hopper and the tank ceiling. The post-impact flow field is shown in Figure 5.14(c). It is reversing its direction and there is some fluid fragmentation at the tank top. The mean difference of 24% is a pessimistic prediction as the main source of error is the small phase difference between the Rapid Sloshing Model and CFD solutions.

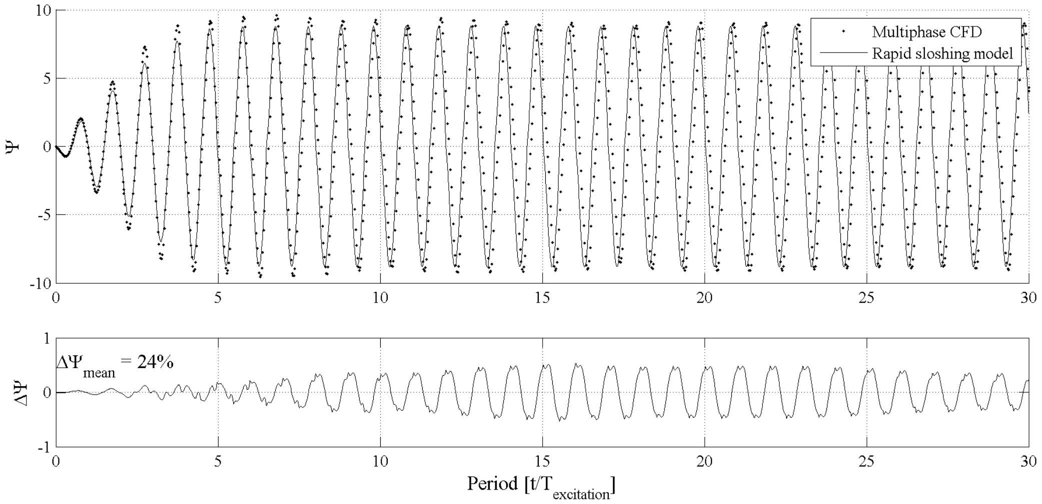

Figure 5.13: Comparison of Rapid Sloshing Model with CFD using normalised fluid momentum Ψ for regular roll with excitation period $T = 1.00T_1$

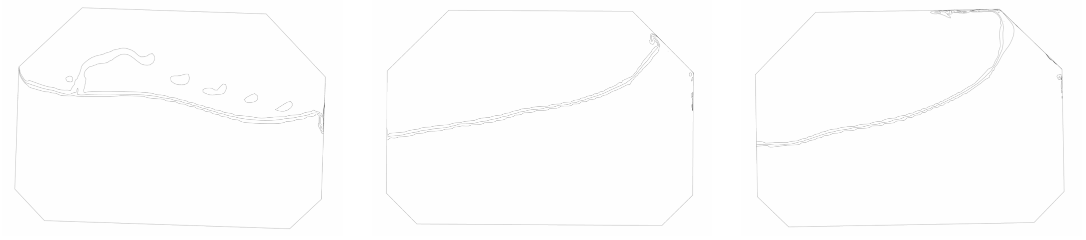

(a) First impact against side wall (b) Second impact at hopper (c) Third impact at top wall

Figure 5.14: Volume fraction contours of $r_{water} = 0.05$, 0.50 and 0.95 for transverse tank section subjected to roll motion with excitation period $T = 1.00T_1$

The next example in Figure 5.15 uses the larger excitation period $T = 1.05T_1$ and there is more significant disagreement between the CFD result and the sloshing model. While the two solutions remain in phase, the transition between the start-up transient and the steady state flow field is not as well predicted as in the previous cases. This may be attributable to the fluid impact, where the three separate phases of fluid impact are not adequately represented with a single potential function.

The excitation period is increased further to $T = 1.25T_1$ for the final roll test. In this case, the non-periodic behaviour seen previously with surge is observed in Figure 5.16 as well. The momentum history obtained from the Rapid Sloshing Model shows generally good agreement with the CFD model and the error remains constant during the duration of the simulations. There are some differences in the flow evolution between the beating peaks and the mean error is 5.5%.

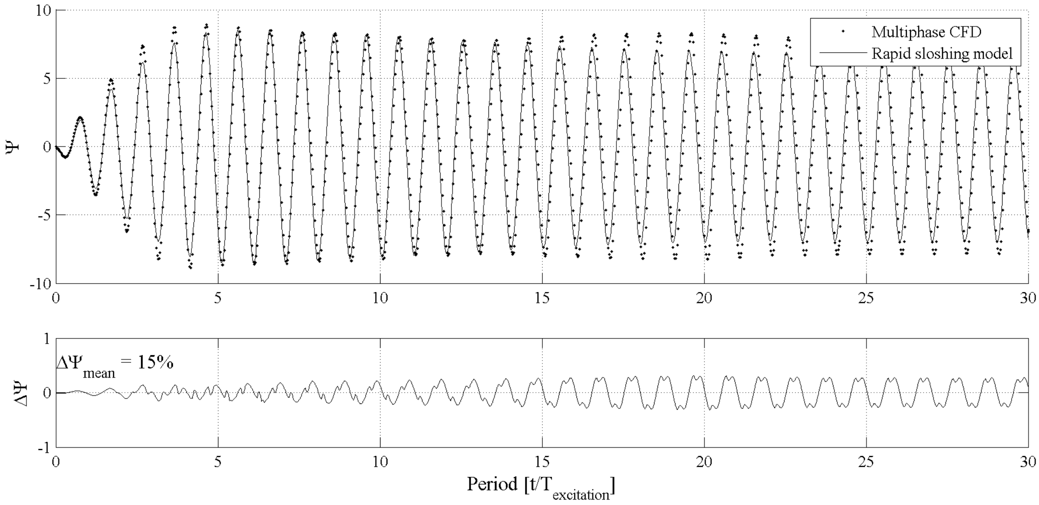

Figure 5.15: Comparison of Rapid Sloshing Model with CFD using normalised fluid momentum Ψ for regular roll with excitation period $T = 1.05T_1$

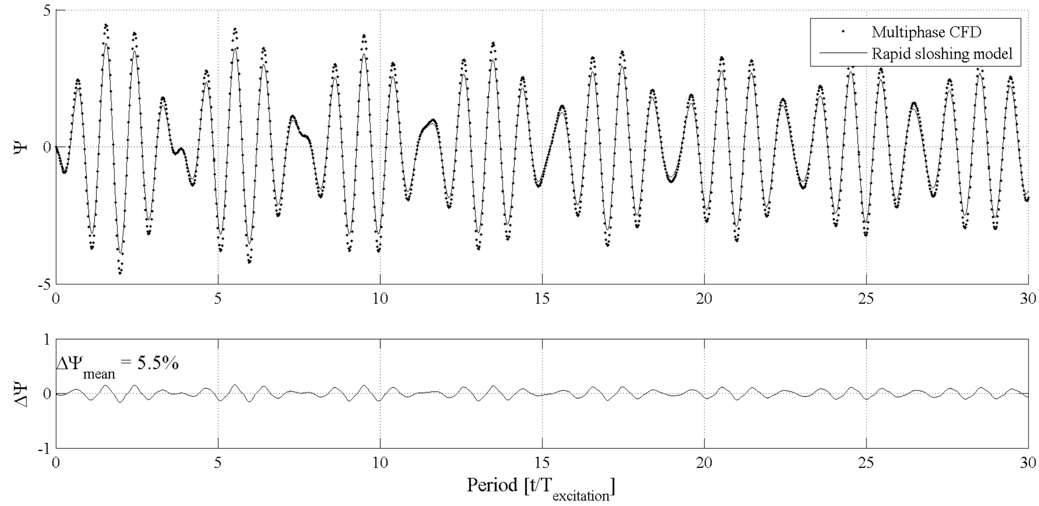

Figure 5.16: Comparison of Rapid Sloshing Model with CFD using normalised fluid momentum Ψ for regular roll with excitation period $T = 1.25T_1$

5.3.3 Analysis

Figures 5.17 and 5.18 show the frequency domain analysis for the sloshing cases in the transverse cross section. In the sway cases the dominant peak is located at the excitation period, with a secondary peak at resonance. This peak is well defined in Figure 5.17(d), but in Figures 5.17(a) and 5.17(c) there is no separate peak at the resonant frequency. The Rapid Sloshing Model solution predicts the knuckle in Figure 5.17(a), but there are differences at resonance in Figure 5.17(c). The value and location of the peak in the spectrum is well predicted by the Rapid Sloshing Model solution in all four cases considered and the solutions from the CFD and the sloshing model show good agreement in the low frequency range.

The results for roll in Figure 5.18 are similar, with a dominant peak at the excitation frequency and secondary peaks at resonance. There is good agreement between Rapid Sloshing Model and CFD in the spectrum in Figure 5.18(a) with the peak at the excitation frequency and knuckle at resonance well predicted by the Rapid Sloshing Model . A similar result is observed in Figure 5.18(b) where the peak is at resonance. A secondary peak at $T = 0.4T_1$ is also reasonably well predicted with the Rapid Sloshing Model solution and the low frequency behaviour of the Rapid Sloshing Model solution matches that of the CFD solution. Although the response peak is well predicted in all four roll validation cases, the Rapid Sloshing Model and CFD solutions in Figure 5.18(c) show more substantial differences in the low frequency region. Better agreement and two distinct response peaks are observed in Figure 5.18(d) and the low frequency behaviour of the Rapid Sloshing Model solution is in good agreement with CFD.

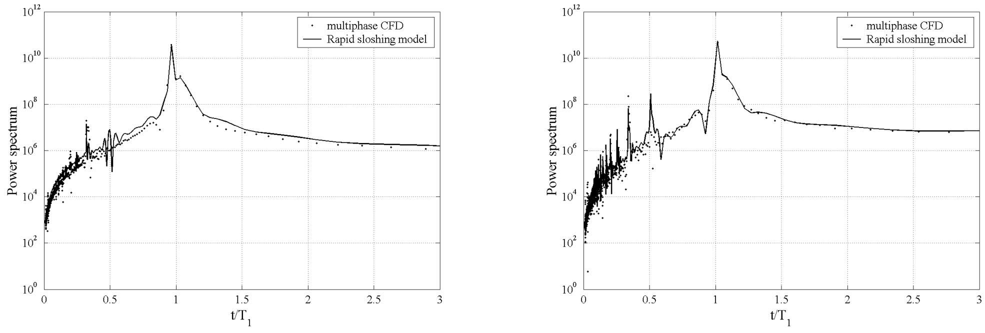

(a) $T = 0.95T_1$ (b) $T = 1.00T_1$

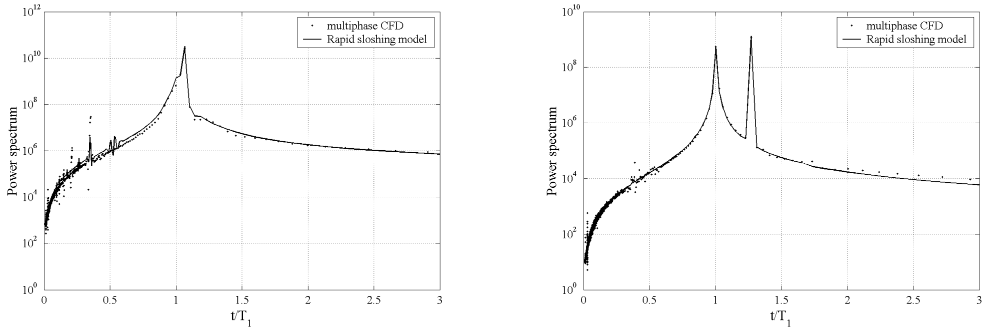

(c) $T = 1.05T_1$ (d) $T = 1.25T_1$

Figure 5.17: Comparison of power spectra for sloshing induced by regular sway

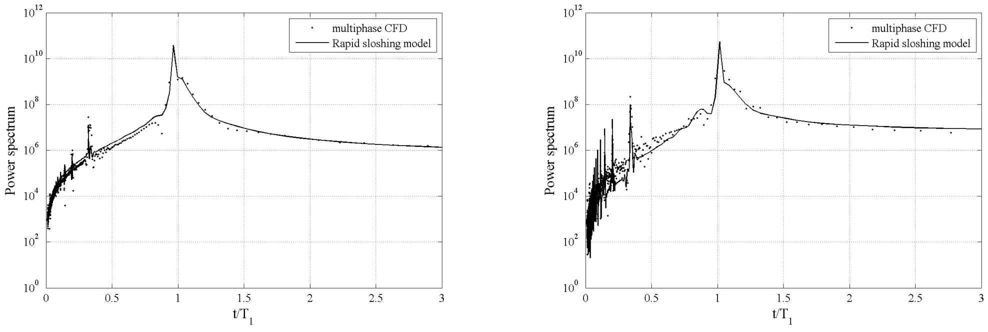

(a) $T = 0.95T_1$ (b) $T = 1.00T_1$

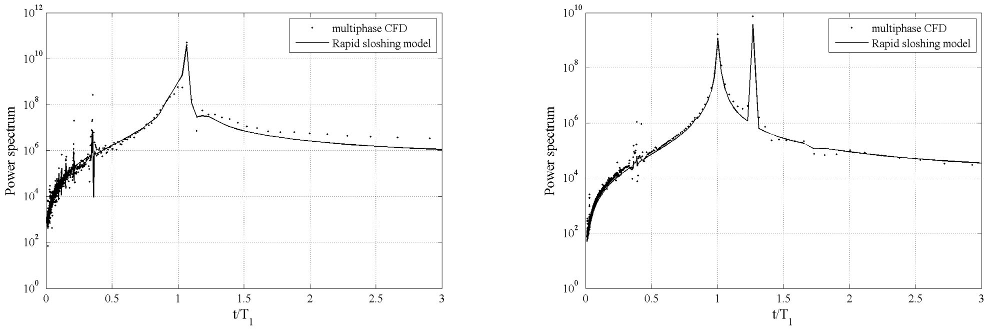

(c) $T = 1.05T_1$ (d) $T = 1.25T_1$

Figure 5.18: Comparison of power spectra for sloshing induced by regular roll

5.4 Irregular motions

The two previous validation stages for surge, sway and roll motions have all assumed that the excitation motion is periodic. This type of motion regime cannot be expected from a real ship and the third stage of the sloshing case study investigates the response of the Rapid Sloshing Model to an irregular surge motion profile[1]. The motion profile is obtained using a standard ITTC two-parameter wave spectrum (Faltinsen, 1993), which can be written as

$$\frac{S(\omega)}{H_{1/3}^2 T_I} = \frac{0.11}{2\pi}\left(\frac{\omega T_I}{2\pi}\right)^{-5} \exp\left(-0.44\left(\frac{\omega T_I}{2\pi}\right)^{-4}\right) \tag{5.8}$$

where the significant wave height $H_{1/3}$ is 6 m, the wave period T_I is 10 s and ω is wave frequency. The relationship between the j^{th} frequency component and the corresponding wave elevation A_j is given as

$$A_j^2 = 2S(\omega_j)\,\Delta\omega \tag{5.9}$$

where $\Delta\omega$ is the constant difference between successive frequencies (Faltinsen, 1993). The resulting wave elevation is then given as

$$\sigma = \sum_{j=1}^{N} A_j \sin(\omega_j t - k_j x + \epsilon_j) \tag{5.10}$$

where k_j is the j^{th} wave number, x is a location along the direction of wave propagation and ϵ_j is a random phase angle with a uniform distribution between 0 and 2π. This wave spectrum is selected because it is a broad band spectrum compared to other sea spectra. The resulting vessel acceleration profile is determined using ship-specific Response Amplitude Operators and scaling laws (Lloyd, 1989) and the power spectrum of the motion profile obtained is shown in Figure 5.19. The second and third resonant sloshing periods, given by Equation (2.3) as $T_2 = 0.62T_1$ and $T_3 = 0.50T_1$, are also in the range of excited motion frequencies. The simulation time is 200 s which corresponds to approximately 35 min on a typical LNG carrier.

The first test (case A) is the direct application of the motion profile obtained from Equation (5.10) to the longitundinal tank cross-section using the pendulum sloshing model settings from surge in Section 5.2.1. Figure 5.20(a) shows that for case A there is good agreement between the CFD solution and the Rapid Sloshing Model . The mean error of 4.3% is similar to those observed with periodic surge motions. The areas with more significant

---

[1] The cases considered in this section are identified by upper-case Latin characters

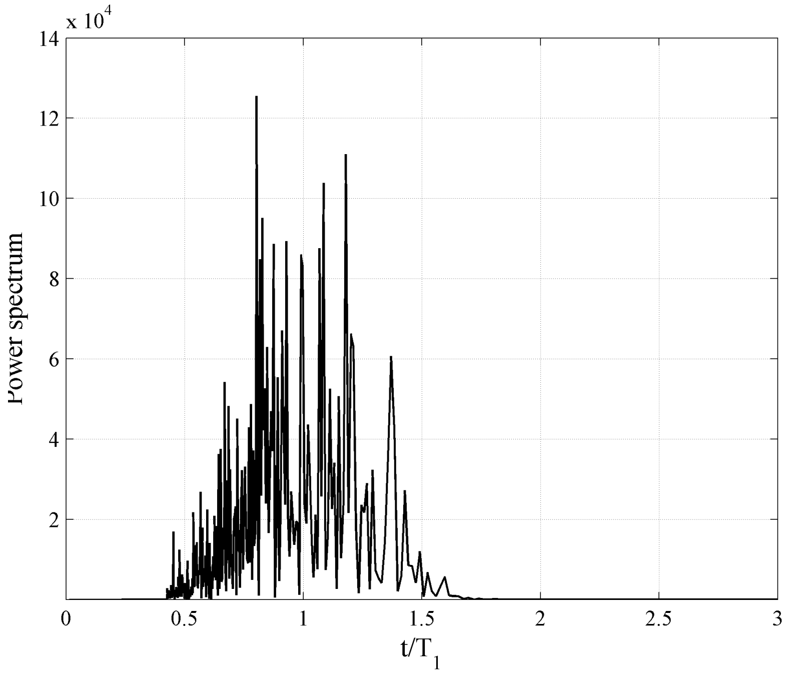

Figure 5.19: Power spectrum of the surge acceleration profile applied to the tank. The first, second and third resonant frequencies are excited.

differences around 20 s, between 90 s and 110 s and the last 20 s of the simulation are enlarged in Figure 5.20(b). After the motion is initiated the CFD and sloshing model solutions are coincident until the onset of the first impacts at about 20 s. There are small differences between the two solutions after the impacts, but the sloshing model and CFD solution soon regain agreement. Near the mid-point of the simulation at 100 s the momentum predicted by the sloshing model is about 15% greater than the CFD solution. Towards the end of the simulation where there is a non-periodic sloshing response, the two solutions are again in good agreement.

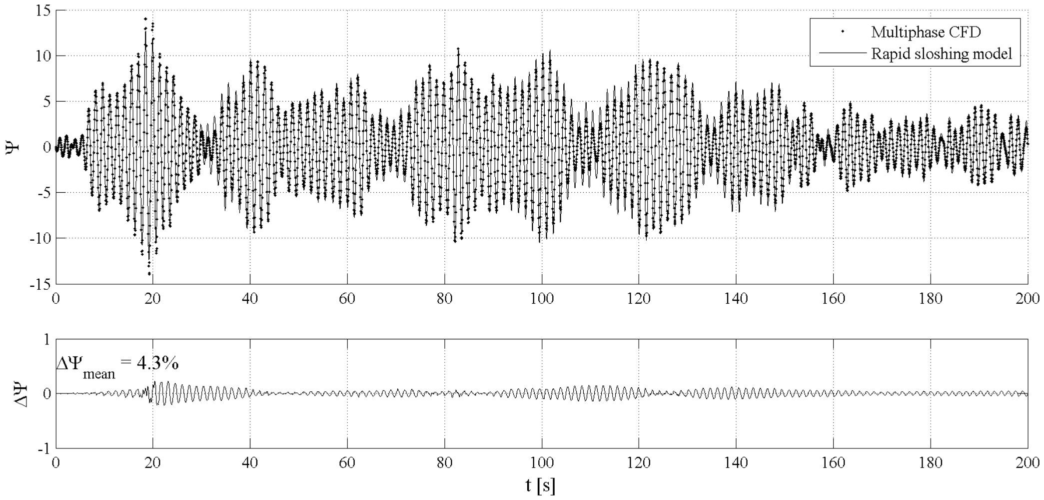

(a) full simulation

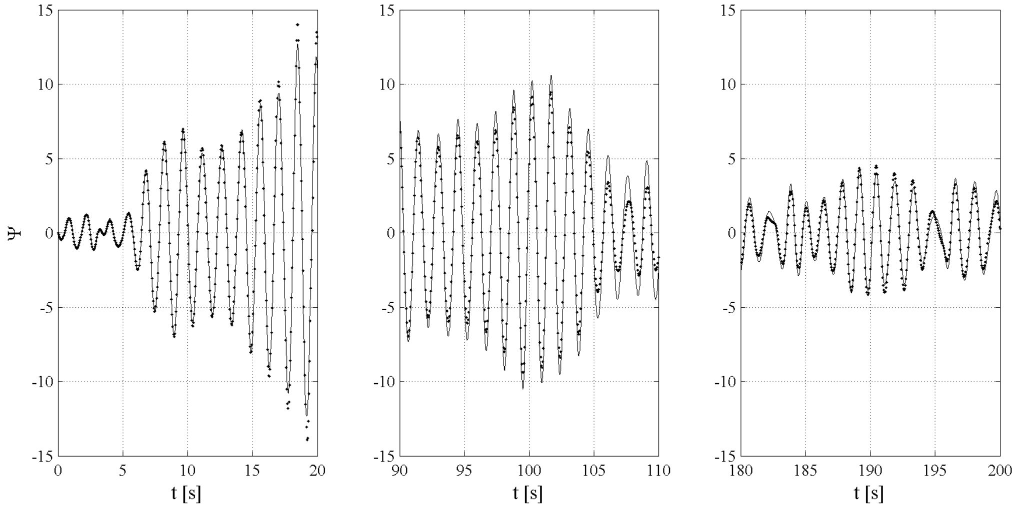

(b) zoom on regions of interest

Figure 5.20: Comparison of Rapid Sloshing Model with CFD using normalised fluid momentum Ψ for irregular surge (case A)

The second case B investigates the effect of the top wall impact on the sloshing response by increasing the tank height to 1.2 m. The resulting momentum history is shown in Figure 5.21, with a similar level of agreement as in the previous case. Although the mean error has increased to 7.2% in this case it is evenly distributed throughout the simulation. The three snapshots highlighted in the previous case are also examined in greater detail and the first momentum peak at 20 s is well predicted by the sloshing model. The CFD and Rapid Sloshing Model data for the subsequent flow evolution near 100 s show excellent agreement, but there are some more pronounced differences toward the end of the simulation at 180 s.

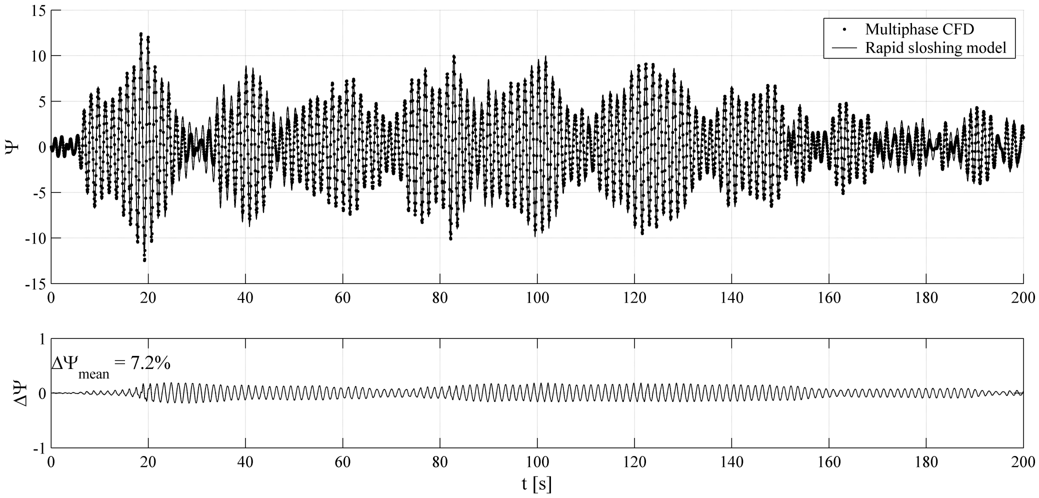

(a) full simulation

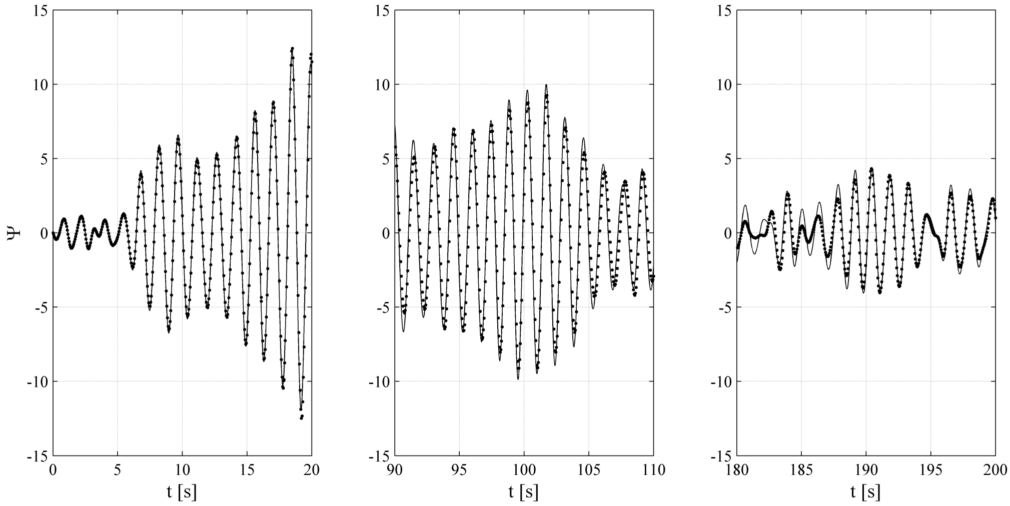

(b) zoom on regions of interest

Figure 5.21: Comparison of Rapid Sloshing Model with CFD using normalised fluid momentum Ψ for irregular surge with raised tank ceiling (case B)

The motion profile in case B is also applied to a conventional pendulum sloshing model with a $\sin(\theta)$ and a linearised $\sin(\theta) \approx \theta$ restoring force term (Dodge, 2000) and a linear damping coefficient. Figure 5.22 shows the effect of using the Rapid Sloshing Model approach adopted in this paper as neither pendulum model can capture the sloshing behaviour after the first 10 s. The momentum predicted by the conventional pendulum models usually exceeds the CFD results but there is a phase between 35 and 45 s where the pendulum models underestimate the momentum by about 75%. The linearised pendulum equation results in a slightly larger mean error of 64% compared to the 50% error with the conventional pendulum equation.

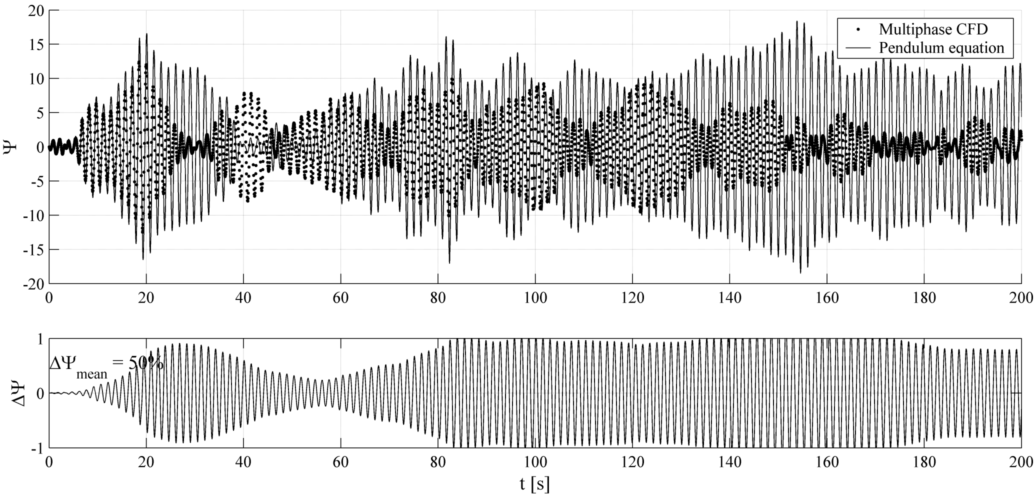

(a) pendulum equation with $\sin(\theta)$

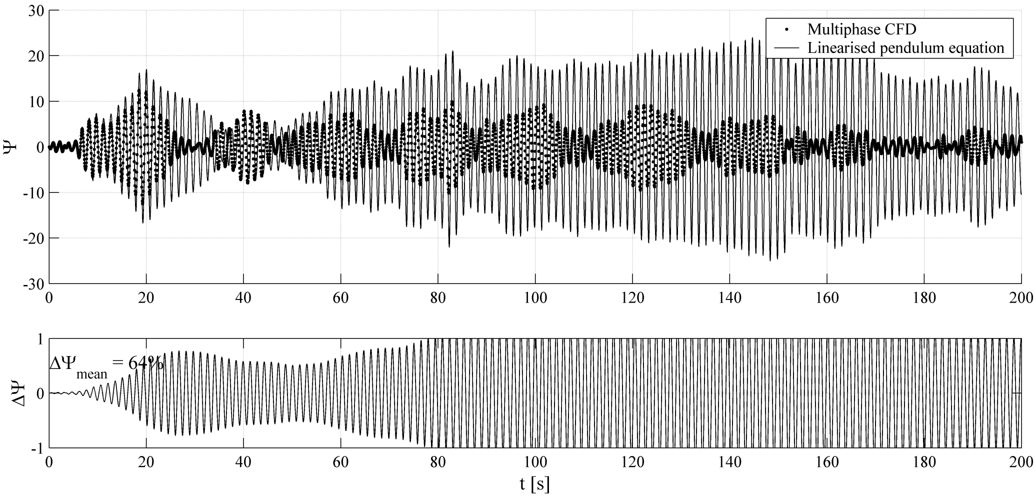

(b) linearised pendulum equation

Figure 5.22: Comparison of normalised fluid momentum Ψ for case B with conventional pendulum models

The final validation case C with irregular tank motions introduces a more severe motion regime by using the same time series as in the previous two cases and increasing the acceleration magnitude four-fold. This produces greater nonlinearities in the sloshing response throughout the 200 s considered and the results, obtained using the 1.2 m high tank used previously, are shown in Figure 5.23. The peak magnitude of Ψ has doubled and a comparison of the two plots in Figures 5.21 and 5.23 illustrates some of the complexities of sloshing.

The maximum momentum occurs between 10 s and 20 s as in the previous case, but the transition is sharper and the Rapid Sloshing Model has some difficulties in replicating this behaviour. After about 25 s, there is again good agreement between the two methods and the next peak phase between 35 s and 45 s is well predicted with the Rapid Sloshing Model . After about 80 s there is a significant peak in the momentum and the rapid sloshing model and CFD solutions show good agreement in the snapshot between 90 s and 110 s. There is a substantial spike at about 155 s compared to the gradual decrease observed in Figure 5.21 at the same time which underlines the nonlinearities in a sloshing flow and its sensitivity to history effects. In the final 20 s of that simulation, there is again agreement between the CFD solution and the Rapid Sloshing Model. The mean error of 8.3% is, despite the substantial increase in motion amplitude, similar to that observed in other simulation.

Case C is also simulated using the conventional and linearised pendulum equations and the results are shown in Figure 5.24. After about 10 s, both pendulum models fail to replicate the sloshing behaviour and the absence of an impact model results in further differences. The linearised pendulum equation generally overpredicts the fluid momentum and its mean error of 77% is only slightly larger than the 70% observed with a conventional pendulum equation. This suggests that the key influence on the sloshing response is the restoring force model rather than its linearization.

The frequency domain analysis of the sloshing response obtained with irregular surge motion is shown in Figure 5.25. The spectra for case A in Figures 5.25(a)–5.25(b) and case B in Figures 5.25(c)–5.25(d) are similar, with a well-defined peak at the first resonant frequency. When the excitation amplitude is increased, the response peak is broader but the shape of this spectrum in Figure 5.25(e)–5.25(f) is comparable to the two previous cases. The solution was computed in fast time and most of the computational effort was expended interpolating the motion profile on the time steps used for the numerical solution of the differential equations.

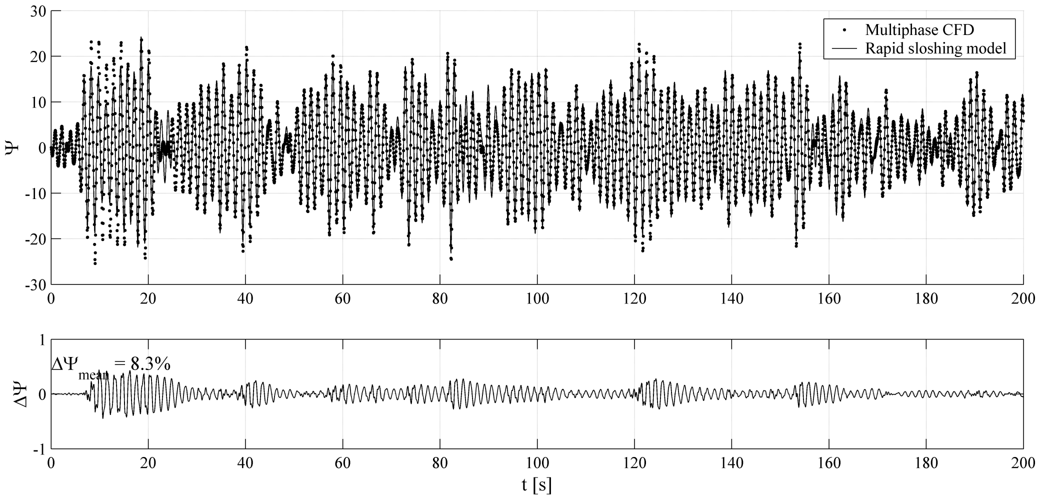

(a) full simulation

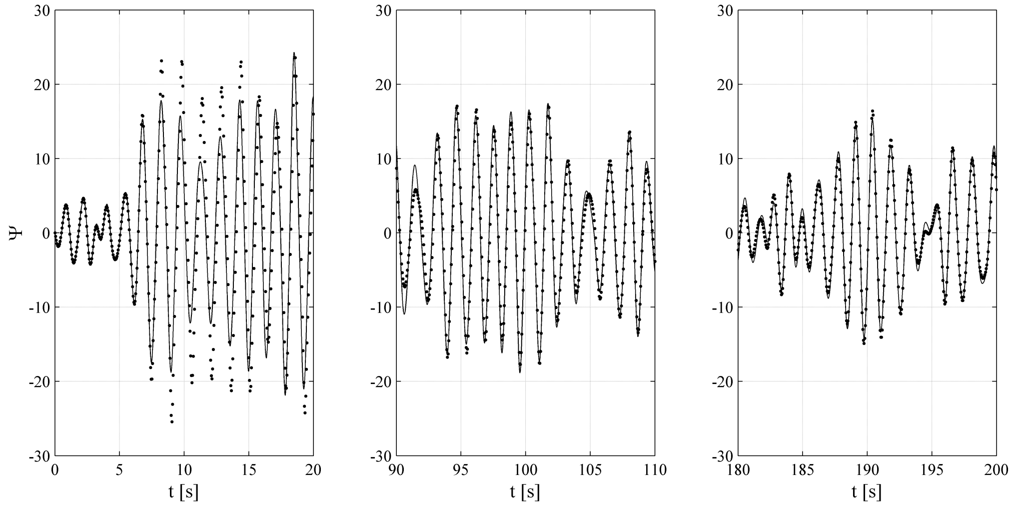

(b) zoom on regions of interest

Figure 5.23: Comparison of Rapid Sloshing Model with CFD using normalised fluid momentum Ψ for irregular surge with raised tank ceiling and quadrupled acceleration amplitude (case C)

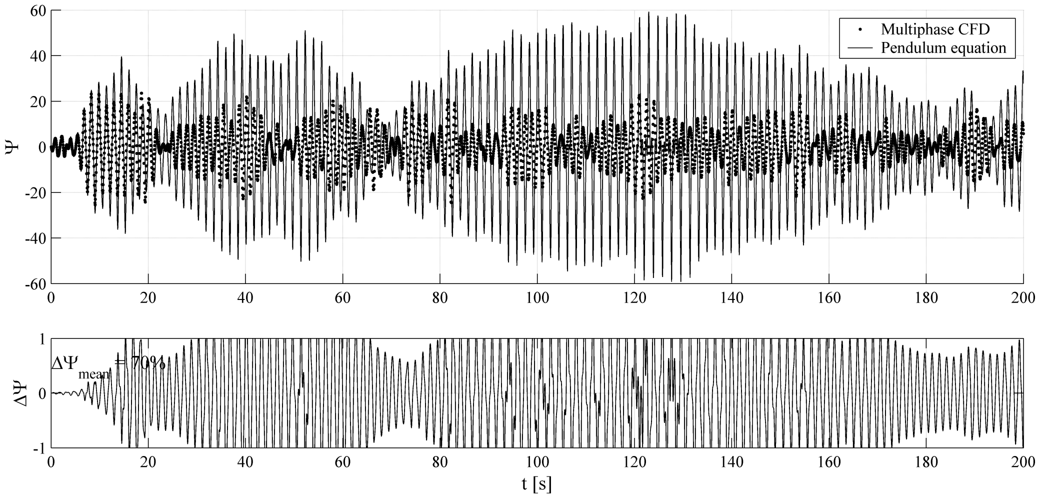

(a) pendulum equation with $\sin(\theta)$

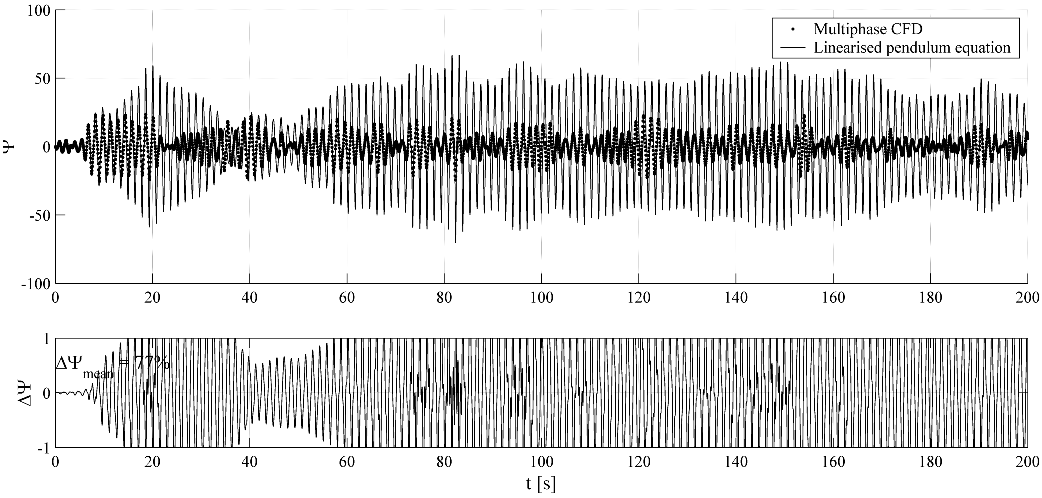

(b) linearised pendulum equation

Figure 5.24: Comparison of normalised fluid momentum Ψ for case C with conventional pendulum models

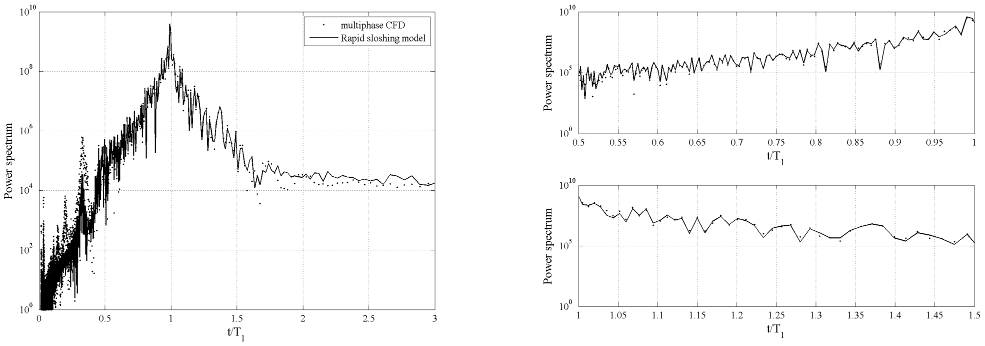

(a) Case A: full spectrum (b) Case A: zoom near resonance

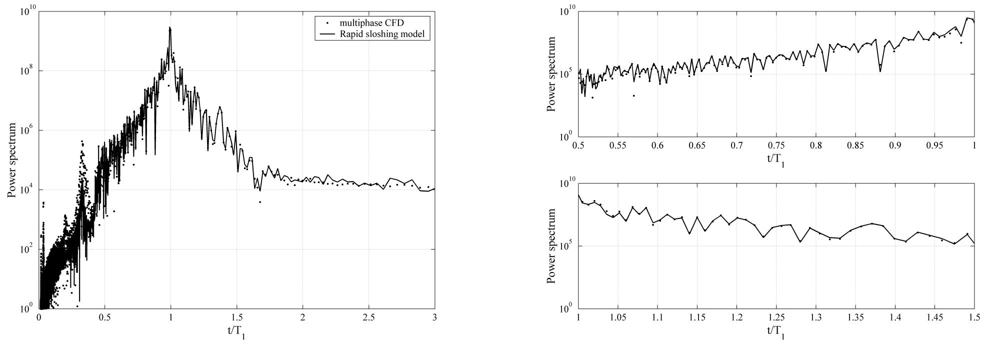

(c) Case B: full spectrum (d) Case B: zoom near resonance

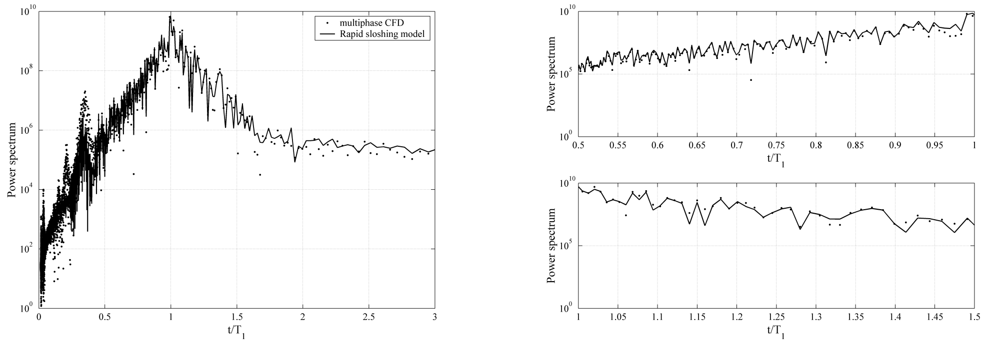

(e) Case C: full spectrum (f) Case C: zoom near resonance

Figure 5.25: Frequency domain analysis of the sloshing response for irregular surge (case A-C)

The momentum histories obtained with the Rapid Sloshing Model shown in Figures 5.20 – 5.23 are used to obtain the dynamic sloshing force using the relation

$$F_D = \frac{d}{dt}\left(P\right), \tag{5.11}$$

where F_D is the dynamic force. The time derivative of momentum was calculated numerically using the GRADIENT function in MATLAB (Mathworks, Inc, 2007) and a second order central difference scheme. The dynamic force is non-dimensionalised using the initial free surface height such that

$$\mathrm{Non-dimensional\ force} = \frac{F_D}{\rho g h b}, \tag{5.12}$$

where b is tank width, g gravity, h filling height and ρ density. The corresponding values for F_D were obtained from the CFD simulation by integration of the dynamic pressure on the tank walls.

Figure 5.26 compares the non-dimensional dynamic force for case A and there is agreement between the CFD and the Rapid Sloshing Model solutions. The mean error has increased from 4.3% to 7.5% which is mainly attributable to disagreements between 100 and 120 s as shown in Figure 5.26(b). The dynamic force in the initial transient phase with impacts is predicted with good accuracy using the Rapid Sloshing Model and Figure 5.26(a) shows that the two solutions remain in phase throughout the 200 s time frame considered.

The non-dimensional dynamic force for case B is shown in Figure 5.27. The CFD and Rapid Sloshing Model solutions are in good agreement and the mean error of 8.3% for the momentum-based comparison in Figure 5.21 is similar to the 9.6% observed using the dynamic force calculation. The peaks in the first 20 s of the simulation are reproduced with the Rapid Sloshing Model but the Rapid Sloshing Model overpredicts the force in the region between 100 and 120 s as shwon in Figure 5.27(b).

The final comparison with the dynamic sloshing force is made using case C where the motion amplitude is increased four-fold and the comparison between the CFD and Rapid Sloshing Model solutions is shown in Figure 5.28. In this case there are more significant differences between the CFD and Rapid Sloshing Model solutions in the initial 20 s and the mean error has increased to 13% compared to 8.3% in the momentum-based comparison. The force predictions from the Rapid Sloshing Model do not reproduce the peaks between 10 s and 20 s and the peaks at 122 s are missed. Otherwise the CFD and Rapid Sloshing Model solutions are in good agreement when using the dynamic force as a basis for comparison.

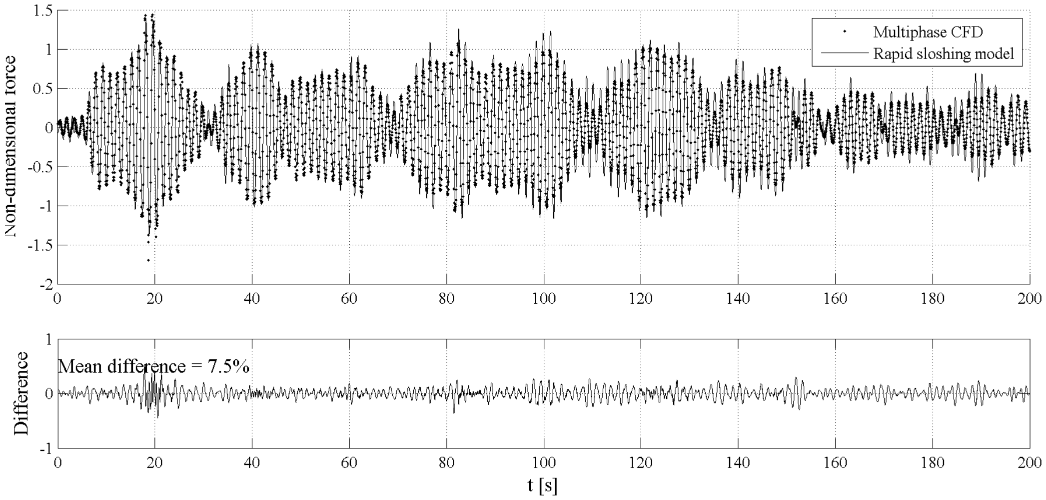

(a) full simulation

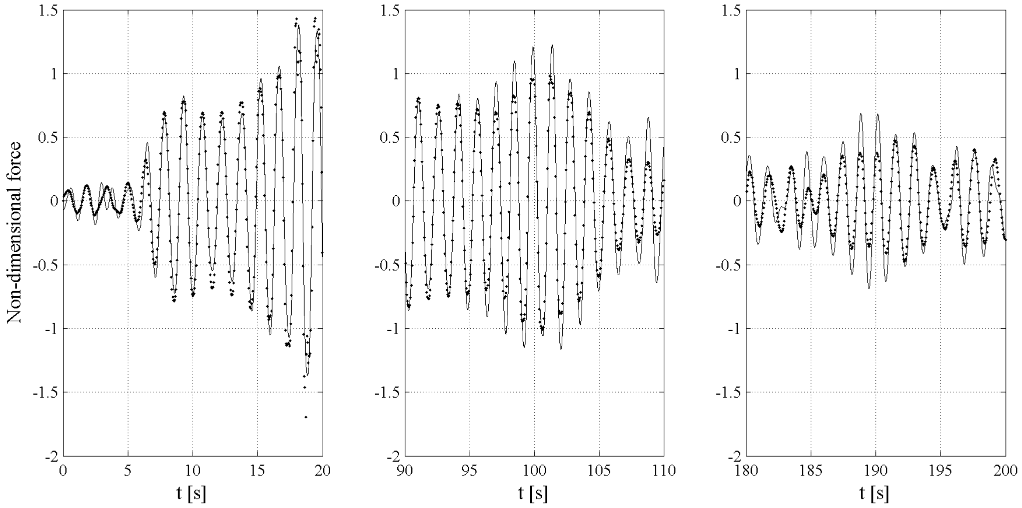

(b) zoom on regions of interest

Figure 5.26: Comparison of Rapid Sloshing Model with CFD using normalised sloshing force on tank for irregular surge (case A)

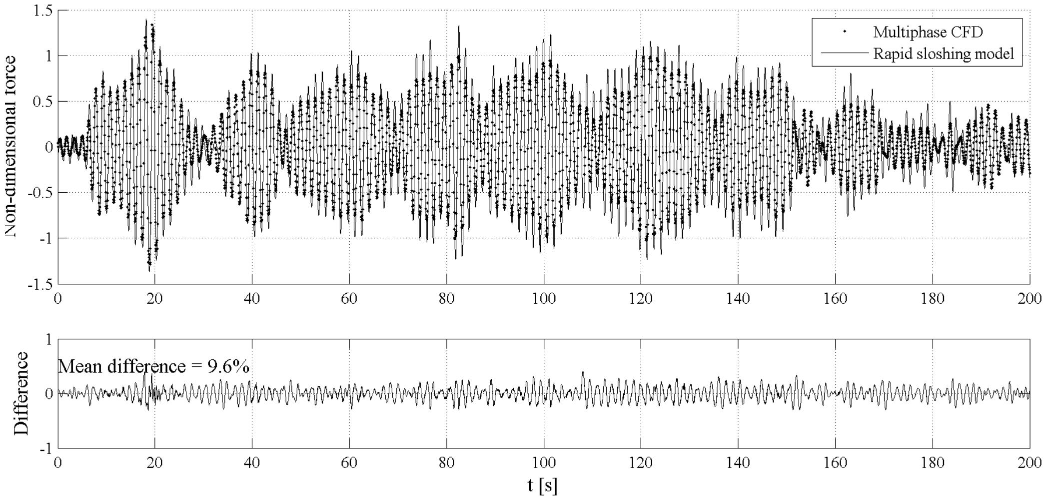

(a) full simulation

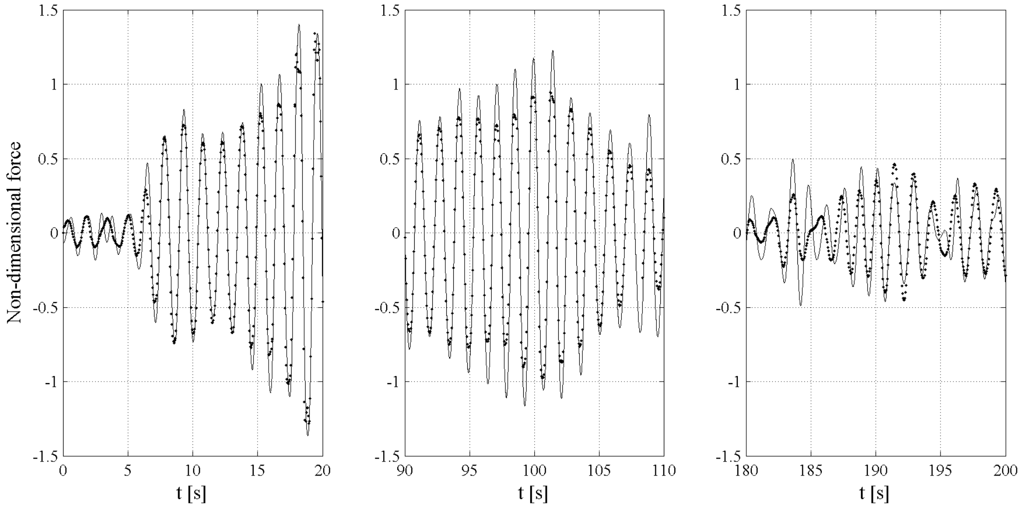

(b) zoom on regions of interest

Figure 5.27: Comparison of Rapid Sloshing Model with CFD using normalised sloshing force on tank for irregular surge with raised tank ceiling (case B)

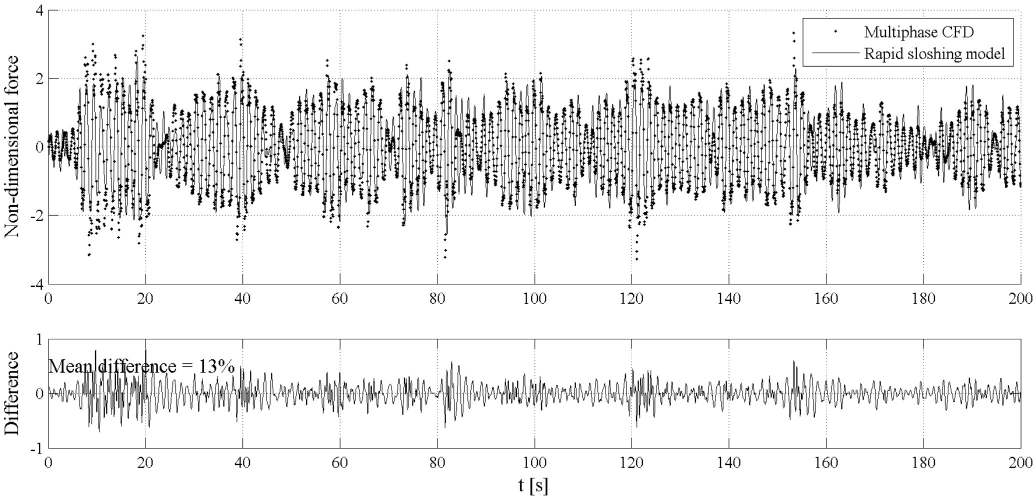

(a) full simulation

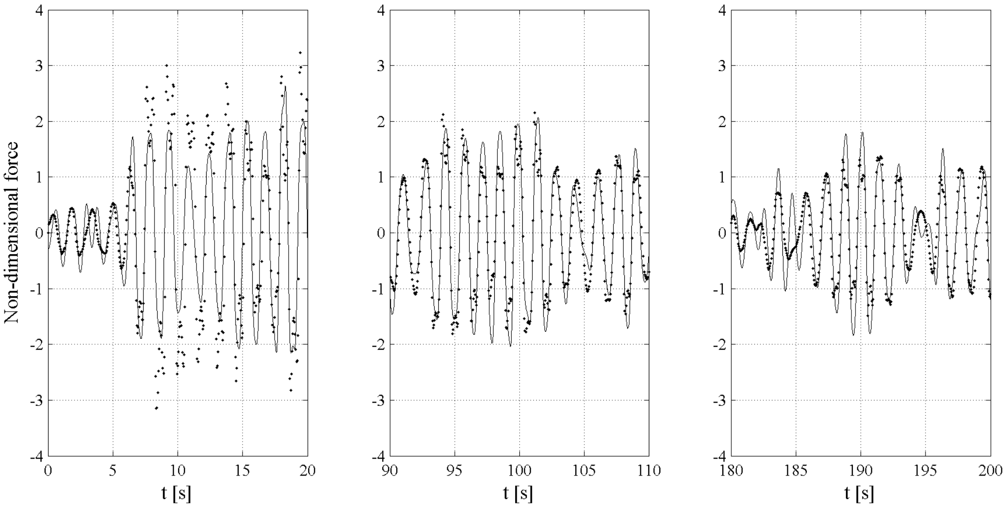

(b) zoom on regions of interest

Figure 5.28: Comparison of Rapid Sloshing Model with CFD using normalised sloshing force on tank for irregular surge with raised tank ceiling (case C)

5.5 Combined tank motions

The final stage of the sloshing case study is the simulation of sloshing caused by the simultaneous surge and pitch motion of the tank[2]. The two-degree of freedom model in Equation (4.25) was used in Section 5.3.2, but the sloshing response was dominated by the roll motion. In this section, four motion profiles with surge and pitch displacement amplitudes similar to previous cases are imposed on the tank. The centre of rotation is at the centre of area of the tank as in the corresponding experiment by Hinatsu (2001). The sloshing model settings are the same as in the surge validation study in Section 5.2.1.

In case a, shown in Figure 5.29, the excitation motion is at resonance and the surge and pitch amplitudes are 0.015 m and 2 deg, respectively. There are fluid impacts after the first three oscillations and the impacts continue for the entire simulation. There is good agreement between the CFD solution and sloshing model throughout the duration of the simulation and the difference remains constant. The mean error of 7% is comparable to other cases considered in this sloshing case study.

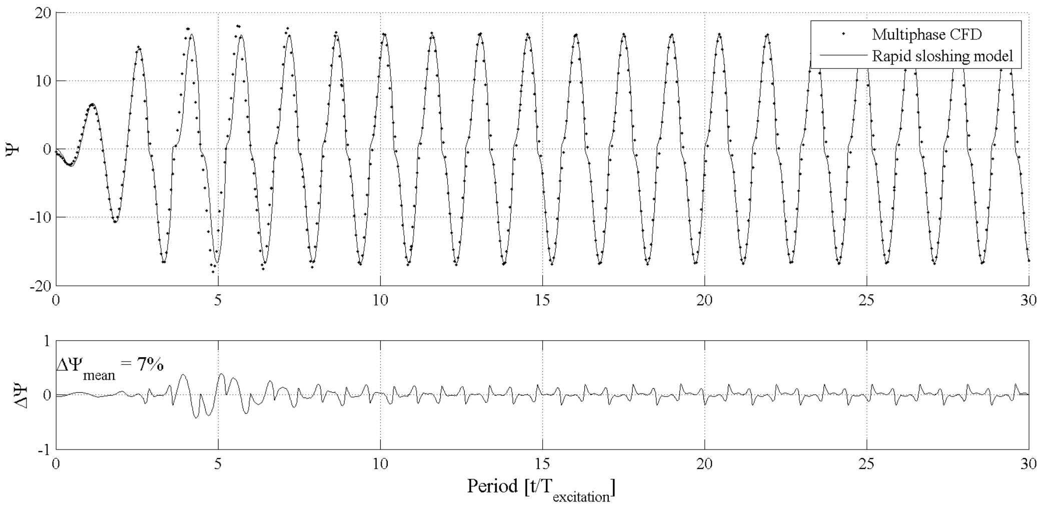

Figure 5.29: Comparison of Rapid Sloshing Model with CFD using normalised fluid momentum Ψ for combined surge and pitch – case a

The second validation case, case b, uses the same surge and pitch amplitude as in the previous case, but the excitation periods are different, with the surge excitation period at resonance and the pitch excitation period $T_{pitch} = 1.10T_1$. This case is unlikely to be experienced by a real ship as the motions are excited by the same wave profile, but this case illustrates the ability of the sloshing model to handle such motion profiles. The resulting sloshing response is depicted in Figure 5.30 and, although there is some disagreement between the CFD solution between the beating phases, the peaks during impact are predicted with good accuracy and the solutions are in phase throughout the 30 oscillations

---

[2] The cases considered in this section are identified by lower-case Latin characters

shown.

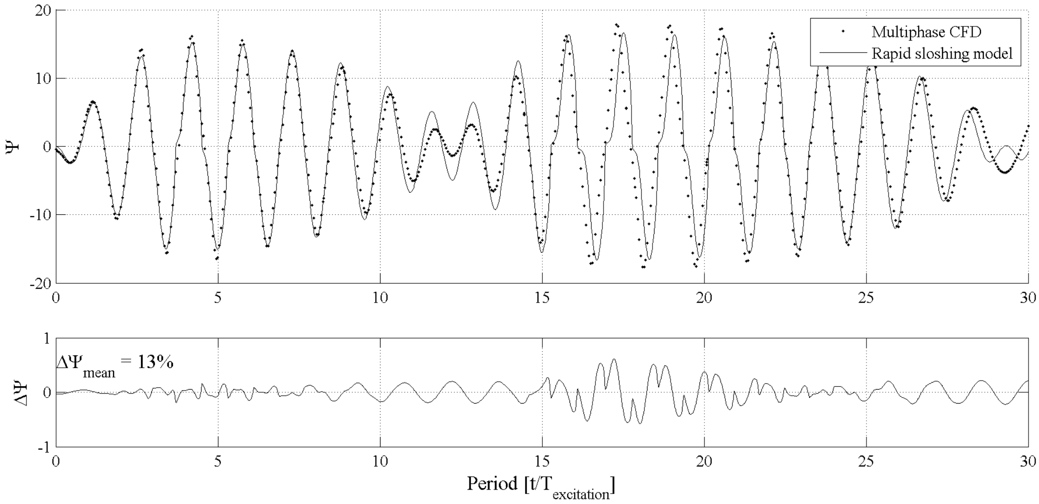

Figure 5.30: Comparison of Rapid Sloshing Model with CFD using normalised fluid momentum Ψ for combined surge and pitch – case b

Case c, shown in Figure 5.31, uses an excitation period $T = 1.0362T_1$ for both surge and pitch. The response is similar to that observed in Figure 5.29 and the error envelope remains constant after the initial transient with a mean error of 13%.

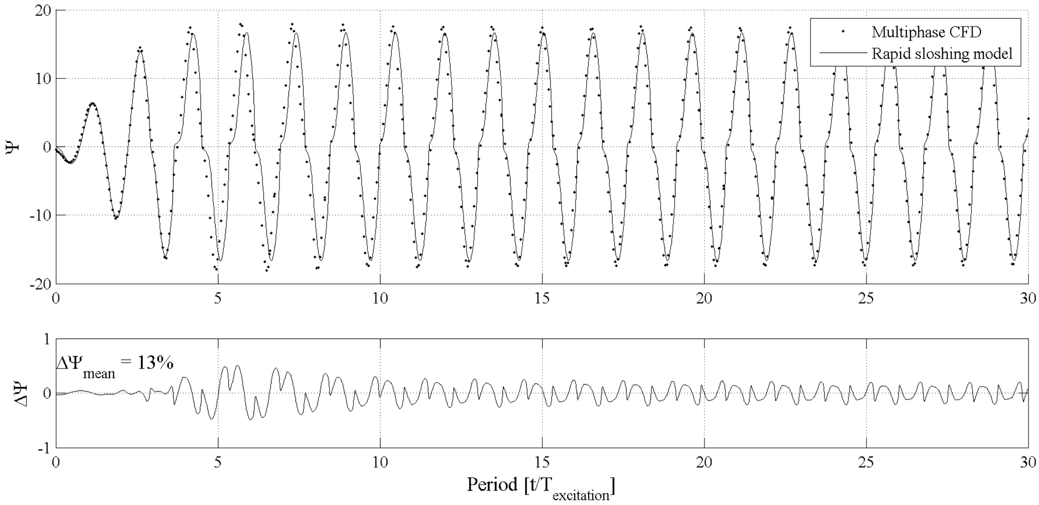

Figure 5.31: Comparison of Rapid Sloshing Model with CFD using normalised fluid momentum Ψ for combined surge and pitch – case c

In the fourth two degree of freedom validation test case, case d, in Figure 5.32, the pitch amplitude is increased to 5 deg and the surge period $T_{surge} = 0.95T_1$, which was more problematic for simulation using the proposed sloshing model. The fluid momentum peaks calculated using the pendulum model and CFD are of similar magnitude, but the two solutions differ when descending through $\Psi = 0$. This is explained by the impact model and the violent nature of the sloshing response. The mean error of 16% is due to the

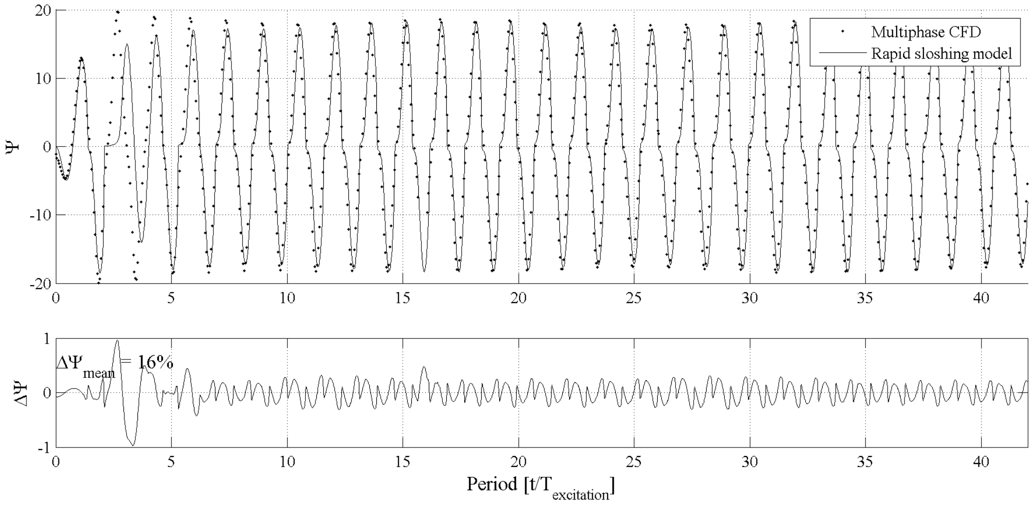

Figure 5.32: Comparison of Rapid Sloshing Model with CFD using normalised fluid momentum Ψ for combined surge and pitch – case d

difference between the solutions at at the initial transient which caused by the impact model.

Figure 5.33 shows the free surface location during one half oscillation for case d. In Figure 5.33(a) the flow has struck the top wall and a jet is forming which has progressed across half the tank width in 0.15 s as shown in Figure 5.33(b). The flow direction is changing in Figure 5.33(c) and the jet has reached the right side wall. A hydraulic jump forms close to the right wall in Figure 5.33(d) and 0.05 s later the first fluid impact occurs at the right side wall, shown in Figure 5.33(e). During and after impact illustrated in Figures 5.33(f) and 5.33(g) there is air entrapment and bubble formation and the fluid is moving up to the top wall. The impact against the top wall is shown in Figure 5.33(h) and the post-impact jet is illustrated in Figure 5.33(i).

The frequency domain analysis of the cases considered in stage four of the validation is shown in Figure 5.34. The spectrum for case a in Figure 5.34(a) is similar to the pure surge resonance case, but the local trough on the high-frequency side of resonance is not replicated. The response spectrum for case b in Figure 5.34(b) with two distinct excitation periods has a peak at the resonant frequency and a smaller separate peak at the pitch excitation period. There is a further peak near the resonance period and there is a distinct difference between the CFD solution and the sloshing model at the second resonant period $T_2 = 0.62T_1$.

In Figure 5.34(c), the response spectrum of case c with identical surge and pitch excitation frequencies is similar to that in Figure 5.34(a), although the peak is not as sharp. In both cases, the CFD and sloshing model spectra are similar at low frequency. The final case, case d, in Figure 5.34(d) with increased pitch amplitude shows greater differences in the

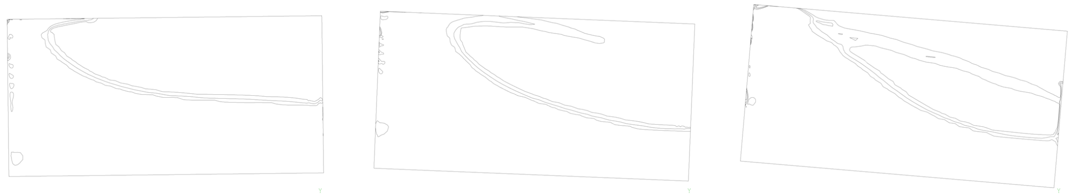

(a) $t = 46.55$ s (b) $t = 46.70$ s (c) $t = 46.90$ s

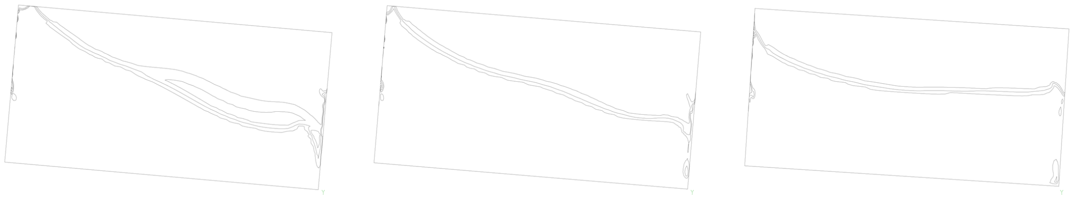

(d) $t = 47.00$ s (e) $t = 47.05$ s (f) $t = 47.15$ s

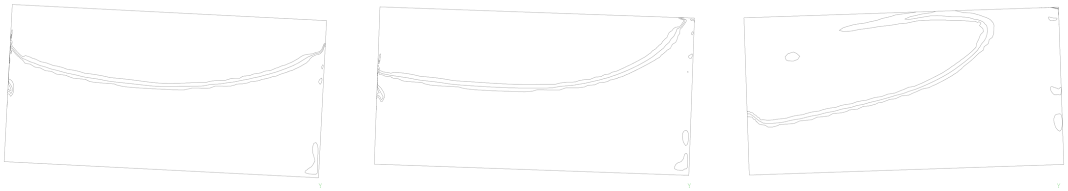

(g) $t = 47.20$ s (h) $t = 47.25$ s (i) $t = 47.45$ s

Figure 5.33: Volume fraction contours of r_{water} = 0.05, 0.50 and 0.95 during one half oscillation for case d

response spectrum. The distinct peaks near resonance are not captured well but the high frequency peak at $t/T_1 = 0.3$ is captured with surprising accuracy.

5.6 Closure

The Rapid Sloshing Model methodology outlined in Chapter 4 has been applied to a range of representative sloshing cases for both longitudinal and transverse membrane tank cross sections. The restoring force can be represented with a polynomial or periodic function and both approaches have been applied for the longitudinal and transverse cross sections respectively. Irregular excitation profiles have been simulated with a mean error comparable to periodic excitations. The simulation of combined motions was carried out with the Rapid Sloshing Model as well and although the error was found to be somewhat larger than in the 1 DOF motion simulations there was generally good agreement between results from the Rapid Sloshing Model and the CFD solution.

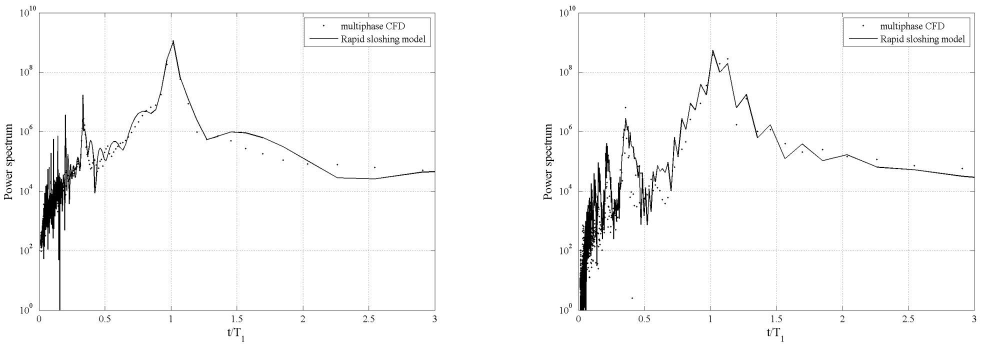

(a) case a

(b) case b

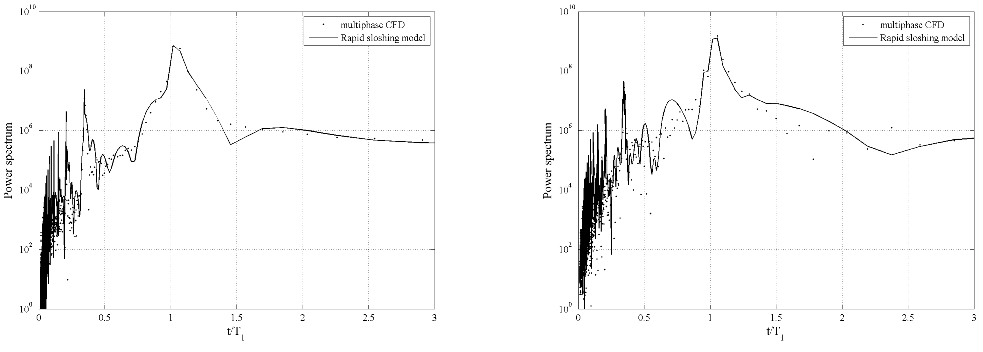

(c) case c

(d) case d

Figure 5.34: Comparison of power spectra for combined surge and pitch induced sloshing

It is found that the restoring force has a significant influence on the prediction of non-periodic transient sloshing responses and the use of a pendulum approximation does not adequately capture the behaviour of the restoring force. Figure 5.35 compares the detuning characteristics of the sloshing flows in this chapter. The filling level in the longitudinal section is slightly below the critical depth which results in a hard spring sloshing response. This implies that the value of the restoring force function is greater than the linearised ($\beta = 0$) response (i.e. β in the Duffing Equation (4.3) is greater than zero). Conversely for the transverse cross section where the filling ratio is above the critical depth the restoring force function is below the linearised response, which corresponds to ($\beta < 0$) and a soft-spring response.

The restoring force models for the simulations carried out in this chapter were obtained with only one CFD simulation but the inclusion of more CFD simulations can provide a better approximation of the restoring force. The large amount of sloshing data required for LNG carrier class approval can be used to optimise the restoring force coefficients for a particular tank shape. The effect of damping can be considerable when long time series are simulated and the damping coefficient is obtained by measurement of the logarithmic decrement in the CFD simulation. Turbulence was included in the CFD simulations and

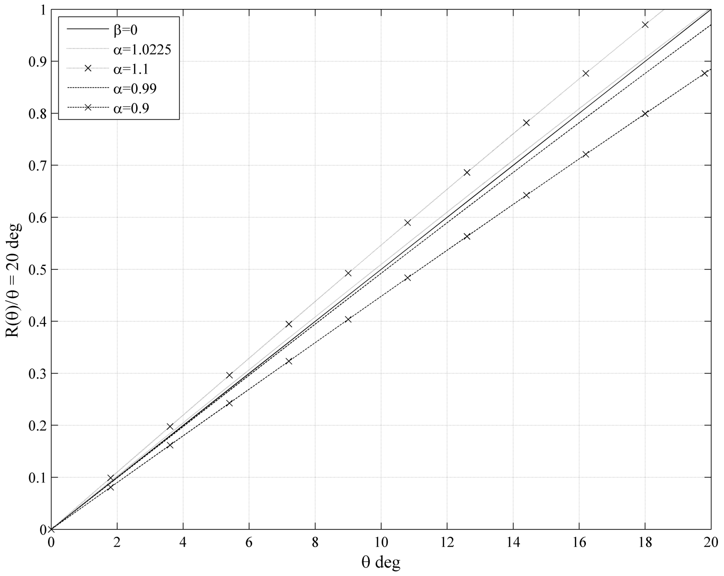

Figure 5.35: Detuning characteristics of the restoring force

consequently in the damping model. The damping characteristics of LNG and particularly the effect of the corrugations in the Mk III containment system warrant further investigation. Additional damping is introduced by sloshing impacts which is included in the impact model.

The impact model proposed by Pilipchuk and Ibrahim (1997) is a weak point of the current phenomenological approach. The main attraction of the impact potential approach is its simplicity and the ability to model the effects of complicated physics on the evolution of a sloshing flow. The enhancements made to the model with the inclusion of realistic impact physics has resulted in considerably more faithful representation of sloshing impacts. The impact model is improved further in Section 6.3 for sloshing impacts at low filling levels.

Chapter 6

Sloshing Guidance System

6.1 Implementation with a Rapid Sloshing Model

The changing commercial constraints of LNG carrier operation and recent sloshing incidents (Hine, 2008) have raised awareness of and renewed concerns about sloshing with LNG carrier owners and operators. The approach toward a non-intrusive sloshing guidance system developed in this thesis was introduced to industry at Gastech 2008 and several LNG carrier and terminal operators as well as classification societies expressed in interest in the sloshing guidance system concept (Rose and Burnay, 2008). A brochure for the proposed sloshing guidance system is included in Appendix E.

Figure 6.1 shows the concept of operation of the sloshing guidance system and the important role played by the Rapid Sloshing Model. By replacing the predefined tank motions which were applied in the previous chapter with the LNG carrier motions measured during operation, the Rapid Sloshing Model methodology can be applied to provide a low-cost non-intrusive sloshing guidance system based on a desktop or laptop PC.

The Rapid Sloshing Model is set up using the procedure in Chapter 4 using already available sloshing data from model tests and/or CFD simulation carried out during the LNG carrier design and class approval phases. Lloyd's Register (2005) require numerous CFD simulations or model tests to determine the sloshing loads and this data can also be used for post-setup validation of the Rapid Sloshing Model. Two separate Rapid Sloshing Models would be used for longitudinal and transverse motion giving a 3 + 3 DOF system and the beam of the sometimes slightly tapered No 1 tank (which is the most forward) can be represented by the average beam of the tank.

As shown in Figure 6.1 the required data inputs for the sloshing guidance system are vessel accelerations and angular displacements which can be measured using a 6 DOF accelerometer and digital spirit levels for the longitudinal and transverse directions. The

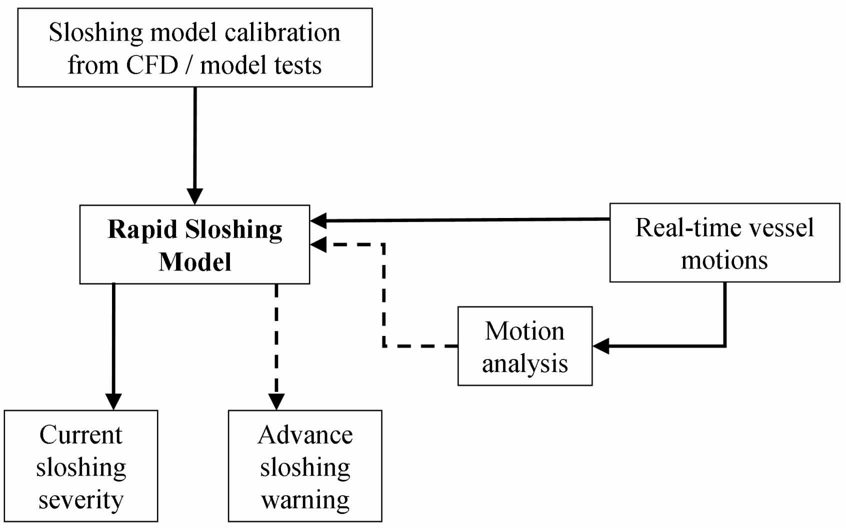

Figure 6.1: Rapid Sloshing Model used for real-time sloshing guidance

motions at each tank can be measured using separate sensors but the measurement of vessel motions at one easily accessible location such as the bridge and deducing the motions at the tanks using a rigid ship assumption reduces the required number of sensors. By minimising the number of required data inputs the costs of cabling and other associated system and maintenance costs are reduced significantly and the system is easy to retrofit to existing LNG carriers.

Signal conditioning for the removal of high frequency noise and drift can be carried out on a desktop PC using commercial software packages or custom software. The Rapid Sloshing Model can be run on the same desktop PC in a MATLAB environment or using bespoke software. The results from the rapid sloshing model can be presented for each LNG tank using traffic light system, as a percentage of a critical level determined during setup or the probability of exceeding a particular threshold level.

More sophisticated visual outputs analogous to the polar plot of sloshing risk in Figure 2.3 are also feasible and a predictive capability can be implemented using motion trend analysis or wave radar data and vessel RAOs. The sloshing guidance system concept has progressed to the proposal stage by BMT SeaTech Ltd and details are given in Appendices D and F.

6.2 Rapid Sloshing Model Application: Frequency domain seakeeping analysis

When the Rapid Sloshing Model methodology is set up with CFD or model test data for a particular tank and filling level the sloshing responses to a wide range of excitation motions can be computed in a short amount of time. This can be exploited in linear frequency domain seakeeping analysis for building a coupled model (Lee *et al.*, 2009). The equation of motion for a coupled sloshing - seakeeping system traveling in regular waves can be expressed by Equation (6.1), where [ ] denotes a 6×6 matrix (Rognebakke and Faltinsen, 2003; Malenica *et al.*, 2003).

$$\begin{aligned}\Big(-\omega_e^2\Big([M]_{ship}+[A]_{ship}+[A]_{slosh}\Big)\\ -i\omega_e\Big([B]_{ship}+[B]_{slosh}\Big)\\ +[C]_{ship}+[C]_{slosh}\Big)\,\{\xi\}=\{F_{wave}\}\,,\end{aligned} \tag{6.1}$$

where ω_e is wave encounter frequency, $[M]_{ship}$ mass of ship excluding liquid cargo, $[A]_{ship}$ hydrodynamic added mass of ship, $[A]_{slosh}$ hydrodynamic added mass due to liquid sloshing in tank, $[B]_{ship}$ hydrodynamic damping of ship, $[B]_{slosh}$ damping due to sloshing, $[C]_{ship}$ hydrostatic restoring coefficients of ship, $[C]_{slosh}$ hydrostatic restoring coefficients of liquid in tank, $\{\xi\}$ rigid body motion vector and $\{F_{wave}\}$ excitation vector due to incident and diffracted waves (Lee *et al.*, 2009).

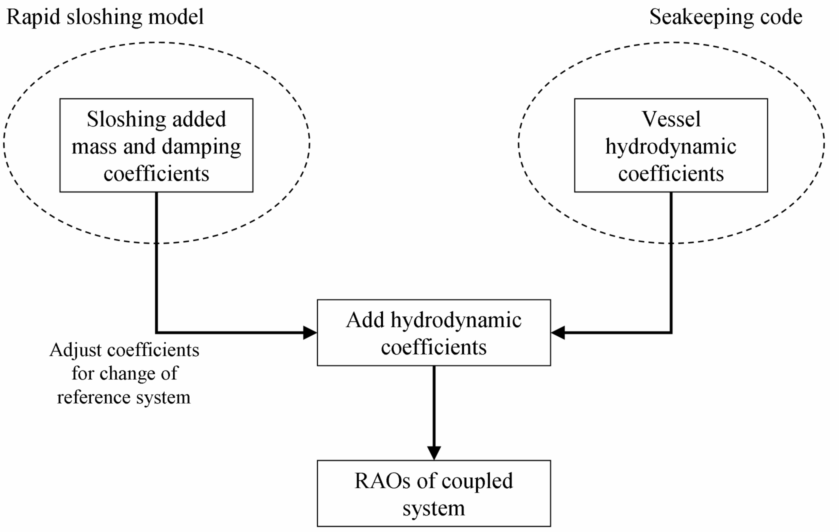

Figure 6.2: Rapid Sloshing Model used in coupled sloshing-seekeaping frequency domain analysis

In Equation (6.1) the hydrodynamic coefficients for the sloshing fluid can be obtained using a sloshing model and the coefficients for the vessel are obtained with a conventional seakeeping code as illustrated in Figure 6.2. The hydrodynamic coefficients are then moved into the same coordinate system and the RAOs are then obtained by the solution of the combined system.

The dynamic sloshing forces and moments, which can be obtained from the displacement angle θ using the formulations given by Abramson (1966), are cast into the hydrodynamic coefficients of added mass (or inertia) and liquid damping. These are obtained from the Rapid Sloshing Model solution for a periodic displacement $a\sin(\omega t)$ with amplitude a and frequency ω. The coefficients are extracted with Fourier analysis of the dynamic force (or moment) over a moving window of one excitation period T width, as proposed by Yeung *et al.* (1998). For example, the added mass for sway is

$$A_{22} = \frac{1}{\pi a \omega} \int\limits_{t-T/2}^{t+T/2} F_x(t)\sin(\omega t)\,dt \tag{6.2}$$

and sway liquid damping is

$$B_{22} = -\frac{1}{\pi a} \int\limits_{t-T/2}^{t+T/2} F_x(t)\cos(\omega t)\,dt, \tag{6.3}$$

where $F_x(t)$ denotes the dynamic sway force. Similar terms can be written for the hydrodynamic coefficients for roll and the cross-coupling coefficients.

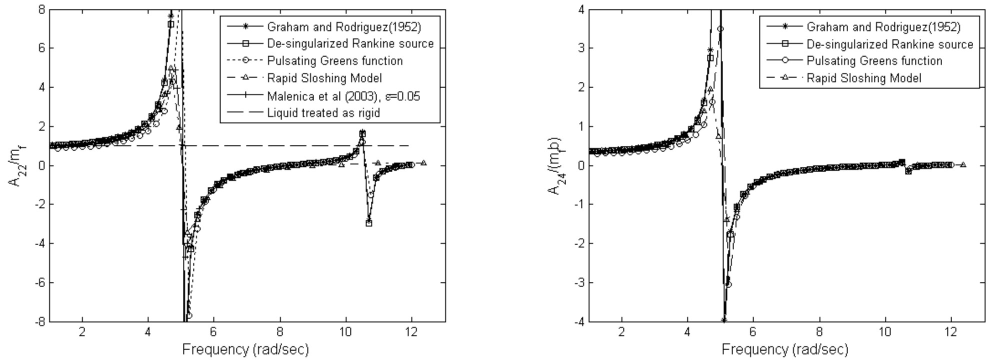

(a) A_{22} (b) A_{24}

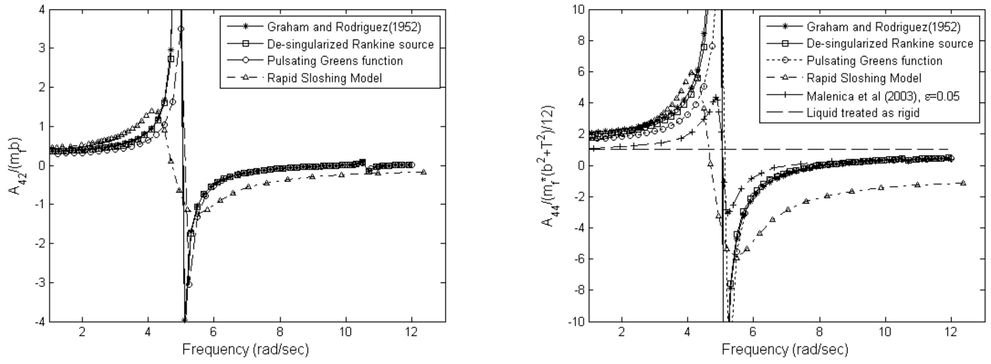

(c) A_{42} (d) A_{44}

Figure 6.3: Sloshing added masses for sway and roll (Lee *et al.*, 2009)

Figure 6.3 compares the added mass and inertia coefficients using the analytic potential flow solution (Graham and Rodriguez, 1952), the pulsating Green function method, de-singularised Rankine source method and the Rapid Sloshing Model. As a reference, another available numerical prediction by Malenica *et al.* (2003) is included which used a velocity potential approach with energy dissipation at the boundary layer and on tank walls. For the direct comparison of aforementioned methods with the case of liquid treated as rigid body, sway added mass is non-dimensionalised by liquid mass in the tank, m_f, and roll added inertia by the moment of inertia of the rigid liquid mass, $m_f(b_f^2 + T^2)/12$.

The added mass for sway is shown in Figure 6.3(a). All five methods predict the first resonance frequency of the liquid, 4.94 rad s^{-1}, which can be obtained using the fundamental solution given by Ibrahim (2005). As expected, the added masses obtained from the analytic solution and de-singularised Rankine source methods have a nearly identical magnitude, tending towards infinity at resonance. However, the added mass values obtained from the Rapid Sloshing Model, Green function and Malenica *et al.* (2003) have finite magnitudes in the vicinity of the first resonance frequency. This is due to the incorporation of viscous damping effects and the nonlinearities (excitation amplitude $x_0/L = 0.05$) in RSM, wave making damping due to radiation condition in Green's function and the damping parameter ε in the work by Malenica *et al.* (2003). The second resonance frequency obtained from the analytic solution and de-singularised Rankine source method are very close to the fundamental solution of 10.63 rad s^{-1}. As the second mode is confined to a narrow frequency range, there is generally good agreement between the different sloshing models. The cross coupling coefficients A_{24} and A_{42} are depicted in Figure 6.3(b) and 6.3(c), respectively. While there is good agreement between the analytic potential flow solution, Rankine method and the Rapid Sloshing Model methodology for A_{24}, there are small differences in A_{42}. These differences can be attributed to viscous effects and nonlinearities.

Roll added inertia, non-dimensionalised by the mass moment of inertia of the liquid inside the tank treated as a rigid body, is compared in Figure 6.3(d), again with a reference dashed line which refers to the case of rigid liquid. All five methods predict the first resonance frequency of 4.94 rad s^{-1}. As in the previous case for sway, the Rapid Sloshing Model methodology still shows a finite value near the resonance frequency and the slope of roll added inertia across the resonance frequency is not significant compared to the other methods. However, there is a discernible difference after the first resonance frequency between RSM and the other four potential based methods. In Figure 6.3(d) it is found that non-dimensionalised roll added inertia obtained from the analytic solution, Green's function method, Rankine source method and RSM do not approach to unity at low frequency while the prediction by Malenica *et al.* (2003) approaches unity. After the resonance frequency of about 5 rad s^{-1}, the roll added inertia predicted with the Rapid Sloshing Model methodology is smaller than that of the potential based analytic solution, while that predicted by Malenica *et al.* (2003) is larger.

6.3 Rapid Sloshing Model Application: Low filling level sloshing

Another application of the Rapid Sloshing Model methodology in the design phase is pre-screening and voyage analysis. During LNG carrier design a sloshing test matrix which usually encompasses approximately 100 different scenarios needs to be analysed. When using the Rapid Sloshing Model approach cases with dangerous sloshing can be highlighted for further analysis the required computational effort or experimental cost can be reduced by several orders of magnitude. Using already available experimental or numerical data the Rapid Sloshing Model approach can be adopted without additional computational or experimental effort and the analysis of LNG carrier voyages for the identification of dangerous sloshing is made possible on a desktop PC using the danger level methodology proposed for the guidance system.

As low filling levels are of particular concern to owners and operators of LNG carriers (Hine, 2008), the procedure in Chapter 4 can be extended to include sloshing at low filling ratios where the sloshing response can be a travelling wave rather than the standing wave observed at higher filling levels in Chapter 5. When a travelling wave is formed the trajectory of the fluid centre of mass is not necessarily along a circular arc as shown in Figure 6.4. For a small motion amplitude ($x_0/L = 0.0125$) the sloshing response is linear and the trajectory of the centre of mass is along a circular arc (indicated by red circles in Figure 6.4). When the motion amplitude is increased to $x_0/L = 0.05$, a travelling wave forms and the trajectory of the centre of mass follows a more complicated path. This is due to the evolution of the travelling wave. A further increase in the motion amplitude to $x_0/L = 0.10$, shown with blue circles results in a similar trajectory but the vertical displacement is increased four-fold. This is due to the absence of the travelling wave impact against the side wall.

When the angle of the centre of mass displacement is less than five degrees the imbalance force behaviour corresponds to that shown in Figure 4.4. As the motion aplitude is increased, the imbalance force in Figure 6.5 differs from the behaviour for filling near the critical depth observed in Figure 4.4 for the filling ratio 0.3 in Chapter 5. Once the angle exceeds the critical angle, $\theta_0 = 8$ deg in this case, the imbalance force behaviour depends on the sloshing response. For $x_0/L = 0.05$, the sharp increase in imbalance force is due to the travelling wave impacting against a side wall. When the motion amplitude

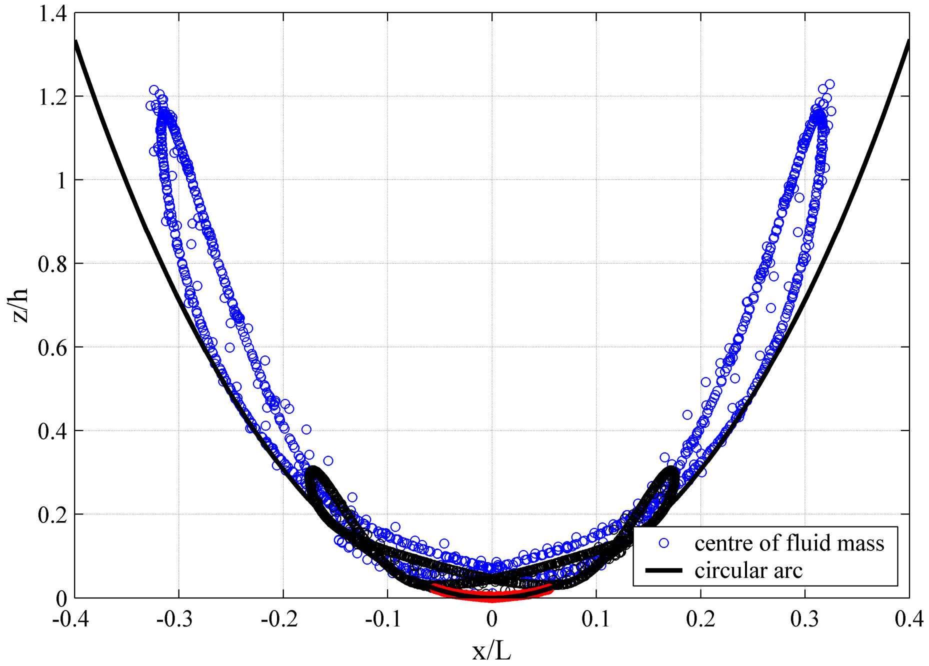

Figure 6.4: Location of the fluid centre of mass during shallow depth sloshing ($h/L = 0.1$) with excitation amplitudes $x_0/L = 0.0125$ (red), $x_0/L = 0.05$ (black) and $x_0/L = 0.1$ (blue) with regular excitation period $T = 0.82T_1$

is increased further the travelling wave is not observed and the imbalance force increase is more gradual. After impact the fluid centre of mass displacement continues to increase but the maximum displacement of the fluid centre of mass is nearly 30 degrees.

These impact dynamics are not represented by the impact model adopted from Pilipchuk and Ibrahim (1997) and a modified two-stage impact model has been developed. This impact model consists of two components:

- A gradually increasing restoring force and corresponding impact damping model, with powers less than 10 (see Figure 4.8, which is analogous to the model by Pilipchuk and Ibrahim (1997) and
- a separate hydrodynamic impact model with a power of about 30 and a velocity dependence but this model is limited near the critical angle of 8 degrees where impact occurs.

Figure 6.6 shows the fluid momentum for sloshing with a motion amplitude $x_0/L = 0.05$ which corresponds to the case used for the study of sloshing impacts in Chapter 3. The Rapid Sloshing Model with the modified impact model gives a good match with the CFD results despite the different sloshing response and the mean error is comparable to results obtained in Chapter 5.

An irregular motion profile is applied to the tank in Figure 6.7 and good agreement

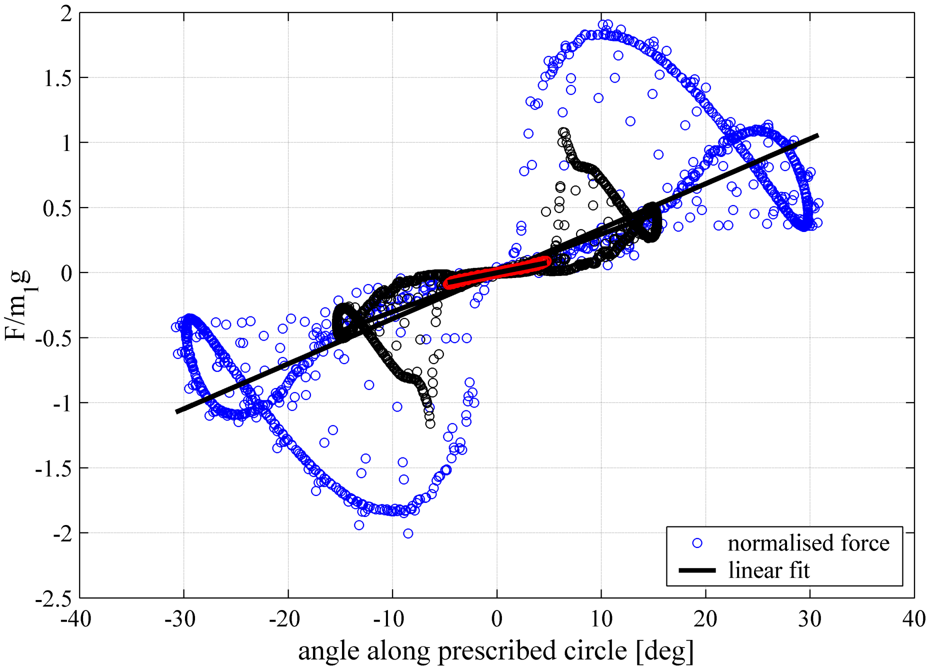

Figure 6.5: Sloshing force compared to the centre of gravity position. Colour coding is as in Figure 6.4

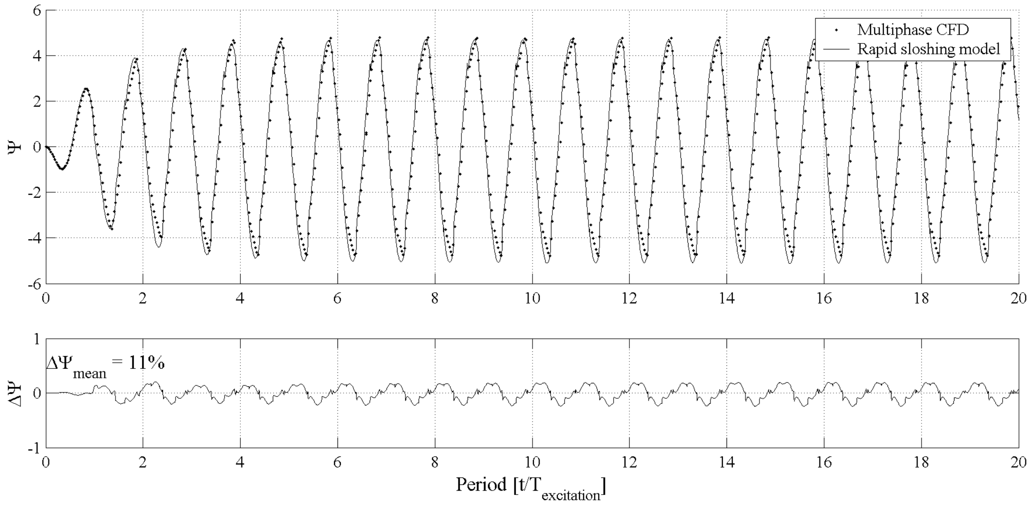

Figure 6.6: Comparison of Rapid Sloshing Model with CFD using normalised fluid momentum Ψ for surge with excitation period $T = 0.82T_1$

is observed between the CFD solution and the Rapid Sloshing Model prediction with a mean error below 10%. There are some errors observed around 20 s which are attributable to wave breaking illustrated in Figure 6.8. Up to 16.8 s the sloshing response has been linear and weakly nonlinear and the free surface is shown in Figure 6.8(a). The free surface in Figure 6.8(b) is similar to the collapsing water column studied by Martin and Moyce (1952). Due to the tank motion and filling level a hydraulic jump starts to form and breaks in Figure 6.8(c). After breaking a new hydraulic jump forms which is well defined in Figures 6.8(d), 6.8(e) and 6.8(f). Figures 6.8(g) and 6.8(h) show the flow just before impact and after impact and Figure 6.8(i) shows the free surface at the maximum displacement of the fluid centre of mass.

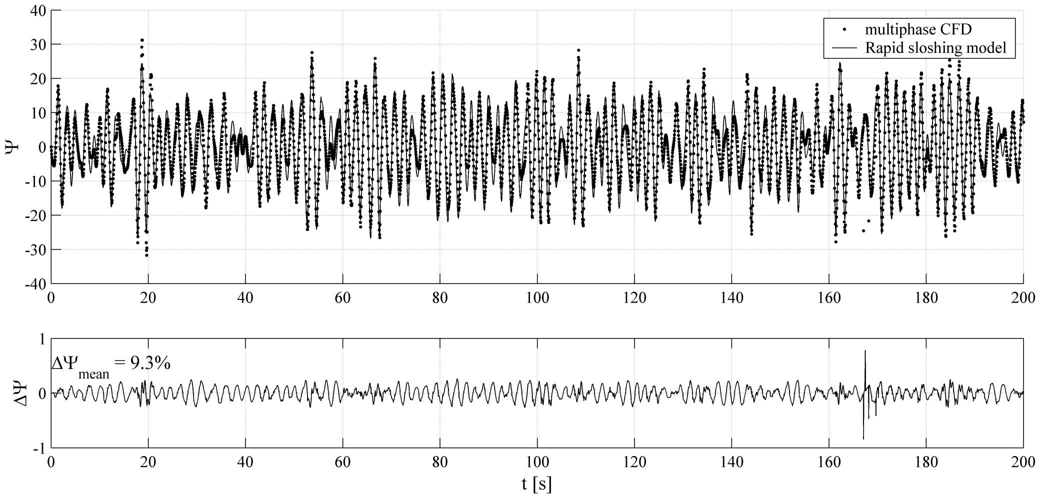

(a) full simulation

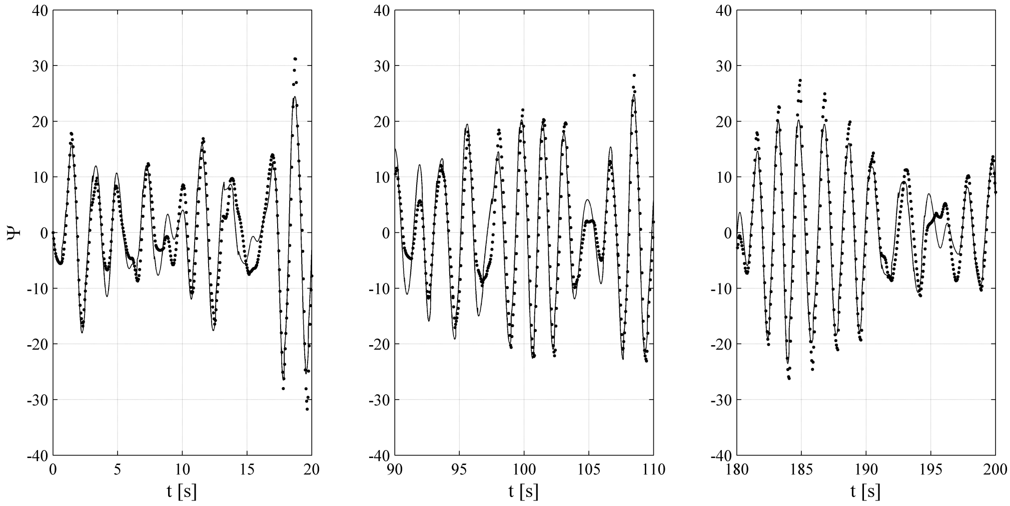

(b) zoom on regions of interest

Figure 6.7: Comparison of Rapid Sloshing Model with CFD using normalised fluid momentum Ψ for irregular surge at filling ratio $h/L = 0.1$

Figure 6.9 compares the momentum observed when applying the same motion profile to a conventional linearised pendulum model (Dodge, 2000) and the CFD solution. As for the medium filling levels the use of the Rapid Sloshing Model methodology produces significantly better correlation with the validated CFD model with a reduction in mean error from 53% to 9.3%.

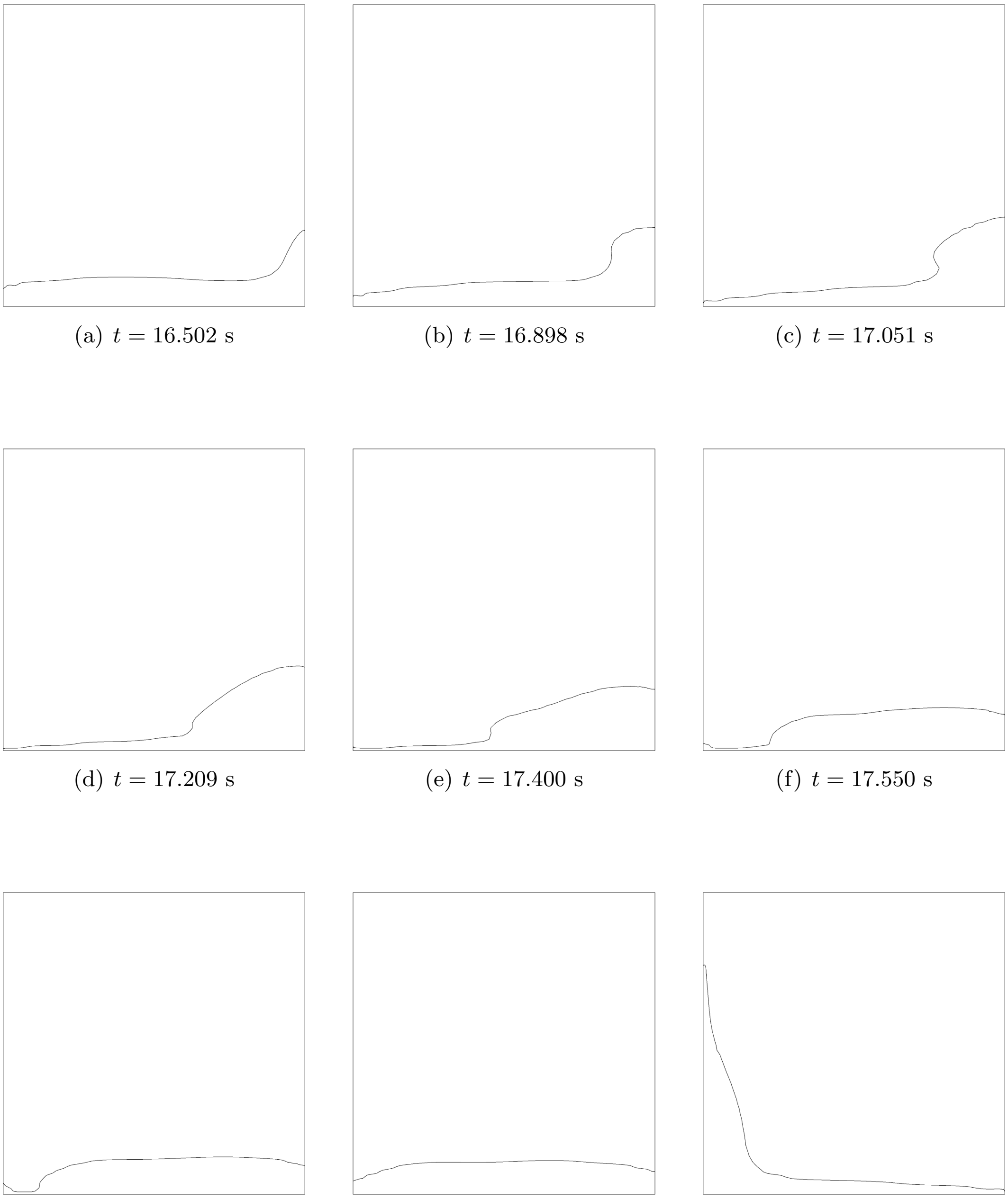

(a) $t = 16.502$ s

(b) $t = 16.898$ s

(c) $t = 17.051$ s

(d) $t = 17.209$ s

(e) $t = 17.400$ s

(f) $t = 17.550$ s

(g) $t = 17.699$ s

(h) $t = 17.751$ s

(i) $t = 17.800$ s

Figure 6.8: Free surface location for irregular sloshing excitation between 16.5 s and 18.0 s

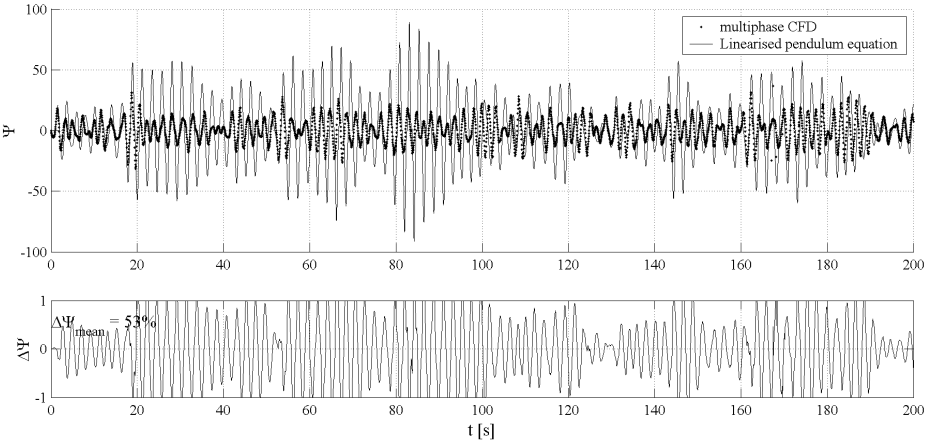

(a) full simulation

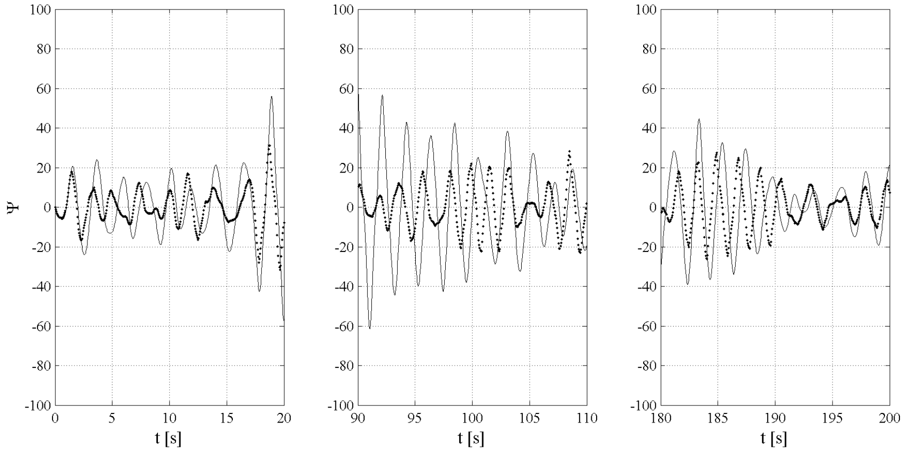

(b) zoom on regions of interest

Figure 6.9: Comparison of normalised fluid momentum Ψ for irregular surge at filling ratio $h/L = 0.1$ with a linearised pendulum model

Chapter 7

Conclusions

In this thesis a mathematical sloshing model suitable for a non-intrusive sloshing guidance system for installation on newbuild and existing LNG carriers has been developed and validated for sloshing near the critical depth. A multiphase CFD model was developed and validated with experimental data and theoretical results. The sloshing model for the concept sloshing guidance system has to satisfy the conflicting demands of faithful representation of the sloshing physics, mathematical robustness, conservation of mass for extremely long simulation times and faster than real time solutions. These requirements rule out most theoretical and numerical approaches as theoretical methods can be unstable during strongly nonlinear sloshing and low filling levels. Numerical methods such as CFD suffer from iterative error propagation and slow solution times.

Therefore a new Rapid Sloshing Model is implemented using a phenomenological modelling approach. The Rapid Sloshing Model is compared to the validated CFD model and it is found that the sloshing response due to periodic translatory motions, rotational motions, simultaneous translatory and rotational motions and irregular translatory motions applied to membrane tank section is usually within 5%–15% of the CFD solution for cases with linear, weakly nonlinear and strongly nonlinear sloshing. The model coefficients are obtained using theoretical and numerical results and the procedure used to set up a Rapid Sloshing Model is also applicable to data obtained with model testing. Other applications of the Rapid Sloshing Model include coupled frequency and time-domain sloshing-seakeeping analysis and a pre-screening tool to aid the assessment of sloshing test matrices in LNG carrier design.

7.1 CFD sloshing model

In the development of the CFD model a grid and time step independence study was carried out. It was found that the CFD simulation of sloshing required a sufficient number of mesh elements and although the bulk fluid motion was captured with a comparatively coarse grid, the pressure oscillation frequency caused by air entrapment required fine spatial resolution. Sloshing impact pressures are sensitive to the shape of the water front and the simulation of sloshing impacts entails accurate discretization of the wave front in space and time for the entire flow field. The simulation of violent sloshing requires a multiphase model capable of modelling fluid mixing and the relative motion between the phases to obtain hydrodynamic impact pressures and pressure oscillation frequencies caused by air entrapment.

The multiphase flow regime and effect of the multiphase model on the solution is examined further using dimensional analysis outlined by Brennen (2005). It is found that for a violent sloshing flow an inhomogeneous multiphase model is the most appropriate to use. The relative velocity between the phases, which is ignored in the homogeneous multiphase model widely used in sloshing CFD analysis, has been found to be significant compared to the global velocity field. Neglecting the motion between the phases results in an incorrect velocity field and causes the sloshing pressure peaks to be underestimated by in excess of 50%. The steady state pressure histories and the power spectrum from the inhomogeneous multiphase solution compare well to the experimental data. Although the pressure history from the homogeneous model appears to agree with experimental data during the initial transient phase, the comparisons of the experimental pressure history with the computational steady-state pressure history illustrates the shortcomings of the homogeneous multiphase model. However, the inhomogeneous multiphase model was found to be 2.3 times more computationally expensive than the homogeneous multiphase model.

Further numerical investigations focused on the frequency of pressure oscillation which occurs when an air bubble is trapped during impact. It has been found that the inclusion of fluid compressibility can have a significant effect on the pressure evolution of a sloshing flow. When fluid impact is not a significant feature of the sloshing then an incompressible fluid model can be used for both fluids. An isothermal compressibility model for air may still be preferable, given the small increase in required computational time. Once fluid impact becomes a defining feature of the sloshing flow, a more complex compressibility model is required to represent the flow physics. The non-dimensional pressure impact parameter ψ which is based on tank size and rise of pressure during impact can be used to determine whether a compressible fluid model should be selected.

7.2 Rapid Sloshing Model

The CFD model is then applied for the development of a simplified mathematical sloshing model designed to be used in the non-intrusive concept sloshing guidance system developed in this thesis. A new phenomenologically-based Rapid Sloshing Model which is based on the pendulum equation has been developed for inclusion in a PC-based onboard sloshing guidance system. The Rapid Sloshing Model can be used for the assessment of sloshing flows in fast time and its applicability includes strongly nonlinear sloshing with fluid impacts. The physics of sloshing flows are identified using numerical or experimental tools and approximated with mathematical models. A procedure is outlined for adapting these models to a particular tank shape and fluid with analytical results and the results of one CFD simulation.

The principal weakness of any phenomenological modelling approach is that there is no explicit physical foundation for the model but pendulum models have been used successfully for the study of space and motor vehicle dynamics where the effect of sloshing is a concern. Since the Rapid Sloshing Model cannot predict a pressure field, the direct assessment of the effect of sloshing impacts on the surrounding tank is not possible in its present form. For LNGC operation this limitation can be overcome with the development of the appropriate warning criteria. Additionally, the Rapid Sloshing Model cannot simulate wave breaking which is a significant source of damping to the fluid motion. This is one of the main sources of error in the simulation carried out for low filling levels with irregular motion and needs to be addressed further.

Given the lack of an explicit physical basis for the pendulum model a systematic sloshing case study was carried out using the Rapid Sloshing Model . The initial validation of the Rapid Sloshing Model uses translation and rotation induced periodic sloshing near the critical depth. There is good agreement between the sloshing model and the corresponding multiphase CFD solution which is independent of the Rapid Sloshing Model solution. Strongly nonlinear sloshing flows with fluid impacts can be represented using the Rapid Sloshing Model approach. An arbitrary surge motion profile obtained from an ITTC wave spectrum describing a realistic seaway is simulated with the Rapid Sloshing Model and the difference to the CFD solution is approximately 6%. It is found that a conventional pendulum model is unable to emulate the sloshing response, with errors up to an order of magnitude greater than those from the Rapid Sloshing Model methodology applied in this study.

Simultaneous rotational and translatory motions with identical and different frequencies are then applied simultaneously and the solutions between CFD and sloshing model continue to show good agreement. The final test is a violent sloshing flow excited by simultaneous sloshing flow and despite the limitations of the impact model the solutions remain in agreement. The advantages of pendulum sloshing model include low computational cost which permits simulation speeds of up to 0.1% of real time on a desktop PC. The pendulum-based sloshing model is not restricted to a particular range of filling levels and because the fluid mass is not part of the numerical solution the resonance characteristics of the system are strictly preserved which enables simulations with very long simulation times. Translatory and rotational motion, or a combination thereof can be defined by either continuous functions or discrete data sets. By replacing user-generated tank accelerations with measured vessel motions the Rapid Sloshing Model can be adopted as an on-board sloshing guidance system with a prediction capability for coupled sway, roll and heave and surge, pitch and heave motions.

7.3 Further work

Both the CFD model and the Rapid Sloshing Model can be improved further for a more faithful representation of LNG sloshing. In the current CFD model there is no allowance for the implicit treatment of air bubbles, and their explicit inclusion requires an extremely fine mesh which increases the computational cost of the simulation considerably. While dimensional analysis suggests that thermal effects do not affect the sloshing response the cryogenic nature of LNG requires further investigation to ascertain the validity of approximating LNG at $-163°$ C with water at $15°$ C. More importantly, the simplification of the vapour-liquid system into two fluids with no phase change may not be valid when impact pressures are similar to the critical pressure.

The properties of LNG and the increased surface roughness of some LNG containment systems can be included by changing the damping characteristics and the impact model can be extended to include fluid structure interaction effects (Ibrahim, 2005). The current impact model is optimised for hydrodynamic impacts where the impact coincides with the maximum displacement of the fluid centre of mass. Flow features observed during impacts at lower filling ratios such as wave overturning and air pocket formation do not support this assumption and a modified impact model was developed for the low filling level sloshing simulation in Chapter 6. Before using the Rapid Sloshing Model methodology for low filling level sloshing a validation study similar to that in Chapter 5 should be carried out. Nonetheless, the test case with irregular motions at low filling levels was simulated successfully with a mean error similar to that for the corresponding case with medium filling level. The extension of the Rapid Sloshing Model approach to 3D sloshing is a more challenging step as the resonant frequencies in the longitudinal and transverse directions are not normally equivalent. Moreover the significant computational requirements for the simulation of 3D sloshing would require the adaption of the procedure in Chapter 4 to experimental data. This can be carried out using Particle Image Velocimetry to obtain the velocity field of the fluid and high speed video recording to determine the free surface location and the centre of mass of the sloshing fluid. A alternative to the Rapid Sloshing

Model is the use of the multimodal method developed by Faltinsen *et al.* (2000) in the proposed sloshing guidance system concept but further increases in the calculation speed would be required before its use.

The remaining step towards a non-intrusive sloshing guidance system is the integration of the Rapid Sloshing Model with the required sensors and development of visual output and warning criteria. The warning criteria require approval by the relevant classification society and visual outputs which permit the easy interpretation of the sloshing severity need to be developed as well. This is an area of expertise of the industrial partner company BMT SeaTech (with the hull stress monitoring package SMART$^{\mathrm{STRESS}}$), who are currently in negotiation with several operators of LNG carriers for trialling the proposed sloshing guidance system.

Appendices

Appendix A

List of Publications

Journal papers

1. B. Godderidge, S.R. Turnock, M. Tan, and C. Earl. An Investigation of Multiphase CFD modelling of a lateral sloshing tank. *Computers and Fluids* **38** pp 183-193, 2009.
2. B. Godderidge, S.R. Turnock, C. Earl and M. Tan. Effect of Fluid Compressibility on the Simulation of Sloshing. *Ocean Engineering* (in press), 2009.
3. B. Godderidge, M. Tan, C. Earl, and S.R. Turnock. The effect of an internal pump tower on fluid sloshing in a rectangular container. *International Journal for Maritime Engineering*, (revised manuscript submitted), 2009.
4. B. Godderidge, S.R. Turnock, N. Cowlan and M. Tan. A rapid method for the simulation of sloshing; Part I: A mathematical model based on the pendulum equation. *Computers and Fluids*, 2009. (submitted for review).
5. B. Godderidge, S.R. Turnock, N. Cowlan and M. Tan. A rapid method for the simulation of sloshing; Part II: Sloshing in rectangular and octagonal containers at intermediate filling levels. *Computers and Fluids*, 2009. (submitted for review).

Conference papers

1. B. Godderidge, M. Tan, S.R. Turnock, and C. Earl. Multiphase CFD modelling of a lateral sloshing tank. *Proc 9th Numerical Towing Tank Symposium*, Nantes, 2006
2. B. Godderidge, M. Tan, C. Earl, and S.R. Turnock. Boundary layer resolution for modeling of a sloshing liquid. *17th Intl Soc Offshore and Polar Engrs Conf*, Lisbon, 2007.

3. B. Godderidge, M. Tan, S.R. Turnock, and C. Earl. Grid Resolution for the Simulation of Sloshing using CFD. *Proc 10th Numerical Towing Tank Symposium*, Hamburg, 2007.
4. B. Godderidge, S.R. Turnock, C. Earl and M. Tan. Identification of Dangerous LNG Sloshing Using a Rapid Sloshing Model validated with CFD. *18th Intl Soc Offshore and Polar Engrs Conf*, Vancouver, 2008.
5. B. Godderidge, M. Tan, C. Earl, and S.R. Turnock. The effect of an internal pump tower on fluid sloshing in a rectangular container. *CFD 2008*, Royal Institution of Naval Architects, 2008.
6. S. Schreier, B. Godderidge, M. Paschen, S.R. Turnock, M. Tan and N. Cowlan. Assessment of transient sloshing due to encounter of an LNG carrier with a steep wave. *28th Intl Conf Ocean, Offshore and Arctic Eng*, 2009.
7. B. Godderidge, S.R. Turnock, N. Cowlan and M. Tan. Sloshing Symposium Comparative Study: Simulation of lateral sloshing with multiphase CFD. *19th Intl Soc Offshore and Polar Engrs Conf* 2009.
8. Y-B. Lee, B. Godderidge, P. Temarel, M. Tan, S.R. Turnock and N. Cowlan. Coupling between ship motion and sloshing using potential flow analysis and pendulum modelling *19th Intl Soc Offshore and Polar Engrs Conf* 2009.
9. B. Godderidge, N. Cowlan and S. Schreier. A Rapid Sloshing Model for LNG carriers - Increased operational safety and reduced design analysis times. *24th Gastech Conference and Exhibition*, Abu Dhabi, 2009.

Others

1. B. Godderidge, M. Tan, and S.R. Turnock. A verification and validation study of the application of computational fluid dynamics to the modelling of lateral sloshing. *Ship Science Report 140*, University of Southampton, 2006.
2. B. Godderidge, A. Phillips, S. Lewis, S.R. Turnock, D.A. Hudson, and M. Tan. The simulation of free surface flows with Computational Fluid Dynamics. *ANSYS UK Users Conference* 2008, Oxford. (invited paper)
3. B. Godderidge and S.L . Burnay. Real time sloshing detection with the Rapid Sloshing Model. *Society of International Gas Tanker and Terminal Operators - Western European Regional Forum*, London, 6 November 2008. (invited presentation)
4. B. Godderidge. Unsteady rotational forces in the moving frame of reference model for CFX-11. University of Southampton, 2008.

5. B. Godderidge. Adaptive second order time marching scheme validation. University of Southampton, 2008.

Appendix B

CFD model for Rapid Sloshing Model validation

The computational meshes for the longitudinal and transverse cross sections used in Chapter 5 are shown in Figures B.1 and B.2 respectively. The longitudinal mesh contains 8,745 elements (8,109 hexahedral and 636 wedge) and the refined region at the top corners contains 5,266 hexahedral elements. The transverse mesh contains 18,038 elements (16,767 hexahedral and 1,326 wedge) and the refined region at the top corners contains 8,016 hexahedral elements. The advantage of the hybrid grid approach used in this study is that only the regions of interest were refined while maintaining a hexahedral-dominant grid. This resulted in a more efficient use of computational resources.

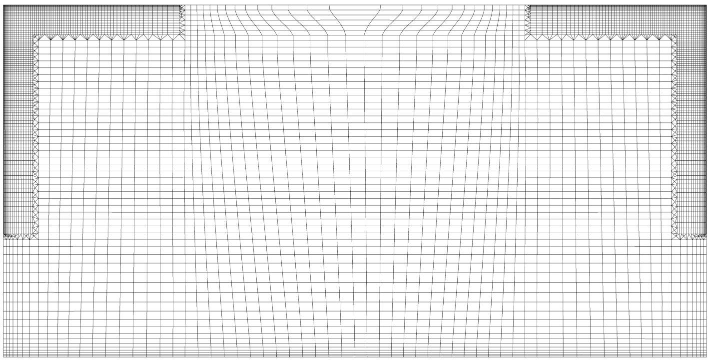

Figure B.1: Computational mesh for the longitudinal tank cross-section

The numerical investigations were carried out using the commercial CFD code CFX-11.1[1] and the computational parameters were selected based on the sensitivity study in Chapter 3. It was found that the second order time marching scheme is most appropriate, as mass and momentum are conserved over a large number of time steps which is often requried for the simulation of violent sloshing. The magnitude of each time step was controlled

---

[1] The simulations were run on a 64 bit, 2.2 GHz processor with 2 GB of RAM at the University of Southampton Iridis 2 computational facility

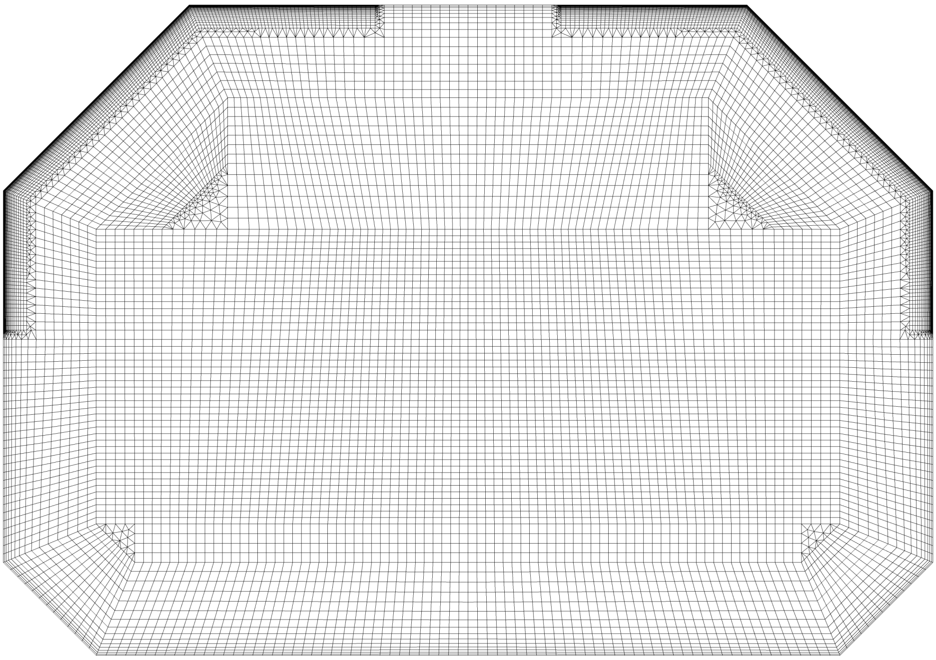

Figure B.2: Computational mesh for the transverse tank cross-section

dynamically using the root mean square of the local cell Courant number C_N computed over the entire velocity field. A maximum threshold value of $C_{N,RMS} = 0.15$ identified in Section 3.2.3 and the convergence criteria was applied in line with the recommendations given by ANSYS Zwart (2004). The computational parameters used in the simulations are summarised in Table B.1.

Table B.1: CFD model description and parameters

Water	Incompressible fluid
Air	Ideal gas
Sloshing motion	Body force (translation) and rotating frame of reference (rotation)
Turbulence model	Standard k-ε with scalable wall function
Spatial discretization	Gradient-dependent first or second order
Temporal discretization	Second order backward Euler
Timestep control	$C_{N,RMS} \leq 0.15$
Convergence control	RMS residual $\leq 10^{-5}$

Appendix C

Rapid Sloshing Model setup

The use of the Rapid Sloshing Model methodology is illustrated using the sloshing tank analysed for the sloshing-seakeeping interaction application in Section 6.2. The fluid is in a rectangular container with a length of 0.8 m, filling level 0.19 m, giving a filling ratio of 0.2375 and a tank height of 0.6 m.

The first stage of setting up a Rapid Sloshing Model is determining the length of the pendulum by matching the first resonant sloshing frequency of 4.94 rad s^{-1} with with the pendulum resonant frequency. This gives a pendulum length of 0.4024 m. The next stage is determining the effective sloshing mass, which in the present case can be determined using Equation (4.15) as 0.69.

The linear damping coefficient is determined from the measured logarithmic decrement in Section 4.1.2 as 0.023 and the third-order damping coefficient is obtained using the ratio of first to third-order damping coefficient from Decent (1997). There is no impact model used as the tank is sufficiently high so that there are no impacts against the top wall and the sloshing response is consistent with a standing wave. The simulation of a lower filling level with a travelling wave would require the inclusion of an impact model.

The restoring force function uses CFD results and the procedure in Section 4.1.1. Step one fits a circular arc to the trajectory of the centre of mass location which is obtained from CFD, which is shown in Figure C.1. This is then used to plot the lateral imbalance force, which is also obtained from CFD against the angle of displacement of the centre of mass which is shown in Figure C.2. For the present case the restoring force $R(\theta)$ is $\sin \alpha\theta$, where $\alpha = 1.03$ is determined from the gradient of the imbalance force at $\theta = 0$. Table C.1 summarises the coefficients used for the Rapid Sloshing Model.

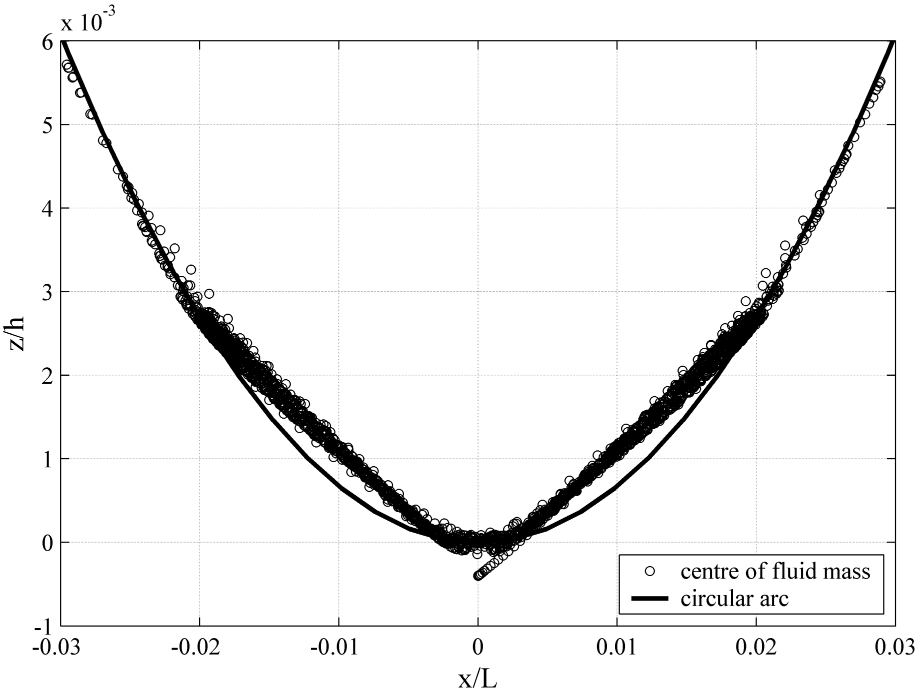

Figure C.1: Location of the fluid centre of mass during sloshing motion

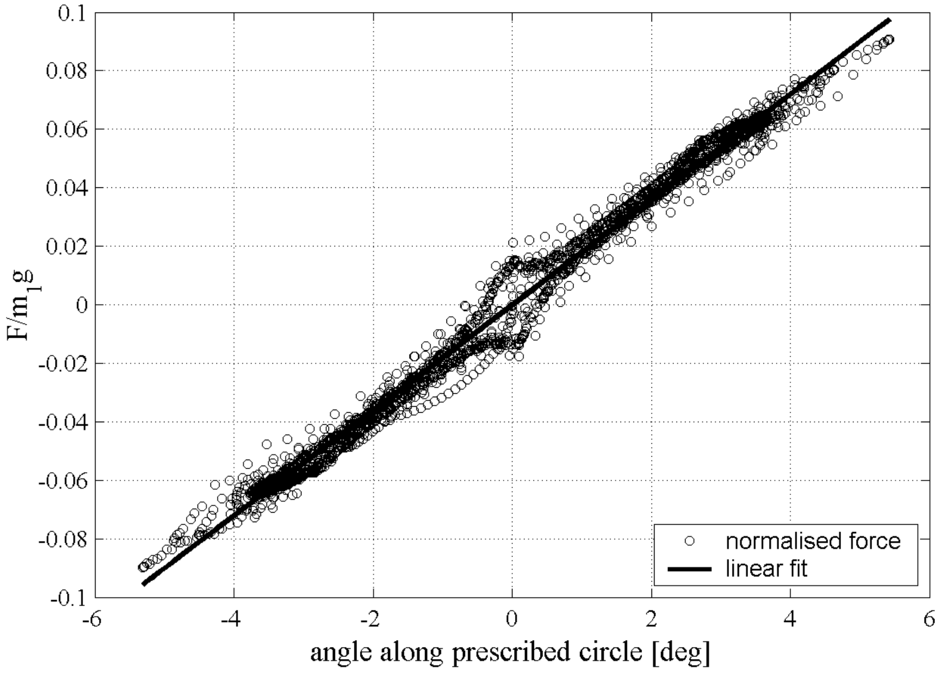

Figure C.2: Sloshing force compared to the centre of gravity position

Forces and moments due to sloshing can be obtained from the pendulum model using the linear approach by Abramson (1966), where the force is given as

$$F = -m_0 \ddot{x_0} + m_0 h_0 \ddot{\chi} - m_1 g \theta \tag{C.1}$$

and the moment is given as

$$M = -m_0 h_0 \ddot{x}_0 - \left(I_0 + m_0 h_0^2\right) \ddot{\chi} - m_1 g h_1 \theta \tag{C.2}$$

where m_0 is the fixed mass with inertia I_0, h_0 the distance from the fixed mass and h_1 the distance from the pendulum hinge point to the quiescent fluid centre of mass and $\ddot{x}_0$ and $\ddot{\chi}$ the translatory and angular motions imposed on the sloshing tank.

Table C.1: Rapid Sloshing Model settings for sloshing-seakeeping study

Length	0.4024 m
Effective mass fraction	0.69
Linear damping coefficient	0.023
Third-order damping coefficient	0.0345
Restoring force: function	$\sin \alpha\theta$
Restoring force: coefficients	$\alpha = 1.03$
Impact model: θ_{crit}	-
Impact model: force coefficients	-
Impact model: damping coefficients	-

Appendix D

Sloshing Guidance System concept: BMT SeaTech position paper

A part of BMT in Maritime Transport

Rapid Sloshing Model Overview

ISSUE 1

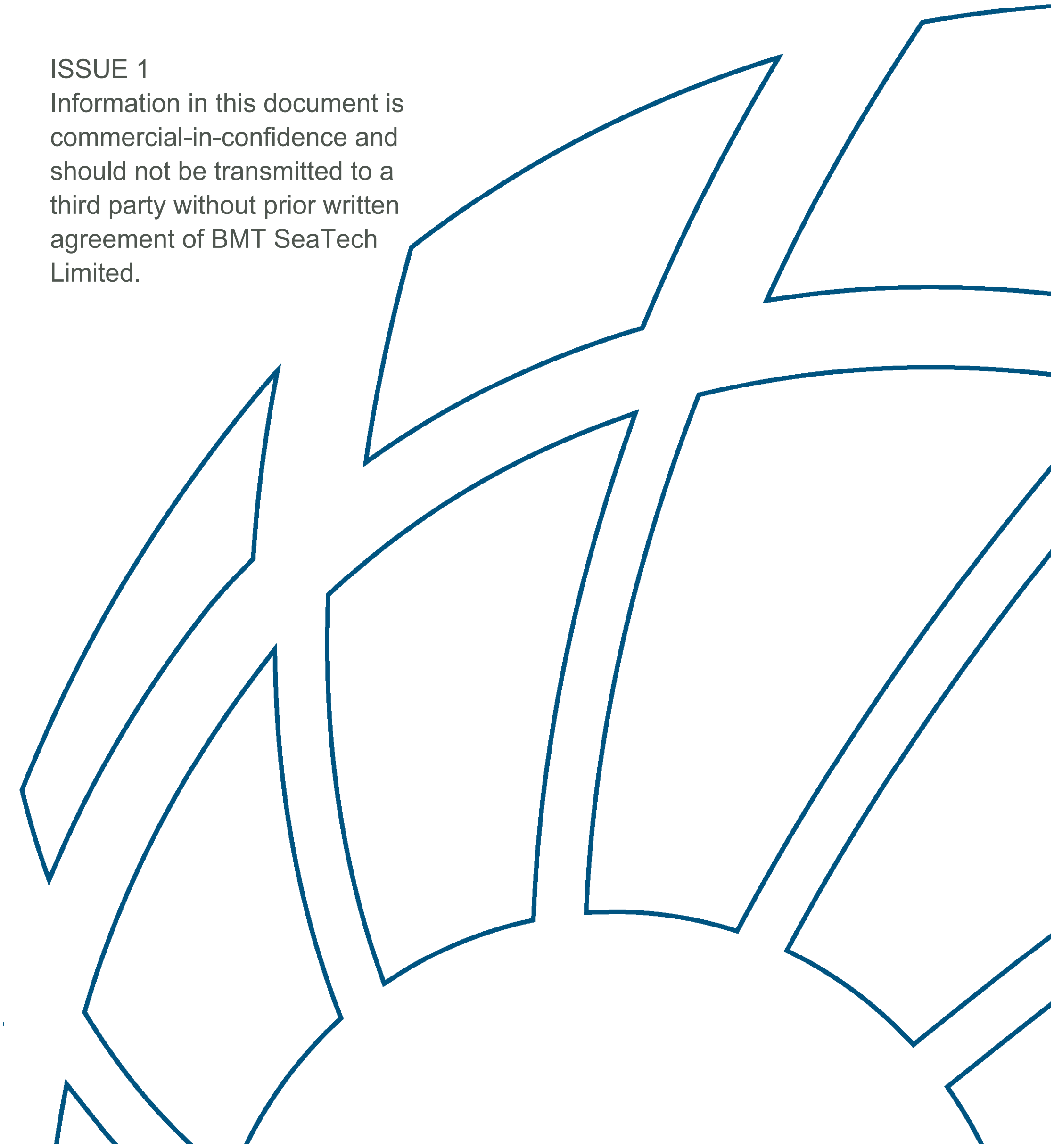

A Fast-Time Mathematical Model for the Rapid Simulation of LNG Sloshing

Introduction

Sloshing remains a concern in the safe operation of Liquefied Natural Gas (LNG) carriers. LNG carriers and floating LNG storage and re-gasification units are at risk due to motion induced tank sloshing loads with potentially significant societal, financial, and environmental impact. The development of a new generation of LNG carriers and the ship operator-driven demand for a broader range of permissible tank filling levels have led to renewed interest in the study of sloshing by designers, operators and classification societies.

The safe operation of a ship requires decisions to be made regarding the optimum speed and heading to avoid excessive sloshing induced loads on the cargo containment system and hull. This is not a simple task for the ship's officers and it is advantageous to provide them with additional, accurate real-time data to aid decision making.

However, the cryogenic nature of the cargo presents significant problems for monitoring these loads using instrumentation within the LNG tanks or the containment system.

Whilst the accuracy of experimental, theoretical and computational investigations of sloshing flows is well documented [1], these methods require considerable resources for limited simulation times making them unsuitable for an onboard warning system.

BMT SeaTech is addressing these concerns by developing a sloshing warning system that uses a simplified mathematical model to simulate the bulk fluid motion. This modelling approach has two main benefits:

1) It can calculate the severity of the current sloshing motion in real time from measured vessel motions with no intrusive tank instrumentation.

2) It provides a capability for fast-time calculation of sloshing, allowing the prediction of short-term trends in sloshing intensity giving the opportunity for preventative actions to be taken.

BMT SeaTech Ltd

BMT SeaTech Ltd supplies a range of support services and specialist software products to improve the operational efficiency and safety of our clients' vessels. We have extensive experience and a proven track record in naval architecture, on-board monitoring and ship-performance analysis and can tailor these to meet individual requirements. In conjunction with industry partners, ship operators and Masters, we have developed the SMART product suite, which monitors and reports on the safety and performance aspects of a ship's operation. Current components within the suite include the widely used hull stress monitoring system SMART$^{\text{STRESS}}$ and the performance monitoring package SMART$^{\text{POWER}}$.

Figure 1 - Typical Display from BMT SeaTech's Hull Stress Monitoring System

Rapid Mathematical Sloshing Model

Sloshing is a complex physical phenomenon which depends on the properties of the fluid, tank shape and excitation and the flow history. A sloshing warning system must take all of the above into account.

A model based on a pendulum that represents the motion of the fluid centre of gravity has been used previously to include sloshing effects in stability analyses of engineering artefacts such as spacecraft [2]. Aliabadi *et al* [3] used an undamped linear pendulum to simulate periodic sloshing and reported reasonable agreement with Computational Fluid Dynamics (CFD) at low tank filling levels. The principal advantages of the pendulum model are the relative simplicity of the governing equations, the strict conservation of mass and suitability for a high-order time integration scheme to conserve momentum over large numbers of time steps. However, a simple pendulum is not able to model large fluid motions accurately or account for the transient behaviour of a sloshing flow.

BMT SeaTech is currently developing an enhanced pendulum model to predict sloshing as the basis of an on-board sloshing warning system. It is anticipated that the model will also have applications in design studies and the definition of safe operational envelopes.

The pendulum damping, mass and restoring force coefficients are obtained from a limited number of CFD simulations, typically the analysis in the design condition of the resonance in surge, sway, pitch and roll. These coefficients provide the initial set-up of the rapid sloshing model. Comparison is then made between the model time series and the CFD data to confirm the accuracy and provide data for further refinement of the coefficients if required.

In operation the linear and angular motions are applied to the pendulum through the acceleration vector and forces caused by the change of the frame of reference. The source of the accelerations may be real-time ship data or artificially generated (e.g. for validation purposes or short-term predictions). The rapid sloshing model predicts the severity of the sloshing in terms of the fluid’s momentum.

An overview of the system is shown in Figure 2.

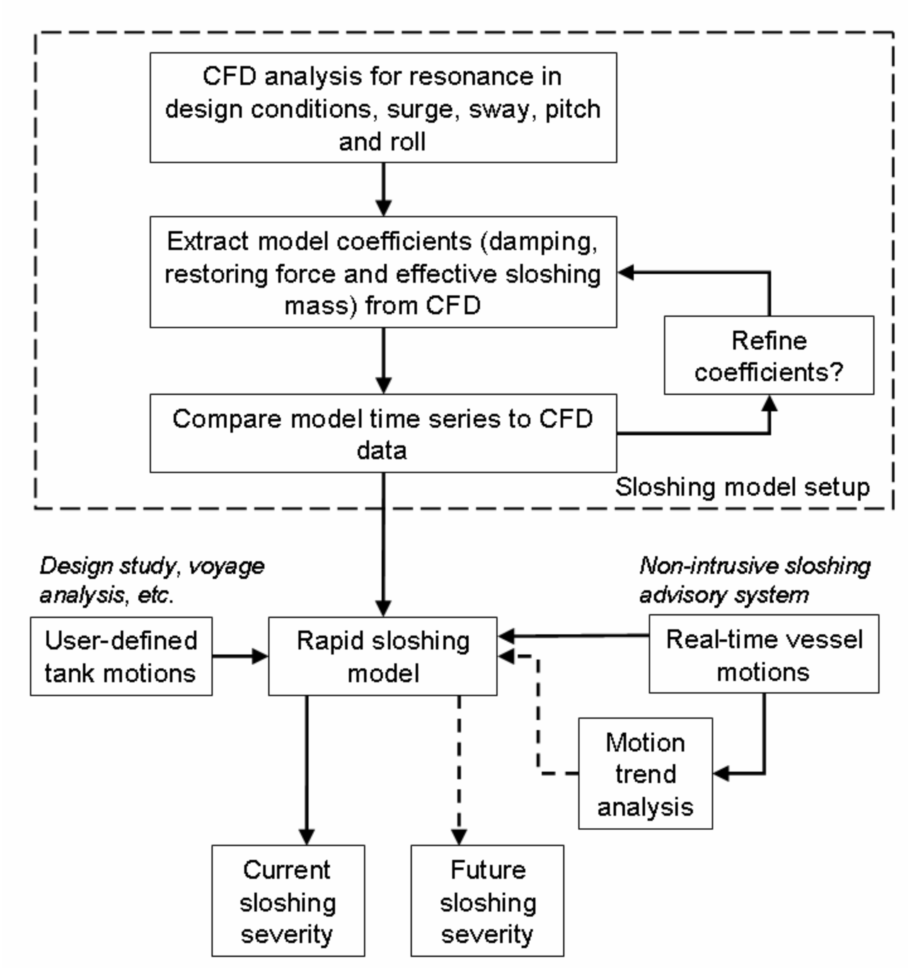

Figure 2 - Overview of the Rapid Sloshing Model

The principal strengths of this sloshing model are its simplicity, flexibility and speed (one hour of simulation can be computed on a desktop PC in approximately five seconds of real time). The speed of the model also allows short-term trends in sloshing intensity to be investigated giving early warning and the opportunity for preventative actions to be taken.

Validation

To date the validation of the rapid sloshing model has been carried out using multiphase CFD. The CFD model has been validated with experimental data in [4]. The pendulum load prediction is compared to the CFD model. Regular linear and angular excitations situated near the first resonant frequency are used in the initial tests. The values obtained by the pendulum are within 5% of the peak values observed from the corresponding CFD models. Further testing is carried out using combined linear and angular excitations as well as multiple simultaneous linear and multimodal excitations to simulate realistic motions. The transition between excitation frequencies is investigated using the pendulum and this is validated with CFD as well.

Additional advances in the models capabilities are to be presented in a paper accepted for publication in ISOPE 2008.

Further improvements to the sloshing model for the warning system are currently under development. These include:

- Improvements to the sloshing impact model
- Extending the 2D pendulum model to a full 3D 6 degree of freedom pendulum
- Validation using scale model test data

References

[1] R A Ibrahim. *Liquid Sloshing Dynamics*. Cambridge University Press, 2005.

[2] H N Abramson. The dynamic behavior of liquids in moving containers, with applications to space vehicle technology. Technical Report SP-106, National Aeronautics and Space Administration, 1966.

[3] S Aliabadi, A Johnson, and J Abedi. Comparison of finite element and pendulum models for simulation of sloshing. *Computers and Fluids*, 32:535–545, 2003.

[4] B Godderidge, S Turnock, M Tan, and C Earl. An Investigation of Multiphase CFD modelling of a lateral sloshing tank. *Computers and Fluids (in print)*, 2008.

Appendix E

Sloshing Guidance System concept: BMT SeaTech brochure

A part of BMT in Maritime Transport

BMT SeaTech

"Where will our knowledge take you?"

Marine Safety and Compliance

Structures – LNG Sloshing

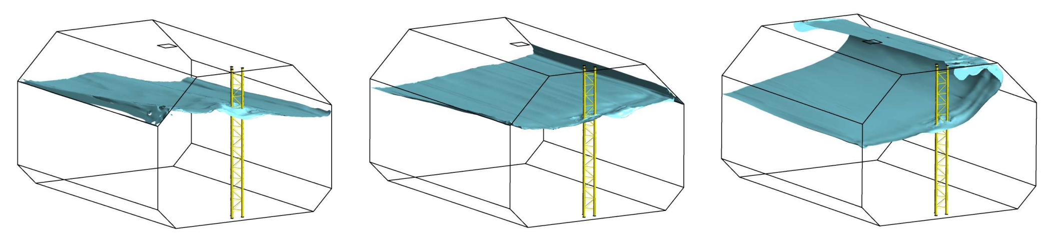

BMT SeaTech is a world-leading consultancy with expertise in hydrodynamic modelling, structural design and vessel structural load monitoring.

Current products include the widely used hull stress monitoring system SMART^{STRESS} and the performance monitoring package SMART^{POWER}

Several years of research into sloshing on LNG tankers have culminated in the development of a unique mathematical sloshing model which can predict sloshing severity in fast time.

Sloshing is one of the main risks in the operation of LNG carriers. Greater vessel size, ship-to-ship transfer and offshore loading/unloading increase the probability of incurring sloshing damage during vessel operation. The sensitivity of sloshing to tank shape, filling level and vessel motion history complicates the identification of safe operational envelopes for deck officers.

The structural loads from LNG sloshing impacts can exceed the static load by more than 100 times. When gas bubbles are formed during impact, the pressure load may oscillate near resonant frequencies of the membrane and pump tower components. This can result in catastrophic structural failure.

The identification of dangerous sloshing usually requires expensive mathematical and experimental modelling. Common mathematical models are constrained by available computational resources and the reliability of experiments is often compromised by the scaling of the tank motion.

BMT SeaTech staff have been instrumental in the development a fast, cost-effective sloshing model to overcome these drawbacks. On a standard PC, the fast sloshing model can accurately predict sloshing severity several hundred times faster than real time. This model is ideal for use in a non-intrusive onboard sloshing guidance system with an advance warning capability.

Date February 2008 Ref No. MSC 141.0

BMT SeaTech Ltd
Grove House, 7 Ocean Way, Meridians Cross, Ocean Village, Southampton SO14 3TJ,
Telephone + 44 (0) 23 8063 5122
web address www.bmtseatech.co.uk

An LNG tanker in heavy weather: sloshing can become a problem...

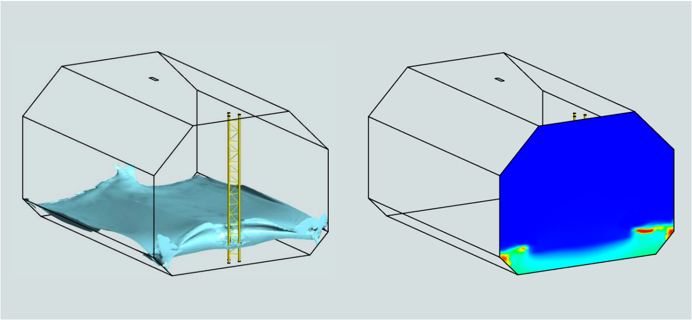

...but how severe is the sloshing response – and could the crew avoid it?

BMT SeaTech's proposed sloshing guidance system will

- **maintain a stronger LNG value chain: avoid vessel downtime due to sloshing damage;**
- **give predictions of sloshing loads in real time;**
- **provide advance warning of dangerous sloshing;**
- **only require vessel motion inputs: no instrumentation in LNG tanks;**
- **be customised with existing design information;**
- **identify critical sloshing for targeted tank inspections and maintenance;**
- **protect your investment from sloshing damage;**
- **demonstrate the quality and safety of your fleet to charterers;**
- **potentially reduce insurance premiums**
- **help know the safe operating limits of your ship more accurately;**
- **extend the life of your ship, protect your crew and safeguard the environment;**

The fast sloshing model

The fast sloshing model simulates the sloshing of LNG using an approach called phenomenological modelling. This results in a mathematical description of sloshing which can be solved several hundred times faster than real time on a desktop PC. It is customised for individual LNG tank geometries. Vessel motions and filling levels are required to assess the sloshing severity.

The fast sloshing model is ideally suited for an onboard sloshing guidance system. It does not require any instrumentation in the LNG cargo tanks to obtain the sloshing response.

How does it work?

The fast sloshing model is based on the mathematical representation of a three dimensional pendulum with non-uniform natural frequencies. The influence of the tank shape and LNG properties are included by tuning the damping and restoring forces. When the model is customised for a certain tank shape, even violent chaotic sloshing is exactly replicated.

The model is tuned with existing vessel design information. Angular and linear accelerations and the filling level are the only inputs required to operate the model.

Successful validation has been carried out with state-of-the-art multiphase CFD and experiments. It has been shown that the sloshing model can predict regular and chaotic sloshing behaviours of fluids in a variety of tank shapes. In realistic blind simulations the correct sloshing response spectra and the unique sloshing time histories have been obtained.

Towards a sloshing guidance system

Evolving operating profiles make LNG carriers more vulnerable to sloshing damage. BMT SeaTech's sloshing model can determine the severity of LNG sloshing in fast time without resorting to instrumentation in the LNG tanks or the containment system. The fast time modelling capability can be used for advance predictions of the sloshing risk.

This lends the fast sloshing model to form an integral part of a non-intrusive onboard sloshing guidance system for LNG carriers. The concept has been validated successfully in a simulated environment. We are now seeking partners to test the proposed sloshing guidance system in operational conditions on an LNG carrier.

Date February 2008 Ref No. MSC 141.0

BMT SeaTech Ltd
Grove House, 7 Ocean Way, Ocean Village, Southampton, SO14 3TJ, UK
+44 (0) 23 8063 5122
www.bmtseatech.co.uk

Appendix F

Sloshing Guidance System concept: Presentation to SIGTTO

Real time sloshing detection with the Rapid Sloshing Model

SIGTTO Regional Forum
06 November 2008

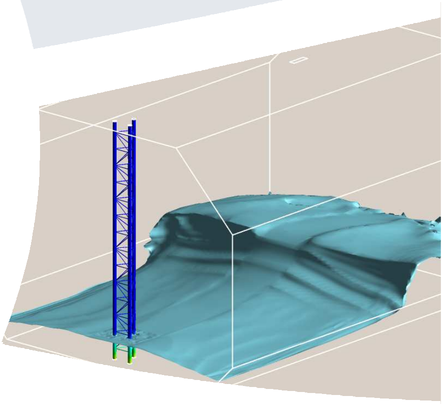

BMT SeaTech

Sloshing: an overview

What influences sloshing?

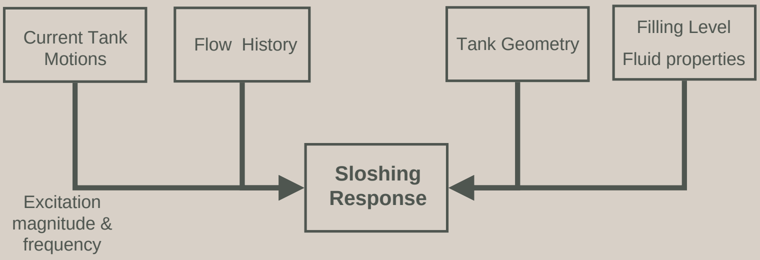

Current Tank Motions

Flow History

Tank Geometry

Filling Level
Fluid properties

Sloshing Response

Excitation magnitude & frequency

BMT SeaTech

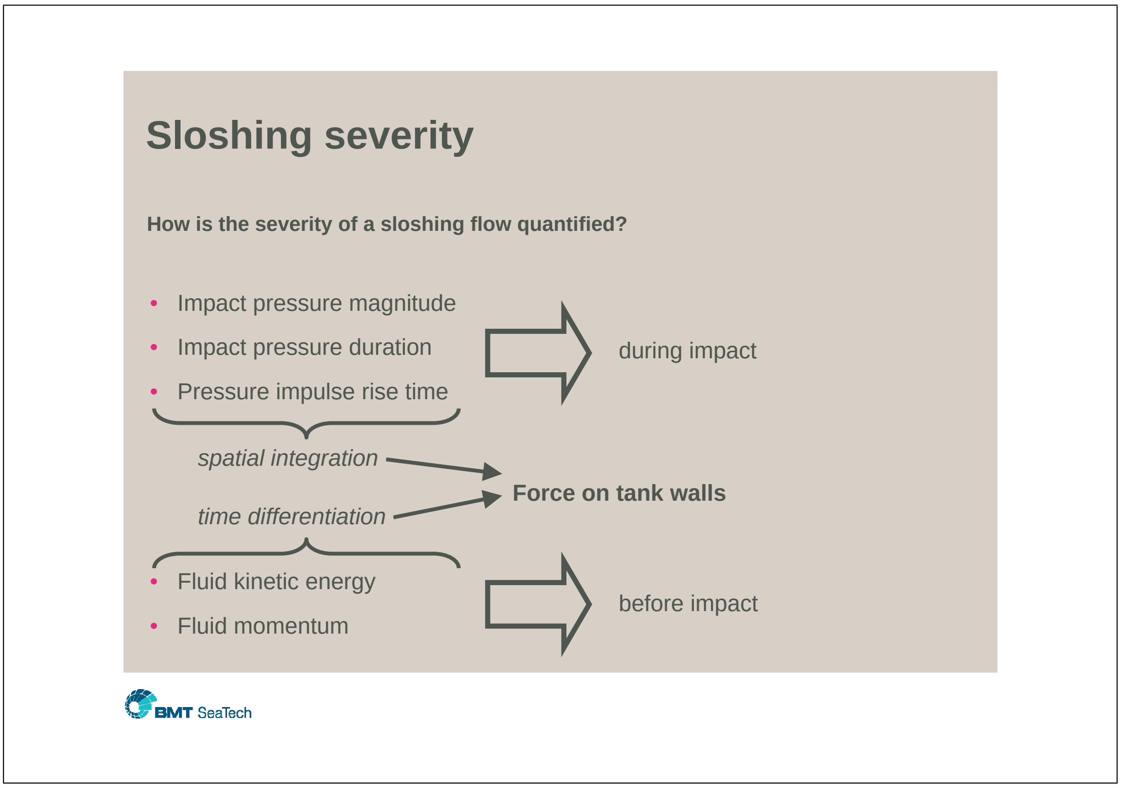

Sloshing severity

How is the severity of a sloshing flow quantified?

- Impact pressure magnitude
- Impact pressure duration
- Pressure impulse rise time

during impact

spatial integration

time differentiation

Force on tank walls

- Fluid kinetic energy
- Fluid momentum

before impact

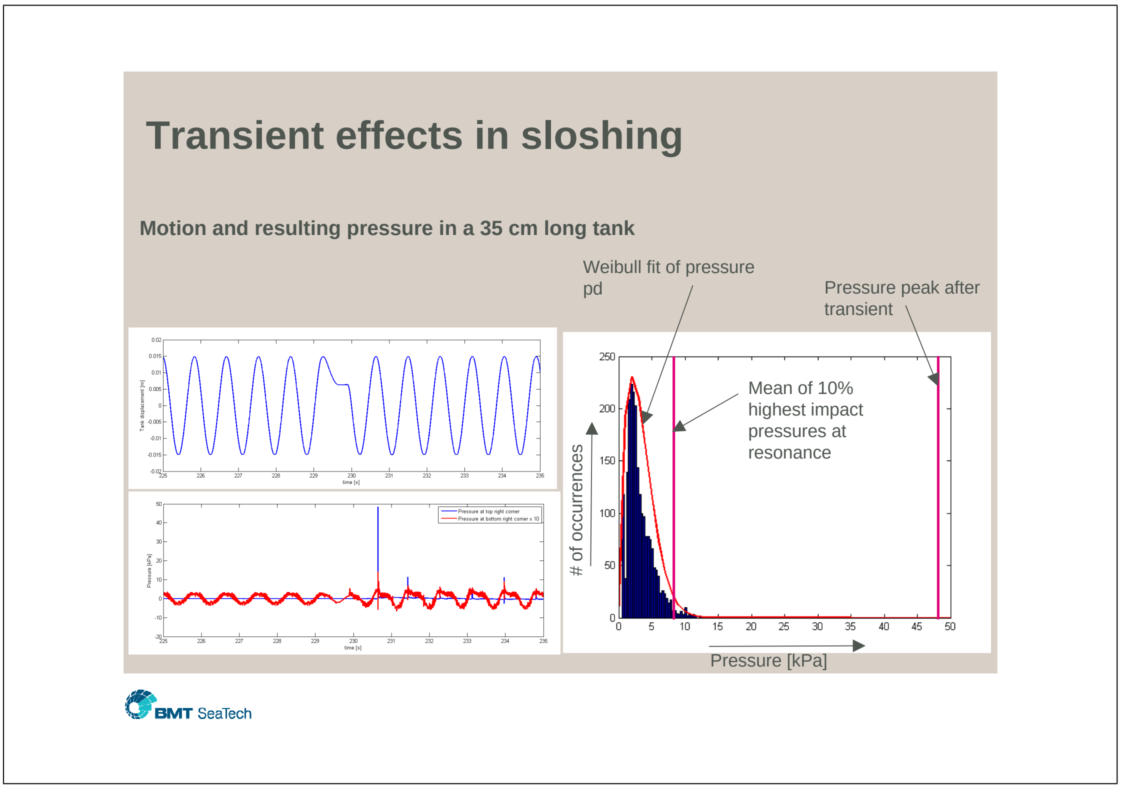

Transient effects in sloshing

Motion and resulting pressure in a 35 cm long tank

Weibull fit of pressure pd

Pressure peak after transient

Mean of 10% highest impact pressures at resonance

Avoid sloshing damage with an advisory system

Take the vessel motions to determine the sloshing response

The sloshing response depends on the:

- Tank geometry
- Filling level
- Excitation magnitude
- Excitation frequency
- Flow history

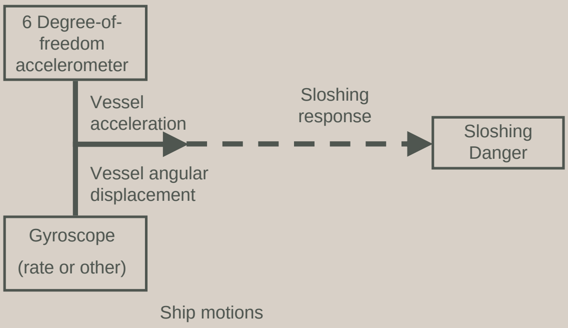

6 Degree-of-freedom accelerometer

Vessel acceleration

Vessel angular displacement

Gyroscope (rate or other)

Sloshing response

Sloshing Danger

Ship motions

Rapid sloshing model: how does it work?

Phenomenological modelling

- Represent sloshing with a simplified system
- Use existing design information to customise model
- Use on-board data with no intrusive instrumentation
- Include effects of pump tower, corrugation, etc.

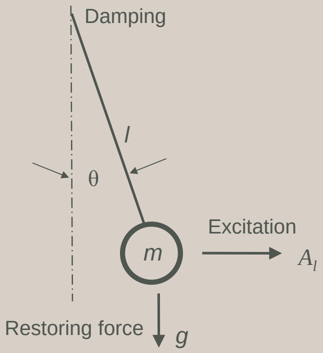

Validation

Regular, surge-induced sloshing at resonance: comparison between multiphase CFD and Rapid Sloshing Model*

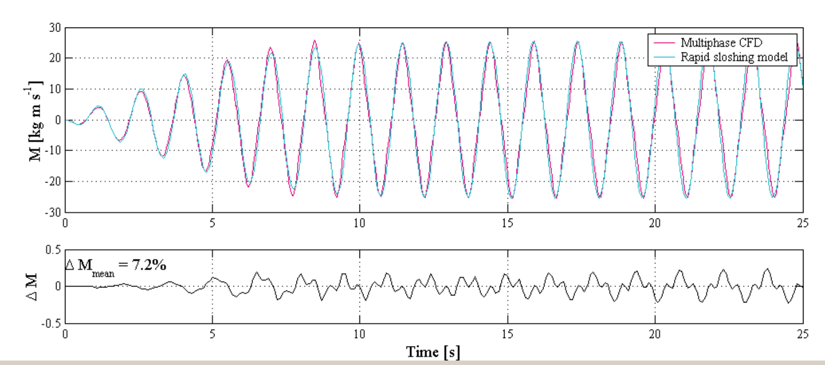

Godderidge, Turnock, Earl and Tan. Identification of Dangerous LNG Sloshing Using a Rapid Sloshing Model validated with CFD. ISOPE 2008.

BMT SeaTech

Validation

Regular, pitch-induced sloshing in transverse LNG tank cross section: comparison between multiphase CFD and Rapid Sloshing Model

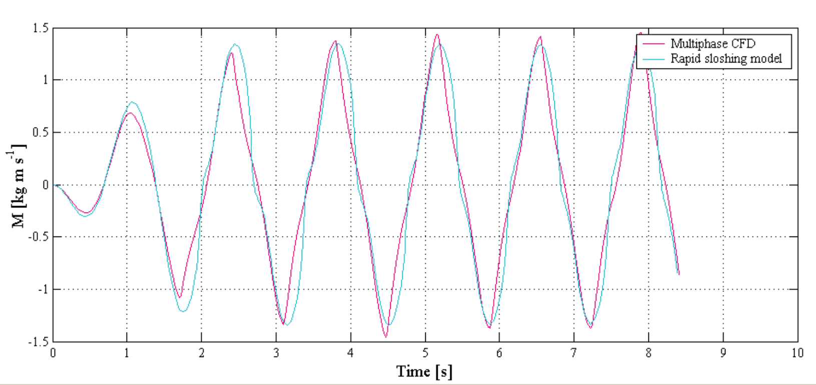

BMT SeaTech

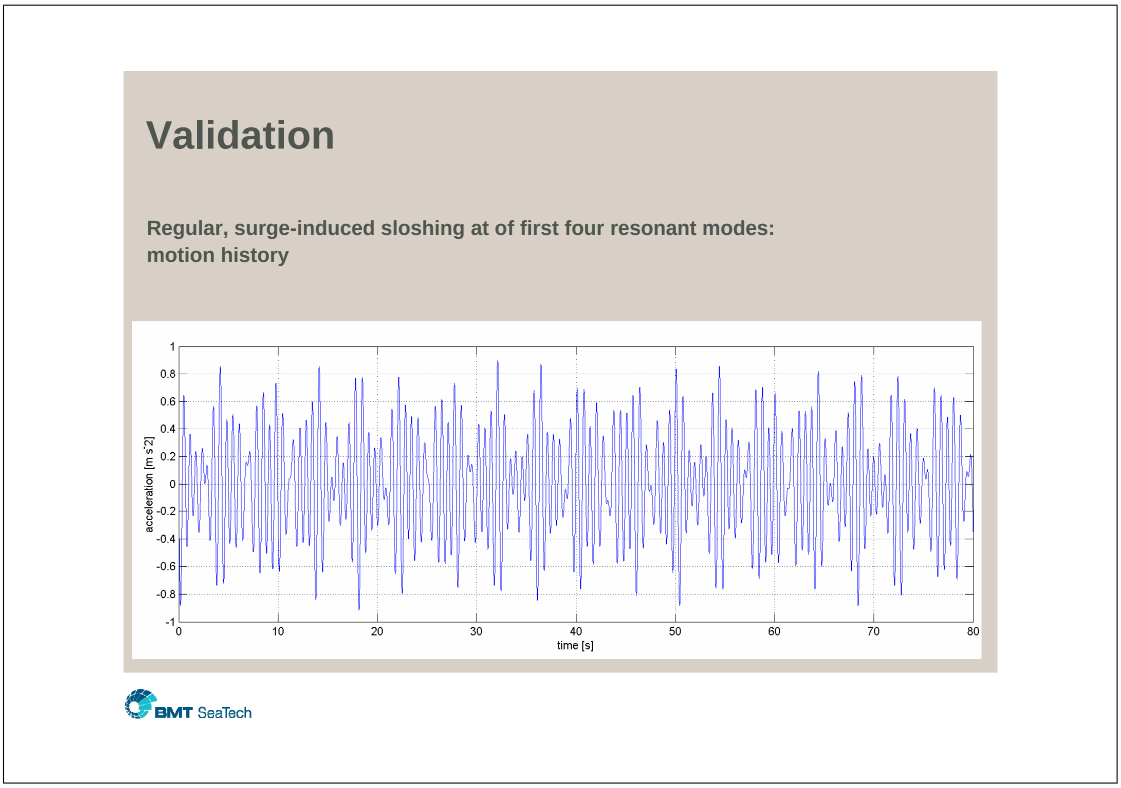

Validation

Regular, surge-induced sloshing at of first four resonant modes: motion history

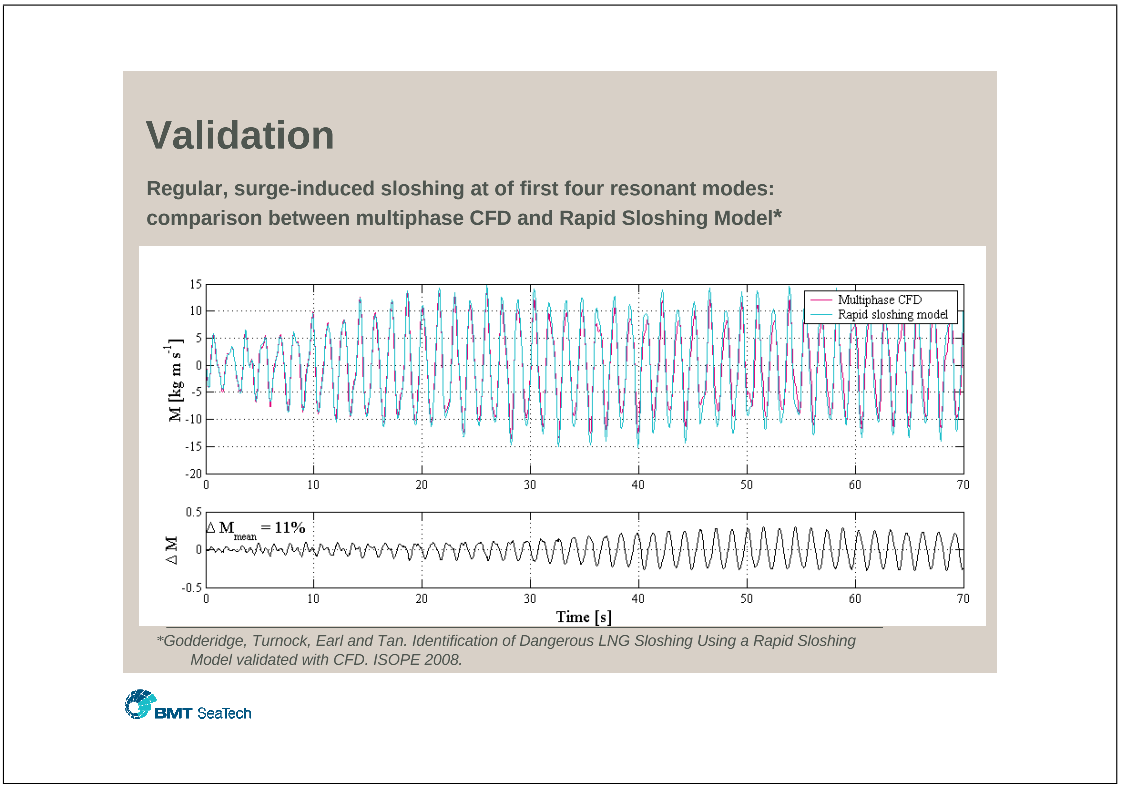

Validation

Regular, surge-induced sloshing at of first four resonant modes: comparison between multiphase CFD and Rapid Sloshing Model*

*Godderidge, Turnock, Earl and Tan. Identification of Dangerous LNG Sloshing Using a Rapid Sloshing Model validated with CFD. ISOPE 2008.

Validation

Longitudinal cross section with regular surge induced sloshing: bore formation, video

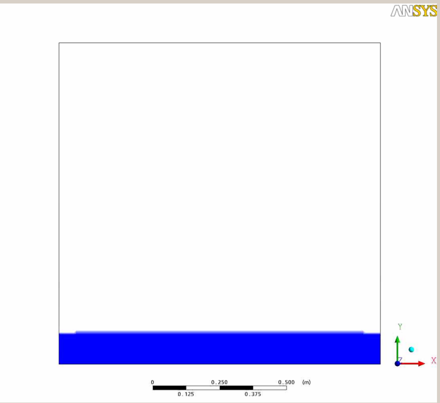

BMT SeaTech

Validation

Bore formation at low filling level: comparison between multiphase CFD and Rapid Sloshing Model

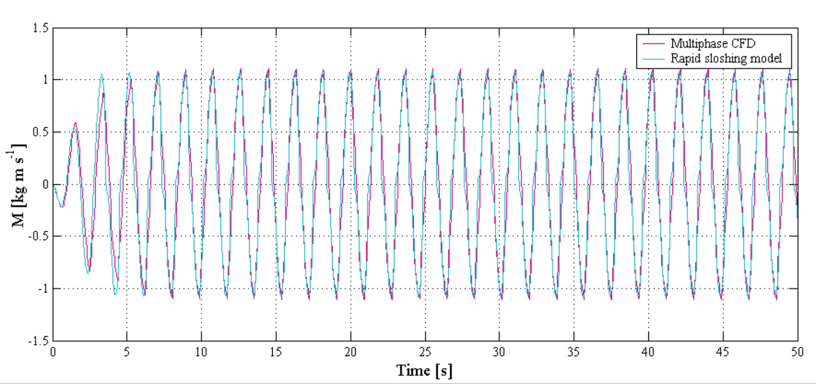

BMT SeaTech

Validation: proof of concept

- State-of-the art CFD is as good as the Rapid Sloshing Model
- The Rapid Sloshing Model simulates sloshing in 1/700th of real time
- Fast time prediction of dangerous LNG sloshing

Prediction of dangerous LNG sloshing

Application overview

- Random seaway defined by ITTC two parameter spectrum
- Motions scaled to experimental size (1:40 scale)
- Filling level 60% of tank height
- Rapid Sloshing Model set up using previous simulation at resonance

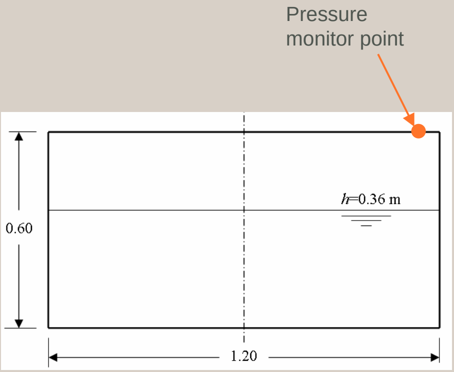

Prediction of dangerous LNG sloshing: motion profile

Longitudinal cross section with irregular surge: tank accelerations

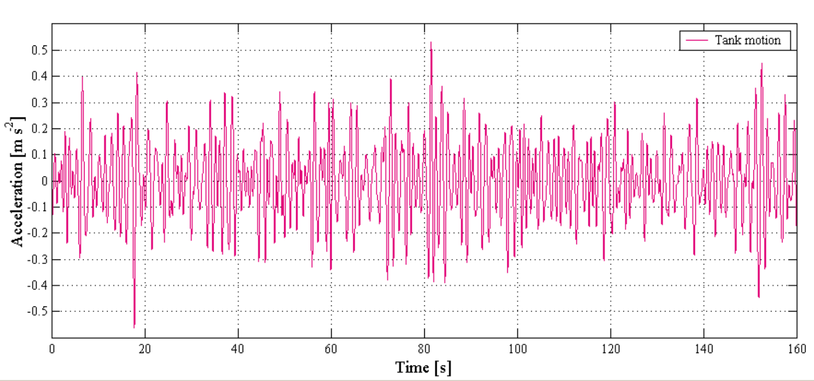

BMT SeaTech

Prediction of dangerous LNG sloshing: analysis

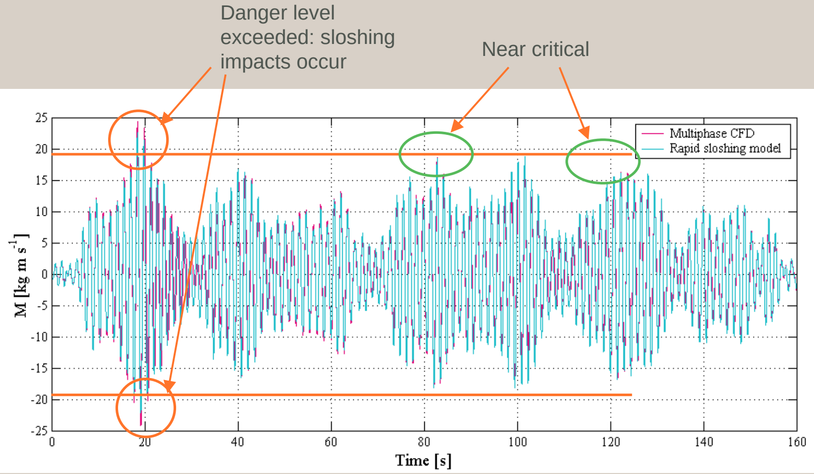
Danger level exceeded: sloshing impacts occur

Near critical

BMT SeaTech

Prediction of dangerous LNG sloshing: analysis

Pressure history at top right corner of tank

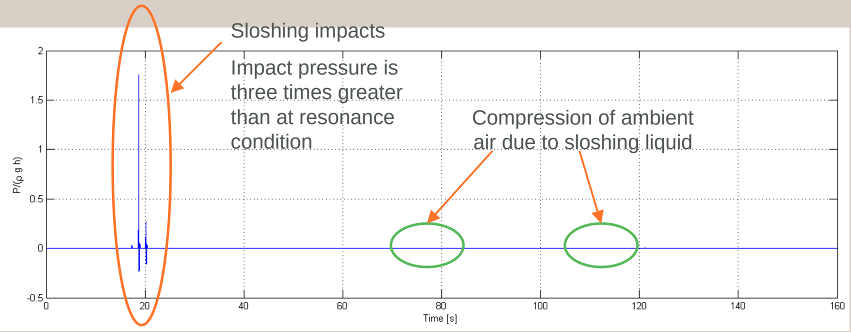

Sloshing impacts

Impact pressure is three times greater than at resonance condition

Compression of ambient air due to sloshing liquid

BMT SeaTech

Prediction of dangerous LNG sloshing: case study conclusions

- **Set up Rapid Sloshing Model with standard CFD or experimental data**

- **Simulate sloshing accurately with recorded tank (or LNGC) motion as input**

- **Identify occurrence and severity of sloshing impacts in fast time**

BMT SeaTech

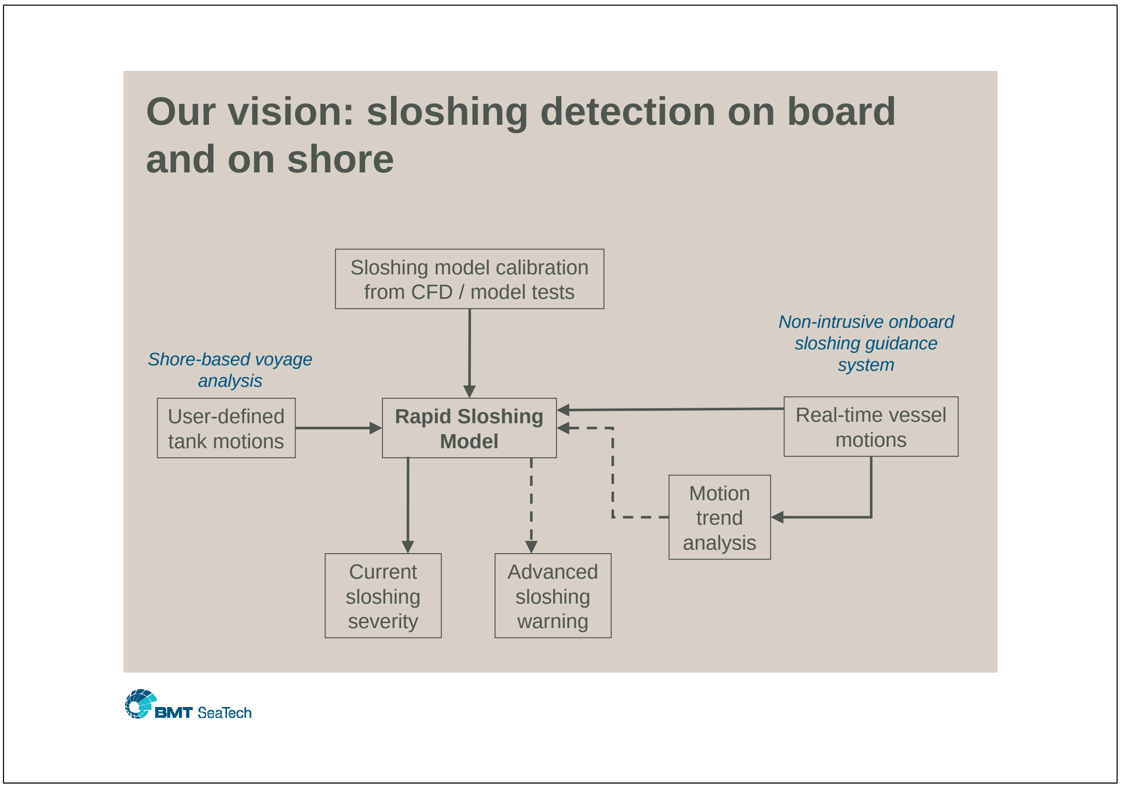

Our vision: sloshing detection on board and on shore

Sloshing model calibration from CFD / model tests

Shore-based voyage analysis

User-defined tank motions

Rapid Sloshing Model

Non-intrusive onboard sloshing guidance system

Real-time vessel motions

Motion trend analysis

Current sloshing severity

Advanced sloshing warning

BMT SeaTech

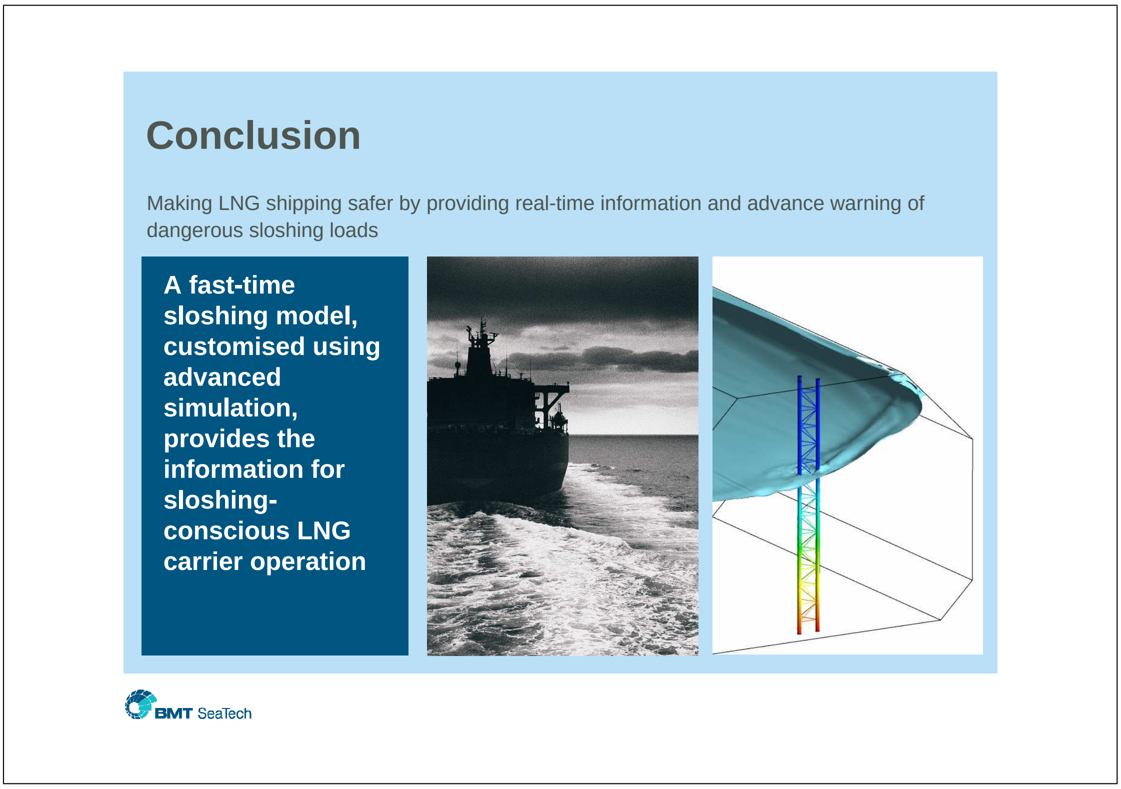

Conclusion

Making LNG shipping safer by providing real-time information and advance warning of dangerous sloshing loads

A fast-time sloshing model, customised using advanced simulation, provides the information for sloshing-conscious LNG carrier operation

BMT SeaTech

References

Abramson, H. (1966). The dynamic behavior of liquids in moving containers, with applications to space vehicle technology. Technical Report SP-106, National Aeronautics and Space Administration.

Abramson, H., Bass, R., Faltinsen, O., and Olsen, H. (1974). Liquid slosh in LNG carriers. In *10th Symposium on Naval Hydrodynamics*.

Abramson, H., Chu, W., and Kana, D. (1966). Some studies of nonlinear lateral sloshing in rigid containers. *Journal of Applied Mechanics 4*, 777–784.

Aliabadi, S., Johnson, A., and Abedi, J. (2003). Comparison of finite element and pendulum models for simulation of sloshing. *Computers and Fluids 32*, 535–545.

American Bureau of Shipping (2004). Dynamic strength analysis of membrane type LNG containment system due to sloshing impact load. Technical report, American Bureau of Shipping.

American Bureau of Shipping (2006). Guidance notes on strength assessment of membrane-type LNG containment systems under sloshing loads. Technical report, American Bureau of Shipping.

American Institute of Aeronautics and Astronautics (1998, January). *AIAA Guide for the Verification and Validation of Computational Fluid Dynamics Simulations* (AIAA Standards Series ed.). American Institute of Aeronautics and Astronautics.

Anderson, Jr, J. (1995). *Computational Fluid Dynamics: The Basics with Applications.* McGraw Hill, Inc.

ANSYS Inc (2005). *CFX-10 Users Guide.* ANSYS Inc.

ANSYS Inc (2007). *CFX-11 Users Guide.* ANSYS Inc.

Arswendy, A. and Moan, T. (2006). Sloshing response of LNG tank. In *25th International Conference on Offshore Mechanics and Arctic Engineering.*

aus der Wiesche, S. (2003). Computational slosh dynamics: Theory and industrial application. *Computational Mechanics 30*, 374–387.

aus der Wiesche, S. (2006). Noise due to sloshing within automotive fuel tanks. *Forschung im Ingenieurwesen 70*, 13–24.

Barth, T. and Jesperson, D. (1989). The design and application of upwind schemes on unstructured meshes. In *AIAA Paper 89-0366*.

Bass, R., Bowles, E., and Cox, P. (1980). Liquid dynamic loads in LNG cargo tanks. *SNAME Transactions 88*, 103–126.

Bass, R., Bowles, Jr, E., Trundell, R., Navickas, J., Peck, J., Yoshimura, N., Endo, S., and Pots, B. (1985). Modelling criteria for scaled LNG sloshing experiments. *Transactions of the American Society of Mechanical Engineers 107*, 272–280.

Benford, H. and Fox, W. (Eds.) (1993). *A Half Century of Maritime Technology*. Society of Naval Architects and Marine Engineers.

Bishop, R. and Price, W. (1979). *Hydroelasticity of Ships*. Cambridge University Press.

Brennen, C. (2005). *Fundamentals of Multiphase Flow*. Cambridge University Press, New York.

Bunnik, T. and Huijsmans, R. (2007). Large scale LNG sloshing model tests. In *Proceedings of the 17th International Offshore and Polar Engineering Conference*.

Chauvin, J. (1996). Membrane tank LNG carriers. *Revue de l'Institut Francais du Petrole 51*, 691–710.

Chen, Y., Djidjeli, K., and Price, W. (2009). Numerical simulation of liquid sloshing phenomena in partially filled containers. *Computers and Fluids 38*, 830–842.

Chester, W. (1968). Resonant oscillations in water waves. i. theory. *Philosophical Transactions of Royal Society: Mathematical, Physical and Engineering Sciences 306*, 5–22.

Chester, W. and Bones, J. (1968). Resonant oscillations in water waves. II. experiment. *Philosophical Transactions of Royal Society: Mathematical, Physical and Engineering Sciences 306*, 23–39.

Colagrossi, A. and Landrini, M. (2003). Numerical simulation of interfacial flows by smoothed particle hydrodynamics. *Journal of Computational Physics 191*, 448–475.

Colicchio, G. (2004). *Violent disturbance and fragmentation of free surfaces*. Ph. D. thesis, University of Southampton.

Corrignan, P. (1994). *Analyse Physique des Phenomenes Associes au Ballottement de Liquide dans des Reservoirs (Sloshing).* Ph. D. thesis, Universite de Nantes.

Crooks, E. (2007). Qatar plans LNG first. *Financial Times 13 March.*

Cuneo, J., Gilmore, G., and Tornay, E. (1981). Service experience with 125 000 m^3 LNG vessels of spherical tank design. *SNAME Transactions 88*, 127–150.

Dai, L., Xu, L., and Setiawan, B. (2004). A new non-linear approach to analysing the dynamic behaviour of tank vehicles subjected to liquid sloshing. *Proceedings of the Institution of Mechanical Engineers 219 (Multi-Body Dynamics)*, 75–86.

Decent, S. (1997). The nonlinear damping of parametrically excited two dimensional gravity waves. *Fluid Dynamics Research 19*, 201–217.

Department of Trade and Industry (2007, May). *Meeting the Energy Challenge.* HM Government.

Dias, F., Dutykh, D., and Ghidaglia, J. (2009). A two-fluid model for violent aerated flows. *Computers and Fluids (manuscript submitted).*

Directorate-General for Energy and Transport (2008, November). *Second Strategic Energy Review - Securing our Energy Future.* European Commission.

Dodge, F. (2000). The new dynamic behaviour of liquids in moving containers. Technical report, Southwest Research Institute.

Dogliani, M. (1994). EUROSLOSH summary report. Technical Report BE-4354, European Union.

Economist (2004, 26 August). The future's a gas. pp. 53–54.

Economist (2006, 7 January). Nervous energy. pp. 63–65.

El Moctar, O. (2006). Assessment for tankers. *Shipping World and Shipbuilder 204*, 28–31.

El-Sayad, M., Hanna, S., and Ibrahim, R. (1999). Parametric excitation of nonlinear elastic systems involving hydrodynamic sloshing impact. *Nonlinear Dynamics 18*, 25–50.

Escobedo, J. and Mansoori, G. (1996). Surface tension prediction for pure fluids. *AIChE Journal 42*(5), 1425–1433.

Faltinsen, O. (1974). A nonlinear theory of sloshing in rectangular tanks. *Journal of Ship Research 18*, 224–241.

Faltinsen, O. (1978). A numerical nonlinear method of sloshing in tanks with 2D flow. *Journal of Ship Research 22*, 193–202.

Faltinsen, O. (1993). *Sea Loads on Ships and Offshore Structures.* Cambridge University Press.

Faltinsen, O. and Rognebakke, O. (1999). Sloshing and slamming in tanks. In *13th International Conference on Hydrodynamics in Ship Design; 2nd International Symposium on Ship Manoeuvring*, pp. 160–168.

Faltinsen, O. and Rognebakke, O. (2000). Sloshing. In *NAV2000: International Conference on Ship and Ship Research, Venice.*

Faltinsen, O., Rognebakke, O., Lukovsky, I., and Timokha, A. (2000). Multidimensional modal analysis of nonlinear sloshing in a rectangular tank with finite water depth. *Journal of Fluid Mechanics 407*, 201–234.

Faltinsen, O., Rognebakke, O., and Timokha, A. (2003). Resonant three-dimensional nonlinear sloshing in a square-base basin. *Journal of Fluid Mechanics 487*, 1–42.

Faltinsen, O., Rognebakke, O., and Timokha, A. (2005). Resonant three-dimensional nonlinear sloshing in a square-base basin. part 2. effect of higher modes. *Journal of Fluid Mechanics 523*, 199–218.

Faltinsen, O., Rognebakke, O., and Timokha, A. (2006). Resonant three-dimensional nonlinear sloshing in a square-base basin. part 3. base ratio perturbations. *Journal of Fluid Mechanics 551*, 93–116.

Faltinsen, O. and Timokha, A. (2001). An adaptive multimodal approach to nonlinear sloshing in a rectangular tank. *Journal of Fluid Mechanics 432*, 167–200.

Faltinsen, O. and Timokha, A. (2002). Asymptotic modal approximation of nonlinear resonant sloshing in a rectangular tank with small fluid depth. *Journal of Fluid Mechanics 470*, 319–357.

Fay, J. (2007). Spread of large LNG pools on the sea. *Journal of Hazardous Materials 140*, 541–551.

Ferziger, J. and Peric, M. (2002). *Computational Methods for Fluid Dynamics.* Axel-Springer Verlag.

Ffooks, R. (1993). *Natural Gas by Sea: The Development of a new Technology.* Witherby.

Finnemore, E. and Franzini, J. (2002). *Fluid mechanics with engineering applications.* McGRaw-Hill.

Forestier, J. and Austin, S. (2009). Hull structure monitoring system and VDR. Technical Report D20-D21-D22, University of Southampton.

Fox, D. and Kuttler, J. (1983). Sloshing frequencies. *Journal of Applied Mathematics and Physics 34*, 668–696.

Frandsen, J. (2004). Sloshing motions in excited tanks. *Journal of Computational Physics 196*, 53–87.

Gaillarde, G., Ledoux, A., and Lynch, M. (2004). Coupling between LNG and vessels motion for partially filled tanks: effect on seakeeping. In *Royal Institution of Naval Architects: Design and Operation of Gas Carriers.*

Gertsch, J., McLanders, A., Rogers, S., Schroedel, S., Taliwal, V., and Wilson, C. (2004, December). Curve rollover warning system for trucks. World Intellectual Property Organization. Publication Number: WO 2004/110809 A1.

Gingold, R. and Monaghan, J. (1977). Smoothed particle hydrodynamics: theory and application to non-spherical stars. *Monthly Notices of the Royal Astronomical Society 181*, 375–389.

Ginsburg, H.-J. and Bläske, G. (2007). Wir können sparen: Interview with Claude Mandil, International Energy Agency Executive Director. *WirtschaftsWoche 26*, 26–29.

Godderidge, B. (2004). Numerical simulation of two dimensional viscous free surface flow using a particle method. Master's thesis, University of Southampton.

Godderidge, B. (2008a). Adaptive second order time marching scheme validation. Technical report, University of Southampton.

Godderidge, B. (2008b). Unsteady rotational forces in the moving frame of reference model for CFX-11. Technical report, University of Southampton.

Godderidge, B., Cowlan, N., and Schreier, S. (2009). A rapid sloshing model for LNG carriers - increased operational safety and reduced design analysis times. In *24th Gastech Conference.*

Godderidge, B., Tan, M., Earl, C., and Turnock, S. (2007). Boundary layer resolution for modeling of a sloshing liquid. In *Proceedings of the 17th International Offshore and Polar Engineering Conference.*

Godderidge, B., Tan, M., and Turnock, S. (2006). A verification and validation study of the application of computational fluid dynamics to the modelling of lateral sloshing. Ship Science Report 140, University of Southampton.

Godderidge, B., Tan, M., Turnock, S., and Earl, C. (2007). Grid resolution for the simulation of sloshing using CFD. In *10th Numerical Towing Tank Symposium.*

Godderidge, B., Turnock, S., Cowlan, N., and Tan, M. (2009a). A rapid method for the simulation of sloshing; Part I: A mathematical model based on the pendulum equation. *Computers and Fluids*. submitted for review.

Godderidge, B., Turnock, S., Cowlan, N., and Tan, M. (2009b). A rapid method for the simulation of sloshing; Part II: Sloshing in rectangular and octagonal containers at intermediate filling levels. *Computers and Fluids*. submitted for review.

Godderidge, B., Turnock, S., Cowlan, N., and Tan, M. (2009c). Sloshing symposium comparative study: Simulation of lateral sloshing with multiphase cfd. In *Proceedings of the 19th International Offshore and Polar Engineering Conference*.

Godderidge, B., Turnock, S., Earl, C., and Tan, M. (2008). Identification of dangerous LNG sloshing using a rapid sloshing model validated with CFD. In *Proceedings of the 19th International Offshore and Polar Engineering Conference*.

Godderidge, B., Turnock, S., Earl, C., and Tan, M. (2009). Effect of fluid compressibility on the simulation of sloshing. *Ocean Engineering*. in press.

Godderidge, B., Turnock, S., Tan, M., and Earl, C. (2009). An investigation of multiphase CFD modelling of a lateral sloshing tank. *Computers and Fluids 38*, 183–193.

Graczyk, M., Moan, T., and Rognebakke, O. (2006). Probabilistic analysis of characteristic pressure for LNG tanks. *Journal of Offshore Mechanics and Arctic Engineering 128*, 133–144.

Graham, E. and Rodriguez, A. (1952). The characteristics of fuel motion which affect airplane dynamics. *Journal of Applied Mechanics September*, 381–388.

Hadzic, I., Mallon, F., and Peric, M. (2002). Numerical simulation of sloshing. Technical report, Technische Universität Hamburg-Harburg.

Hamlin, N. (1990). Liquid sloshing in cargo tanks. Technical Report SSC-336, Ship Structure Committee.

Hamlin, N., Lou, Y., Maclean, W., Seibold, F., and Chandras, L. (1986). Liquid sloshing in slack ship tanks - theory, observations and experiments. *SNAME Transactions 94*, 159–195.

Hansen, H. (1976). Damage experience, potential damages, current problems involving slosh considerations. In *Seminar on Liquid Sloshing*. Det Norske Veritas.

Harlow, F. and Welch, J. (1965). Numerical calculation of time-dependent viscous incompressible flow of fluid with free surface. *Physics of Fluids 8*, 2182–2189.

Henderson, D. and Miles, J. (1994). Surface-wave damping in a circular cylinder with a fixed contact line. *Journal of Fluid Mechanics 275*, 285–299.

Hinatsu, M. (2001). Experiments of two-phase flows for the joint research. In *Proceedings of SRI-TUHH mini-Workshop on Numerical Simulation of Two-Phase Flows*. National Maritime Research Institute & Technische Universität Hamburg-Harburg: NMRI.

Hine, L. (2008). GTT tweaks blueprints to combat sloshing damage. *LNG Unlimited 28 November*, 6.

Hirsch, C. (1988). *Numerical Computation of Internal and External Flows. Vol 1: Fundamentals of Numerical Discretisation*. John Wiley and Sons.

Hirt, C. and Nichols, B. (1981). Volume of fluid (VOF) method for the dynamics of free boundaries. *Journal of Computational Physics 39*, 201–225.

Huang, Z., Esenkov, O., o'Donnel, B., Yung, T., and Sandström, R. (2007). Improved predictions of full-scale roll motions for vessels with large liquid tanks. In *Proceedings of the 17th International Offshore and Polar Engineering Conference*.

Hull, P. and Muller, G. (2002). An investigation of breaker heights, shapes and pressures. *Ocean Engineering 29*, 59–79.

Ibrahim, R. (2005). *Liquid Sloshing Dynamics*. Cambridge University Press.

Ibrahim, R. and El-Sayad, M. (1999). Simultaneous parametric and internal resonances in systems involving strong non-linearities. *Journal of Sound and Vibration 225*, 857–885.

Ishii, M. and Hibiki, T. (2006). *Thermo-Fluid Dynamics of Two-Phase Flow*. Springer Verlag.

Ishimaru, J., Kawabata, K., Morita, H., Ikkai, H., and Suetake, Y. (2004). Building of advanced large sized membrane type LNG carrier. *Mitsubishi Heavy Industries Technical Review 41*, 1–7.

Ivings, M., Lea, C., Ledin, H., Pritchard, D., Santon, R., and Saunders, C. (2004). Outstanding safety questions concerning the use of gas turbines for power generationsummary report. Technical report, Health and Safety Laboratory, HM Government Health and Safety Executive.

Jensen, J. (2002). LNG and pipeline economics. In *The Geopolitics of Gas Meeting*. James A. Baker III Institute for Public Policy, Rice University and Program on Energy and Sustainable Development, Stanford University.

Jeon, S., Kim, H., Park, J., Kwon, S., Ryu, M., Hwang, Y., and Jung, J. (2008). Experimental investigation of scale effect in sloshing phenomenon. In *27th Symposium on Naval Hydrodynamics.*

Kaminski, M., Besnier, F., Du, S., Ergin, A., Hermundstad, O., Hong, S., Iaccarino, R., Liu, J., Mumm, H., Murawski, L., and Shuri, H. (2006). Committee II.2 Dynamic Response. In *16th International Ship and Offshore Structures Congress*, pp. 287.

Keulegan, G. (1959). Energy dissipation in standing waves in rectangular basins. *Journal of Fluid Mechanics 6*, 33–50.

Kieffer, S. (1977). Sound speed in liquid-gas mixtures: Water-air and water-steam. *Journal of Geophysical Research B: Solid Earth 82*, 2895–2904.

Kim, J., Kim, K., Kim, P., and Shin, Y. (2005). Sloshing-ship motion coupling effect for the sloshing impact load on the LNG containment system. In *Proceedings of the 15th International Offshore and Polar Engineering Conference.*

Kim, M., Kim, D., Kang, S., and Lee, J. (2006). An interlaminar strain measurement for insulation panels of LNG carriers. *Strain 42*, 97–106.

Koshizuka, S., Nobe, A., and Oka, Y. (1998). Numerical analysis of breaking waves using the moving particle semi-implicit method. *International Journal for Numerical Methods in Fluid 26*, 751–769.

Koshizuka, S. and Oka, Y. (1996). Moving particle semi-implicit method for fragmentation of incompressible fluid. *Nuclear Science and Engineering 123*, 421–434.

Koshizuka, S., Tamako, H., and Oka, Y. (1995). A particle method for incompressible viscous flow with fluid fragmentation. *Computational Fluid Dynamics Journal 4*, 29–46.

Lamb, H. (1879). *Hydrodynamics.* Cambridge University Press.

Lanczos, C. (1986). *The Variational Principles of Mechanics.* Dover Publications.

Lea, C. (2003). Guidance for NSD on the assessment of CFD simulations in safety cases. Technical report, Health and Safety Laboratory, HM Government Health and Safety Executive.

Lee, D., Kim, M., Kwon, S., Kim, J., and Lee, Y.-B. (2007). A parametric sensitivity study on LNG tank sloshing loads by numerical simulations. *Ocean Engineering 34*, 3–9.

Lee, Y.-B., Godderidge, B., Temarel, P., Tan, M., Turnock, S., and Cowlan, N. (2009). Coupling between ship motion and sloshing using potential flow analysis and pendulum modelling. In *Proceedings of the 19th International Offshore and Polar Engineering Conference.*

Lepelletier, T. and Raichlen, F. (1988). Nonlinear oscillations in rectangular tanks. *Journal of Engineering Mechanics 114*, 1–23.

Lewis, S., Hudson, D., and Turnock, S. (2008). Improvement to body impact predictions using CFD through analysis of an unsteady boundary layer. In *11th Numerical Towing Tank Symposium.*

Liddle, D. (2009, February). Containment systems for LNG ships. Presentation to the Southern Joint Branch at the University of Southampton.

Liu, G. and Liu, M. (2003). *Smoothed Particle Hydrodynamics: a Meshfree Particle Method*. World Scientific Publishing.

Lloyd, A. (1989). *Seakeeping: Ship Behaviour in Rough Weather.* Ellis Horwood, Chichester.

Lloyd's Register (2005). Comparative sloshing analysis of LNG ship containment systems. ShipRight Additional Design Procedures.

Lloyds Register (2008). Guidance on the operation of membrane LNG ships to reduce the risk of damage due to sloshing. Technical report, Lloyds Register.

Lloyd's Register (2009). Sloshing assessment guidance document for membrane tank LNG operations. ShipRight Additional Design Procedures.

Lloyd's Register Denmark (2007). Risk assessment of operation of LNG tankers. In *LNG Conference 12-06-2007: Liquefied Natural Gas - the energy source of the future.*

Lucy, L. (1977). A numerical approach to the testing of the fission hypothesis. *Astronomical Journal 82*, 10131024.

Lugni, C., Brocchini, M., Dolcini, A., Palladino, F., Bulgarelli, U. P., and Faltinsen, O. M. (2005). An experimental investigation on the flip-through phenomenon. In *20th International Workshop on Water Waves and Floating Bodies.*

Lugni, C., Brocchini, M., and Faltinsen, O. (2006). Wave impact loads: The role of the flip-through. *Physics of Fluids 18*(12), 122101.

MacDonald, J. (2005). Structural and containment system design aspects of large LNG ships. In *Norshipping 2005.*

MacDonald, J. and Maguire, J. (2008). Lloyd's register's guidance on the operation of membrane LNG ships to avoid the risk of sloshing damage. In *23rd Gastech Conference and Exhibition, Bangkok*.

Malenica, S., Mravak, Z., Besse, P., Kaminski, M., and Bogaert, H. (2009). Full scale experiments and new methodology to assess the structural behaviour of a membrane LNGC containment system under breaking waves project SLOSHEL. In *24th Gastech Conference*.

Malenica, S., Zalar, M., and Chen, X. (2003). Dynamic coupling of seakeeping and sloshing. In *13th International Conference for Offshore and Polar Engineering*.

Mann, D. (Ed.) (1977). *LNG Materials and Fluids*. Cryogenics Division, National Bureau of Standards.

Martel, C., Nicolas, J., and Vega, J. (1998). Surface-wave damping in a brimful circular cylinder. *Journal of Fluid Mechanics 360*, 213–228.

Martin, J. and Moyce, W. (1952). An experimental study of the collapse of liquid columns on a rigid horizontal plane, in a medium of lower, but comparable, density. *Philosophical Transactions of the Royal Society of London. Series A, Mathematical and Physical Sciences 244*, 325–334.

Mathworks, Inc (2007). *MATLAB 2007b Users Guide*. Mathworks, Inc.

Melamies, I. (2007). Liquid gas transport: economically and safely thanks to plasma pretreatment. *Adhesion 6*, 12–15.

Mikelis, N. and Journee, J. (1984). Experimental and numerical simulations of sloshing behaviour in liquid cargo tanks and its effect on ship motions. In *National Conference on Numerical Methods for Transient and Coupled Problems*.

Mikelis, N., Miller, J., and Taylor, K. (1984). Sloshing in partially filled liquid tanks and its effect on ship motions: numerical simulations and experimental verification. *RINA Transactions 1*, 267–281.

Miles, J. (1967). Surface-wave damping in closed basins. *Proceedings of the Royal Society of London 297*, 459–475.

Mokhatab, S. and Wood, D. (2007). Breaking the offshore LNG stalemate. *World Oil 228*(4).

Molin, B., Remy, F., Rigaud, S., and Jouette (de), C. (2002). LNG-FPSOs: frequency domain, coupled analysis of support and liquid cargo motions. In *10th Congress of the International Maritime Association of the Mediterranean*.

Molteni, D. and Colagrossi, A. (2008). Oblique impact of a jet on a plane surface solved by SPH: suggestions to improve the results of the pressure profiles. In *3rd SPHERIC Workshop*.

Monteiro Marques, M. (1994). An existence, uniqueness and regularity study of the dynamics of systems with one-dimensional friction. *European Journal of Mechanics 13*, 277–306.

Nakamura, A. and Manabe, R. (2007). LNG-FPSO: A key technology for natural gas era. In *17th International Offshore and Polar Engineering Conference*.

Oil Online (2006, 24 April). Lloyd's Register to class world's largest LNG ships.

Okhotsimskii, O. (1960). Theory of the motion of a body with cavities partially filled with liquid. Technical Report TT-F-33, NASA.

Olsen, H. (1976a). Local impact pressures in basically prismatic tanks. In *Seminar on Liquid Sloshing*. Det Norske Veritas.

Olsen, H. (1976b). What is sloshing? In *Seminar on Liquid Sloshing*. Det Norske Veritas.

Paik, J. (2006). Limit state design technology for a membrane type liquid natural gas cargo containment system under sloshing impacts. *Marine Technology 43*, 126–134.

Peregrine, D. (2003). Water-wave impact on walls. *Annual Review of Fluid Mechanics 35*, 23–43.

Peters, R. (2003). Nonlinear damping of the linear pendulum. Available on arxiv http://arxiv.org/abs/physics/0306081.

Pilipchuk, V. and Ibrahim, R. (1997). The dynamics of a non-linear system simulating liquid sloshing impact in moving structures. *Journal of Sound and Vibration 205*, 593–615.

Pilipchuk, V. and Ibrahim, R. (2000). Dynamics of a two-pendulum model with impact interaction and an elastic support. *Nonlinear Dynamics 21*, 221–247.

Pope, S. (2000). *Turbulent Flows*. Cambridge University Press.

Price, W. and Chen, Y. (2006). A simulation of free surface waves for incompressible two-phase flows using a curvilinear level set formulation. *International Journal for Numerical Methods in Fluids 51*, 305–330.

QNET CFD (2002). Turbulence modelling: Part 2: Limitations of k-epsilon model. In *QNET CFD*.

Reddy, D. and Radosavljevic, D. (2006). Verification of numerical methods applied to sloshing studies in membrane tanks of LNG ships. In *ICSOT 2006, The Royal Institution of Naval Architects.*

Rhee, S. (2005). Unstructured grid based Reynolds-Averaged Navier-Stokes method for liquid tank sloshing. *Transactions of the American Society of Mechanical Engineers 127*, 572–582.

Rhie, C. and Chow, W. (1982). A numerical study of the turbulent flow past an isolated airfoil with trailing edge separation. In *AIAA Paper 82-0998.*

Rizzuto, E. and Tedeschi, R. (1997). Surveys of actual sloshing loads onboard of ships at sea. In *NAV 97: International Conference on Ship and Marine Research.*

Roache, P. (1997). Quantification of uncertainty in Computational Fluid Dynamics. *Annual Review of Fluid Mechanics 29*, 123–160.

Rognebakke, O. and Faltinsen, O. (2003). Coupling of sloshing and ship motions. *Journal of Ship Research 47*, 208–221.

Rognebakke, O. and Faltinsen, O. (2005). Sloshing impact with air cavity in rectangular tank with a high filling ratio. In *20th International Workshop on Water Waves and Floating Bodies.*

Rose, J. and Burnay, S. (2008, March). Gastech 2008 visit report. BMT SeaTech Internal Report.

Rouvari Oy (2005). Sloshing monitoring at sea on LNG carriers. Museokatu 9B, 00100 Helsinki, Finland. Company Brochure.

Rumold, W. (2001). Modeling and simulation of vehicles carrying liquid cargo. *Multibody System Dynamics 5*, 351–374.

Saunders, C. (2003). Outstanding safety questions concerning the analysis of ventilation and gas dispersion in gas turbine enclosures: Best practice guidelines on in-situ testing. Technical report, Health and Safety Laboratory, HM Government Health and Safety Executive.

Schreier, S., Godderidge, B., Paschen, M., Turnock, S., M.Tan, and Cowlan, N. (2009). Assessment of transient sloshing due to encounter of an LNG carrier with a steep wave. In *29th Conference for Offshore Mechanics and Arctic Engineering.*

Schreier, S. and Paschen, M. (2008). Sloshing in LNG tanks assessment of high and low pressures. In *27th International Conference on Offshore Mechanics and Arctic Engineering.*

Select Committee on Business and Enterprise (2008). Business and enterprise - eleventh report.

Setzmann, U. and Wagner, W. (1991). A new equation of state and tables of thermodynamic properties for methane covering the range from the melting line to 625 K at pressures up to 1000 MPa. *Journal of Physical and Chemical Reference Data 20*, 1061–1151.

Shampine, L. and Gordon, M. (1975). *Computer Solution of Ordinary Differential Equations.* W.H. Freeman and Co.

Sherstyuk, A. (2000). Speed of sound in a homogeneous liquid-gas mixture. *Chemical and Petroleum Engineering 36*, 363–366.

Shin, Y., Kim, J., Lee, H., and Hwang, C. (2003). Sloshing impact of LNG cargoes in membrane containment systems in the partially filled condition. Technical report, American Bureau of Shipping.

Simonsen, C. and Stern, F. (2003). Verification and validation of RANS maneuvering simulation of esso osaka: effects of drift and rudder angle on forces and moments. *Computers and Fluids 32*, 1325–1356.

Speziale, C., Sarkar, S., and Gatsi, T. (1991). Modelling the pressure-strain correlation of turbulence: an invariant dynamical systems approach. *Journal of Fluid Mechanics 227*, 245–272.

Standing, R., Amaratunga, S., Lopez-Calleja, F., Orme, S., and Eichaker, R. (2003). Marine hydrodynamics modelling using CFD. In *CFD 2003: Computational Fluid Dynamics Technology in Ship Hydrodynamics.*

Stern, F., Wilson, R., Coleman, H., and Paterson, E. (2001). Comprehensive approach to verification and validation of CFD simulations - Part 1: methodology and procedures. *Journal of Fluids Engineering 123*, 793–802.

Strogatz, S. (1994). *Nonlinear Dynamics and Chaos.* Perseus Book Publishing.

Sumner, I., Stofan, A., and Shramo, D. (1964). Experimental sloshing characteristics and a mechanical analogy of liquid sloshing in a scale-model centaur liquid oxygen tank. Technical Report TM X-999, National Aeronautics and Space Administration.

Sussman, M., Smareka, P., and Osher, S. (1994). A level set approach for computing solutions to incompressible two-phase flows. *Journal of Computational Physics 114*, 146–159.

Teekay LNG Partners, LP (2006). *Annual Report.* United States Securities and Exchange Commission.

Thompson, J., Soni, B., and Weatherill, N. (Eds.) (1999). *Handbook of Grid Generation.* CRC Press.

Tinsley, D. (2007). DNV study to track LNG sloshing forces. *Lloyds List 29 May*, 4.

Todd, M. and Vohra, S. (1998). Transient dynamics of a lightly damped, roll-forced pendulum. *Dynamical Systems 13*, 95–115.

Topliss, M., Cooker, M., and Peregrine, D. (1992). Pressure oscillations during wave impact on vertical walls. In *23rd International Conference on Coastal Engineering.* American Society of Civil Engineers.

Valsgard, S. and Tveitnes, T. (2003). LNG technological developments and innovations challenges with sloshing model testing. AS Paper Series 2003-P005, Det Norske Veritas.

Versteeg, H. and Malalasekera, W. (1995). *An Introduction to Computational Fluid Dynamics: The Finite Volume Method.* Prentice Hall.

vom Baur, M. (2009, January). Floating production and terminal units for LNG: State of development and challenges. Presentation at Rostock University.

Wagner, W., Cooper, J., Dittmann, A., Kijima, J., Kretzschmar, H.-J., Kruse, A., Mares, R., Oguchi, K., Sato, H., Stöcker, I., Sifner, O., Takaishi, Y., Tanishita, I., Trüenbach, J., and Willkommen, T. (2000). The IAPWS industrial formulation 1997 for the thermodynamic properties of water and steam. *Journal of Engineering for Gas Turbines and Power 122*, 150–182.

Waterhouse, D. (1994). Resonant sloshing near a critical depth. *Journal of Fluid Mechanics 281*, 313–318.

Wilcox, D. (1998). *Turbulence Modelling for CFD.* DCW Industries.

Wilson, R., Stern, F., Coleman, H., and Paterson, E. (2001). Comprehensive approach to verification and validation of CFD simulations - Part 2: application for RANS simulation of a cargo/container ship. *Journal of Fluids Engineering 123*, 803–810.

Wolfson Unit for Marine Technology and Industrial Aerodynamics (2000). *Shipmotions user manual.* Wolfson Unit for Marine Technology and Industrial Aerodynamics.

WS Atkins Consultants (2003). MARNET best practice guidelines for marine applications of computational fluid dynamics. Technical report, MARNET.

Xing, J. (1992). *User Manual: Fluid-structure interaction analysis program-FSIAP*. University of Southampton.

Yeung, R., Liao, S.-W., and Rodier, D. (1998). Hydrodynamic coefficients of rolling rectangular cylinders. *International Journal of Offshore and Polar Engineering 8*, 241–250.

Zwart, P. (2004). Numerical modelling of free surface and cavitating flows. *Industrial two-phase flow CFD: von Karman Institute Lecture Series 2004-2005*, 25.